

UNITED STATES AIR FORCE
SUMMER RESEARCH PROGRAM -- 1997
SUMMER FACULTY RESEARCH PROGRAM FINAL REPORTS

VOLUME 3A
PHILLIPS LABORATORY

RESEARCH & DEVELOPMENT LABORATORIES

5800 Uplander Way
Culver City, CA 90230-6608

Program Director, RDL
Gary Moore

Program Manager, AFOSR
Major Linda Steel-Goodwin

Program Manager, RDL
Scott Licoscas

Program Administrator, RDL
Johnetta Thompson

Program Administrator
Rebecca Kelly-Clemmons

Submitted to:

AIR FORCE OFFICE OF SCIENTIFIC RESEARCH
Bolling Air Force Base
Washington, D.C.
December 1997

20010319 060

AQM01-06-1200

REPORT DOCUMENTATION PAGE

Public reporting burden for this collection of information is estimated to average 1 hour per response, including the time for reviewing the collection of information. Send comments regarding this burden estimate or any other aspect of this collection of information, Operations and Reports, 1215 Jefferson Davis Highway, Suite 1204, Arlington, VA 22202-4302, and to the Office of Management and

AFRL-SR-BL-TR-00-

Completing and reviewing
this report for information

0753

1. AGENCY USE ONLY (Leave blank)		2. REPORT DATE December, 1997	
4. TITLE AND SUBTITLE 1997 Summer Research Program (SRP), Summer Faculty Research Program (SFRP), Final Reports, Volume 3A, Phillips Laboratory		5. FUNDING NUMBERS F49620-93-C-0063	
6. AUTHOR(S) Gary Moore			
7. PERFORMING ORGANIZATION NAME(S) AND ADDRESS(ES) Research & Development Laboratories (RDL) 5800 Uplander Way Culver City, CA 90230-6608		8. PERFORMING ORGANIZATION REPORT NUMBER	
9. SPONSORING/MONITORING AGENCY NAME(S) AND ADDRESS(ES) Air Force Office of Scientific Research (AFOSR) 801 N. Randolph St. Arlington, VA 22203-1977		10. SPONSORING/MONITORING AGENCY REPORT NUMBER	
11. SUPPLEMENTARY NOTES			
12a. DISTRIBUTION AVAILABILITY STATEMENT Approved for Public Release		12b. DISTRIBUTION CODE	
13. ABSTRACT (Maximum 200 words) The United States Air Force Summer Research Program (USAF-SRP) is designed to introduce university, college, and technical institute faculty members, graduate students, and high school students to Air Force research. This is accomplished by the faculty members (Summer Faculty Research Program, (SFRP)), graduate students (Graduate Student Research Program (GSRP)), and high school students (High School Apprenticeship Program (HSAP)) being selected on a nationally advertised competitive basis during the summer intersession period to perform research at Air Force Research Laboratory (AFRL) Technical Directorates, Air Force Air Logistics Centers (ALC), and other AF Laboratories. This volume consists of a program overview, program management statistics, and the final technical reports from the SFRP participants at the Phillips Laboratory.			
14. SUBJECT TERMS Air Force Research, Air Force, Engineering, Laboratories, Reports, Summer, Universities, Faculty, Graduate Student, High School Student		15. NUMBER OF PAGES	
		16. PRICE CODE	
17. SECURITY CLASSIFICATION OF REPORT Unclassified	18. SECURITY CLASSIFICATION OF THIS PAGE Unclassified	19. SECURITY CLASSIFICATION OF ABSTRACT Unclassified	20. LIMITATION OF ABSTRACT UL

GENERAL INSTRUCTIONS FOR COMPLETING SF 298

The Report Documentation Page (RDP) is used in announcing and cataloging reports. It is important that this information be consistent with the rest of the report, particularly the cover and title page. Instructions for filling in each block of the form follow. It is important to *stay within the lines* to meet *optical scanning requirements*.

Block 1. Agency Use Only (*Leave blank*).

Block 2. Report Date. Full publication date including day, month, and year, if available (e.g. 1 Jan 88). Must cite at least the year.

Block 3. Type of Report and Dates Covered. State whether report is interim, final, etc. If applicable, enter inclusive report dates (e.g. 10 Jun 87 - 30 Jun 88).

Block 4. Title and Subtitle. A title is taken from the part of the report that provides the most meaningful and complete information. When a report is prepared in more than one volume, repeat the primary title, add volume number, and include subtitle for the specific volume. On classified documents enter the title classification in parentheses.

Block 5. Funding Numbers. To include contract and grant numbers; may include program element number(s), project number(s), task number(s), and work unit number(s). Use the following labels:

C - Contract	PR - Project
G - Grant	TA - Task
PE - Program Element	WU - Work Unit Accession No.

Block 6. Author(s). Name(s) of person(s) responsible for writing the report, performing the research, or credited with the content of the report. If editor or compiler, this should follow the name(s).

Block 7. Performing Organization Name(s) and Address(es). Self-explanatory.

Block 8. Performing Organization Report Number. Enter the unique alphanumeric report number(s) assigned by the organization performing the report.

Block 9. Sponsoring/Monitoring Agency Name(s) and Address(es). Self-explanatory.

Block 10. Sponsoring/Monitoring Agency Report Number. (*If known*)

Block 11. Supplementary Notes. Enter information not included elsewhere such as: Prepared in cooperation with....; Trans. of....; To be published in.... When a report is revised, include a statement whether the new report supersedes or supplements the older report.

Block 12a. Distribution/Availability Statement. Denotes public availability or limitations. Cite any availability to the public. Enter additional limitations or special markings in all capitals (e.g. NOFORN, REL, ITAR).

DOD - See DoDD 5230.24, "Distribution Statements on Technical Documents."

DOE - See authorities.

NASA - See Handbook NHB 2200.2.

NTIS - Leave blank.

Block 12b. Distribution Code.

DOD - Leave blank.

DOE - Enter DOE distribution categories from the Standard Distribution for Unclassified Scientific and Technical Reports.

Leave blank.

NASA - Leave blank.

NTIS -

Block 13. Abstract. Include a brief (*Maximum 200 words*) factual summary of the most significant information contained in the report.

Block 14. Subject Terms. Keywords or phrases identifying major subjects in the report.

Block 15. Number of Pages. Enter the total number of pages.

Block 16. Price Code. Enter appropriate price code (*NTIS only*).

Blocks 17. - 19. Security Classifications. Self-explanatory. Enter U.S. Security Classification in accordance with U.S. Security Regulations (i.e., UNCLASSIFIED). If form contains classified information, stamp classification on the top and bottom of the page.

Block 20. Limitation of Abstract. This block must be completed to assign a limitation to the abstract. Enter either UL (unlimited) or SAR (same as report). An entry in this block is necessary if the abstract is to be limited. If blank, the abstract is assumed to be unlimited.

SFRP FINAL REPORT TABLE OF CONTENTS

i-xviii

1. INTRODUCTION	1
2. PARTICIPATION IN THE SUMMER RESEARCH PROGRAM	2
3. RECRUITING AND SELECTION	3
4. SITE VISITS	4
5. HBCU/MI PARTICIPATION	4
6. SRP FUNDING SOURCES	5
7. COMPENSATION FOR PARTICIPATIONS	5
8. CONTENTS OF THE 1996 REPORT	6

APPENDICIES:

A. PROGRAM STATISTICAL SUMMARY	A-1
B. SRP EVALUATION RESPONSES	B-1

SFRP FINAL REPORTS

PREFACE

Reports in this volume are numbered consecutively beginning with number 1. Each report is paginated with the report number followed by consecutive page numbers, e.g., 1-1, 1-2, 1-3; 2-1, 2-2, 2-3.

This document is one of a set of 16 volumes describing the 1997 AFOSR Summer Research Program. The following volumes comprise the set:

Due to its length, Volume 3 is bound in two parts, 3A and 3B. Volume 3A contains #1-18. Volume 3B contains reports #19-30. The Table of Contents for Volume 3 is included in both parts.

VOLUME

TITLE

1	Program Management Report
	<i>Summer Faculty Research Program (SFRP) Reports</i>
2A & 2B	Armstrong Laboratory
3A & 3B	Phillips Laboratory
4A & 4B	Rome Laboratory
5A , 5B & 5C	Wright Laboratory
6	Arnold Engineering Development Center, United States Air Force Academy and Air Logistics Centers
	<i>Graduate Student Research Program (GSRP) Reports</i>
7A & 7B	Armstrong Laboratory
8	Phillips Laboratory
9	Rome Laboratory
10A & 10B	Wright Laboratory
11	Arnold Engineering Development Center, United States Air Force Academy, Wilford Hall Medical Center and Air Logistics Centers
	<i>High School Apprenticeship Program (HSAP) Reports</i>
12A & 12B	Armstrong Laboratory
13	Phillips Laboratory
14	Rome Laboratory
15B&15B	Wright Laboratory
16	Arnold Engineering Development Center

SRP Final Report Table of Contents

Author	University/Institution Report Title	Armstrong Laboratory Directorate	Vol-Page
DR Jean M Andino	University of Florida , Gainesville , FL Atmospheric Reactions of Volatile Paint Components a Modeling Approach	AL/EQL	2- 1
DR Anthony R Andrews	Ohio University , Athens , OH Novel Electrochemiluminescence Reactions and Instrumentation	AL/EQL	2- 2
DR Stephan B Bach	Univ of Texas at San Antonio , San Antonio , TX Investigation of Sampling Interfaces for Portable Mass Spectrometry and a survey of field Portable	AL/OEA	2- 3
DR Marilyn Barger	Florida A&M-FSU College of Engineering , Tallahassee , FL Analysis for The Anaerobic Metabolites of Toulene at Fire Training Area 23 Tyndall AFB, Florida	AL/EQL	2- 4
DR Dulal K Bhaumik	University of South Alabama , Mobile , AL The Net Effect of a Covariate in Analysis of Covariance	AL/AOEP	2- 5
DR Marc L Carter, PhD, PA	Hofstra University , Hempstead , NY Assessment of the Reliability of Ground Based Observers for the Detecton of Aircraft	AL/OEO	2- 6
DR Huseyin M Cekirge	Florida State University , Tallahassee , FL Developing a Relational Database for Natural Attenuation Field Data	AL/EQL	2- 7
DR Cheng Cheng	Johns Hopkins University , Baltimore , MD Investigation of Two Statistical Issues in Building a Classification System	AL/HRM	2- 8
DR Gerald P Chubb	Ohio State University , Columbus , OH Use of Air Synthetic Forces For GCI Training Exercises	AL/HR1	2- 9..
DR Sneed B Collard, Jr.	University of West Florida , Pensacola , FL Suitability of Ascidians as Trace Metal Biosenosrs-Biomonitors In Marine Environments An Assessment	AL/EQL	2- 10
DR Catherine A Cornwell	Syracuse University , Syracuse , NY Rat Ultrasound Vocalization Development and Neurochemistry in Stress-Sensitive Brain Regions	AL/OER	2- 11

SRP Final Report Table of Contents

Author	University/Institution Report Title	Armstrong Laboratory Directorate	Vol-Page
DR Baolin Deng	New Mexico Tech , Socorro , NM Effect of Iron Corrosion Inhibitors on Reductive Degradation of Chlorinated Solvents	AL/EQL	2- 12
DR Micheal P Dooley	Iowa State University , Ames , IA Copulatory Response Fertilizing Potential, and Sex Ratio of Offsprings Sired by male rats Ecposed in	AL/OER	2- 13
DR Itiel E Dror	Miami University , Oxford , OH The Effect of Visual Similarity and Reference Frame Alignment on the Recognition of Military Aircraf	AL/HRT	2- 14
DR Brent D Foy	Wright State University , Dayton , OH Advances in Biologivcally-Based Kinetic Modeling for Toxicological Applications	AFRL/HES	2- 15
DR Irwin S Goldberg	St. Mary's Univ , San Antonio , TX Mixing and Streaming of a Fluid Near the Entrance of a Tube During Oscillatory Flow	AL/OES	2- 16
DR Ramesh C Gupta	University of Mainè at Orono , Orono , ME A Dynamical system approach in Biomedical Research	ALOES	2- 17
DR John R Herbold	Univ of Texas at San Antonio , San Antonio , TX A Protocol for Development of Amplicons for a Rapid and Efficient Methoiid of Genotyping Hepatitis C	AL/AOEL	2- 18
DR Andrew E Jackson	Arizona State University , Mesa , AZ Development fo a Conceptual Design for an Information Systems Infrastructure To Support the Squadron	AL/HRA	2- 19
DR Charles E Lance	Univ of Georgia Res Foundation , Athens , GA Replication and Extension of the Schmidt, Hunter, and Outerbridge (1986) Model of Job Performance R	AL/HRT	2- 20
DR David A Ludwig	Univ of N.C. at Greensboro , Greensboro , NC Mediating effect of onset rate on the relationship between+ Gz and LBNP Tolerance	AL/AOCY	2- 21
DR Robert P Mahan	University of Georgia , Athens , GA The Effects of Task Structure on Cognitive Organizing Principles Implaicatins for Complex Display	AL/CFTO	2- 22

SRP Final Report Table of Contents

Author	University/Institution Report Title	Armstrong Laboratory Directorate	Vol-Page
DR Phillip H Marshall	Texas Tech University , Lubbock , TX Preliminary report on the effects of varieties of feedback training on single target time-to-contac	AL/HRM	2- 23
DR Bruce V Mutter	Bluefield State College , Bluefield , WV	AL/EQP	2- 24
DR Allen L Nagy	Wright State University , Dayton , OH The Detection of Color Breakup In Field Sequential Color Displays	AL/CFBV	2- 25
DR Brent L Nielsen	Auburn University , Auburn , AL Rapid PCR Detection of Vancomycin Resistance of Enteroccus Species in infected Urine and Blood	AL/AOEL	2- 26
DR Thomas E Nygren	Ohio State University , Columbus , OH Group Differences in perceived importance of swat workload dimensions: Effects on judgment and perf	AL/CFHP	2- 27
DR Edward H Piepmeier	Oregon State University , Corvallis , OR	AL/AOHR	2- 28
DR Judy L Ratliff	Murray State Univ , Murray , KY Accumulation of Storntium and Calcium by Didemnum Conchyliatum	AL/EQL	2- 29
DR Joan R Rentsch	Wright State University , Dayton , OH the Effects of Individual Differences and Team Processed on Team Member Schema Similarity and task P	AL/CFHI	2- 30
DR Paul D Retzlaff	Univ of Northern Colorado , Greeley , CO The Armstrong Laboratory Aviation Personality Survey (ALAPS) Norming and Cross - Validation	AL/AOCN	2- 31
DR David B Reynolds	Wright State University , Dayton , OH Modeling Heat Flux Through Fabrics Exposed to a Radiant Souource and Analysis of Hot Air Burns	AL/CFBE	2- 32
DR Barth F Smets	University of Connecticut , Storrs , CT Desorption and Biodegradation of Dinitrotoluenes in aged soils	AL/EQL	2- 33

SRP Final Report Table of Contents

Author	University/Institution Report Title	Phillips Laboratory Directorate	Vol-Page
DR Graham R Allan	National Avenue , Las Vegas , NM Temporal and Spatial Characterisation of a Synchronously-Pumped Periodically-Poled Lithium Niobate O	PL/LIDD	3- 1
DR Mark J Balas	Univ of Colorado at Boulder , Boulder , CO Nonlinear Tracking Control for a Precision Deployable Structure Using a Partitioned Filter Approach	PL/SX	3- 2
DR Mikhail S Belen'kii	Georgia Inst of Technology , Atlanta , GA Multiple Aperture Averaging Technique for Measurment Full Aperture Tilt with a Laser Guide Star and	PL/LIG	3- 3
DR Gajanan S Bhat	Univ of Tennessee , Knoxville , TN Spinning Hollow Fibers From High Performance Polymers	PL/RK	3- 4
DR David B Choate	Transylvania Univ , Lexington , KY Blackhole Analysis	PL/VTMR	3- 5
DR Neb Duric	University of New Mexico , Albuquerque , NM Image Recovery Using Phase Diversity	AFRL/DEB	3- 6
DR Arthur B Edwards	9201 University City Blvd. , Charlotte , NC Theory of Protons in Buried Oxides	PL/VTMR	3- 7
DR Gary M Erickson	Boston University , Boston , MA Modeling The Magnetospheric Magnetic Field	PL/GPSG	3- 8
DR Hany A Ghoneim	Rochester Inst of Technol , Rochester , NY Focal Point Accuracy Assesement of an Off-Axis Solar Caoncentrator	PL/RKES	3- 9
DR Subir Ghosh	Univ of Calif, Riverside , Riverside , CA Designing Propulsion Reliability of Space Launch Vehicles	PL/RKBA	3- 10
DR George W Hanson	Univ of Wisconsin - Milwaukee , Milwaukee , WI Asymptotic analysis of the Natural system modes of coupled bodies in the large separatin, Low-Freque	AFRL/DEH	3- 11

SRP Final Report Table of Contents

Author	University/Institution Report Title	Phillips Laboratory Directorate	Vol-Page
DR Brian D Jeffs	Brigham Young University , Provo , UT Blind Bayesian Restoration of Adaptive Optics Images Using Generalized Gaussian Markov Random Field	AFRL/DES _____	3- 12
DR Christopher H Jenkins	S Dakota School of Mines/Tech , Rapid City , SD Mechnics of Surface Precosion for Membrane Reflectors	PL/VTVS _____	3- 13
DR Dikshitulu K Kalluri	University of Lowell , Lowell , MA Mode Conversion in a Time-Varying Magnetoplasma Medium	PL/GPID _____	3- 14
DR Aravinda Kar	University of Central Florida , Orlando , FL Measurement of the Cutting Performance of a High Beam Quality Chemical Oxygen-Iodine Laser on Aerosp	AFRL/DEO _____	3- 15
DR Bernard Kirtman	Univ of Calif, Santa Barbara , Santa Barbara , CA Quantum Chemical Characterization of the elكتروnic Structure and Reactions of Silicon Dangling Bon	PL/VTMR _____	3- 16
DR Spencer P Kuo	Polytechnic University , Farmingdale , NY Excitation of Oscillating Two Stream Instability by Upper Hybrid Pump Waves in Ionospheric Heating	PL.GPI _____	3- 17
DR Henry A Kurtz	Memphis State University , Memphis , TN H2 Reactions at Dangling Bonds in SIO2	PL/VTMR _____	3- 18
DR Min-Chang Lee	Massachusetts Inst of Technology , Cambridge , MA Laboratory Studies of Ionospheric Plasma Effects Produced by Lightning-induced Whistler Waves	PL/GPSG _____	3- 19
DR Donald J Leo	University of Toledo , Toledo , OH Microcontroller-Based Implementation of Adaptive Structural Control	AFRL/VSD _____	3- 20
DR Hua Li	University of New Mexico , Albuquerque , NM	PL/LIDD _____	3- 21
DR Hanli Liu	Univ of Texas at Arlington , Arlington , TX Experimental Validation of Three-Dimensional Reconstruction of Inhomogenety Images in Turbid Media	AFRL/DEB _____	3- 22

SRP Final Report Table of Contents

Author	University/Institution Report Title	Phillips Laboratory Directorate	Vol-Page
DR M. Arfin K Lodhi	Texas Tech University , Lubbock , TX Thermoelectric Energy Conversion with solid Electrolytes	PL/VTRP	3- 23
DR Tim C Newell	University of New Mexico , Albuquerque , NM Study of Nonlinear Dynamics in a Diode Pumped Nd:YAG laser	PL/LIGR	3- 24
DR Michael J Pangia	Georgia College & State University , Milledgeville , GA Preparatory Work Towards a Computer Simulation of Electron beam Operations on TSS 1	PL/GPSG	3- 25
DR Vladimir O Papitashvili	Univ of Michigan , Ann Arbor , MI Modeling of Ionospheric Convection from the IMF and Solar Wind Data	PL/GPSG	3- 26
DR Jaime Ramirez-Angulo	New Mexico State University , Las Cruces , NM	PL/VTMR	3- 27
DR Louis F Rossi	University of Lowell , Lowell , MA Analysis of Turbulent Mixing in the Stratosphere & Troposphere	PL/GPOL	3- 28
DR David P Stapleton	University of Central Oklahoma , Edmond , OK Atmospheric Effects Upon Sub-Orbital Boost glide Spaceplane Trajectories	PL/RKBA	3- 29
DR Jenn-Ming Yang	Univ of Calif, Los Angeles , Los Angeles , CA Thermodynamic Stability and Oxidation Behavior of Refractory (Hf, Ta, Zr) Carbide/boride Composites	PL/RKS	3- 30

SRP Final Report Table of Contents

Author	University/Institution Report Title	Rome Laboratory Directorate	Vol-Page
DR A. F Anwar	University of Connecticut , Storrs , CT Properties of Quantum Wells Formed In AlGaIn/GaN Heterostructures	RL/ERAC _____	4- 1
DR Milica Barjaktarovic	Wilkes University , Wilkes Barre , PA Assured Software Design: Privacy Enhanced Mail (PEM) and X.509 Certificate Specification	AFRL/IFG _____	4- 2
DR Stella N Batalama	SUNY Buffalo , Buffalo , NY Adaptive Robust Spread-Spectrum Receivers	AFRL/IFG _____	4- 3
DR Adam W Bojanczyk	Cornell University , Ithaca , NY Lowering the Computational Complexity of Stap Radar Systems	RL/OCSS _____	4- 4
DR Nazeih M Botros	So. Illinois Univ-Carbondale , Carbondale , IL A PC-Based Speech Synthesizing Using Sinusoidal Transform Coding (STC)	RL/ERC-1 _____	4- 5
DR Nikolaos G Bourbakis	SUNY Binghamton , Binghamton , NY Eikones-An Object-Oriented Language For Image Analysis & Process	AFRL/IF _____	4- 6
DR Peter P Chen	Louisiana State University , Baton Rouge , LA Reconstructing the information Warfare Attack Scenario Guessing what Actually Had Happened Based on	RL/CA-II _____	4- 7
DR Everett E Crisman	Brown University , Providence , RI A Three-Dimensional, Dielectric Antenna Array Re-Configurable By Optical Wavelength Multiplexing	RL/ERAC _____	4- 8
DR Digendra K Das	SUNYIT , Utica , NY A Study of the Emerging Diagnostic Techniques in Avionics	RL/ERSR _____	4- 9
DR Venugopala R Dasigi	Southern Polytechnic State Univ , Marietta , GA Information Fusion for text Classification-an Experimental Comparison	AFRL/IFT _____	4- 10
DR Richard R Eckert	SUNY Binghamton , Binghamton , NY Enhancing the Rome Lab ADII virtual environment system	AFRL/IFSA _____	4- 11

SRP Final Report Table of Contents

Author	University/Institution Report Title	Rome Laboratory Directorate	Vol-Page
DR Micheal A Fiddy	University of Lowell , Lowell , MA Target Identification from Limited Backscattered Field Data	RL/ERCS	4- 12
DR Lili He	Nothern Illinois University , Dekalb , IL the Study of Caaractreistics of CdS Passivation on InP	RL/EROC	4- 13
DR Edem Ibragimov	Michigan Tech University , Houghton , MI Effects of Surface Scattering in 3-D Optical Mass Storage	RL/IRAP	4- 14
DR Phillip G Kornreich	Syracuse University , Syracuse , NY Analysis of Optically Active Material Layer Fibers	RL/OCPA	4- 15
DR Kuo-Chi Lin	University of Central Florida , Orlando , FL A Study on The Crowded Airspace Self Organized Criticality	AFRL/IFSB	4- 16
Dr. Beth L Losiewicz	Colorado College , Colorado Spring , CO The Miami Corpus Latin American Dialect Database continued Research and Documentation	RL/IRAA	4- 17
DR John D Norgard	Univ of Colorado at Colorado Springs , Colorado Spring , CO Microwave Holography using Infrared Thermograms of Electromagnetic Fields	RL/ERST	4- 18
DR Jeffrey B Norman	Vassar College , Poughkeepsie , NY Gain Spectra of Beam-Coupling In Photorefractive Semiconductors	RL/OCPA	4- 19
DR Dimitrios N Pados	State Univ. of New York Buffalo , Buffalo , NY Joint Domain Space-Time Adaptive Processing w/Small Training Data Sets	AFRL/SNR	4- 21
DR Brajendra N Panda	University of North Dakota , Grand Forks , ND A Model to Attain Data Integrity After System Invasion	AFRL/IFG	4- 22
DR Michael A Pittarelli	SUNY OF Tech Utica , Utica , NY Phase Transitions in probability Estimation and Constraint Satisfaction Problems	AFRL/IFT	4- 23

SRP Final Report Table of Contents

Author	University/Institution Report Title	Rome Laboratory Directorate	Vol-Page
DR Salahuddin Qazi	SUNY OF Tech Utica , Utica , NY Low Data rate Multimedia Communication Using Wireless Links	RL/IWT	4- 24
DR Arindam Saha	Mississippi State University , Mississippi State , MS An Implementationa of the message passing Interface on Rtems	RL/OCSS	4- 25
DR Ravi Sankar	University of South Florida , Tampa , FL A Study ofIntegrated and Intelligent Network Management	RL/C3BC	4- 26
DR Mark S Schmalz	University of Florida , Gainesville , FL Errors inherent in Reconstruction of Targets From multi-Look Imagery	AFRL/IF	4- 27
DR John L Stensby	Univ of Alabama at Huntsville , Huntsville , AL Simple Real-time Tracking Indicator for a Frequency Feedback Demodulator	RL/IRAP	4- 28
DR Micheal C Stinson	Central Michigan University , Mt. Pleasant , MI Destructive Objects	RL/CAII	4- 29
DR Donald R Ucci	Illinois Inst of Technology , Chicago , IL Simulation of a Robust Locally Optimum Receiver in correlated Noise Using Autoregressive Modeling	RL/C3BB	4- 30
DR Nong Ye	Arizona State University , Tempe , AZ A Process Engineering Approach to Continuous Command and Control on Security-Aware Computer Networks	AFRL/IFSA	4- 31

SRP Final Report Table of Contents

Author	University/Institution Report Title	Wright Laboratory Directorate	Vol-Page
DR William A Baeslack	Ohio State University , Columbus , OH	WL/MLLM _____	5- 1
DR Bhavik R Bakshi	Ohio State University , Columbus , OH Modeling of Materials Manufacturing Processes by NonlinearContimuum Regression	WL/MLIM _____	5- 2
DR Brian P Beecken	Bethel College , St. Paul , MN Contribution of a Scene Projector's Non-Uniformity to a Test Article's Output Image Non-Uniformity	AFRL/MN _____	5- 3
DR John H Beggs	Mississippi State University , Mississippi State , MS The Finite Element Method in Electromagnetics For Multidisciplinary Design	AFRL/VA _____	5- 4
DR Kevin D Belfield	University of Detroit Mercy , Detroit , MI Synthesis of Novel Organic Compounds and Polymers for two Photon Asorption, NLO, and Photorefractive	WL/MLBP _____	5- 5
DR Raj K Bhatnagar	University of Cincinnati , Cincinnati , OH A Study of Intra-Class Variability in ATR Systems	AFRL/SN _____	5- 6
DR Victor M Birman	Univ of Missouri - St. Louis , St Louis , MO Theoretical Foundations for Detection of Post-Processing Cracks in Ceramic Matrix Composites Based o	WL/FIBT _____	5- 7
DR Gregory A Blaisdell	Purdue University , West Lafayette , IN A Review of Benchmark Flows for Large EddySimulation	AFRL/VA _____	5- 8
DR Octavia I Camps	Pennsylvania State University , University Park , PA MDL Texture Segmentation Compressed Images	WL/MNGA _____	5- 9
DR Yiding Cao	Florida International Univ , Miami , FL A Feasibility Study of Turbine Disk Cooling by Employing Radially Rotating Heat Pipes	WL/POTT _____	5- 10
DR Reaz A Chaudhuri	University of Utah , Salt Lake City , UT A Novel Compatibility/Equilibrium Based Iterative Post-Processing Approach For Axisymmetric brittle	WL/MLBM _____	5- 11

SRP Final Report Table of Contents

Author	University/Institution Report Title	Wright Laboratory Directorate	Vol-Page
DR Mohamed F Chouikha	Howard University , Washington , DC Detection Techniques Use in Forward-Looking Radar Signal Procesing a Literature Review	WL/AAMR _____	5- 12
DR Milton L Cone	Embry-Riddle Aeronautical University , Prescott , AZ Scheduling in the Dynamic System Simulation Testbed	WL/AACF _____	5- 13
DR Robert C Creese	West Virginia University , Morgantown , WV Feature Based Cost Modeling	WL/MTI _____	5- 14
DR William Crossley	Purdue University , West Lafayette , IN Objects and Methods for Aircraft Conceptual Design and Optimization in a Knowledge-Based Environment	WL/FIBD _____	5- 15
DR Gene A Crowder	Tulane University , New Orleans , LA Vibrational Analysis of some High-Energy Compounds	WL/MNM _____	5- 16
DR Richard W Darling	University of South Florida , Tampa , FL Geometrically Invariant NonLinear recursive Filters, with Applicaation to Target Tracking	WL/MNAG _____	5- 17
DR Robert J DeAngelis	Univ of Nebraska - Lincoln , Lincoln , NE Quantitative Description of Wire Tecxtures In Cubic Metals	WL/MNM _____	5- 18
DR Bill M Diong	Pan American University , Edinburg , TX Analysis and Control Design for a Novel Resonant DC-DC Converter	WL/POOC _____	5- 19
DR John K Douglass	University of Arizona , Tucson , AZ Guiding Missiles "On The Fly:" Applications of Neurobiologica Princioles to Machine Vision For Arma	AFRL/MN _____	5- 20
DR Mark E Eberhart	Colorado School of Mines , Golden , CO Modeling The Charge Redistribution Associated with Deformation and Fracture	WL/MLLM _____	5- 21
DR Gregory S Elliott	Rutgers:State Univ of New Jersey , Piscataway , NJ On the Development of Planar Doppler Velocimetry	WL/POPT _____	5- 22

SRP Final Report Table of Contents

Author	University/Institution Report Title	Wright Laboratory Directorate	Vol-Page
DR Elizabeth A Ervin	University of Dayton , Dayton , OH Eval of the Pointwise K-2 Turbulence Model to Predict Transition & Separation in a Low Pressure	WL/POTT _____	5- 23
DR Altan M Ferendeci	University of Cincinnati , Cincinnati , OH Vertically Interconnected 3D MMICs with Active Interlayer Elements	WL/AADI _____	5- 24
DR Dennis R Flentge	Cedarville College , Cedarville , OH Kinetic Study of the Thermal Decomposition of t-Butylphenyl Phosphate Using the System for Thermal D	WL/POSL _____	5- 25
DR George N Frantziskonis	University of Arizona , Tucson , AZ Multiscale Material Characterization and Applications	WL/MLLP _____	5- 26
DR Zewdu Gebeyehu	Tuskegee University , Tuskegee , AL Synthesis and Characterization of Metal-Xanthic Acid and -Amino Acid Complexes Useful Ad Nonlinear	WL/MLPO _____	5- 27
DR Richard D Gould	North Carolina State U-Raleigh , Raleigh , NC Reduction and Analysis of LDV and Analog Raw Data	WL/POPT _____	5- 28
DR Michael S Grace	University of Virginia , Charlottesville , VA Structure and Function of an Extremely Sensitive Biological Infrared Detector	WL/MLPJ _____	5- 29
DR Gary M Graham	Ohio University , Athens , OH Indicial Response Model for Roll Rate Effects on A 65-Degree Delta wing	WL/FIGC _____	5- 30
DR Allen G Greenwood	Mississippi State University , Mississippi Sta , MS An Object-Based approach for Integrating Cost Assessment into Product/Process Design	WL/MTI _____	5- 31
DR Rita A Gregory	Georgia Inst of Technology , Atlanta , GA Range Estimating for Research and Development Alternatives	WL/FIVC _____	5- 32
DR Mark T Hanson	University of Kentucky , Lexington , KY Anisotropy in Epic 96&97: Implementation and Effects	WL/MNM _____	5- 33

SRP Final Report Table of Contents

Author	University/Institution Report Title	Wright Laboratory Directorate	Vol-Page
DR Majeed M Hayat	University of Dayton , Dayton , OH A Model for Turbulence and Photodetection Noise in Imaging	WL/AAJT _____	5- 34
DR Larry S Helmick	Cedarville College , Cedarville , OH NMA Study of the Decomposition Reaction Path of Demnum fluid under Tribological Conditions	WL/MLBT _____	5- 35
DR William F Hosford	Univ of Michigan , Ann Arbor , MI INTENSITY OF [111]AND [100] TEXTURAL COMPONENTS IN COMPRESSION-FORGED TANTALUM	AFRL/MN _____	5- 36
DR David E Hudak	Ohio Northern University , Ada , OH A Study fo a Data-Parallel Imlementation of An Implicit Solution fo the 3D Navier-Stokes Equations	WL/FIMC _____	5- 37
DR David P Johnson	Mississippi State University , Mississippi , MS An Innovative Segmented Tugsten Penetrating Munition	WL/MNAZ _____	5- 38
DR Ismail I Jouny	Lafayette College , Easton , PA	WL/AACT _____	5- 39
DR Edward T Knobbe	Oklahoma State University , Stillwater , OK Organically Modified silicate Films as Corrosion Resistant Treatments for 2024-T3 Alumium Alloy	WL/MLBT _____	5- 40
DR Seungug Koh	University of Dayton , Dayton , OH Numerically Efficinet Direct Ray Tracing Algorithms for Automatic Target Recognition using FPGAs	WL/AAST _____	5- 41
DR Ravi Kothari	University of Cincinnati , Cincinnati , OH A Function Approximation Approach for Region of Interest Selection in synthetic Aperture Radar Image	WL/AACA _____	5- 42
DR Douglas A Lawrence	Ohio University , Athens , OH On the Analysis and Design of Gain scheduled missile Autopilots	WL/MNAG _____	5- 43
DR Robert Lee	Ohio State University , Columbus , OH Boundary Conditions applied to the Finite Vlume Time Domain Method for the Solution of Maxwell's Equ	WL/FIM _____	5- 44

SRP Final Report Table of Contents

Author	University/Institution Report Title	Wright Laboratory Directorate	Vol-Page
DR Junghsen Lich	Wright State University , Dayton , OH Develop an Explosive Simulated Testing Apparatus for Impact Physics Research at Wright Laboratory	WL/FIV	5- 45
DR James S Marsh	University of West Florida , Pensacola , FL Distortion Compensation and Elimination in Holographic Reocnstruction	WL/MNSI	5- 46
DR Mark D McClain	Cedarville College , Cedarville , OH A Molecular Orbital Theory Analysis of Oligomers of 2,2'-Bithiazole and Partially Reduced 3,3'-Dimet	WL/MLBP	5- 47
DR William S McCormick	Wright State University , Dayton , OH Some Observations of Target Recognition Using High Range Resolution Radar	WL/AACR	5- 48
DR Richard O Mines	University of South Florida , Tampa , FL Testing Protocol for the Demilitarization System at the Eglin AFB Herd Facility	WLMN/M	5- 49
DR Dakshina V Murty	University of Portland , Portland , OR A Useful Benchmarking Method in Computational Mechanics, CFD, adn Heat Tansfer	WL/FIBT	5- 50
DR Krishna Naishadham	Wright State University , Dayton , OH	WL/MLPO	5- 51
DR Serguei Ostapenko	University of South Florida , Tampa , FL	WL/MLPO	5- 52
DR Yi Pan	University of Dayton , Dayton , OH Improvement of Cache Utilization and Parallel Efficiency of a Time-Dependnet Maxwell Equation Solver	AFRL/VA	5- 53.
DR Rolfe G Petschek	Case Western Reserve Univ , Cleveland , OH AB INITIO AUANTUM CHEMICAL STUDIES OF NICKEL DITHIOLENE COMPLEX	WL/MLPJ	5- 54
DR Kishore V Pochiraju	Stevens Inst of Technology , Hoboken , NJ Refined Reissner's Variational Solution in the Vicinity of Stress Singularities	AFRL/ML	5- 55

SRP Final Report Table of Contents

Author	University/Institution Report Title	Wright Laboratory Directorate	Vol-Page
DR Muhammad M Rahman	University of South Florida , Tampa , FL Computation of Free Surface Flows with Applications in Capillary Pumped Loops. Heat Pipes, and Jet I	WL/POOB _____	5- 56
DR Mateen M Rizki	Wright State University , Dayton , OH Classification of High Range Resolution Radar Signatures Using Evolutionary Computation	WL/AACA _____	5- 57
DR Shankar M Sastry	Washington University , St Louis . MO	WL/MLLM _____	5- 58
DR Martin Schwartz	University of North Texas , Denton , TX Computational Studies of Hydrogen Abstraction From Haloalkanes by the Hydroxyl Radical	WL/MLBT _____	5- 59
DR Rathinam P Selvam	Univ of Arkansas , Fayetteville , AR Computation of Nonlennear Viscous Panel Flutter Using a Full-Implicit Aeroelastic Solver	WL/FIMC _____	5- 60
DR Yuri B Shtessel	Univ of Alabama at Huntsville , Huntsville , AL Smoothed Sliding Mode control Approach For Addressing Actuator Deflection and Deflection Rate Saturata	AFRL/VA _____	5- 61
DR Mario Sznaier	Pennsylvania State University , University Park , PA Suboptimal Control of Nonlennear Systems via Receding Horizon State Dependent Riccati Equations	WL/MNAG _____	5- 62
DR Barney E Taylor	Miami Univ. - Hamilton , Hamilton , OH Photoconductivity Studies of the Polymer 6FPBO	WLMLBP _____	5- 63
DR Joseph W Tedesco	Auburn University , Auburn , AL high Velocity Penetration of Layered Concrete Targets with Small Scale Ogive-nose Steel projectiles	WL/MNSA _____	5- 64
DR Krishnaprasad Thirunarayan	Wright State University , Dayton , OH A VHDL MODEL SYNTHESIS APPLET IN TCL/TK	WL/AAST _____	5- 65

SRP Final Report Table of Contents

Author	University/Institution Report Title	Wright Laboratory Directorate	Vol-Page
DR Karen A Tomko	Wright State University , Dayton , OH Grid Level Parallelization of an Implicit Solution of the 3D Navier-Stokes Equations	WL/FIMC	5- 66
DR Max B Trueblood	University of Missouri-Rolla , Rolla , MO A Study of the Particulate Emissions of a Well-Stirred Reactor	WL/POSC	5- 67
DR Chi-Tay Tsai	Florida Atlantic University , Boca Raton , FL Dislocation Dynamics in Heterojunction Bipolar Transistor Under Current Induced Thermal St	WL/AA	5- 68
DR John L Valasek	Texas A&M University , College Station , TX Two Axis Pneumatic Vortex Control at High Speed and Low Angle-of-Attack	WL/FIMT	5- 69
DR Mitch J Wolff	Wright State University , Dayton , OH An Experimental and Computational Analysis of the Unsteady Blade Row Potential Interaction in a Tr	WL/POTF	5- 70
DR Rama K Yedavalli	Ohio State University , Columbus , OH Improved Aircraft Roll Maneuver Performance Using Smart Deformable Wings	WL/FIBD	5- 71

Author	University/Institution Report Title	Arnold Engineering Development Center Directorate	Vol-Page
DR Csaba A Biegl	Vanderbilt University , Nashville , TN Parallel processing for Turbine Engine Modeling and Test Data validation	AEDC/SVT _____	6- 1
DR Frank G Collins	Tennessee Univ Space Institute , Tullahoma , TN Design of a Mass Spectrometer Sampling Probe for The AEDC Impulse Facility	AEDC _____	6- 2
DR Kenneth M Jones	N Carolina A&T State Univ , Greensboro , NC	AEDC/SVT _____	6- 3
DR Kevin M Lyons	North Carolina State U-Raleigh , Raleigh , NC Velocity Field Measurements Using Filtered-Rayleigh Scattering	AEDC/SVT _____	6- 4
DR Gerald J Micklow	Univ of Alabama at Tuscaloosa , Tuscaloosa , AL	AEDC/SVT _____	6- 5
DR Michael S Moore	Vanderbilt University , Nashville , TN Extension and Installation of the Model-Integrated Real-Time Imaging System (Mirtis)	AEDC/SVT _____	6- 6
DR Robert L Roach	Tennessee Univ Space Institute , Tullahoma , TN Investigation of Fluid Mechanical Phenomena Relating to Air Injection Between the Segments of an Arc	AEDC _____	6- 7
DR Nicholas S Winowich	University of Tennessee , Knoxville , TN	AEDC _____	6- 8
DR Daniel M Knauss	Colorado School of Mines , Golden , CO Synthesis of salts With Delocalized Anions For Use as Third Order Nonlinear Optical Materials	USAFA/DF _____	6- 9
DR Jeffrey M Bigelow	Oklahoma Christian Univ of Science & Art , Oklahoma City , OK Raster-To-Vector Conversion of Circuit Diagrams: Software Requirements	OCALC/TI _____	6- 10

SRP Final Report Table of Contents

Author	University/Institution Report Title	Arnold Engineering Development Center Directorate	Vol-Page
DR Paul W Whaley	Oklahoma Christian Univ of Science & Art , Oklahoma City , OK A Probabilistic framework for the Analysis of corrosion Damage in Aging Aircraft	OCALC/L _____	6- 11
DR Bjong W Yeigh	Oklahoma State University , Stillwater , OK Logistics Asset Management : Models and Simulations	OCALC/TI _____	6- 12
DR Michael J McFarland	Utah State University , Logan , UT Delisting of Hill Air Force Base's Industrial Wastewater Treatment Plant Sludge	OC-ALC/E _____	6- 13
DR William E Sanford	Colorado State University , Fort Collins , CO Nuerical Modeling of Physical Constraints on in-Situ Cosolvent Flushing as a Groundwater Remedial Op	OO-ALC/E _____	6- 14
DR Sophia Hassiotis	University of South Florida , Tampa , FL Fracture Analysis of the F-5, 15%-Spar Bolt	SAALC/TI _____	6- 15
DR Devendra Kumar	CUNY-City College , New York , NY A Simple, Multiversion Concurrency Control Protocol For Internet Databases	SAALC/LD _____	6- 16
DR Ernest L McDuffie	Florida State University , Tallahassee , FL A Propossed Exjpert System for ATS Capability Analysis	SAALC/TI _____	6- 17
DR Prabhaker Mateti	Wright State University , Dayton , OH How to Provide and Evaluate Computer Network Security	SMALC/TI _____	6- 18
DR Mansur Rastani	N Carolina A&T State Univ , Greensboro , NC Optimal Structural Design of Modular Composite bare base Shelters	SMALC/L _____	6- 19
DR Joe G Chow	Florida International Univ , Miami , FL Re-engineer and Re-Manufacture Aircraft Sstructural Components Using Laser Scanning	WRALC/TI _____	6- 20

1. INTRODUCTION

The Summer Research Program (SRP), sponsored by the Air Force Office of Scientific Research (AFOSR), offers paid opportunities for university faculty, graduate students, and high school students to conduct research in U.S. Air Force research laboratories nationwide during the summer.

Introduced by AFOSR in 1978, this innovative program is based on the concept of teaming academic researchers with Air Force scientists in the same disciplines using laboratory facilities and equipment not often available at associates' institutions.

The Summer Faculty Research Program (SFRP) is open annually to approximately 150 faculty members with at least two years of teaching and/or research experience in accredited U.S. colleges, universities, or technical institutions. SFRP associates must be either U.S. citizens or permanent residents.

The Graduate Student Research Program (GSRP) is open annually to approximately 100 graduate students holding a bachelor's or a master's degree; GSRP associates must be U.S. citizens enrolled full time at an accredited institution.

The High School Apprentice Program (HSAP) annually selects about 125 high school students located within a twenty mile commuting distance of participating Air Force laboratories.

AFOSR also offers its research associates an opportunity, under the Summer Research Extension Program (SREP), to continue their AFOSR-sponsored research at their home institutions through the award of research grants. In 1994 the maximum amount of each grant was increased from \$20,000 to \$25,000, and the number of AFOSR-sponsored grants decreased from 75 to 60. A separate annual report is compiled on the SREP.

The numbers of projected summer research participants in each of the three categories and SREP "grants" are usually increased through direct sponsorship by participating laboratories.

AFOSR's SRP has well served its objectives of building critical links between Air Force research laboratories and the academic community, opening avenues of communications and forging new research relationships between Air Force and academic technical experts in areas of national interest, and strengthening the nation's efforts to sustain careers in science and engineering. The success of the SRP can be gauged from its growth from inception (see Table 1) and from the favorable responses the 1997 participants expressed in end-of-tour SRP evaluations (Appendix B).

AFOSR contracts for administration of the SRP by civilian contractors. The contract was first awarded to Research & Development Laboratories (RDL) in September 1990. After completion of the

1990 contract. RDL (in 1993) won the recompetition for the basic year and four 1-year options.

2. PARTICIPATION IN THE SUMMER RESEARCH PROGRAM

The SRP began with faculty associates in 1979; graduate students were added in 1982 and high school students in 1986. The following table shows the number of associates in the program each year.

YEAR	SRP Participation, by Year			TOTAL
	SFRP	GSRP	HSAP	
1979	70			70
1980	87			87
1981	87			87
1982	91	17		108
1983	101	53		154
1984	152	84		236
1985	154	92		246
1986	158	100	42	300
1987	159	101	73	333
1988	153	107	101	361
1989	168	102	103	373
1990	165	121	132	418
1991	170	142	132	444
1992	185	121	159	464
1993	187	117	136	440
1994	192	117	133	442
1995	190	115	137	442
1996	188	109	138	435
1997	148	98	140	427

Beginning in 1993, due to budget cuts, some of the laboratories weren't able to afford to fund as many associates as in previous years. Since then, the number of funded positions has remained fairly constant at a slightly lower level.

3. RECRUITING AND SELECTION

The SRP is conducted on a nationally advertised and competitive-selection basis. The advertising for faculty and graduate students consisted primarily of the mailing of 8,000 52-page SRP brochures to chairpersons of departments relevant to AFOSR research and to administrators of grants in accredited universities, colleges, and technical institutions. Historically Black Colleges and Universities (HBCUs) and Minority Institutions (MIs) were included. Brochures also went to all participating USAF laboratories, the previous year's participants, and numerous individual requesters (over 1000 annually).

RDL placed advertisements in the following publications: *Black Issues in Higher Education*, *Winds of Change*, and *IEEE Spectrum*. Because no participants list either *Physics Today* or *Chemical & Engineering News* as being their source of learning about the program for the past several years, advertisements in these magazines were dropped, and the funds were used to cover increases in brochure printing costs.

High school applicants can participate only in laboratories located no more than 20 miles from their residence. Tailored brochures on the HSAP were sent to the head counselors of 180 high schools in the vicinity of participating laboratories, with instructions for publicizing the program in their schools.

High school students selected to serve at Wright Laboratory's Armament Directorate (Eglin Air Force Base, Florida) serve eleven weeks as opposed to the eight weeks normally worked by high school students at all other participating laboratories.

Each SFRP or GSRP applicant is given a first, second, and third choice of laboratory. High school students who have more than one laboratory or directorate near their homes are also given first, second, and third choices.

Laboratories make their selections and prioritize their nominees. AFOSR then determines the number to be funded at each laboratory and approves laboratories' selections.

Subsequently, laboratories use their own funds to sponsor additional candidates. Some selectees do not accept the appointment, so alternate candidates are chosen. This multi-step selection procedure results in some candidates being notified of their acceptance after scheduled deadlines. The total applicants and participants for 1997 are shown in this table.

1997 Applicants and Participants			
PARTICIPANT CATEGORY	TOTAL APPLICANTS	SELECTEES	DECLINING SELECTEES
SFRP	490	188	32
(HBCU/MI)	(0)	(0)	(0)
GSRP	202	98	9
(HBCU/MI)	(0)	(0)	(0)
HSAP	433	140	14
TOTAL	1125	426	55

4. SITE VISITS

During June and July of 1997, representatives of both AFOSR/NI and RDL visited each participating laboratory to provide briefings, answer questions, and resolve problems for both laboratory personnel and participants. The objective was to ensure that the SRP would be as constructive as possible for all participants. Both SRP participants and RDL representatives found these visits beneficial. At many of the laboratories, this was the only opportunity for all participants to meet at one time to share their experiences and exchange ideas.

5. HISTORICALLY BLACK COLLEGES AND UNIVERSITIES AND MINORITY INSTITUTIONS (HBCU/MIs)

Before 1993, an RDL program representative visited from seven to ten different HBCU/MIs annually to promote interest in the SRP among the faculty and graduate students. These efforts were marginally effective, yielding a doubling of HBCU/MI applicants. In an effort to achieve AFOSR's goal of 10% of all applicants and selectees being HBCU/MI qualified, the RDL team decided to try other avenues of approach to increase the number of qualified applicants. Through the combined efforts of the AFOSR Program Office at Bolling AFB and RDL, two very active minority groups were found, HACU (Hispanic American Colleges and Universities) and AISES (American Indian Science and Engineering Society). RDL is in communication with representatives of each of these organizations on a monthly basis to keep up with their activities and special events. Both organizations have widely-distributed magazines/quarterlies in which RDL placed ads.

Since 1994 the number of both SFRP and GSRP HBCU/MI applicants and participants has increased ten-fold, from about two dozen SFRP applicants and a half dozen selectees to over 100 applicants and two dozen selectees, and a half-dozen GSRP applicants and two or three selectees to 18 applicants and 7 or 8 selectees. Since 1993, the SFRP had a two-fold applicant increase and a two-fold selectee increase. Since 1993, the GSRP had a three-fold applicant increase and a three to four-fold increase in selectees.

In addition to RDL's special recruiting efforts, AFOSR attempts each year to obtain additional funding or use leftover funding from cancellations the past year to fund HBCU/MI associates. This year, 5 HBCU/MI SFRPs declined after they were selected (and there was no one qualified to replace them with). The following table records HBCU/MI participation in this program.

SRP HBCU/MI Participation, By Year				
YEAR	SFRP		GSRP	
	Applicants	Participants	Applicants	Participants
1985	76	23	15	11
1986	70	18	20	10
1987	82	32	32	10
1988	53	17	23	14
1989	39	15	13	4
1990	43	14	17	3
1991	42	13	8	5
1992	70	13	9	5
1993	60	13	6	2
1994	90	16	11	6
1995	90	21	20	8
1996	119	27	18	7

6. SRP FUNDING SOURCES

Funding sources for the 1997 SRP were the AFOSR-provided slots for the basic contract and laboratory funds. Funding sources by category for the 1997 SRP selected participants are shown here.

1997 SRP FUNDING CATEGORY	SFRP	GSRP	HSAP
AFOSR Basic Allocation Funds	141	89	123
USAF Laboratory Funds	48	9	17
HBCU/MI By AFOSR (Using Procured Addn'l Funds)	0	0	N/A
TOTAL	9	98	140

SFRP - 188 were selected, but thirty two canceled too late to be replaced.

GSRP - 98 were selected, but nine canceled too late to be replaced.

HSAP - 140 were selected, but fourteen canceled too late to be replaced.

7. COMPENSATION FOR PARTICIPANTS

Compensation for SRP participants, per five-day work week, is shown in this table.

1997 SRP Associate Compensation

PARTICIPANT CATEGORY	1991	1992	1993	1994	1995	1996	1997
Faculty Members	\$690	\$718	\$740	\$740	\$740	\$770	\$770
Graduate Student (Master's Degree)	\$425	\$442	\$455	\$455	\$455	\$470	\$470
Graduate Student (Bachelor's Degree)	\$365	\$380	\$391	\$391	\$391	\$400	\$400
High School Student (First Year)	\$200	\$200	\$200	\$200	\$200	\$200	\$200
High School Student (Subsequent Years)	\$240	\$240	\$240	\$240	\$240	\$240	\$240

The program also offered associates whose homes were more than 50 miles from the laboratory an expense allowance (seven days per week) of \$50/day for faculty and \$40/day for graduate students. Transportation to the laboratory at the beginning of their tour and back to their home destinations at the end was also reimbursed for these participants. Of the combined SFRP and GSRP associates, 65 % (194 out of 286) claimed travel reimbursements at an average round-trip cost of \$776.

Faculty members were encouraged to visit their laboratories before their summer tour began. All costs of these orientation visits were reimbursed. Forty-three percent (85 out of 188) of faculty associates took orientation trips at an average cost of \$388. By contrast, in 1993, 58 % of SFRP associates took

orientation visits at an average cost of \$685; that was the highest percentage of associates opting to take an orientation trip since RDL has administered the SRP, and the highest average cost of an orientation trip. These 1993 numbers are included to show the fluctuation which can occur in these numbers for planning purposes.

Program participants submitted biweekly vouchers countersigned by their laboratory research focal point, and RDL issued paychecks so as to arrive in associates' hands two weeks later.

This is the second year of using direct deposit for the SFRP and GSRP associates. The process went much more smoothly with respect to obtaining required information from the associates, only 7% of the associates' information needed clarification in order for direct deposit to properly function as opposed to 10% from last year. The remaining associates received their stipend and expense payments via checks sent in the US mail.

HSAP program participants were considered actual RDL employees, and their respective state and federal income tax and Social Security were withheld from their paychecks. By the nature of their independent research, SFRP and GSRP program participants were considered to be consultants or independent contractors. As such, SFRP and GSRP associates were responsible for their own income taxes, Social Security, and insurance.

8. CONTENTS OF THE 1997 REPORT

The complete set of reports for the 1997 SRP includes this program management report (Volume 1) augmented by fifteen volumes of final research reports by the 1997 associates, as indicated below:

1997 SRP Final Report Volume Assignments

LABORATORY	SFRP	GSRP	HSAP
Armstrong	2	7	12
Phillips	3	8	13
Rome	4	9	14
Wright	5A, 5B	10	15
AEDC, ALCs, WHMC	6	11	16

APPENDIX A -- PROGRAM STATISTICAL SUMMARY

A. Colleges/Universities Represented

Selected SFRP associates represented 169 different colleges, universities, and institutions.
GSRP associates represented 95 different colleges, universities, and institutions.

B. States Represented

SFRP -Applicants came from 47 states plus Washington D.C. Selectees represent 44 states.

GSRP - Applicants came from 44 states. Selectees represent 32 states.

HSAP - Applicants came from thirteen states. Selectees represent nine states.

Total Number of Participants	
SFRP	189
GSRP	97
HSAP	140
TOTAL	426

Degrees Represented			
	SFRP	GSRP	TOTAL
Doctoral	184	0	184
Master's	2	41	43
Bachelor's	0	56	56
TOTAL	186	97	298

SFRP Academic Titles	
Assistant Professor	64
Associate Professor	70
Professor	40
Instructor	0
Chairman	1
Visiting Professor	1
Visiting Assoc. Prof.	1
Research Associate	9
TOTAL	186

Source of Learning About the SRP		
Category	Applicants	Selectees
Applied/participated in prior years	28%	34%
Colleague familiar with SRP	19%	16%
Brochure mailed to institution	23%	17%
Contact with Air Force laboratory	17%	23%
<i>IEEE Spectrum</i>	2%	1%
<i>BIIHE</i>	1%	1%
Other source	10%	8%
TOTAL	100%	100%

APPENDIX B -- SRP EVALUATION RESPONSES

1. OVERVIEW

Evaluations were completed and returned to RDL by four groups at the completion of the SRP. The number of respondents in each group is shown below.

Table B-1. Total SRP Evaluations Received

Evaluation Group	Responses
SFRP & GSRPs	275
HSAPs	113
USAF Laboratory Focal Points	84
USAF Laboratory HSAP Mentors	6

All groups indicate unanimous enthusiasm for the SRP experience.

The summarized recommendations for program improvement from both associates and laboratory personnel are listed below:

- A. Better preparation on the labs' part prior to associates' arrival (i.e., office space, computer assets, clearly defined scope of work).
- B. Faculty Associates suggest higher stipends for SFRP associates.
- C. Both HSAP Air Force laboratory mentors and associates would like the summer tour extended from the current 8 weeks to either 10 or 11 weeks; the groups state it takes 4-6 weeks just to get high school students up-to-speed on what's going on at laboratory. (Note: this same argument was used to raise the faculty and graduate student participation time a few years ago.)

2. 1997 USAF LABORATORY FOCAL POINT (LFP) EVALUATION RESPONSES

The summarized results listed below are from the 84 LFP evaluations received.

1. LFP evaluations received and associate preferences:

Table B-2. Air Force LFP Evaluation Responses (By Type)

Lab	Evals Recv'd	How Many Associates Would You Prefer To Get ?								(% Response)			
		SFRP				GSRP (w/Univ Professor)				GSRP (w/o Univ Professor)			
		0	1	2	3+	0	1	2	3+	0	1	2	3+
AEDC	0	-	-	-	-	-	-	-	-	-	-	-	-
WHMC	0	-	-	-	-	-	-	-	-	-	-	-	-
AL	7	28	28	28	14	54	14	28	0	86	0	14	0
USAF A	1	0	100	0	0	100	0	0	0	0	100	0	0
PL	25	40	40	16	4	88	12	0	0	84	12	4	0
RL	5	60	40	0	0	80	10	0	0	100	0	0	0
WL	46	30	43	20	6	78	17	4	0	93	4	2	0
Total	84	32%	50%	13%	5%	80%	11%	6%	0%	73%	23%	4%	0%

LFP Evaluation Summary. The summarized responses, by laboratory, are listed on the following page. LFPs were asked to rate the following questions on a scale from 1 (below average) to 5 (above average).

2. LFPs involved in SRP associate application evaluation process:
 - a. Time available for evaluation of applications:
 - b. Adequacy of applications for selection process:
3. Value of orientation trips:
4. Length of research tour:
5.
 - a. Benefits of associate's work to laboratory:
 - b. Benefits of associate's work to Air Force:
6.
 - a. Enhancement of research qualifications for LFP and staff:
 - b. Enhancement of research qualifications for SFRP associate:
 - c. Enhancement of research qualifications for GSRP associate:
7.
 - a. Enhancement of knowledge for LFP and staff:
 - b. Enhancement of knowledge for SFRP associate:
 - c. Enhancement of knowledge for GSRP associate:
8. Value of Air Force and university links:
9. Potential for future collaboration:
10.
 - a. Your working relationship with SFRP:
 - b. Your working relationship with GSRP:
11. Expenditure of your time worthwhile:

(Continued on next page)

12. Quality of program literature for associate:
13. a. Quality of RDL's communications with you:
 b. Quality of RDL's communications with associates:
14. Overall assessment of SRP:

Table B-3. Laboratory Focal Point Responses to above questions

	<i>AEDC</i>	<i>AL</i>	<i>USAF</i>	<i>PL</i>	<i>RL</i>	<i>WHMC</i>	<i>WL</i>
<i># Evals Recv'd</i>	0	7	1	14	5	0	46
<i>Question #</i>							
2	-	86 %	0 %	88 %	80 %	-	85 %
2a	-	4.3	n/a	3.8	4.0	-	3.6
2b	-	4.0	n/a	3.9	4.5	-	4.1
3	-	4.5	n/a	4.3	4.3	-	3.7
4	-	4.1	4.0	4.1	4.2	-	3.9
5a	-	4.3	5.0	4.3	4.6	-	4.4
5b	-	4.5	n/a	4.2	4.6	-	4.3
6a	-	4.5	5.0	4.0	4.4	-	4.3
6b	-	4.3	n/a	4.1	5.0	-	4.4
6c	-	3.7	5.0	3.5	5.0	-	4.3
7a	-	4.7	5.0	4.0	4.4	-	4.3
7b	-	4.3	n/a	4.2	5.0	-	4.4
7c	-	4.0	5.0	3.9	5.0	-	4.3
8	-	4.6	4.0	4.5	4.6	-	4.3
9	-	4.9	5.0	4.4	4.8	-	4.2
10a	-	5.0	n/a	4.6	4.6	-	4.6
10b	-	4.7	5.0	3.9	5.0	-	4.4
11	-	4.6	5.0	4.4	4.8	-	4.4
12	-	4.0	4.0	4.0	4.2	-	3.8
13a	-	3.2	4.0	3.5	3.8	-	3.4
13b	-	3.4	4.0	3.6	4.5	-	3.6
14	-	4.4	5.0	4.4	4.8	-	4.4

3. 1997 SFRP & GSRP EVALUATION RESPONSES

The summarized results listed below are from the 257 SFRP/GSRP evaluations received.

Associates were asked to rate the following questions on a scale from 1 (below average) to 5 (above average) - by Air Force base results and over-all results of the 1997 evaluations are listed after the questions.

1. The match between the laboratories research and your field:
2. Your working relationship with your LFP:
3. Enhancement of your academic qualifications:
4. Enhancement of your research qualifications:
5. Lab readiness for you: LFP, task, plan:
6. Lab readiness for you: equipment, supplies, facilities:
7. Lab resources:
8. Lab research and administrative support:
9. Adequacy of brochure and associate handbook:
10. RDL communications with you:
11. Overall payment procedures:
12. Overall assessment of the SRP:
13.
 - a. Would you apply again?
 - b. Will you continue this or related research?
14. Was length of your tour satisfactory?
15. Percentage of associates who experienced difficulties in finding housing:
16. Where did you stay during your SRP tour?
 - a. At Home:
 - b. With Friend:
 - c. On Local Economy:
 - d. Base Quarters:
17. Value of orientation visit:
 - a. Essential:
 - b. Convenient:
 - c. Not Worth Cost:
 - d. Not Used:

SFRP and GSRP associate's responses are listed in tabular format on the following page.

Table B-4. 1997 SFRP & GSRP Associate Responses to SRP Evaluation

	Arnold	Brooks	Edwards	Eglin	Griffis	Hanscom	Kelly	Kirtland	Lackland	Robins	Tyndall	WPAFB	average
# res	6	48	6	14	31	19	3	32	1	2	10	85	257
1	4.8	4.4	4.6	4.7	4.4	4.9	4.6	4.6	5.0	5.0	4.0	4.7	4.6
2	5.0	4.6	4.1	4.9	4.7	4.7	5.0	4.7	5.0	5.0	4.6	4.8	4.7
3	4.5	4.4	4.0	4.6	4.3	4.2	4.3	4.4	5.0	5.0	4.5	4.3	4.4
4	4.3	4.5	3.8	4.6	4.4	4.4	4.3	4.6	5.0	4.0	4.4	4.5	4.5
5	4.5	4.3	3.3	4.8	4.4	4.5	4.3	4.2	5.0	5.0	3.9	4.4	4.4
6	4.3	4.3	3.7	4.7	4.4	4.5	4.0	3.8	5.0	5.0	3.8	4.2	4.2
7	4.5	4.4	4.2	4.8	4.5	4.3	4.3	4.1	5.0	5.0	4.3	4.3	4.4
8	4.5	4.6	3.0	4.9	4.4	4.3	4.3	4.5	5.0	5.0	4.7	4.5	4.5
9	4.7	4.5	4.7	4.5	4.3	4.5	4.7	4.3	5.0	5.0	4.1	4.5	4.5
10	4.2	4.4	4.7	4.4	4.1	4.1	4.0	4.2	5.0	4.5	3.6	4.4	4.3
11	3.8	4.1	4.5	4.0	3.9	4.1	4.0	4.0	3.0	4.0	3.7	4.0	4.0
12	5.7	4.7	4.3	4.9	4.5	4.9	4.7	4.6	5.0	4.5	4.6	4.5	4.6
Numbers below are percentages													
13a	83	90	83	93	87	75	100	81	100	100	100	86	87
13b	100	89	83	100	94	98	100	94	100	100	100	94	93
14	83	96	100	90	87	80	100	92	100	100	70	84	88
15	17	6	0	33	20	76	33	25	0	100	20	8	39
16a	-	26	17	9	38	23	33	4	-	-	-	30	
16b	100	33	-	40	-	8	-	-	-	-	36	2	
16c	-	41	83	40	62	69	67	96	100	100	64	68	
16d	-	-	-	-	-	-	-	-	-	-	-	0	
17a	-	33	100	17	50	14	67	39	-	50	40	31	35
17b	-	21	-	17	10	14	-	24	-	50	20	16	16
17c	-	-	-	-	10	7	-	-	-	-	-	2	3
17d	100	46	-	66	30	69	33	37	100	-	40	51	46

4. 1997 USAF LABORATORY HSAP MENTOR EVALUATION RESPONSES

Not enough evaluations received (5 total) from Mentors to do useful summary.

5. 1997 HSAP EVALUATION RESPONSES

The summarized results listed below are from the 113 HSAP evaluations received.

HSAP apprentices were asked to rate the following questions on a scale from
1 (below average) to 5 (above average)

1. Your influence on selection of topic/type of work.
2. Working relationship with mentor, other lab scientists.
3. Enhancement of your academic qualifications.
4. Technically challenging work.
5. Lab readiness for you: mentor, task, work plan, equipment.
6. Influence on your career.
7. Increased interest in math/science.
8. Lab research & administrative support.
9. Adequacy of RDL's Apprentice Handbook and administrative materials.
10. Responsiveness of RDL communications.
11. Overall payment procedures.
12. Overall assessment of SRP value to you.
13. Would you apply again next year? Yes (92 %)
14. Will you pursue future studies related to this research? Yes (68 %)
15. Was Tour length satisfactory? Yes (82 %)

	Arnold	Brooks	Edwards	Eglin	Griffiss	Hanscom	Kirtland	Tyndall	WPAFB	Totals
# resp	5	19	7	15	13	2	7	5	40	113
1	2.8	3.3	3.4	3.5	3.4	4.0	3.2	3.6	3.6	3.4
2	4.4	4.6	4.5	4.8	4.6	4.0	4.4	4.0	4.6	4.6
3	4.0	4.2	4.1	4.3	4.5	5.0	4.3	4.6	4.4	4.4
4	3.6	3.9	4.0	4.5	4.2	5.0	4.6	3.8	4.3	4.2
5	4.4	4.1	3.7	4.5	4.1	3.0	3.9	3.6	3.9	4.0
6	3.2	3.6	3.6	4.1	3.8	5.0	3.3	3.8	3.6	3.7
7	2.8	4.1	4.0	3.9	3.9	5.0	3.6	4.0	4.0	3.9
8	3.8	4.1	4.0	4.3	4.0	4.0	4.3	3.8	4.3	4.2
9	4.4	3.6	4.1	4.1	3.5	4.0	3.9	4.0	3.7	3.8
10	4.0	3.8	4.1	3.7	4.1	4.0	3.9	2.4	3.8	3.8
11	4.2	4.2	3.7	3.9	3.8	3.0	3.7	2.6	3.7	3.8
12	4.0	4.5	4.9	4.6	4.6	5.0	4.6	4.2	4.3	4.5
Numbers below are percentages										
13	60%	95%	100%	100%	85%	100%	100%	100%	90%	92%
14	20%	80%	71%	80%	54%	100%	71%	80%	65%	68%
15	100%	70%	71%	100%	100%	50%	86%	60%	80%	82%

TEMPORAL AND SPATIAL CHARACTERISATION OF A SYNCHRONOUSLY-PUMPED
PERIODICALLY-POLED LITHIUM NIOBATE OPTICAL PARAMETRIC OSCILLATOR

Dr. Graham R. Allan
Assistant Professor
Department of Physics

New Mexico Highlands University
National Avenue
Las Vegas NM 87701

Final Report for:
Summer Faculty Research Program
Phillips Laboratory

Sponsored By:
Air Force Office of Scientific Research
Bolling Air Force Base
Washington DC

&

Phillips Laboratory

August 97

TEMPORAL AND SPATIAL CHARACTERISATION OF A SYNCHRONOUSLY-PUMPED PERIODICALLY-POLED LITHIUM NIOBATE OPTICAL PARAMETRIC OSCILLATOR

Graham R. Allan

Abstract

The successful operation and characterisation of a synchronously pumped optical parametric oscillator is reported. The OPO uses an optically pumped (cw-modelocked Nd:YAG laser) 5 cm crystal of periodically-poled lithium niobate in a temperature stabilised oven. The OPO produces pulses of ~100 ps duration in the wavelength range of ~1.5 μ m. Anomalous switching behaviour has been observed when the system is near synchronism and a reduction in the transmitted pump noise is seen for incident powers around threshold. Strong pump depletion was observed in both the spatial and temporal profiles of the pump. Parasitic losses in the signal involving mixing and second harmonic generation were observed.

TEMPORAL AND SPATIAL CHARACTERISATION OF A SYNCHRONOUSLY-PUMPED PERIODICALLY-POLED LITHIUM NIOBATE OPTICAL PARAMETRIC OSCILLATOR

Graham R. Allan

Introduction

Optical parametric oscillators, OPO's, are now well established as a means of generating widely-tunable coherent radiation in regions of the electromagnetic spectrum which are normally difficult to access via conventional coherent sources. However, "low" output powers still limits the utility of OPO's as a tool in nonlinear optics research. In addressing this limitation we continue to investigate Periodically-Poled Lithium Niobate, PPLN, in a synchronously pumped OPO. Previous work reported on the characterisation of a 13 mm crystal of PPLN in a synchronously pumped OPO; in this report the experimental work concentrates on a higher-gain system. As the small-signal gain is proportional to the square of the gain medium length, a longer crystal of PPLN is used. The dynamics of this synchronously pumped OPO are again characterised using standard cw and temporally and spatially resolved detection techniques. This allows study of dynamical effects within an individual pulse, such as pump depletion and back conversion.

Experimental

The experimental system consists of essentially three components; the pump laser, the OPO and the diagnostics. A schematic of the general experimental layout is shown in figure 1. The pump source is a commercial, cw, mode-locked ND:YAG laser operating at 1.064 μm and producing nominally 100 ps FWHM pulses in a 76 MHz train with ~20 W of average power. Before injection into the OPO cavity the pump laser is mechanically chopped at 40 Hz with a 100:1 duty cycle. The peak intensity is controlled by the halfwave plate and analyzer (HWPP) and monitored by a photodetector. In our experiments the mechanical chopping reduces the average power of the pump laser seeding the OPO to ~100 mW. The crystal is maintained at a temperature 60° C which has the effect of postponing the onset of photorefractive in lithium niobate, in our case almost indefinitely. The nonlinear optical crystal, a piece of periodically poled lithium niobate, is 50 mm x 10 mm by 500 μm thick with several poled regions aligned along the long axis. The input and output surfaces of the chip are anti-reflection coated with a

broadband antireflection coating and yields ~98% throughput at 1064 μm and from 97-98 % for signal radiation around 1.5 μm .

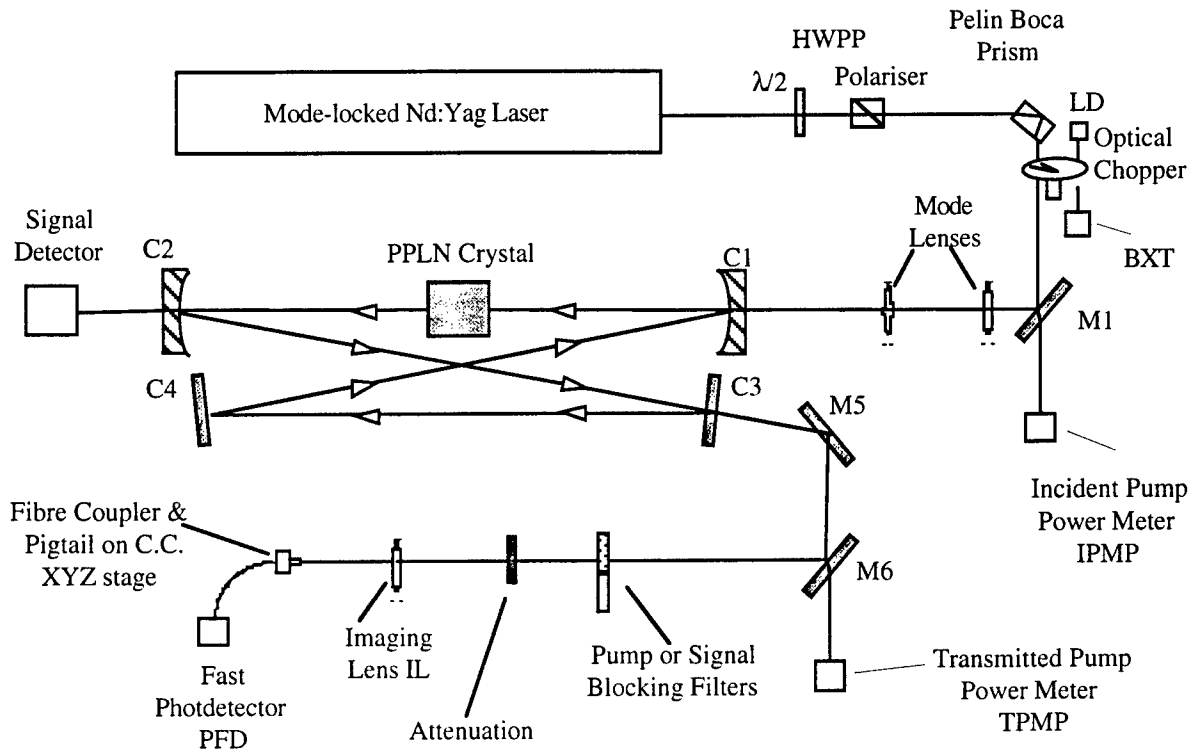


Figure 1. Schematic of the experimental layout showing the cavity geometry.

The OPO cavity is a continuous-wave synchronously pumped design forming a tightly folded bow-tie ring resonator in the vertical plane, approximately 1 m long and 2.5 cm high between two 75 cm radius of curvature concave mirrors and two plane mirrors. The OPO cavity produces a signal mode spot size of 150 μm to which the pump is matched using external, (to the cavity), mode-matching lenses. All the mirrors are highly transmissive at the pump and idler wavelengths, 1.064 μm and 3.4 μm to 3.8 μm , respectively, and highly reflective from 1.49 μm to 1.53 μm . A pair of intracavity glass plates mounted on rotation stages are used to synthesize an output coupler. The two plates were inserted with opposite tilt to cancel parallax. Changing the angle of the plates alters the Fresnel losses, thereby synthesizing output. The output coupling can be varied smoothly from as much as 18% output coupling, when the plates are near normal incidence, to less than 0.1% at Brewster's angle. In operation the OPO's output is synchronous with the 76 MHz pulsed output of the pump laser; however the injected pump power is mechanically chopped and so produces burst of synchronous pulses at 76 MHz within the chopper window. The

chopper blade clears the incident pump beam in $\sim 25\mu\text{s}$ and the chopper window remains open for approximately 250 μs . The OPO typically reaches steady state in less than 50 μs , after which the output power remains constant until the chopper window closes. The long term stability of the system was good - typical characterisation runs can take approximately an hour, over which time the OPO was well behaved and continued to display such behavior over many hours.

The rest of the system comprises the diagnostics, which are designed to simultaneously monitor the averaged incident pump power, transmitted pump power and signal power, and the temporally and spatially resolved transmitted pump or signal. To monitor the averaged powers we used slow-response, large-area, photodetectors to integrate over the spatial and temporal profiles of the mode-locked pulses from the laser and OPO: The incident pump power is monitored with photodetector (IPMP); the signal power transmitted through high-reflectivity mirror (C2) is monitored by photodetector (SIG) and the residual pump power transmitted through the lithium niobate crystal (PPLN); and cavity high-reflector (C3) is picked off by a beam splitter (BS) and monitored by photodetector (TPMP). For spatial and temporal resolution we use a fast-response, small-area, fiber-coupled photodetector and a series of dichroic filters. The input end of the fiber is positioned in the image plane of an optical system that images the output face of the PPLN OPO crystal. The 75 cm curved mirror on the left of the diagram and a lens (IL) act as a compound optical system that images the output of the PPLN crystal into a plane where the input end of the optical fiber is scanned. The position of the image plane is determined by inserting a mask in the OPO cavity at the output face of PPLN crystal. This partially blocks a weak incident pump and produces a well known interference pattern. Spatial scans were then performed to exactly determine the image plane. Transverse translation of the mask by a known amount and recording the spatial profile allowed us to deduce the magnification of the imaging system. The output end of the optical fiber is connected to a fast-response photodiode (FPD). The dichroic filters (DF) are mounted on a motorized translation stage to allow computer controlled monitoring of signal or pump wavelengths.

A boxcar integrator, triggered by an auxiliary laser diode (LD) and photodiode (BXT) is used to measure the slow large-area photodetector voltages. The integrating window is 30 μs long and is positioned approximately 175 μs from the opening edge of the chopper window. This is well within the steady state operation of the system. The signal from the fast-response photodiode is sent to an analog sampling head. The sampling head is triggered by the 38 MHz signal that drives the pump-laser's mode locker. The delay between the triggering and sampling of the

photodiode's electrical signal is controlled by the computer through an external input of the sampling head. The temporal resolution of the sampling head binning enabled us to resolve structure of the order of 20 ps. The output of the sampling head was sent to the boxcar triggered at the chopper frequency. The boxcar's integrating window's width and delay were adjusted within the chopper window enabling one to temporally resolve the transmitted pump and signal behaviour through switch-on to steady state. The output voltages of the integrator were recorded by computer.

Results and Discussions

In this section data on cavity optimisation, threshold, optimal out-coupling, and the spatially and temporally resolved transmitted pump are presented. To obtain optimal performance from the OPO the signal power of the OPO cavity was studied as a function of synchronicity (OPO cavity length) and for several incident powers, see Figure 2. Zero on the horizontal axis was chosen to correspond to the maximum signal efficiency and positive cavity length detuning corresponds to longer cavity lengths. The incident power was varied using the half-wave plate and polarizer (HWPP) combination between the laser and OPO resonator, while the cavity length was changed using an optically encoded motorized translation stage. The cavity continues to oscillate over ~ 5 mm of detuning, which corresponds to an overall change in optical length of 10 mm. The signal detuning was asymmetrical, oscillation occurring over a greater range of cavity detuning to the shorter cavity side of synchronism. On synchronism a prominent increase in signal power was seen at higher incident powers.

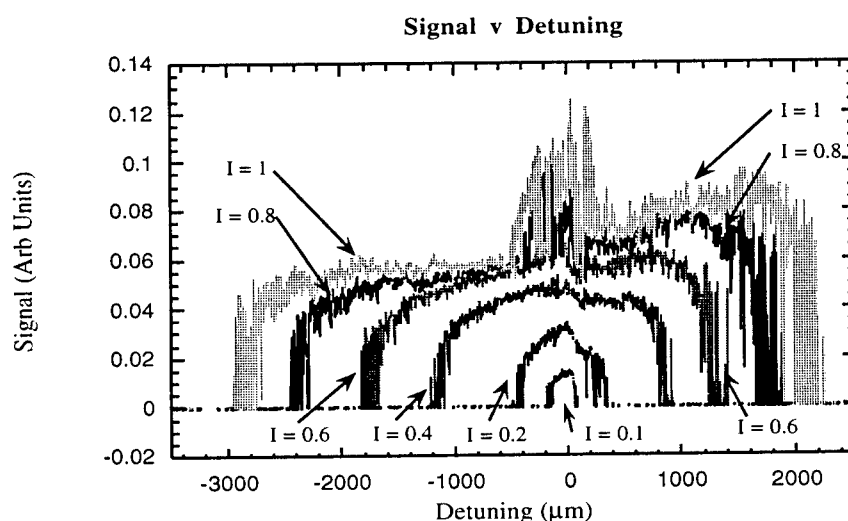
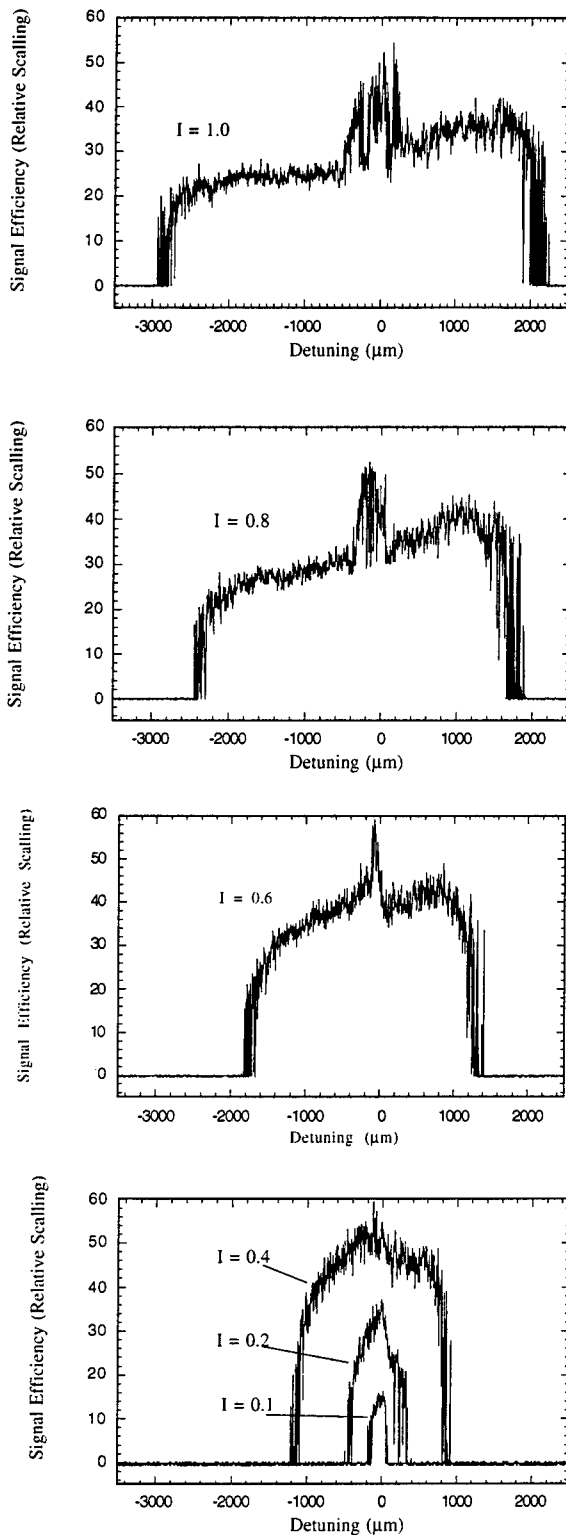


Figure 2. Signal as a function of cavity detuning for six different incident powers.

In figure 2a the signal efficiency is plotted as a function of cavity detuning. Signal efficiency is defined as signal power divided by incident pump power. Zero cavity detuning is determined from these plots and corresponds to maximum



signal efficiency. Maximum signal efficiency occurs for approximately 10 W, ($I = 0.6$), of average incident power, and over a narrow band around synchronism. These data represent the relative signal efficiency. The absolute signal efficiency requires scaling the signal power and incident power by the requisite attenuation factors. The position of the peak signal efficiency remains unchanged throughout the measured power range.

In figure 2B the transmitted pump power normalized by dividing by the incident pump power is plotted for the same conditions as figure 2A. From these curves it is evident that the system achieved about 70% pump depletion over the integrated temporal and spatial profile of the transmitted pump. However this was not for the highest incident pump powers. For the higher powers the pump depletion peaked at $\sim 60\%$ at synchronism and maintained about 50 % depletion over the detuning range. In contrast, the on-axis temporally resolved pump depletion was a remarkable 90 % for almost all powers measured, figure 2c. Only for the highest and lowest powers measured did

the peak pump depletion reduce. The reduction for $I = 1$ is attributed to back conversion while at low incident powers, $I = 0.1$, there was insufficient conversion to completely deplete the onaxis pump at its temporal center.

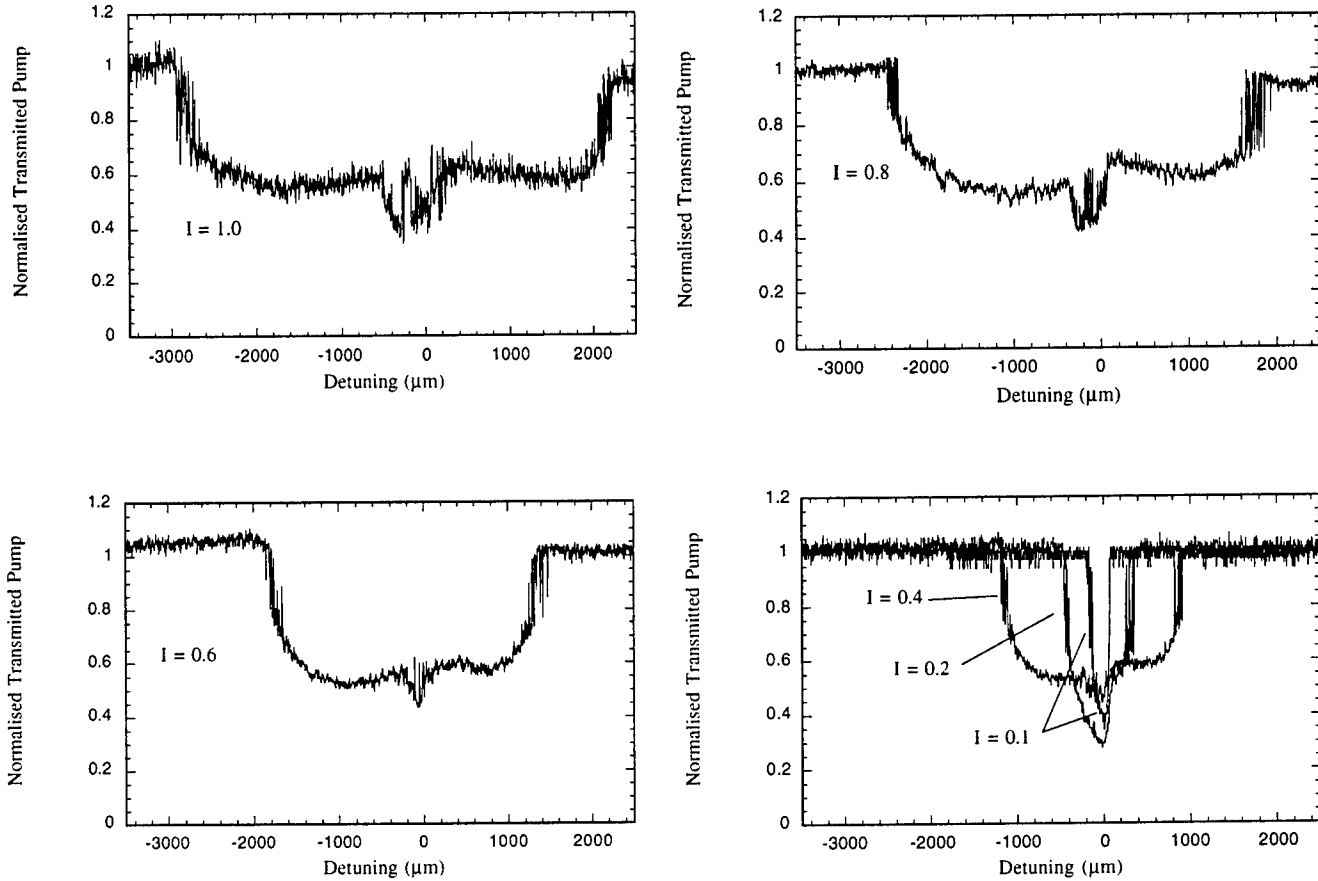


Figure 2A. Four plots showing pump depletion as a function of cavity detuning for different incident powers. The maximum pump depletion corresponds to max signal generation.

To characterise the operation of a pulsed OPO and to fully observe effects such as pump depletion and back conversion one must resolve structure within the temporal and spatial envelope of a pulse, which, for this system, requires a temporal resolution of the order of 20 ps and a spatial resolution of the order of 10 μm . Such a detection system is described in the experimental section.

To observe the onaxis pump-depletion the cavity-length detuning scans were repeated using the fibre coupled fast photodetector to monitor the spatial and temporal center of the transmitted pump. The spatial center was obtained from a two-dimensional scan of the transmitted-pump's intensity profile with the OPO off-resonance. A narrow, variable-delayed sampling window of ~ 20 ps width was set to record the peak of the spatially resolved transmitted pump

signal. These results are recorded in figure 2C. Again zero on the horizontal axis correspond to the maximum signal efficiency, synchronism, and positive cavity length detuning corresponds to longer cavity lengths. It is clear that the transmitted pump depletion measured by the fast system is greater than the slow, large-area photodiode measurements. The peak onaxis pump depletion is 90 %.

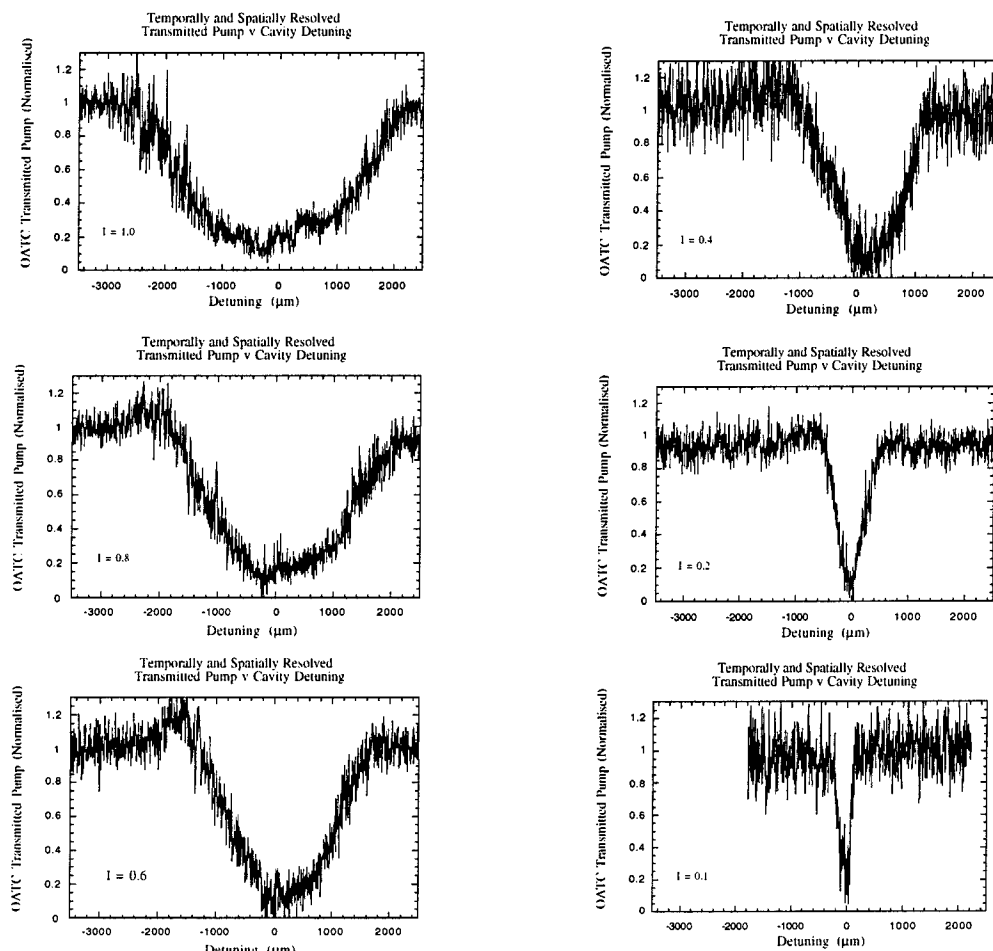


Figure 2C. Pump depletion as a function of cavity length as measured by the fast photodetector and fiber. The onaxis pump depletion is typically 90%

Further characterisation required monitoring the transmitted pump and signal as a function of incident power. The cavity was set on synchronism and carefully aligned for lowest oscillation threshold. In figure 3a (top) the transmitted pump power and signal power are plotted as a function of incident pump power. In this experiment twenty discrete measurements were taken and plotted for each incident power. The vertical spread in the data gives an indication of the pulse to pulse stability of the OPO. Typical threshold for a well-aligned 5 cm PPLN system was $\sim 0.06 I$. Above threshold the signal increased linearly until about twice threshold where the signal tended to saturate. The rollover point corresponds to an increase in pump transmission. A notable feature is the reduction in the

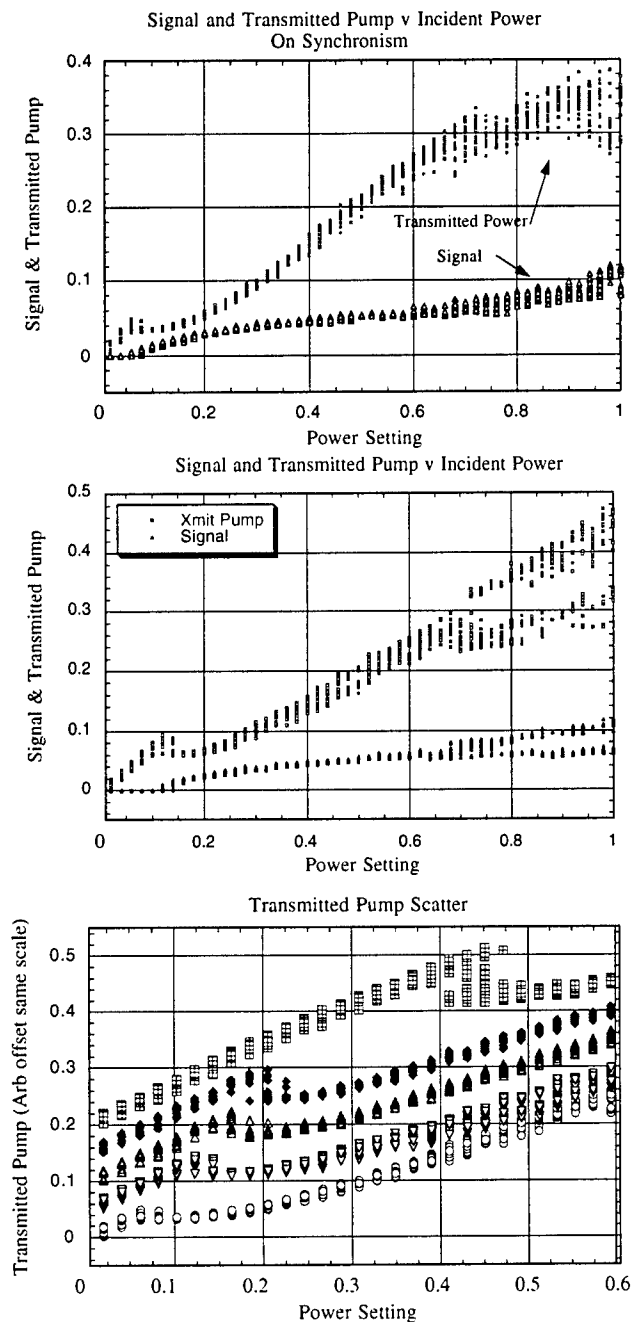


Figure 3A, 3B and 3C. See text for details.

the intracavity signal is sufficiently strong to generate second harmonic at $0.747 \mu\text{m}$. Sum frequency mixing with idler produces red at $0.624 \mu\text{m}$. The blue light ($0.493 \mu\text{m}$) corresponds to a possible impurity transition from iron.

transmitted pump noise just after threshold. However at ~ 10 times threshold the transmitted pump and signal experienced a greater pulse to pulse instability. Detuning the cavity length ($200 \mu\text{m}$ shorter), increased threshold and at higher incident powers both the signal power and transmitted pump power display switching between distinct output level, which can be clearly seen in figure 3B (middle). These data would be obscured if presented using an averaged output with error bars. The source of the switching and the meaning of the distinct levels of output is not well understood and is an area of continued investigation. In figure 3C (lower plot), several traces around threshold are presented for various fixed cavity detuning and all exhibit a reduction in transmitted pump noise.

In addition to the signal and transmitted pump, several other emissions from the OPO cavity were observed and measured using a 0.5 m spectrometer. Tentative identification of each emission is recorded in the Table 1. It is important to note that

Table 1

Identificaton	Wavelength (μm)
Signal	1.486
Pump	1.064
Second Harmonic of the Signa	0.747
Sum of Signal and Pump	0.624
Second Harmonic of the Pump	0.532
Recombination Radiation	0.493

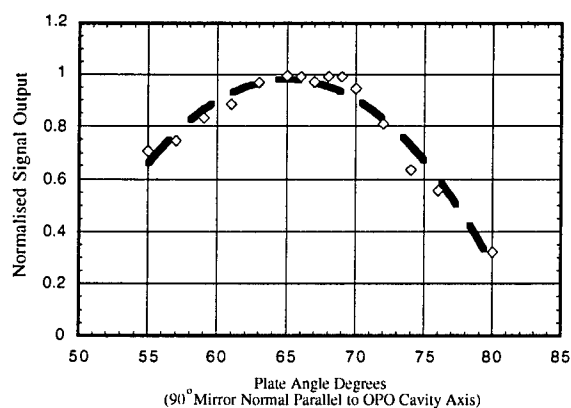


Figure 4. Normalised signal v intracavity “brewster plate” angle. Maximum signal corresponds to ~4% outcoupling at ~12 W pumping

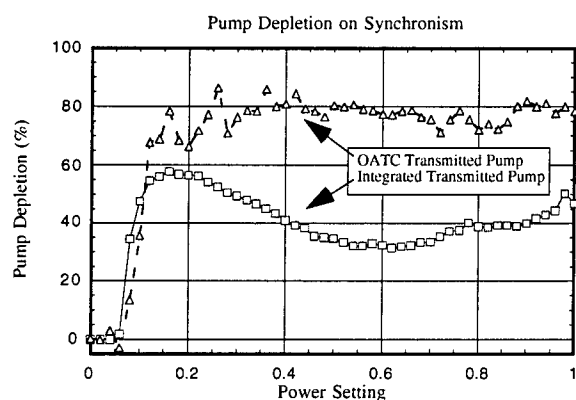


Figure 5. Percentage pump depletion as a function of incident power. The triangles correspond to the temporally and spatially resolved data.

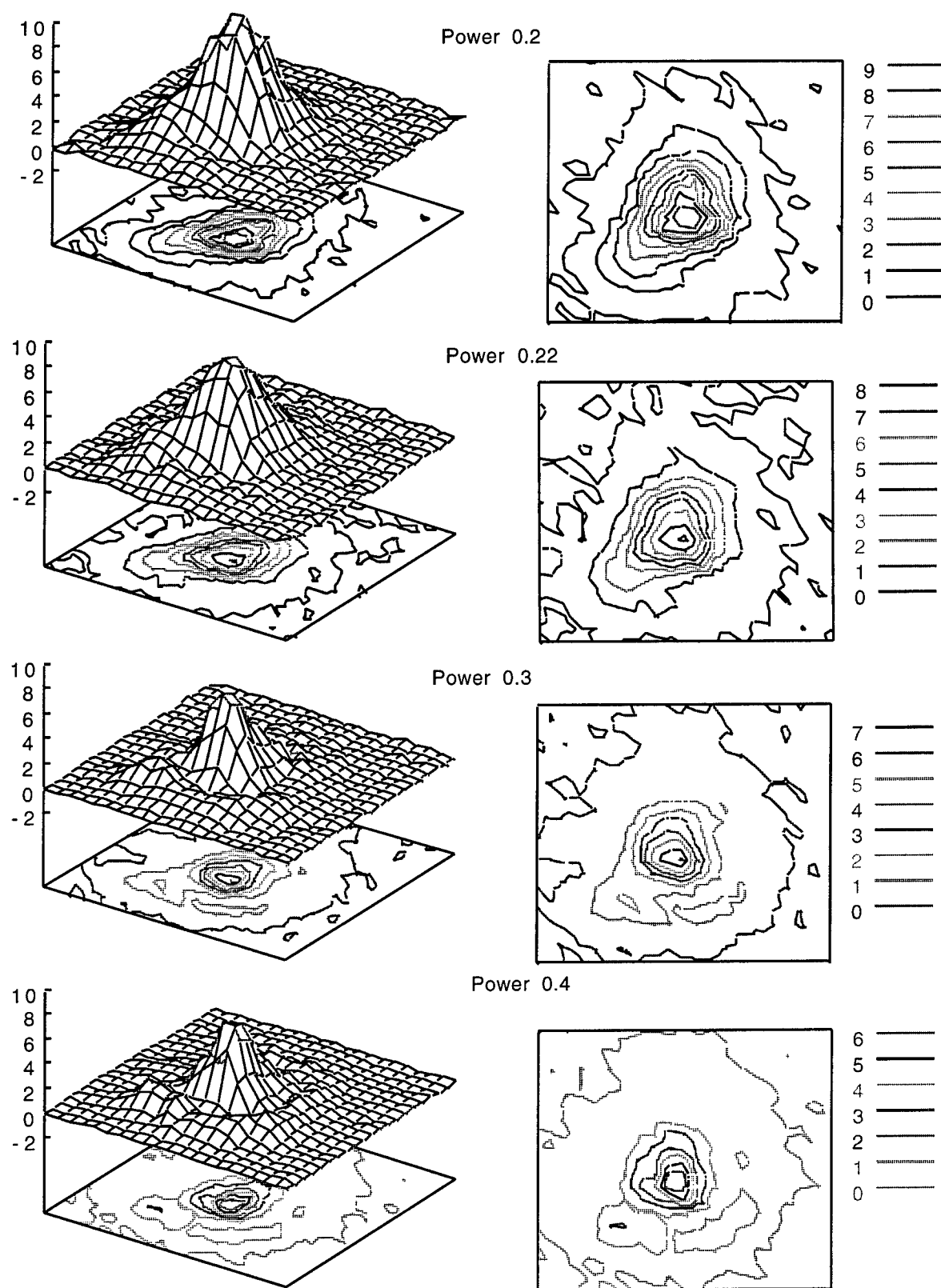
To determine optimum conditions for pump to signal conversion we monitored the intracavity signal power as a function of output coupling. The two intracavity glass plates changed the cavity loss through the angular dependence of the Fresnel loss. As the plates' angles were adjusted the cavity length was tuned to maintain synchronism. The normalised intracavity signal power is then plotted as a function of angle. The results are plotted in figure 4. The output signal, normalised, is plotted as a function plate angle. The solid line is a guide for the eye and minimum outcoupling is $\sim 55.4^\circ$, Brewster's angle. Maximum efficiency occurs at $\sim 68^\circ$ output coupling for ~ 12 Watts of incident pump power. The on-axis behaviour, at the peak of the transmitted pump's temporal pulse was further studied as a function of incident pump power. Again the cavity was positioned on synchronism and the fiber was in the image plane at the peak of the pump pulse with the fast detector sampling window set at the center of the pulse. Figure 5 is a plot of the percentage pump depletion, recorded on axis at the temporal center (OATC) of the pulse as a function of increasing power, (open triangles), also shown for comparison are the slow, large area photodetector measurements

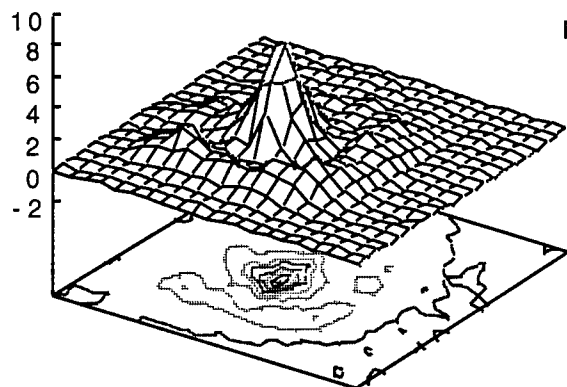
(open squares). The temporally and spatially resolved transmitted pump again showed greater on-axis pump depletion than the averaged transmitted pump. The peak, on-axis pump depletion measured at the temporal center

of the pulse is ~80 % and occurred at approximately five times threshold where the pump-depletion remained relatively constant up to fifteen times threshold. A 1.5 μm high reflector mirror, was positioned upstream of the fibre input to ensure measurement of the transmitted pump radiation (1.064 μm) and not a combination of pump and signal wavelengths. The difference in detected signal corresponded to the transmission at 1.064 μm of the 1.5 μm optic. The difference in maximum pump depletion between figures 3 and 5 is ascribed to slightly different alignment.

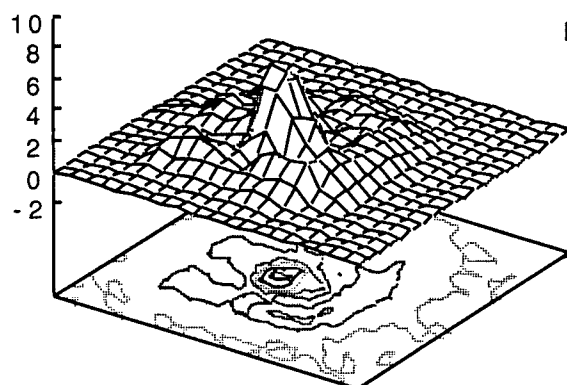
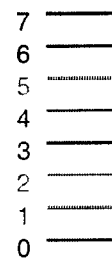
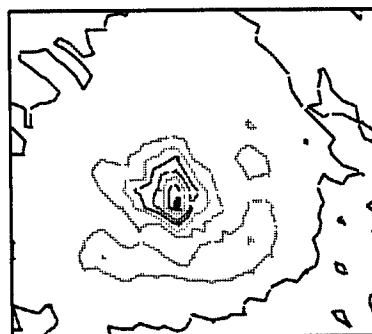
To further characterise the system and observe pump depletion and back-conversion, the transmitted pump's spatial profile was recorded as a function of incident power. The effect of pump depletion should "eat" away at the center of the transmitted pump, producing a "volcano like" spatial profile. Since back-conversion is also a $\chi^{(2)}$ effect, strongest back-conversion is expected to take place at the peak of the signal pulse. For a well aligned system, on synchronism, back-conversion would appear as an increase in pump intensity, narrower in profile than the pump. Back conversion should be manifest as an increase in transmitted pump intensity, which will tend to fill in the "crater". Experimental data, recorded in figure 6, tend to confirm this. In this experiment the cavity was carefully aligned for temporal and spatial overlap between the circulating signal and pump. The temporal window of the sampling head was set at the peak of the pump pulse, and the signal on the fiber recorded as a function of position. A series of profiles was recorded starting below threshold and increasing to maximum incident power. The vertical scale indicates the absolute magnitude of the transmitted pump. A series of imaged profile of the transmitted pump is recorded in Figure 6 as a function of incident power. The first plot is for the OPO off resonance, power 0.2 I and close to threshold. Above threshold the overall profile decreases, with maximum depletion taking place at the center of the beam. As the incident power is increased further, power > 0.4 I, the overall profile starts to grow a narrow cone in the region where, the pump has been depleted, there is strongest signal and optimum spatial overlap between pump and signal (synchronism). This central cone is ascribed to back conversion. The cone continues to grow with increasing incident power. Figures 6, power =0.9 clearly shows a narrow central cone surrounded by an annulus formed by the remainder of the incident pump that has not been down converted. The central cone is formed by the back conversion of signal and idler into the pump wavelength. At the maximum power some broadening of the central cone was observed. This may be attributable to the now increasing pump intensity again converting to signal at the peak.

Figure 6. Sequence of intensity profiles and contour plots showing the transmitted pump as a function of increasing incident power.

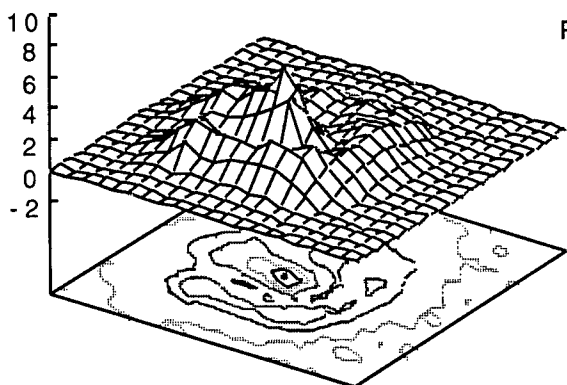
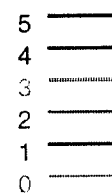
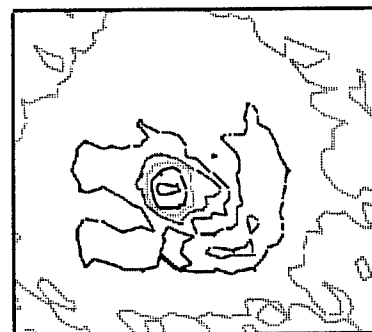




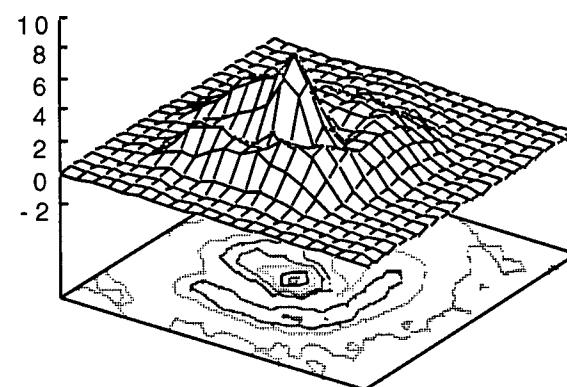
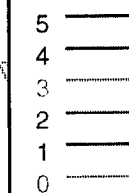
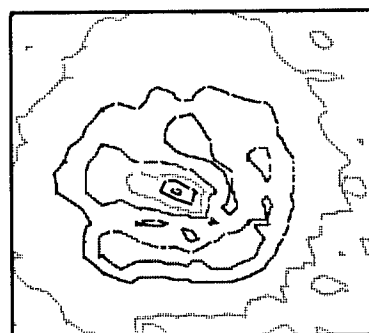
Power 0.5



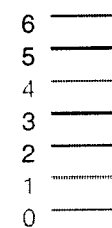
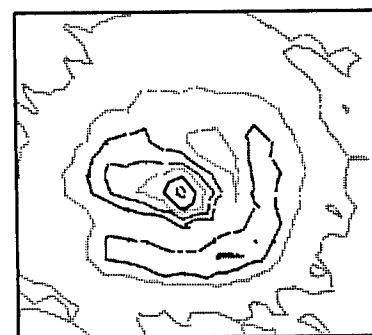
Power 0.6

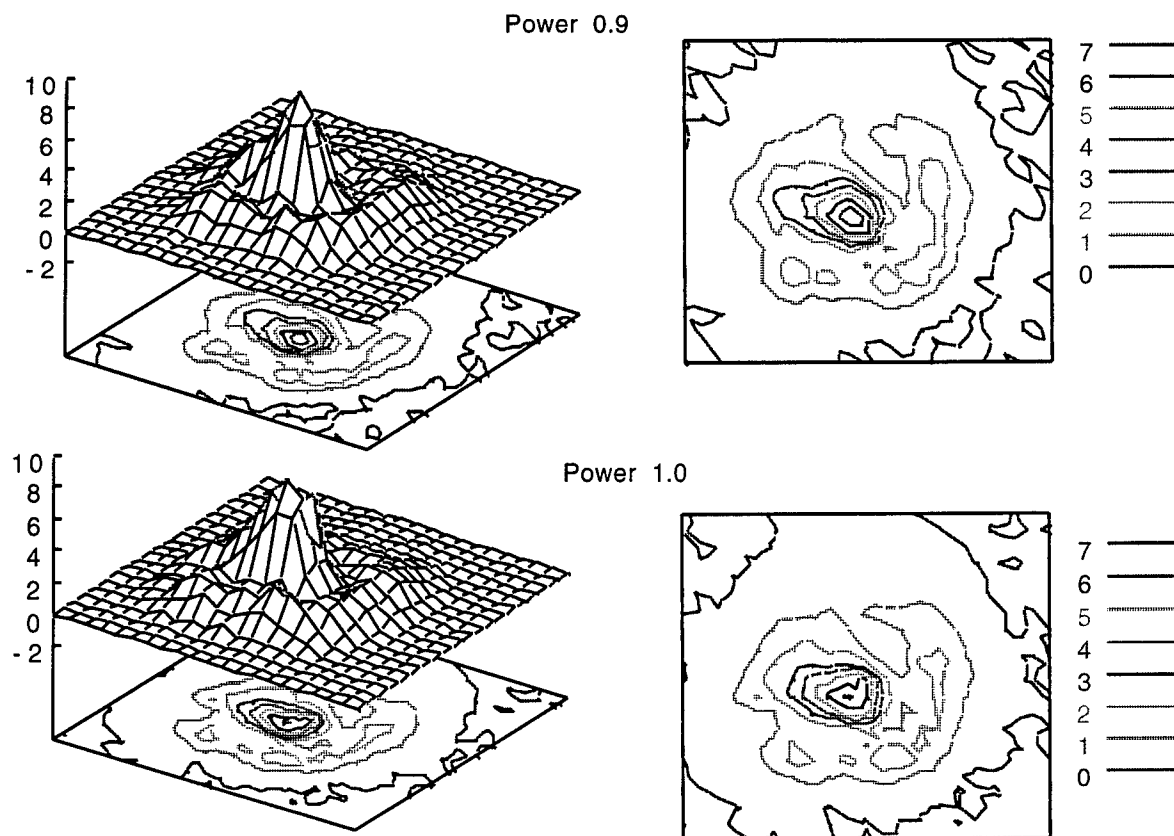


Power 0.7



Power 0.8

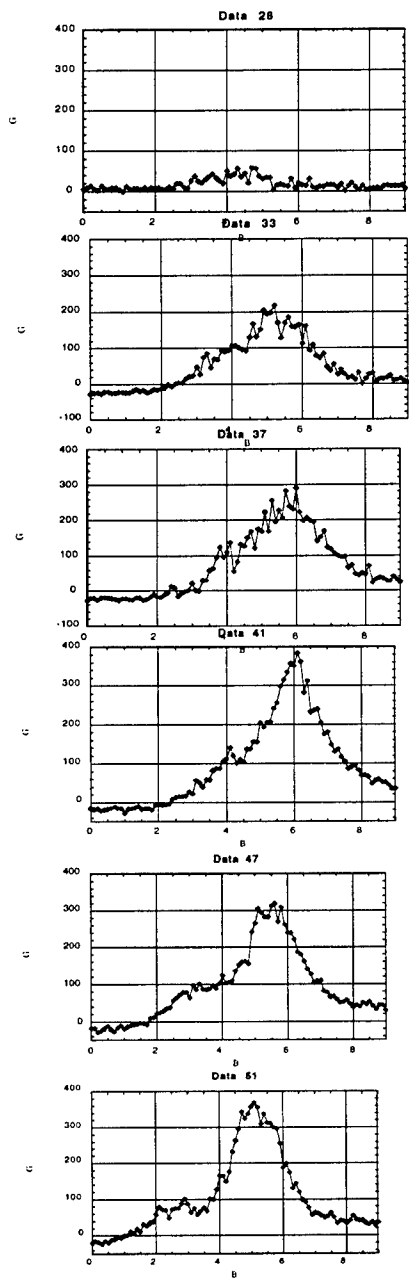




Temporal Profile

The operation of the OPO from switch-on through steady-state operation was also studied. A considerable wealth and volume of data was taken during these experiments and only preliminary (raw) data presented here. The onaxis temporal profiles of the transmitted pump pulse and signal pulse were recorded for various time delays within the chopper window. Again the fiber was positioned in the image plane at the spatial center of the transmitted pulse. Due to dispersion and cavity alignment the center of the transmitted pump did not always coincide exactly with the signal profile. On switching from transmitted pump to signal detection not only was the blocking filter changed but the fiber was also repositioned for the corresponding center. The following results show typical operation of OPO for strong pumping and for pump pulse of ~ 100 ps FWHM at various times within the $250 \mu\text{s}$ chopper window. The width of each plot is 500 ps. Figure 7 is a composite plot of 6 temporal profiles each taken $\sim 30 \mu\text{s}$ later than the previous pulse during the chopper window. The first $50 \mu\text{s}$ corresponds to switch-on; after $\sim 100 \mu\text{s}$ the system approaches equilibrium. In the first plot (top) the leading edge of the transmitted pump has already been depleted in the high gain system at the strongest pumping levels. After $\sim 100 \mu\text{s}$ a strong peak is observed in the trailing edge of the pulse. This is attributed to back conversion and the system oscillation with a slight cavity detuning. Switch-off is essentially the reverse of Figure 7.

Figure 7. Temporal profile of the transmitted pump for different times within the chopper window. The horizontal width is 500 ps.



Conclusions

In this report the successful operation and characterisation of 5 cm of PPLN in a cw-modelocked Nd:YAG synchronously-pumped OPO cavity is described. The OPO produced pulses of ~100 ps duration in the wavelength range of ~1.5 μ m. Anomalous switching behaviour was observed when the system was near synchronism and a reduction in the transmitted pump noise was seen for incident powers around threshold. Strong pump depletion was observed in both the spatial and temporal profiles of the pump.

Acknowledgements.

I would like to thank Dr. Karl Koch, Captain Mike Dearborn and Dr Gerald Moore of Phillips Laboratory for their cooperation and assistance throughout all phases of this work. I would also like to acknowledge Phillips Lab, RDL and AFOSR for their support.

NONLINEAR TRACKING CONTROL
FOR A PRECISION DEPLOYABLE STRUCTURE
USING A PARTITIONED FILTER APPROACH

Mark J. Balas
Professor
Department of Aerospace Engineering Sciences

University of Colorado
Boulder, CO 80309-0429

Final Report for:
Summer Faculty Research Program
USAF Phillips Laboratory
Albuquerque, NM

Sponsored by:
Air Force Office of Scientific Research
Bolling Air Force Base, DC

September 1997

NONLINEAR TRACKING CONTROL
FOR A PRECISION DEPLOYABLE STRUCTURE
USING A PARTITIONED FILTER APPROACH

Mark J. Balas
Professor
Department of Aerospace Engineering Sciences
University of Colorado

Abstract

As part of the Integrated Ground Demonstration Laboratory (IGDL) mission, the feasibility of a large, deployable, sparse aperture, space telescope is being studied under the UltraLITE project. Precision tracking of the deployable structure via a speaker voice-coil actuated white-light interferometer is the subject of this report.

We have established a new tracking control approach using a partitioned Kalman filter based on measurements of the actuator current and the normalized fringe intensity from an avalanche photo diode. This control has the potential to maintain the optical path difference of the interferometer within desired nanometer tolerances. The theory to support this tracking controller is developed in this report.

NONLINEAR TRACKING CONTROL FOR A PRECISION DEPLOYABLE STRUCTURE USING A PARTITIONED FILTER APPROACH

Mark J. Balas

1.0 Introduction

Under the UltraLITE project, experiments are being developed at the US Air Force Phillips Laboratory to determine the feasibility of large, deployable, sparse aperture, space-based telescopes. This has resulted in a proposed UltraLITE deployable test structure as part of the Integrated Ground Demonstration Laboratory (IGDL) to measure and control subwavelength (nanometer) structural disturbances.

White light interferometry has been chosen to measure accurately structural disturbances on the nanometer scale. Since the coherence length of white light is on the order of hundreds of nanometers, the precision structure may induce disturbances well beyond the range of the interferometer sensor. Consequently, the interferometer must track the structure to produce zero optical path difference (OPD) to provide structure position without signal loss. This is done using a voice-coil actuated mirror (called "the Speaker") as the reference optical path. The speaker must be controlled to lock on and track the structure motion, and that control system is the subject of this paper.

2.0 The Speaker Model

The voice-coil actuated mirror actually consists of four speaker actuators attached to the mirror to control piston, tip, and tilt. We focus here on the piston control only and consider a single speaker:

$$m\ddot{x} + d\dot{x} + kx = \beta i \quad (1a)$$

$$L \frac{di}{dt} + Ri = V - \beta \dot{x} \quad (1b)$$

where x is the speaker position, i the speaker current, and V the voltage applied to the speaker.

The speaker parameters m , d , k , L , R , and βl are all constants determined by experimental testing. Since the inductance L is very small ($L = 6 \times 10^{-5} \text{ H}$), we will take it as zero. Then (1b) becomes

$$i = \frac{V - \beta l \dot{x}}{R} \quad (2)$$

which expresses the speaker current as the difference between the current due to the impressed voltage $\left(\frac{V}{R}\right)$ and the current due to the back-emf $\left(\frac{\beta l \dot{x}}{R}\right)$. If we use (2) in (1a), we obtain

$$m\ddot{x} + \tilde{d}\dot{x} + kx = \frac{\beta l}{R} V \quad (3)$$

where $\tilde{d} \equiv d + \frac{(\beta l)^2}{R}$. The net effect is to enhance the modeled speaker damping d by the amount $\frac{(\beta l)^2}{R}$.

We define $u_1 \equiv V$ (the speaker control input), $y_1 \equiv i$ (the measured speaker current), and $z_1 \equiv x$ (the speaker position); with the speaker state $x_1 \equiv \begin{bmatrix} x \\ \dot{x} \end{bmatrix}$, we have the following Speaker

Model:

$$\dot{x}_1 = A_1 x_1 + B_1 u_1 \quad (4a)$$

$$z_1 = C_1 x_1 \quad (4b)$$

$$y_1 = E_1 x_1 + F_1 u_1 \quad (4c)$$

where $A_1 \equiv \begin{bmatrix} 0 & 1 \\ -\frac{k}{m} & -\frac{\tilde{d}}{m} \end{bmatrix}$, $B_1 \equiv \begin{bmatrix} 0 \\ \frac{\beta l}{mR} \end{bmatrix}$, $C_1 \equiv [1 \ 0]$, $E_1 \equiv \begin{bmatrix} 0 & -\frac{\beta l}{R} \end{bmatrix}$, and $F_1 \equiv \frac{1}{R}$. This is a two-dimensional, linear, state space model for the speaker which actuates the mirror in the optical path.

It is easy to see that (A_1, B_1) is controllable if and only if $\frac{\beta l}{mR} \neq 0$. Also, (A_1, E_1) is observable if and only if both $\frac{k}{m} \neq 0$ and $\frac{\beta l}{R} \neq 0$. The measured speaker parameters are the following:

$$\begin{cases} m = 0.0025 \\ \beta l = 1.5 \\ k = 5 \times 10^3 \\ d = 0.5 \\ R = 32 \\ L = 6 \times 10^{-5} \approx 0 \end{cases}$$

which yield:

$$A_1 = \begin{bmatrix} 0 & 1 \\ -2 \times 10^6 & -228 \end{bmatrix}, \quad B_1 = \begin{bmatrix} 0 \\ 18.75 \end{bmatrix}$$

$$C_1 = [1 \ 0], \quad E_1 = [0 - 0.0469], \quad F_1 = 0.0313$$

These give rise to a controllable-observable system with the transfer function:

$$T_1(s) = \frac{1}{32} \left[\frac{s^2 + 200s + 2 \times 10^6}{s^2 + 228s + 2 \times 10^6} \right] \quad (5)$$

It is easy to see that the poles and zeroes of (5) are nearly the same, and the undamped natural frequency of the speaker is 225 hz.

3.0 The Tracking Control Problem

The optical path difference (OPD) for the interferometer is given by

$$z = z_1 - z_2 \quad (8)$$

where z_1 is the speaker position and z_2 is the flexible structure position. The purpose of control is to cause the speaker to "track" the motion of the structure, i.e. $\lim_{t \rightarrow \infty} z(t) = 0$.

To solve this tracking control problem we need a model of the structure motion. These models normally are obtained through finite element, flexible structure techniques and result in very large-scale systems. Such high-order models are useful for structure controller design but less helpful for the nanometer scale dynamics involved in our optical problem.

We will assume a model of the structure (9) which is closely related to that of the speaker (4):

$$\dot{x}_2 = A_2 x_2 + B_2 u_2 \quad (9a)$$

$$z_2 = C_2 x_2 \quad (9b)$$

where $\dim x_2 = \dim x_1 = 2$. This may seem rather arbitrary, but for our needs the structure model (9) is more of a mental construct or “metamodel” than an actual representation of all the complex motions of which the structure is capable. As we shall see, only a measurement involving the OPD is available to our controller, nothing more.

Define the state error

$$e \equiv x_1 - x_2 \quad (10)$$

and obtain, from (4) and (9), the following:

$$\dot{e} = A_1 e + B_1 u_1 + (A_1 - A_2)x_2 - B_2 u_2 \quad (11)$$

The form of an ideal tracking control law would be

$$u_1^* = G_1 e + G_x x_2 + G_u u_2 \quad (12)$$

This results in a closed-loop system:

$$\dot{e} = (A_1 + B_1 G_1)e + [A_1 + B_1 G_x - A_2]x_2 + [N_1 G_u - B_2]u_2 \quad (13)$$

and the following OPD:

$$z = z_1 - z_2 = C_1 x_1 - C_2 x_2 = C_1 e + [C_1 - C_2]x_2 \quad (14)$$

If a set of matching conditions:

$$A_2 = A_1 + B_1 G_x \quad (15a)$$

$$B_2 = B_1 G_u \quad (15b)$$

$$C_1 = C_2 \quad (15c)$$

can be satisfied, the closed-loop (13) becomes

$$\begin{cases} \dot{e} = (A_1 + B_1 G_1)e & (16a) \\ z = C_1 e & (16b) \end{cases}$$

Then the controllability of (A_1, B_1) permits the choice of control gains G_1 to achieve arbitrary exponential convergence $\left(\lim_{t \rightarrow \infty} e = 0\right)$ and, hence, $z = C_1 e \rightarrow 0$. The rate of convergence will be determined by the eigenvalues of $A_1 + B_1 G_1$. The matching conditions (15) simply say that it is possible, via feedback, to match the structure and speaker motions. If they could not be satisfied, the speaker would not be capable of tracking the structure motion, i.e. $\lim_{t \rightarrow \infty} z \neq 0$.

There are limitations to the ideal control law (12):

(a) e and x_2 are not measured

(b) u_2 is not measured

For our development (b) is not critical since we may assume $u_2 \equiv 0$ in (9); this means our metamodel is not “driven” by any (deterministic) exogenous inputs. However, (a) must be addressed.

In the next sections, we will develop estimators for x_1 and x_2 from available measurements. This will allow us to create a realizable tracking control law.

4.0 The Linear Speaker Filter

Since (A_1, E_1) is observable, it is possible to recover the speaker position z_1 (and velocity, too) from the measured current via a linear state estimator or Kalman filter:

$$\begin{cases} \dot{\hat{x}}_1 = A_1 \hat{x}_1 + B_1 u_1 + K_1 (y_1 - \hat{y}_1) & (17a) \\ \hat{y}_1 = E_1 \hat{x}_1 + F_1 u_1 & (17b) \end{cases}$$

The input and output noise covariances can be estimated for the speaker and used to solve for the filter gains K_1 using the Riccati equation, e.g. [2]. Alternatively, a deterministic approach using the speaker estimator error $e_1 \equiv \hat{x}_1 - x_1$ yields:

$$\dot{e}_1 = (A_1 - K_1 E_1) e_1 \quad (18)$$

where the filter gains K_1 can be chosen by arbitrary pole placement since (A_1, E_1) is observable. In either case, the estimated speaker state \hat{x}_1 will converge exponentially fast to the actual state x_1 with rate determined by the eigenvalues of $A_1 - K_1 E_1$.

5.0 The Nonlinear Structure Filter

There is no way to measure the OPD directly. Instead it is indirectly measured from the interferometer using an avalanche photo diode (APD) whose output is the normalized intensity:

$$y_2 = h(z) \quad (19)$$

where the nonlinear fringe function $h(\cdot)$ is given by

$$h(z) = \frac{1}{2} + \frac{1}{2} e^{-\frac{1}{4} \left(4\pi \frac{\lambda_p}{\lambda_c} \right)^2 z^2} \cos \left(\frac{4\pi z}{\lambda_c} \right) \quad (20)$$

with center wave length $\lambda_c \sim 600\text{nm}$ and passband $\lambda_p \sim 100\text{nm}$ for our testbed. This function can be derived for a white light interferometer in Twyman-Green configuration; see developments in [3] Chapter 22 and [4] Chapter VII.

A nonlinear state estimator, or extended Kalman filter, can be used to recover the structure state x_2 from the APD output y_2 ; for details, see [5] Chapter 6 or [6] Chapter 6. Our nonlinear structure filter is given by

$$\dot{\hat{x}}_2 = A_2 \hat{x}_2 + K_2 (y_2 - \hat{y}_2) \quad (21a)$$

$$\hat{y}_2 = h(\hat{z}) \quad (21b)$$

$$\hat{z} = \hat{z}_1 - \hat{z}_2 \quad (21c)$$

where \hat{z} is the estimated OPD and \hat{z}_1 and \hat{z}_2 are the estimated speaker and structure position estimates, respectively.

The linearized structure filter is given by

$$\dot{\hat{x}}_2 = A_2 \hat{x}_2 + K_2 (y_2 - \hat{y}_2) \quad (22a)$$

$$\hat{y}_2 = H \hat{z} \quad (22b)$$

$$\hat{z} = \hat{z}_1 - \hat{z}_2 \quad (22c)$$

where (22b) replaces (21b) and

$$H \equiv \left. \frac{dh(\xi)}{d\xi} \right|_{\xi=z_{op}} = -\frac{1}{2} e^{-az_{op}^2} [2az_{op} \cos bz_{op} + b \sin bz_{op}] \quad (23)$$

and $a \equiv \frac{1}{4} \left(4\pi \frac{\lambda_p}{\lambda_c} \right)^2$ and $b \equiv \frac{4\pi}{\lambda_c}$. We see that $h(\cdot)$ is locally invertible when $H \neq 0$; we will

pick any z_{op} where $H \neq 0$.

Define the structure state estimation error $e_2 = \hat{x}_2 - x_2$. From (9) and (22) with (19) linearized by $y_2 = Hz$, we obtain

$$\dot{e}_2 = (A_2 + K_2 H C_2) e_2 - K_2 H C_1 e_1 - B_2 u_2 \quad (24)$$

When we assume $u_2 = 0$, (24) and (18) yield $\lim_{t \rightarrow \infty} e_1(t) = 0$ and $\lim_{t \rightarrow \infty} e_2(t) = 0$ with exponential rates determined by $A_1 - K_1 E_1$ and $A_2 + K_2 H C_2$.

In Sec. 4.0 we have seen that (A_1, E_1) observable would allow an arbitrary rate for $A_1 - K_1 E_1$. Now we see that $(A_2, H C_2)$ observable permits the same for $A_2 + K_2 H C_2$; since H is a nonzero scalar, this condition becomes (A_2, C_2) observable which we can safely assume for our structure metamodel (9). This says that the linearized structure filter (22) will produce a convergent estimator error e_2 when (19) is linearized. Therefore, at least in a neighborhood of the operating point z_{op} , the nonlinear structure filter (21) will also converge.

In some cases, the gain K_2 for the nonlinear filter can be updated by solving a Riccati Equation with $H(k) \equiv \left. \frac{dh(\xi)}{d\xi} \right|_{\xi=\hat{z}(k)}$; this produces a variable filter gain $K_2(k)$. We chose to use constant gains K_2 based on the linearized system with a fixed operating point z_{op} ; this is a much simpler filter to operate.

6.0 Realizable Tracking Controller

Based on Secs. 2-5, we can create a realizable tracking controller:

$$u_1 = G_1 \hat{e} + G_x \hat{x}_2 \quad (25a)$$

$$\hat{e} = \hat{x}_1 - \hat{x}_2 \quad (25b)$$

where \hat{x}_1 is obtained from the linear speaker filter (17) which monitors speaker current and \hat{x}_2 is obtained from the nonlinear speaker filter (21) which monitors the APD output. These two filters are really one composite nonlinear Kalman filter based on the two outputs y_1 and y_2 . However, it is easy to see that the composite filter partitions into the two separate ones, a linear and a nonlinear one; hence, the name partitioned filter approach.

7.0 Closed-Loop Stability Analysis

The closed-loop system (consisting of the speaker (4), the structure metamodel (9), the linear speaker filter (17), the nonlinear structure filter (22), and the realizable tracking control law (25)), can be obtained from

$$u_1 = u_1^* + G_1 e_1 + (G_x - G_1) e_2$$

where u_1^* is the ideal tracking control law and e_1 , e_2 are the speaker and structure filter errors respectively. This produces the following nonlinear closed-loop system:

$$\begin{aligned} \begin{bmatrix} \dot{e} \\ e_2 \\ e_1 \end{bmatrix} &= \begin{bmatrix} A_1 + B_1 G_1 & B_1 (G_x - G_1) & B_1 G_1 \\ 0 & A_2 & 0 \\ 0 & 0 & A_1 - K_1 E_1 \end{bmatrix} \begin{bmatrix} e \\ e_2 \\ e_1 \end{bmatrix} + \begin{bmatrix} -B_2 \\ -B_2 \\ 0 \end{bmatrix} u_2 \\ &\quad + K_2 \begin{bmatrix} 0 \\ h(z) - h(z + C_1 [e_1 - e_2]) \\ 0 \end{bmatrix} \end{aligned} \quad (26)$$

This can be linearized via $h(z) = H(z)$ to produce:

$$\begin{bmatrix} \dot{e} \\ e_2 \\ e_1 \end{bmatrix} = \begin{bmatrix} A_1 + B_1 G_1 & B_1 (G_x - G_1) & B_1 G_1 \\ 0 & A_2 + K_2 H C_1 & K_2 H C_1 \\ 0 & 0 & A_1 - K_1 E_1 \end{bmatrix} \begin{bmatrix} e \\ e_2 \\ e_1 \end{bmatrix} + \begin{bmatrix} -B_2 \\ -B_2 \\ 0 \end{bmatrix} u_2 \quad (27)$$

which is stable when $A_1 + B_1 G_1$, $A_2 + K_2 H C_1$, and $A_1 - K_1 E_1$ are all stable (which they are by our design). Therefore, when $u_2 \equiv 0$, the tracking error e and the filter errors e_1 and e_2 converge to zero with exponential rate. However, if $u_2 \neq 0$ but is a bounded signal (which represents unmodeled structure dynamics), we have the following result:

$$\begin{aligned} \left(\|e(t)\|^2 + \|e_1(t)\|^2 + \|e_2(t)\|^2 \right)^{1/2} &\leq \sqrt{2} K_c e^{-\sigma_c t} \left(\|e(0)\|^2 + \|e_1(0)\|^2 + \|e_2(0)\|^2 \right)^{1/2} \\ &\quad + \frac{K_c \|B_c\|}{\sigma_c} \|u_2(t)\| \end{aligned} \quad (28)$$

where $\|e^{A_c t}\| \leq K_c e^{-\sigma_c t}$; $t \geq 0$ and

$$A_c \equiv \begin{bmatrix} A_1 + B_1 G_1 & B_1 (G_x - G_1) \\ 0 & A_2 + K_2 H C_1 \end{bmatrix} \quad \text{and} \quad B_c \equiv \begin{bmatrix} -B_2 \\ -B_2 \\ 0 \end{bmatrix} \cdot \Lambda. \quad \text{See Appendix for proof of (28).}$$

This shows that in the limit, as $t \rightarrow \infty$ the errors $e(t)$, $e_1(t)$, $e_2(t)$, are ultimately bounded by $\frac{K_c \|B_c\|}{6_c} \|u_2(t)\|$. Thus, when the metamodel of the structure is actually driven by a nonzero $u_2(t)$,

the best outcome is that our tracking controller will produce a bounded tracking error proportional to $\|u_2(t)\|$; otherwise, if $u_2(t) \equiv 0$, the tracking error converges to zero. This clearly illuminates the difference between a perfect and an imperfect world.

7.0 Conclusions

This report details the supporting theory for a new approach to precision tracking control. A partitioned filter method has been shown to yield stable closed-loop control of a voice-coil actuated interferometer to track the motion of a flexible, deployable supporting structure. The partitioned filter uses the separated signals from the actuator current and the normalized intensity of an avalanche photodiode to produce precision control commands.

Ongoing numerical and laboratory experiments at the IGDL facility of the USAF Phillips Laboratory are being performed to validate this approach for future space-based demonstrations.

Acknowledgments

The author is grateful for the support of AFOSR via the Summer Research Program in residence at the USAF Phillips Laboratory, Albuquerque, NM, for the period May 15 to July 15, 1997.

My very special thanks go to the UltraLITE Team, especially Mike Powers, L. (Robbie) Robertson, Karl Schrader, and Jesse Leitner, who made this research such an excellent experience and the IGDL, my home away from home.

References

1. M. Powers, et al. "UltraLITE: Assessment of Lightweight, Large Aperture

Imaging Concepts.”

2. H. Kwakernaak and R. Sivan, Linear Optimal Control Systems, Wiley-Interscience, NY, NY, 1972.
3. G. Reynolds, J. DeVelis, G. Parrent and B. Thompson, The New Physical Optics Notebook: Tutorials on Fourier Optics, SPIE Optical Engr. Press, Bellingham, WA, 1989.
4. M. Born and E. Wolf, Principles of Optics: Electromagnetic Theory of Propagation, Interference, and Diffraction of Light, (6th Edition), Pergamon Press, Oxford, England, 1980).
5. A. Jaswinski, Stochastic Processes and Filtering Theory, Academic Press, NY, 1970.
6. A. Gelb (editor), Applied Optimal Estimation, The MIT Press, Cambridge, MA, 1992.

Appendix: Proof of Eq. (28)

From (27), it is clear that e_1 is not affected by the bounded input u_2 . Consequently our concern is with

$$\begin{bmatrix} \dot{e} \\ e_2 \end{bmatrix} = \begin{bmatrix} A_1 + B_1 G_1 & B_1 (G_x - G_1) \\ 0 & A_2 + K_2 H C_1 \end{bmatrix} \begin{bmatrix} e \\ e_2 \end{bmatrix} + \begin{bmatrix} -B_2 \\ -B_2 \\ 0 \end{bmatrix} u_2$$

which has the form: $\dot{z} = A_c z + B_c u_2$ where A_c is (exponentially) stable.

Now,

$$z(t) = e^{A_c t} z(0) + \int_0^t e^{A_c(t-\tau)} B_c u_2(\tau) d\tau$$

which satisfies:

$$\|z(t)\| \leq K_c \left[e^{-\sigma_c t} \|z(0)\| + \int_0^t e^{-\sigma_c(t-\tau)} \|B_c\| \|u_2(\tau)\| d\tau \right]$$

where $\|z\| \equiv (\|e\|^2 + \|e_1\|^2)^{1/2}$.

Since u_2 is a bounded signal we can write:

$$\|z(t)\| \leq K_c \left[e^{-\sigma_c t} \|z(0)\| + \int_0^t e^{-\sigma_c(t-\tau)} d\tau \|B_c\| \cdot \sup_t \|u_2(t)\| \right]$$

which becomes

$$\|z(t)\| \leq K_c \left[e^{-\sigma_c t} \|z(0)\| + \frac{1 - e^{-\sigma_c t}}{\sigma_c} \|B_c\| \sup_t \|u_2(t)\| \right] \leq K_c \left[e^{-\sigma_c t} \|z(0)\| + \frac{\|B_c\|}{\sigma_c} \sup_t \|u_2(t)\| \right]$$

Because $e_2(t) = e^{(A_1 - K_1 E_1)t} e_2(0)$ we know we can choose K_1 so that $\|e_2(t)\| \leq K_c e^{-\sigma_c t} \|e_2(0)\|$.

Therefore, using

$$\left\| \begin{bmatrix} e \\ e_1 \\ e_2 \end{bmatrix} \right\| \equiv \left(\|e\|^2 + \|e_1\|^2 + \|e_2\|^2 \right)^{1/2} = \left(\|z\|^2 + \|e_2\|^2 \right)^{1/2} \leq \|z\| + \|e_2\|,$$

we obtain

$$\left(\|e\|^2 + \|e_1\|^2 + \|e_2\|^2 \right)^{1/2} \leq K_c e^{-\sigma_c t} [\|z(0)\| + \|e_2(0)\|] + \frac{K_c \|B_c\|}{\sigma_c} \cdot \sup_t \|u_2(t)\|$$

From $\|z(0)\| + \|e_2(0)\| \leq \sqrt{2} \left(\|z(0)\|^2 + \|e_2(0)\|^2 \right)^{1/2}$, we have the desired (28).

**MULTIPLE APERTURE AVERAGING TECHNIQUE FOR MEASUREMENT
FULL APERTURE TILT WITH A LASER GUIDE STAR AND EXPERIMENTAL
STUDY OF TILT ANGULAR ANISOTROPISM**

**Mikhail S. Belen'kii
Assistant Professor
Department of Philosophy**

**Georgia Technology Research Institute
Atlanta, GA 30332**

**Final Report for:
Summer Research Program
Phillips Laboratory**

**Sponsored by:
Air Force Office of Scientific Research
Bolling Air Force Base, Washington, DC**

And

Phillips Laboratory

September 1997

MULTIPLE APERTURE AVERAGING TECHNIQUE FOR MEASUREMENT FULL APERTURE TILT
WITH A LASER GUIDE STAR AND EXPERIMENTAL STUDY OF TILT ANGULAR
ANISOPLANATISM

Mikhail S. Belen'kii
Principal Research Scientist
Georgia Tech Research Institute
Georgia Institute of Technology
Atlanta, GA 30332-0834

Abstract

A method for measuring full aperture tilt with a LGS is developed. The method exploits a single monochromatic LGS formed through the main telescope and uses two arrays of small auxiliary telescopes separated in orthogonal directions to view the LGS. To reduce the contribution of a down propagation path to the measured tilt, four averaging techniques are used. It is shown that the contribution of the down propagation path can be reduced by averaging a LGS image over FOV of the receiver, over the position of the auxiliary telescope in the telescope array, over position of a subaperture within the auxiliary telescope, and over time. We found that the use of the above averaging techniques permits us to achieve the Strehl ratio equal to 0.7 for various seeing conditions, different telescope diameter, and wavelength, including a visible waveband. A designing methodology for the tilt measurement scheme with a LGS is discussed. An experimental study of the tilt angular correlation scale and the tilt angular averaging function is performed. A new approach of measuring tilt angular anisoplanatism is exploited. This approach employs measurements of the random motion of the portions of a moon edge image to assess wavefront tilt. This technique provides a wide, continuous range of angular separations which are not available in observations with a binary stars. This allows measurements of the tilt averaging function. Besides, the moon is sufficiently bright to enable observations with a high resolution CCD imaging system, and, at any given site and time, the moon is more likely to be available for observations than specific binary stars. In this experiment, the statistical properties of tilt angular correlation and the tilt averaging function were studied. According to estimates based on the tilt averaging function, the tilt angular correlation scale increases by increasing the telescope diameter from 40 *arcsec* to 118 *arcsec*. This indicates that the concept of isoplanatic angle is not applicable to tilt-related phenomena. The data obtained can be used for designing the tilt measurement scheme.

MULTIPLE APERTURE AVERAGING TECHNIQUE FOR MEASUREMENT FULL APERTURE TILT WITH A LASER GUIDE STAR AND EXPERIMENTAL STUDY OF TILT ANGULAR ANISOTROPY

Mikhail S. Belen'kii

Introduction

The inability of a laser guide star (LGS) scheme to sense a full aperture tilt places a fundamental limitation on adaptive optics (AO) systems and limits the area of the sky accessible for AO correction. During the last few years, several different techniques for measuring tilt with a LGS were proposed. In particular, Foy et al. {1} suggested a polychromatic LGS method with two multicolor sodium beacons. This technique uses the wavelength dependence of the index of refraction. However, for ordinary atmospheric conditions, the wavelength dependence of the index of refraction is very weak. The difference in the index of refraction only a few percent when the difference in the wavelength is about one decade, which makes implementation of this technique difficult.

Belen'kii {2} suggested the method which uses a single monochromatic LGS and two auxiliary telescopes separated from the main telescope in transverse directions. A LGS is formed by a laser beam transmitting through the main telescope and auxiliary telescopes are used to view the LGS. A tilt component corresponding to the down propagation path in this technique is eliminated by averaging a LGS image over a laser beacon angular extent. This method has several advantages. First, as opposed to the Foy et al. technique {1}, this method is based on the first order, but not second order, effect. Second, the aperture size for an auxiliary telescope is independent of that for the main telescope and can be small. Third, a one-dimensional CCD array can be used to increase the signal-to-noise ratio for an auxiliary telescope because only global motion of the LGS image, as a whole, should be measured. Belen'kii {3} also suggested a tilt measurement scheme with a small aperture beam transmitted from behind a portion of a primary mirror, which does not require transmitting high power laser irradiance through the main optical train, and might be used for the mesospheric sodium layer.

Ragazzoni {4} suggested a LGS scheme with a laser beam launched through a laser projector, which has the same diameter as the main telescope and placed far away from it. The problem with this scheme is that two 8 m laser projectors are required to measure two-axis tilt components for an 8 m telescope. Besides, due to the fact that a LGS is viewed through the main telescope, a large FOV and large separations (up to 600 Km) between the main telescope and beam projectors are required, which is far from practical. Another scheme suggested by Ragazzoni {5} uses time delay effect for the sodium beacon. However, the propagation time delay for the LGS at the altitude $H = 90 \text{ Km}$ is $\tau = 6 \cdot 10^{-4} \text{ s}$. Whereas, the tilt temporal correlation scale for the telescope of diameter $D > 1.5 \text{ m}$, according to the measured data {6} is larger than $t_c > 1 \text{ s}$. Therefore, the ratio τ / t_c is less than $\tau / t_c < 6 \cdot 10^{-4}$. The implication is that expected LGS image motion is small, and the required measurement accuracy is far beyond the capability of current optical sensors.

Even though the LGS techniques suggested in {2,3} do not have the above shortcomings, they, nevertheless, require large FOV and large separations between the main and auxiliary telescopes to achieve the Strehl ratio (SR), which are needed for practical AO systems. In the paper by Belen'kii {7}, a general approach for measuring tilt with a LGS was presented. This approach uses a single LGS and two arrays of auxiliary telescopes placed in orthogonal directions. Angular, spatial, temporal, and multiple aperture averaging techniques are exploited to reduce the tilt component corresponding to the down propagation path. This permits us to diminish FOV of the receiver and the distance between the main telescope and auxiliary telescope array.

Description of principle

A bistatic LGS scheme suggested in Ref. 2 is shown in Fig. 1. A laser beacon formed through the main telescope is observed through an auxiliary telescope. An auxiliary telescope sees a beacon as an extended

object. Light emitted from different portions of the LGS pass through different inhomogeneities, due to the fact the LGS image appears wavy. A waviness scale is determined by the tilt angular correlation scale, θ_r , which is proportional to auxiliary telescope diameter [3,8]. A tilt component corresponding to the down propagation path is eliminated by averaging randomly different motion of the portions of a LGS image over a laser beacon angular extent. To obtain the required amount of averaging, FOV of the receiver, θ_r , should greatly exceed the tilt angular correlation scale, θ_r . The estimates [3,8] show that even for a small aperture telescope, a tilt angular correlation scale is tens of *arcsec*. As a result, large FOV and large separations, Δ , are needed to measure tilt. A modification of this technique considered below simplifies the requirements of the measurement scheme.

An analysis of a LGS scheme shown in Fig.1 reveals that integration of a LGS image over FOV of the receiver is not the only way to reduce the contribution of a down propagation path. Indeed, the tilt measured with the auxiliary telescope consists of two components,

$$\varphi(\theta, R, t) = \varphi_{LB}(t) + \varphi_{DP}(\theta, R, t). \quad (1)$$

The first component, φ_{LB} is the full aperture tilt for the transmitted beam which corresponds to the upward propagation path. The second component, φ_{DP} is the tilt resulting from the down propagation path. There are several fundamental differences between these tilt components. First, the tilt component φ_{DP} depends on angle θ and has randomly different values in different directions, whereas the tilt component φ_{LB} is independent of θ . Second, the tilt component, φ_{DP} depends on the spatial position of the receiving telescope, R , whereas the tilt component, φ_{LB} is independent of R . Finally, both components, φ_{LB} and φ_{DP} depend on time, t . However, if the diameter of the main telescope greatly exceeds that for an auxiliary telescope, its tilt temporal correlation scale is much greater than that for the auxiliary one. All these differences can be used to reduce the contribution of the down propagation path, φ_{DP} to the measured tilt.

Let us assume that an array of N auxiliary telescopes separated from each other at the distance, Δ_1 , are used to measure tilt. Each telescope in the array, as shown in Fig. 2, is pointed at the LGS. Let us also assume the LGS image is integrated over FOV of the receiver, θ_r , over position of an auxiliary telescope in the array, and over time, T , which is much smaller than the tilt temporal correlation scale for the component φ_{LB} corresponding to the transmitted beam, $T \ll t_{LL}$. The integrated LGS tilt is given by

$$\tilde{\varphi}_{AST} = \varphi_{LB}(t) + \frac{1}{\theta_r} \int_0^{\theta_r} \varphi \frac{1}{N} \sum_{i=1}^N \frac{1}{T} \int_0^T d\varphi_{DP}(\theta, R, t). \quad (2)$$

By assuming that angular, spatial, and temporal coordinates are statistically independent, one can estimate variance of the integrated tilt, $\langle \tilde{\varphi}_{AST}^2 \rangle$. It should be noted that motion of the turbulent inhomogeneities due to wind does not affect statistical independence of the spatial and temporal coordinates. Indeed, if the separation is $\Delta_1 \approx 10 \text{ m}$, then for a sodium beacon ($H = 90 \text{ km}$) at the altitude $H = 10 \text{ km}$ the distance between the propagation paths for two auxiliary telescopes is about 9 m . For wind velocity $V = 10 \text{ m/s}$ and integration time $T \leq 0.1 \text{ s}$, displacement of inhomogeneities is less than 1 m , which is much smaller than the distance between the propagation paths. Variance of the integrated tilt equals

$$\langle \tilde{\varphi}_{AST}^2 \rangle = \langle \varphi_{LB}^2 \rangle + \sigma_{DP}^2. \quad (3)$$

Here $\langle \varphi_{LB}^2 \rangle$ is the tilt variance for the transmitted beam, and σ_{DP}^2 is the tilt variance for the down propagation path.

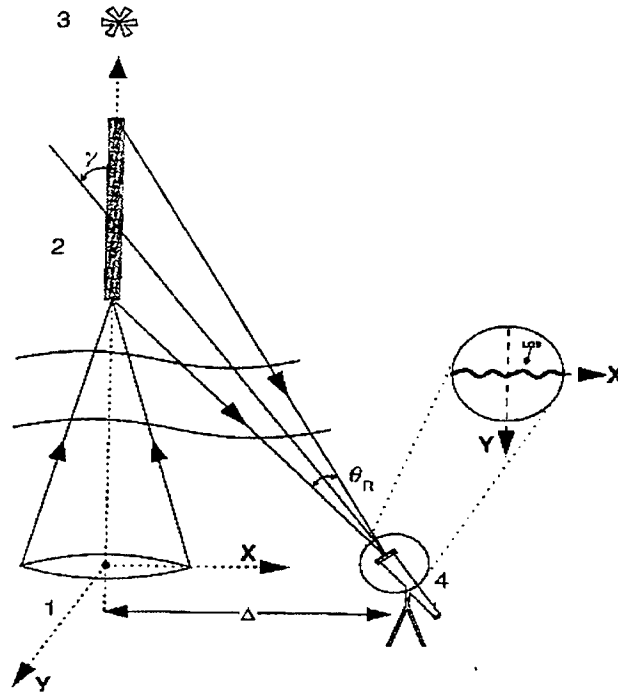


Figure 1. Diagram of the tilt sensing scheme. 1 is the main telescope, 2 is the LGS, 3 is a natural star, 4 is the auxiliary telescope, θ_R is the FOV, χ is the angle between the telescope axes, and Δ is the separation.

This variance is given by

$$\sigma_{DP}^2 = \langle \phi_{PS}^2 \rangle G_A \cdot G_S \cdot G_T. \quad (4)$$

In this equation, $\langle \phi_{PS}^2 \rangle$ is the tilt variance of a point source observed through an auxiliary telescope, G_A , G_S , and G_T are the angular, spatial, and temporal averaging functions, respectively. These averaging functions are

$$G_A(\theta_R / \theta_i) = \frac{2}{\theta_R} \int_0^{\theta_R} b_A(\theta / \theta_i) (1 - \theta / \theta_R) d\theta, \quad (5)$$

$$G_S(N) = \frac{1}{N^2} \sum_{i=1}^N \sum_{j=1}^N b_S(R_i, R_j), \quad (6)$$

$$G_T(T / t_{su}) = \frac{2}{T} \int_0^T b_T(t / t_{su}) (1 - t / T) dt. \quad (7)$$

Here b_A , b_S , and b_T are the tilt angular, spatial, and temporal correlation coefficients, respectively, θ_i and t_{su} are the tilt angular and temporal correlation scale, respectively, for an auxiliary telescope. As each correlation coefficient in Eqs.(5) - (7) is $b_A, b_S, b_T \leq 1$, the tilt averaging functions also satisfy the equation $G_A, G_S, G_T \leq 1$. From Eq. (4) it follows that simultaneous averaging a LGS image over angular, spatial, and temporal coordinates decreases the tilt sensing error, σ_{DP}^2 . In the next sections

angular, spatial, and temporal averaging techniques will be considered in detail. It will be shown that the use of several averaging techniques permits us to increase the accuracy of sensing tilt.

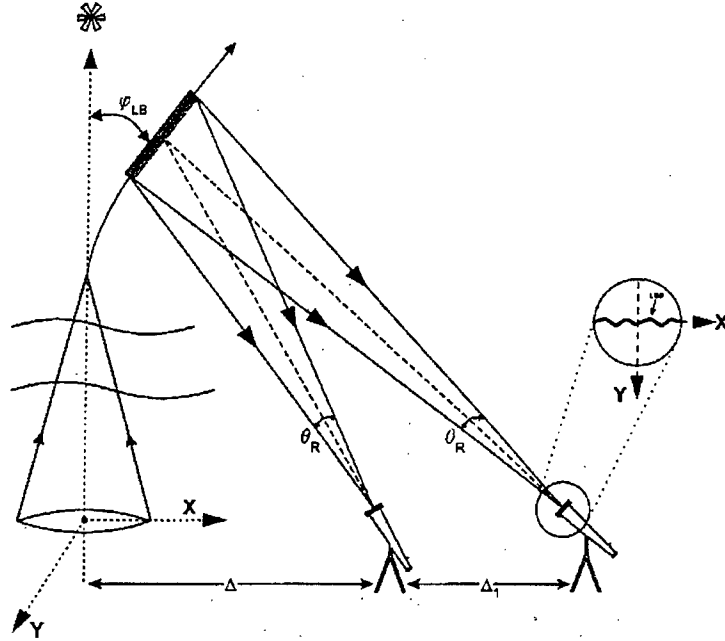


Figure 2. Diagram of tilt sensing scheme using an array of auxiliary telescopes.

Angular averaging technique

Angular averaging of a LGS image over FOV was studied in detail in [3,8]. In these studies, the tilt angular correlation scale, θ_r , and tilt averaging function, G_A , were evaluated. It was shown that the tilt angular correlation scale is given by

$$\theta_r = \alpha (L_0 / D_{au}) D_{au} / \bar{h}. \quad (8)$$

Here D_{au} is the auxiliary telescope diameter, \bar{h} is the effective altitude of the turbulent atmosphere which is determined by the ratio $\bar{h} = \mu_1 / \mu_0$ of first two moments of the vertical profile $C_n^2(h)$: $\mu_0 = \int_0^\infty C_n^2(h) dh$ and $\mu_1 = \int_0^\infty C_n^2(h) h dh$, and α is the coefficient of proportionality which takes into account the effect of the outer scale of turbulence on the tilt angular correlation scale. This coefficient varies in the range $0.8 < \alpha < 3.5$ when the ratio L_0 / D_{au} is in the range $1 < L_0 / D_{au} < 10$.

The tilt averaging function, G_A , calculated in [3,8] is shown in Fig. 2. This plot permits one to estimate the amount of averaging which can be obtained due to integration of a LGS image over a laser beacon angular extent. Quantitative estimates require the tilt angular correlation scale, θ_r . This parameter can either be evaluated theoretically from Eq.(8) if the vertical profile $C_n^2(h)$ and outer scale of turbulence, L_0 , are known, or it can be measured by observing the image motion of the edge of the Moon [12], or real laser beacon.

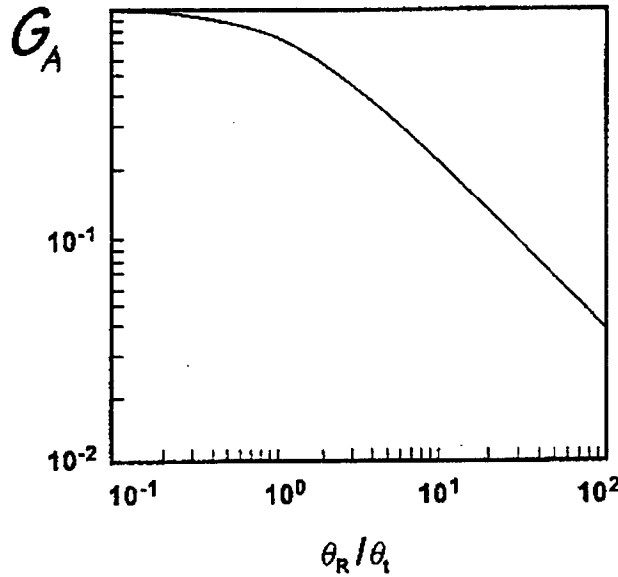


Figure 3. Tilt Angular Averaging Function

Spatial averaging technique

Spatial averaging technique where studied in {7}. This technique requires a linear array of N auxiliary telescopes separated at the distance $\Delta_1 \gg D_{au}$ (see Fig. 2). The integrated tilt measured with the telescope array is equal $\varphi_{\Sigma} = \frac{1}{N} \sum_{j=1}^N \varphi_{Dp}(R_j)$. Variance of the integrated tilt, which is characterized by the averaging function G_S is given by Eq.(6). As the separation Δ_1 greatly exceeds the telescope diameter, the tilts measured with auxiliary telescopes are uncorrelated, $b_S(\Delta_1 / D_{au}) \approx 0$. By taking into account $b_S(R_i, R_j) = \delta_{ij}$, where δ_{ij} is the Kronecker symbol, it can be shown the spatial averaging function is given by

$$G_S = \frac{1}{N}. \quad (9)$$

The implication is that the tilt sensing error, σ_{Dp} , decreases by increasing the number of telescopes, N . Thus, the use of an array of auxiliary telescopes permits us to measure tilt with a LGS more accurately. More over, spatial averaging of a LGS image over the position of the auxiliary telescope in the array also reduces the error caused by uncontrolled motion of an auxiliary telescope. This rms error is reduced by a factor of \sqrt{N} .

Temporal averaging technique

Temporal averaging technique was also conceded in {7}. In the analysis of this technique the fact was taken into account that temporal averaging affects not only the tilt component corresponding to the down propagation path, φ_{Dp} , but also the tilt component $\varphi_{LB}(\lambda)$. This implies that the time integration, on one hand, decreases the contribution of a down propagation path, on another hand, it induces a tilt sensing error. The effectiveness of a temporal averaging technique is characterized by the ratio $\chi^2 = \sigma_{1,T}^2 / \sigma_1^2$. Here $\sigma_{1,T}^2$ is the tilt sensing error under the conditions that the temporal averaging technique is used, and σ_1^2 is the tilt sensing error without the temporal averaging ($T=0$). In {7} it was shown that for ordinary conditions and $T/t_{LB} = 0.1$, where T is the integration time, and t_{LB} is the tilt temporal correlation scale for the main telescope, the above ratio is $\chi = 0.82$. Thus, temporal averaging of

a LGS image can be used along with spatial and angular averaging, to increase the accuracy of measurement of a full aperture tilt.

Strehl ratio estimation

The performance of AO systems is characterized by the Strehl ratio. This ratio for tilt error is give by {9,10}

$$SR = \frac{1}{1 + \frac{\pi^2}{2} \left(\frac{\sigma_1}{\lambda / D} \right)^2}, \quad (9)$$

where σ_1 is the one-axis, rms, tilt sensing error, λ is the wavelength, and D is the main telescope diameter. The tilt sensing error rms is determined by the equation $\sigma_1 = \langle (\varphi - \varphi_{NS})^2 \rangle^{1/2}$, where φ is the tilt measured with a LGS, and φ_{NS} is the full aperture tilt for a natural star measured with the main telescope. The Strehl ratio given by Eq.(9) is equal $SR=0.7$ if the ratio $\sigma_1 / (\lambda / D)$ is $\sigma_1 / (\lambda / D) = 0.3$. Parameters of AO systems, which are needed to achieve the Strehl ratio $SR=0.7$ for good ($\varepsilon_0 = 0.2$ m at $\lambda=0.55$ μ m) and poor ($\varepsilon_0 = 0.07$ m at $\lambda=0.55$ μ m) seeing conditions were estimated in {7}. For a site with good seeing conditions, such as Mauna Kea {11}, $r_0 = 0.235$ m, an auxiliary telescope of diameter $D_{au} = 0.3$ m was considered. For $r_0 = 0.235$ m, $L_0 = 6$ m, and $D_{au} = 0.3$ m the image jitter rms of the point sources estimated from Eq.(15) is $\langle \varphi_{ps}^2 \rangle = 0.18$ arcsec. The number of auxiliary telescopes, N , which are required to achieve the Strehl ratio $SR = 0.7$ for one-axis tilt component for a 8 m telescope and $\lambda=2.2$ μ m for the above conditions is presented in Table 1.

Table 1. Number of Auxiliary Telescopes Needed to Achieve a Strehl Ratio of 0.7 for One-axis Tilt Component with Sodium Beacon at the Site with Good Seeing Conditions

$D = 8 \text{ m}, \lambda = 2.2 \text{ } \mu\text{m}, D_{au} = 0.3 \text{ m}, SR = 0.7$			
θ_R	6 mrad	3 mrad	1.5 mrad
$N(T=0)$	5	8	13
$N(T/t_B = 0.1)$	3	5	10

We see that only from 3 to 5 auxiliary telescopes with FOV from 6 mrad to 3 mrad are needed to achieve the Strehl ratio $SR=0.7$ for one -axis tilt component a 8 m telescope at Mauna Kea . For the larger FOV, a smaller number of telescopes are required. To assess another wave front tilt component an additional telescope array orthogonal to the first array should be used.

For poor seeing conditions, $\varepsilon_0 = 0.07$ m, corresponding to the Starfire Optical Range at Kirtland Air Force Base in Albuquerque, NM, an auxiliary telescope of diameter $D_{au} = 0.2$ m with FOV $\theta_R = 6$ mrad was considered. For a Rayleigh beacon ($10\text{km} \pm 2\text{km}$) and FOV of $\theta_R = 6$ mrad, the separation between the main telescope and the array of auxiliary telescopes is $\Delta=300$ m. The estimated number of auxiliary telescopes, N , needed to achieve the Strehl ratio $SR=0.7$ for one-axis tilt component and the above conditions is given in Table 2. For a 1.5 m telescope, the estimates are obtained without using the temporal averaging ($T = 0$), whereas for a 3.5 m telescope, the temporal averaging is exploited.

It is seen that for a 1.5 m telescope and near IR waveband from 3 to 9 telescopes are needed to achieve the Strehl ratio $SR=0.7$. At the same time, in the visible range, a much large number of telescopes are required. This means that a tilt measurement scheme should be further improved. One more averaging technique uses averaging of a LGS image over subaperture position within an auxiliary telescope.

Table 2. Number of Auxiliary Telescopes Needed to Achieve Strehl Ratio of 0.7 of One-axis Tilt Component with Rayleigh Beacon at the Site with Poor Seeing Conditions

$\theta_R = 6 \text{ mrad}, D_{au} = 0.2 \text{ m}, \Delta = 300 \text{ m}, \text{SR} = 0.7$			
$\lambda [\mu\text{m}]$	2.2	1.25	0.55
$N (D = 1.5 \text{ m}, T = 0)$	3	9	50
$N (D = 3.5 \text{ m}, T/t_{th} = 0.1)$	12	35	--

Multiple aperture averaging technique

Let us assume that an auxiliary telescope consists of multiple subapertures. If subaperture diameters D_{au} , then the tilt angular correlation scale for a LGS image formed by each subaperture is determined by D_{au} , providing effective averaging over the angular coordinate. At the same time, when LGS images are averaged over multiple subapertures the jitter variance of a point source $\langle \phi_{PS}^2 \rangle$ decreases. If each auxiliary telescope of diameter D_Σ consists of M subapertures of diameter D_{au} , where $M = D_\Sigma^2 / D_{au}^2$, then the LGS tilt measured with each subaperture, ϕ_j , can be averaged over multiple subapertures within an auxiliary telescope. The integrated tilt measured with auxiliary telescope is $\tilde{\phi} = \frac{1}{M} \sum_{j=1}^M \phi_j$. In this case, the LGS tilt integrated over angular, spatial, and temporal coordinates is given by

$$\tilde{\phi}_{AST,MA} = \phi_{LB}(\lambda) + \frac{1}{M} \sum_{j=1}^M \frac{1}{\theta} \int_{\theta_R}^{\theta_R} d\theta \frac{1}{N} \sum_{i=1}^N \frac{1}{T} \int_0^T dt \phi_{DP}(\theta, R_j, R_j, t), \quad (10)$$

where R_j is the subaperture coordinate within an auxiliary telescope. Variance of the integrated LGS tilt has the form

$$\sigma_{DP}^2 = \langle \phi_{PS}^2 \rangle \cdot G_A \cdot G_S \cdot G_T \cdot G_{MA} \quad (11)$$

where G_{MA} is the averaging function due to averaging of the LGS image over subapertures within an auxiliary telescope.

The number of auxiliary telescopes which are required to achieve the SR=0.7 for the same conditions as Table 2 calculated in {7} are presented in Table 3. In this case, a multiple aperture averaging technique is used. The auxiliary telescope diameter is $D_\Sigma=0.5\text{m}$, and the subaperture diameter is $D_{au}=0.2\text{m}$. The number of auxiliary telescopes decreases approximately by a factor of three if a multiple aperture averaging technique is exploited. A similar reduction factor can also be obtained for the case of a sodium beacon presented in Table. 1. Thus, only from 4 to 12 multiple aperture auxiliary telescopes are needed to achieve SR = 0.7 for a 3.5 m telescope in near IR.

Table 3. Number of Auxiliary Telescopes Needed to Achieve Strehl Ratio of 0.7 with Rayleigh Beacon and Multiple Aperture Averaging at a Site with Poor Seeing Conditions

$D_\Sigma = 0.5 \text{ m}, \theta_R = 6 \text{ mrad}, D_{au} = 0.2 \text{ m}, \Delta = 300 \text{ m}, \text{SR} = 0.7$			
$\lambda [\mu\text{m}]$	2.2	1.25	0.55
$N (D = 1.5 \text{ m}, T = 0)$	1	3	18
$N (D = 3.5 \text{ m}, T/t_{th} = 0.1)$	4	12	60

Thus, by using a combination of averaging techniques the SR=0.7 can be achieved for various seeing conditions, wide range of telescope diameter, and wavelength, including a visible waveband.

Design methodology for tilt measurement scheme

Information needed for designing the tilt measurement scheme with a LGS can be obtained in two ways. First, three basic parameters, r_0 , θ_0 , and L_0 , needed for the system design can be measured directly. The r_0 data are usually available at astronomical sites. The outer scale of turbulence, L_0 , can be determined from the dependence of the tilt variance on the telescope diameter {6}. The tilt angular correlation scale, θ_0 , or the tilt angular averaging function, G_A , can be measured by observing the edge of the Moon {12}. By knowing the above characteristics, one can estimate for a given main telescope diameter, D , wavelength, λ , auxiliary telescope diameter, D_{av} , and FOV, θ_R , the angular averaging function, G_A , and the number of auxiliary telescopes, N , which are needed to achieve the required Strehl ratio. If it is necessary, a complex auxiliary telescope aperture consisting of multiple subapertures can be used.

A second way is to measure the tilt sensing error $\sigma_1 = \{(\varphi - \varphi_{NS})^2\}^{1/2}$ by observing a real laser beacon through a single aperture auxiliary telescope. The main telescope could be pointed at Polaris to eliminate mechanical motion, and the LGS is observed through an auxiliary telescope with given diameter and FOV. By measuring Polaris motion with the main telescope and LGS motion with the auxiliary telescope, the tilt sensing error σ_1 can be estimated. If the error, caused by focus anisoplanatism, σ_{FA} , is small, the measured tilt error corresponds to $\sigma_1 = \{\varphi_{PS}^2\}^{1/2} \cdot G_A$. By comparing the measured value σ_1 with the ratio D/λ , one can determine the number of auxiliary telescopes which are needed to achieve the required Strehl ratio.

Experimental study of tilt angular anisoplanatism

The performance of the above method of sensing full aperture tilt can be evaluated if the tilt angular correlation scale or tilt angular averaging function are known. Besides, to determine the optimum diameter of an auxiliary telescope, the tilt angular correlation scale or tilt averaging function should be known. However, these data are not available in the literature.

The goal of this experiment is to investigate the statistical properties of wave-front tilt angular correlation and tilt averaging function for various telescope diameter. Typically, the dependence of wave-front aberrations, which include tilt and higher-order wave-front components, on the direction of propagation of an optical wave is referred to as anisoplanatism {13}. The traditional approach for measuring tilt anisoplanatism uses binary stars at various angular separations {14,15}. However, bright binary stars with the required angular separations may not always be visible at a particular site and time, making this approach difficult to reliably implement.

A different approach, which avoids the above difficulty, is suggested in this paper. Rather than measuring the motion of binary stars at fixed angular separations, the random angular motion of an image of the moon's edge is recorded. This approach offers several advantages. First, at any given site and time the moon is more likely to be available than specific binary stars. Second, unlike binary stars, with a limited range of discrete separations, moon edge observations provide a wide and continuous range of angular distances. Third, the determination has been made that the moon's brightness is sufficient to make measurements with a high resolution CCD imaging system. This approach was employed in a recent experiment conducted at the Starfire Optical Range (SOR).

Because the Moon is an extended, incoherent source, light rays emitted from different portions of its edge travel through different inhomogeneities, causing images of the moon's edge to appear wavy. It is reasonable to expect the waviness scale of the image to be related to the area of the sky over which phase fluctuations are correlated, defined as the isoplanatic angle {13}, θ_0 . This angle is given by

$$\theta_0 = (2.91 k^2 \int_0^\infty C_n^2(h) h^{1/3} dh)^{-3/5}, \quad (12)$$

where $\kappa=2\pi/\lambda$ is the wavenumber, and C_n^2 is the refractive index structure characteristic. The isoplanatic angle thus depends on wavelength, but not telescope diameter.

However, in {2} a different angular scale, known as the tilt angular correlation scale, appeared in the analysis. This scale is independent of wavelength, but it depends on telescope diameter, D , and also depends on the outer scale of turbulence. Further investigation {3,8} showed that the waviness scale of an extended incoherent object is determined not by isoplanatic angle, but by the tilt angular correlation scale, which has the form

$$\theta_t = \alpha (L_0 / D) D / \bar{h}. \quad (13)$$

Estimates show that the effective altitude of the turbulent atmosphere is $\bar{h}=934\text{ m}$ for the HV_{57} model corresponding to the SOR site and $\bar{h}=6100\text{ m}$ for the $C_n^2(h)$ vertical profile corresponding to Mauna Kea {11}. The values of a lateral (transverse to angular separation, θ) tilt angular correlation scale, θ_t , are given in Table 1 in {3,8}. An additional goal of this study was to verify that the waviness scale of the moon edge is determined by wave-front tilt correlation, but not by isoplanatic angle.

Experimental set up, data collection, and data processing procedures

In this study, an experimental setup similar to that used for the Polaris jitter observations {6} was used. A diagram of the system is shown in Fig.4.

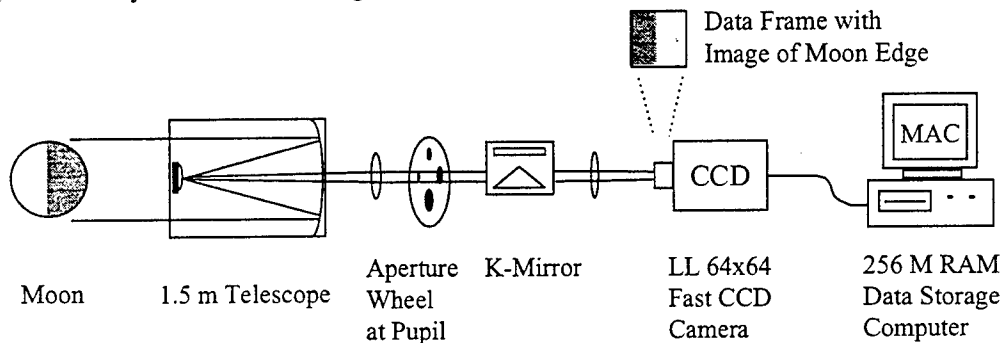


Figure 4. Moon Edge Jitter Experimental Setup

A 1.5 m telescope with aperture masks providing additional effective apertures of 0.1, 0.2, 0.5, and 0.75 m was used. Moon edge images were recorded with a Lincoln Laboratory fast, low noise, high resolution CCD camera (maximum 2 kHz frame rate, 10 photoelectrons/pixel/read noise, 64x64 array, and 27 μm pixel size). In observations performed in 1995 an angular pixel scale of 0.9 *arcsec/pixel* (58x58 *arcsec* FOV) was used. In this case, no control over image orientation was available, so the orientation of moon edge images was arbitrary. In observations performed in 1996, a pixel scale of 0.66 *arcsec/pixel* (42x42 *arcsec* FOV) was used. In this case, a small K-mirror was employed to orient the FOV such that the moon edge was normal to the pixel rows, simplifying data post-processing.

Short exposure images of the moon were collected at a frame rate of 200 Hz (5 ms exposures) for 100 sec or 400 Hz (2.5 ms exposures) for 50 sec. 20,000 frames were collected per data run. Sets of five data runs, one for each aperture, were collected sequentially. Neutral density filters were used to keep transmitted flux approximately constant. In each run (1996 experiment) the image was aligned to place the moon edge approximately near the 32nd (center) pixel in each row. In addition, for each data run, sky background and dome flat frames were collected. On average, an entire data set, including five apertures, backgrounds, and flats, was recorded in 30 min. The moon edge images were recorded during one night in August of 1995, and during four nights in May, June, and August of 1996. The atmospheric coherence diameter (r_0), wind speed, and wind direction near the telescope were recorded as well. During the observations, the coherence diameter was in the range 5-9 cm.

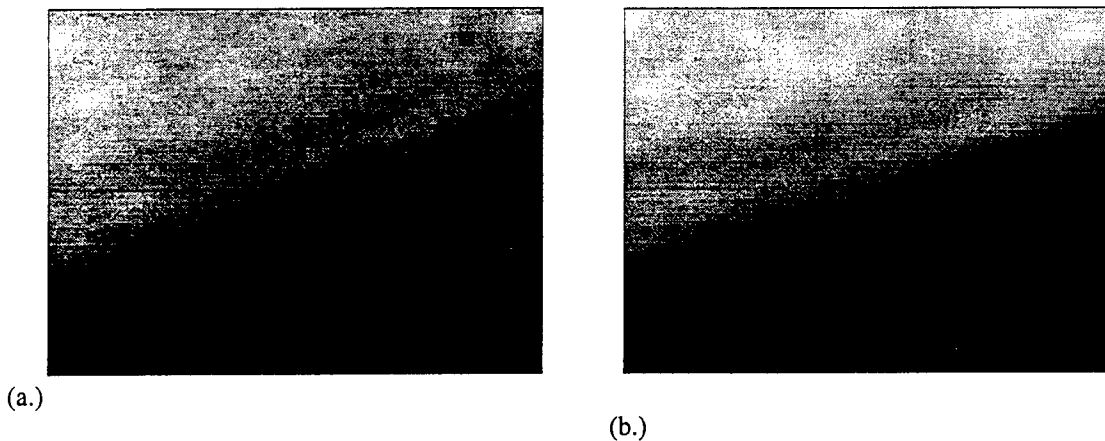
The data were processed frame-by-frame in the following sequence. First, an average dark frame was subtracted from each frame to reduce the non-uniform background response attributed to different amplifiers in the CCD camera. Second, the pixels were combined, eight at a time, to simulate a large field of view in the dimension parallel to the moon's edge, reducing the effective number of rows from 64 to eight. Third, each row of the frame was normalized by the mean of a 16-pixel sample taken from the bright portion of the row. At this point, the dark portion of the row had its mean roughly equal to zero, and the bright portion's mean was close to unity. Fourth, the row was searched to find two pixels straddling the 0.5 threshold. Finally, the edge position was defined via linear interpolation between these pixels. This procedure was repeated, producing a vector of 64 edge positions for each frame.

Once all frames were processed, there were N vectors of eight edge positions each. Each row's edge position was demeaned and normalized by the corresponding standard deviation, using temporal statistics. Thus, each of the eight edge positions had a temporal mean of zero and unity standard deviation.

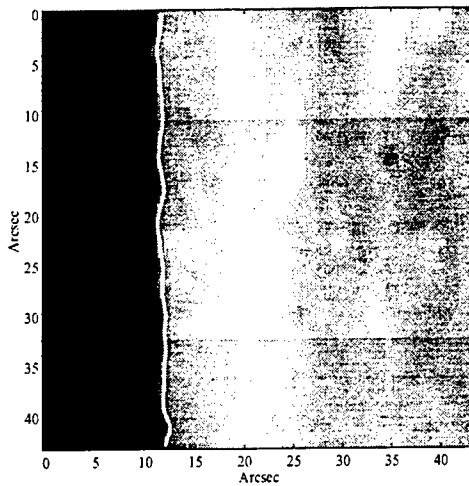
These demeaned and normalized edge positions were then used to compute the correlation coefficient as a function of angular separation and the so-called 'averaging function.' The correlation coefficient was computed as the temporal mean of the product of the first row's edge position with a row separated by a fixed number of rows. Note that no normalization was required, since the row edge positions were already normalized to a variance of unity. Also, the row separation was easily converted into angular separation via the known camera plate scale. Finally, the averaging function was determined by first computing the running mean of the edge positions and then estimating the variance of these means.

Waviness of the moon edge images

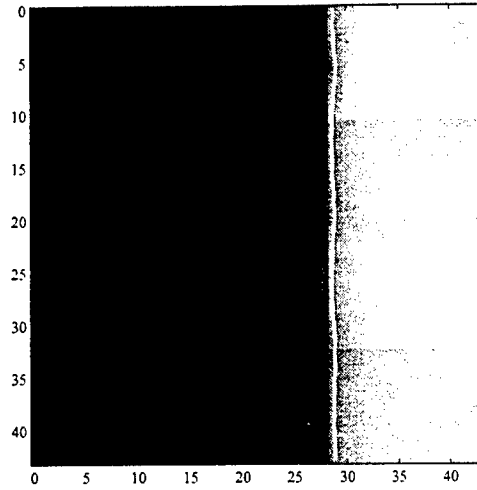
Two Moon edge images from a data set collected in 1995 are shown in Figures 5a. and 5b. Two images recorded in 1996 are presented in Figures 6a and 6b. Note that in the earlier images, the moon edge is not normal to the pixel rows.



Figures 5a and 5b. Moon edge images recorded with 0.1 m (a.) and 1.5 m (b.) aperture masks.



(a.)



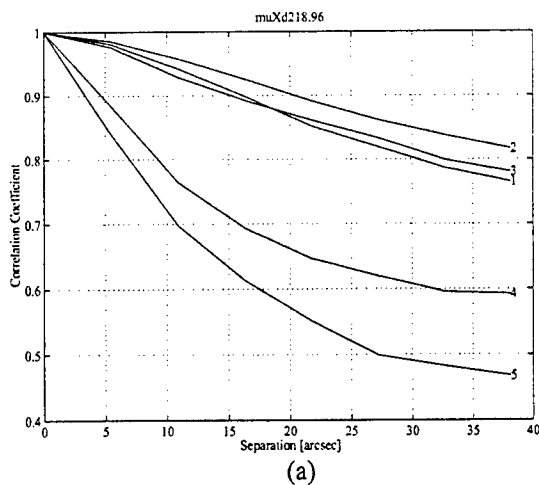
(b.)

Figures 6a and 6b. Moon edge images recorded with 0.1 *m* (a.) and 1.5 *m* (b.) aperture masks. Bright line indicates edge position determined by the processing algorithm.

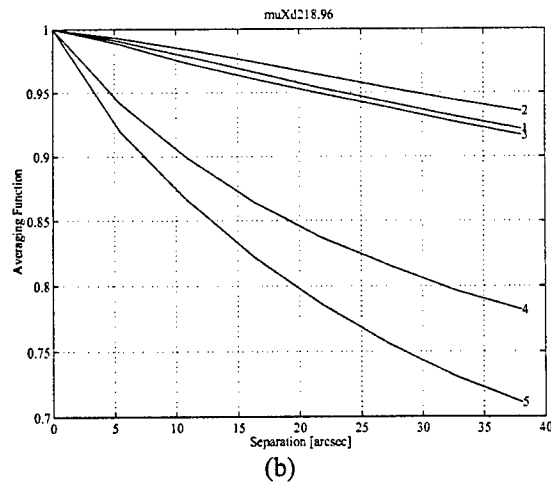
A noticeable waviness is apparent in the moon edge images recorded with the smallest aperture, for which the waviness scale is smaller than the FOV. However, no such distortion appears in the image recorded with the largest aperture because, in this case, the waviness scale is larger than the field of view, and the magnitude of the waviness is reduced. As both images were recorded under the same seeing conditions, it is clear that the waviness scale of the moon edge image does not depend on the isoplanatic angle. The implication is that the concept of isoplanatic angle does not apply to tilt-related phenomena. It is important to note here that uncontrolled telescope motion cannot be manifested as image waviness.

Dependence of tilt angular correlation and the tilt averaging function on telescope diameter

The tilt correlation coefficient and tilt averaging function for two data sets recorded on the same day in 1996 are shown in Figures 7a., 7b., 8a., and 8b. Both functions gradually decrease with increasing angular separation, θ , but decrease much faster for smaller apertures. For example, the correlation coefficient decreases only to 0.8 over 40 arcsec for the largest apertures (curves 1 and 2), whereas it decreases to 0.5-0.6 for the smallest aperture (curves 5).

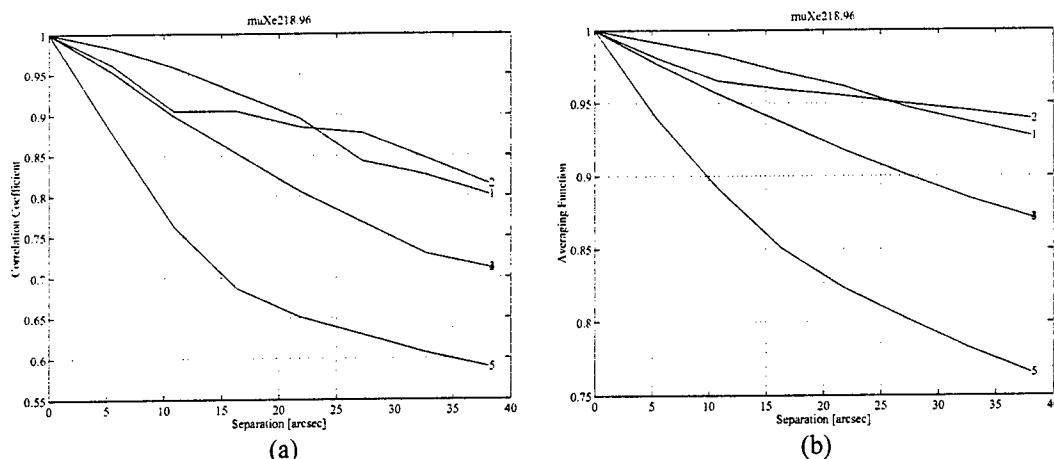


(a)



(b)

Figures 7a. and 7b. Tilt angular correlation coefficient (a) and tilt angular averaging function(b). Curves 1,2,3,4, and 5 correspond to $D=0.1, 0.2, 0.5, 0.75$, and 1.5 *m*, respectively.



Figures 8a. and 8b. Tilt angular correlation coefficient (a) and tilt angular averaging function(b). Curves 1,2,3, and 5 correspond to $D=0.1, 0.2, 0.5$, and 1.5 m, respectively.

By comparing the tilt correlation coefficients presented in Fig.7a with universal theoretical curve for tilt correlation coefficient given in Fig.3 in Ref. 6, the tilt correlation scale, θ_t , can be estimated. This scale equal $\theta_t = 54$ arcsec for $D=0.1$ m, $\theta_t = 74$ arcsec for $D=0.2$ m, and $\theta_t = 152$ arcsec for $D=0.5$ m - 1.5 m. At the same time, by comparing the measured tilt averaging functions given in Fig.3b with the theoretical prediction shown in Fig.2 in Ref. 9, it can be obtained that the tilt correlation scale is $\theta_t = 38$ arcsec for $D=0.1$ m, $\theta_t = 43$ arcsec for $D=0.2$ m, and $\theta_t = 118$ arcsec for $D=0.5$ m - 1.5 m. The inverse order of the curves for the largest apertures in Figs. 3a. and 3b. is most likely due to atmospheric instability over the period of data collection for the five apertures.

By performing similar analysis for the data presented in Figs. 8a, the following estimates for the tilt correlation scale can be obtained: $\theta_t = 70$ arcsec for $D=0.1$ m, $\theta_t = 116$ arcsec for $D=0.5$ m, and $\theta_t = 175$ arcsec for $D=0.75$ m - 1.5 m. The estimates obtained from the tilt averaging functions given in Fig.4b are $\theta_t = 40$ arcsec for $D=0.1$ m, $\theta_t = 88$ arcsec for $D=0.5$ m, and $\theta_t = 116$ arcsec for $D=0.75$ m - 1.5 m. It is seen that, the estimates obtained from the tilt correlation coefficient exceed that inferred from the tilt averaging function. The estimates for θ_t obtained from the tilt averaging function for two data sets are in better agreement than that inferred from the tilt correlation coefficient. Because the tilt averaging function, due to definition, characterizes the reduction in the tilt variance which can be obtained by integrating the image over the FOV of the receiver, the estimates for θ_t inferred from these data are more suitable for estimating the performance of the LGS tilt measurement scheme {2,7}.

The estimates for the tilt angular correlation coefficient, on average, are somewhat less than that predicted by the HV_{5.7} turbulent model (see Table.1 in {3,8}). In particular, for the largest aperture, $D=1.5$ m, the tilt correlation scale in the range 255- 323 arcsec was predicted, whereas the measured tilt correlation scale for this aperture is $\theta_t \leq 152$ arcsec. This indicates the presence of high altitude turbulence which is not accounted for by this model. Finally, the obtained change of the waviness scale of the moon edge image with variation of the telescope diameter provides clear evidence that the concept of isoplanatic angle is not applicable to tilt-related phenomena.

Conclusions

A method for measuring full aperture tilt with a LGS is developed. The method uses a single monochromatic LGS formed through the main telescope and two arrays of auxiliary telescopes separated in orthogonal directions. Four averaging techniques are applied to a LGS image to reduce the contribution of a down propagation path. A LGS image is averaged over the position of the auxiliary telescope in the telescope array, over position of a subaperture within the auxiliary telescope, over FOV of the receiver, and over time. It is shown that the use of a combination of four averaging techniques permits us to achieve the

Strehl ratio equal to 0.7 for various seeing conditions, different telescope diameter, and wavelength, including a visible waveband. A designing methodology for the tilt measurement scheme with a LGS is discussed. An experimental verification of this method should be the next step in development of a tilt retrieval technique with a LGS. An experimental study of the tilt angular correlation scale and the tilt angular averaging function was also performed as a part of the project. A new approach of measuring tilt angular anisoplanatism is exploited. This approach employs measurements of the random motion of the portions of a moon edge image in the direction transverse to the image. This technique has several advantages over the traditional method of using binary stars. They are the following: a) moon edge observations provide a wide, continuous range of angular separations which permits us to measure tilt averaging function directly; b) the moon is sufficiently bright to enable observations with a high resolution CCD imaging system; c) at any given site and time the moon is more likely to be available for observations than specific binary stars. In this experiment, the statistical properties of tilt angular correlation and the tilt averaging function were studied. According to estimates based on the tilt averaging function, the tilt angular correlation scale increases by increasing the telescope diameter from 40 *arcsec* to 118 *arcsec*. This indicates that the concept of isoplanatic angle is not applicable to tilt-related phenomena. The data obtained can be used for designing the tilt measurement scheme.

References

1. R. Foy, A. Migus, F. Biraben, G. Grynberg, P.R. McCullough, and M. Tallon, "The polychromatic artificial Sodium star: a new concept for correction the atmospheric tilt," *Astron. Astrophys.*, **111**, 569-578(1995).
2. M. S. Belen'kii, "Full aperture measurement technique with a laser guide star," in Atmospheric Propagation and Remote Sensing IV, J. Christopher Dainty, Editor, *Proc. SPIE*, **2471**, 289-300(1995).
3. M. S. Belen'kii, "Tilt angular correlation and tilt sensing techniques with a laser guide star," in Optics in Atmospheric Propagation, Adaptive Systems, and Lidar Techniques for Remote Sensing, *Proc. EUROPTO Series*, **2956**, 206-217 (1996).
4. R. Raggazzoni, "Absolute tip-tilt determination with laser beacons," *Astron. Astrophys.* **305**, L13-L16(1996).
5. R. Raggazzoni, "Propagation delay of a laser beacon as a tool to retrieve absolute tilt measurements," *Astrophys. J.* **465**: L73-L75 (1996).
6. M. S. Belen'kii, S. J. Karis, J. M. Brown, and R. Q. Fugate, "Experimental study of the effect of non-Kolmogorov turbulence on star image motion," *Proc. SPIE*, **3126**, (1997) (to be published).
7. M. S. Belen'kii, "Multiple aperture averaging technique for measuring full aperture tilt with a laser guide star," *Proc. SPIE*, **3126**, (1997) (to be published).
8. M. S. Belen'kii, "Principle of equivalency of the phase difference and off-axis tilt sensing technique with a laser guide star," *Proc. SPIE*, **2828**, 280-292 (1996).
9. G. A. Tyler, "The reduction in antenna gain due to random jitter," the Optical Science Company Technical Report No. TR-541, Anaheim, (1983).
10. D. G. Sandler, S. Stahl, J. R. P. Angel, M. Lloyd-Hart, and D. McCarthy, "Adaptive optics for diffraction-limited infrared imaging with 8-m telescopes," *J. Opt. Soc. Am.*, **A 11**, 925-945(1994).
11. R. Racine and B. L. Ellerbroek, "Profiles of night-time turbulence above Mauna Kea and isoplanatism extension in adaptive optics," *SPIE Proc.* **2534**, 248-257 (1995).
12. M. S. Belen'kii, S. J. Karis, J. M. Brown, and R. Q. Fugate, "Measurements of tilt angular anisoplanatism," *Proc. SPIE*, **3126**, (1997) (to be published).
13. D. L. Fried, "Anisoplanatism in adaptive optics," *J. Opt. Soc. Am.*, **72**, 52-61(1982).
14. A. Sivaramakrishnan, R. J. Weymann, and J. Beletic, "Measurements of the angular correlation of stellar centroid motion," *Astron. J.*, **110**, 430-438(1995).
15. K. Berkelfeld and A. Gliddenmann, "Measurements of the isoplanatic angle of the wavefront tilt," Summaries of the papers presented at the topical meeting. Adaptive Optics, Maui, Hawaii, 8-12 July 96, pp206-208.

SPINNING HOLLOW FIBERS FROM HIGH PERFORMANCE POLYMERS

Gajanan S. Bhat
Associate Professor-Textile Science

University of Tennessee
230 Jessie Harris Building
Knoxville, TN 37996

Final Report for:
Summer Faculty Research Program
Phillips Laboratory

Sponsored by:
Air Force Office of Scientific Research
Bolling Air Force Base, DC

and

Phillips Laboratory

August 1997

SPINNING HOLLOW FIBERS FROM HIGH PERFORMANCE POLYMERS

Gajanan S. Bhat
Associate Professor-Textile Science

Abstract

Hollow fibers spun from synthetic polymers have been investigated for a long time, especially for producing high-bulk, low density fabrics. Advantages of hollow fibers over solid round fibers are improved thermal and acoustical properties, reduced pilling, special optical effects and greater dielectric strength. Also, hollow fibers exhibit less fibrillation tendency under flexing conditions. Such fibers produced from a high temperature resistant polymer have advantages in some of the intended applications. A special set-up was built at the Phillips Laboratory of Edwards AFB, CA to spin hollow fibers. Using that set-up, hollow fibers were spun from two grades of Ultem. The same set-up was used to obtain thick coating of Ultem on copper wires. Influence of varying some of the processing conditions on the fiber structure was analyzed. Feasibility of solution processing of Ultem was also investigated.

SPINNING HOLLOW FIBERS FROM HIGH PERFORMANCE POLYMERS

Gajanan S. Bhat

BACKGROUND

Polyimide is a high temperature resistant polymer with excellent mechanical properties. Polyimide fibers have excellent thermal and chemical stability and good mechanical properties as well [1, 2]. The very fact that they have good chemical stability means, they neither dissolve in simple solvents nor melt, and this creates problem for fabrication of products. Copolyimides on the other hand have better tractability and can be dissolved in less exotic solvents. Some of the copolyimides have been tried for the production of fibers and other products due to the ease of fabrication. One such example is the P84 fiber manufactured and marketed by Lenzing Co., Austria, from the 80/20 copolymer produced by Dow Chemical Company [3]. However, even this fiber is partially crosslinked and thus can be dissolved only in aprotic solvents. The polyimide/amide copolymer manufactured by Amoco chemical company, although is claimed to be easily processable, on heat treatment becomes crosslinked [4].

Polyetherimide Fibers

Polyetherimide (PEI) a resin introduced in 1982 by General Electric Company under the tradename Ultem, is a copolymer with ether molecules between imide groups. The fully reacted polyimide with the imide group being part of the linear polymer chain makes this polymer thermoplastic and easily dissolvable. Being an amorphous thermoplastic polyimide, the Ultem resin combines the high performance associated with exotic specialty polymers and the good processability of typical engineering plastics [5]. In addition to high strength and modulus, and heat resistance, the polymer has high dielectric strength, broad chemical resistance, transparency and good processability. Another advantage is that this polymer dissolves readily in methylene chloride.

GE has been marketing this polymer mainly for aerospace, marine, automotive, dielectric and electrical applications, where their longterm high temperature capabilities meet the stringent requirements [6]. Polyimide films are used as electrical insulation for electric motors, magnet wires, and aircraft and missile wiring. Because of their inherent flame resistance, polyimide films are also used as fire barriers in aircraft and marine applications. Polyetherimide exhibits this exceptional

balance of properties without sacrificing processability, providing a material capable of meeting the difficult design requirements of many applications [7]. Many grades of this resin are available, each suitable for certain applications. The lower viscosity materials of the available grades were used for fiber spinning.

Although possibility of spinning fibers from Ultem [8] has been reported, it is not commercially produced. It was demonstrated that Ultem can be extruded into fibers and filaments, and then can be drawn and subsequently processed to textiles in conventional ways. The textile like properties of these fibers enables it to be used in several applications including hot gas filtration and thermoplastic composites. The major advantage of PEI fibers is their ability to retain tensile properties at temperatures above 150 °C. It was clearly demonstrated earlier that Ultem can be melt spun into fibers of different diameters and can be further processed as well [9].

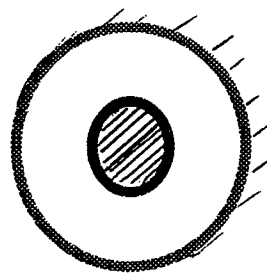
Hollow Fibers

Hollow Fibers spun from synthetic polymers have been investigated for a long time. The interest in hollow fibers has been for producing high-bulk, low density fabrics. Other advantages of hollow fibers over solid round fibers are improved thermal and acoustical properties, reduced pilling, special optical effects and greater dielectric strength [10]. Also, hollow fibers exhibit less fibrillation tendency under flexing conditions. Currently hollow fibers are not commercially produced since other configurations such as the trilobal cross sections are being used for high-bulk textiles. However, the hollow fiber spinning technology is used to develop hollow fiber membranes [11]. Hollow fibers offer several advantages over other membrane configurations as they give high productivity per unit volume and in that membrane supports are not required, which makes the fabrication of membrane devices much simpler. Some of the applications such as high temperature insulation can benefit from using high temperature resistant hollow fibers. Hollow fibers have been shown to have some specific advantages in composites applications as well.

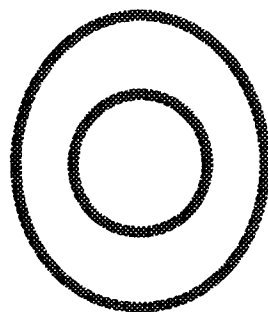
Hollow fibers are produced by one of the three conventional fiber manufacturing methods, wet spinning, dry spinning or melt spinning. In all the cases tubular cross sections are formed by extruding the molten polymer or polymer solution through an annular die or spinneret. In the patent literature the following three types of spinneret designs are described below with their schematics shown in *Figure 1*.

1. This annular spinneret has a solid pin supported in the center of the circular orifice. The polymer is extruded through the annulus. In this type of design, a gas forming additive is incorporated in the polymer melt. The gas fills the core of the fiber as it emerges from the annulus thus preventing the collapse of the fiber before it solidifies.
2. Another spinneret design has a hollow needle or tube supported in the center of the orifice and an inert gas or liquid is injected through the needle to maintain the tubular shape until the solidification or coagulation of the fiber.
3. A third type of hollow fiber spinneret has a C-shaped orifice with the tips of the C overlapping. The polymer solution or melt welds into a tube after extrusion through the C-shaped die. The gas required to keep the fiber hollow is drawn in through the gap in the extruded fiber upstream from the weld point [12].

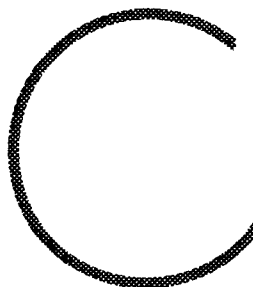
There has been some interest in hollow carbon fibers as it was shown that hollow carbon fibers had higher tensile strength and modulus than that of general solid carbon fibers, which offer some advantages in composite design [13]. Composites formed from hollow fibers showed higher anisotropy in thermal conductivity measurements compared to that formed from solid carbon fibers [14]. When the above mentioned methods were used to produce pitch based carbon fibers each method showed its advantages and disadvantages. It was not possible to produce uniform hollow fibers using the annular die with an insert in the center. Since mesophase pitch solidifies immediately as it comes out of the spinneret, it was observed that with C-shaped dies high melt temperatures and high draw down rates had to be used. Alternatively, a new capillary design consisting of three arc-shaped channels is also being investigated [15]. It is clear that capillary design suitable for one type of polymer is not necessarily effective for another system.



a.



b.



c.

Figure 1. Schematics of Spinneret Types for Hollow Fiber Formation (a) Solid Pin Inside the Orifice (b) Hollow Tube inside the Orifice and © C-Shaped Orifice.

EXPERIMENTAL PROCEDURE

Materials

For this work, Ultem 1000 series (Ultem 1000 and 1010), which is the low viscosity grade polymer, was selected since fiber spinning demands much lower viscosity compared to typical molding processes. The properties of the polymer, including its viscosity behavior have been reported earlier [9]. For solution processing, Methylene Chloride was used as a solvent. For the production of hollow carbon fibers, AR mesophase pitch was used. Ultem polymers were dried in an oven at 150 °C for at least four hours before processing.

Melt Spinning Set-Up

A special melt spinning unit was built for conversion of Ultem and other melt spinnable resins into fibers of required properties. Unlike many other thermoplastic polymers that are typically spun into fibers, such as nylons, polyesters, and polyolefins, Ultem or other high performance materials demand much higher processing temperatures. The system should be capable of withstanding higher temperatures for prolonged periods of time. Also, for hollow fiber formation, special arrangements have to be made as described above. For this reason possibility of processing the polymer through the use of a solvent was also explored.

The spinneret design with a hole-inside-hole type of arrangement was used for this research. Figures 2 and 3 show the schematic of the melt spinning apparatus. The key component is the capillary design which consists of a hole inside the hole. This arrangement allows the polymer melt or solution to come out through the annulus and flow of a fluid through the inner capillary to maintain the hollowness of the fiber till it solidifies. There was also an arrangement to change the position of the inner capillary with respect to the annulus. By simply turning the knob, it is possible to have the capillary in-line with the annulus, projecting below or lagging behind, depending on what is desired. In the studies reported here, capillary was extending below the annulus by one mm. Other features include, spinneret, filter, the thermocouple and air/vacuum connection. The whole system when fully assembled, sits in a temperature controllable heating jacket.

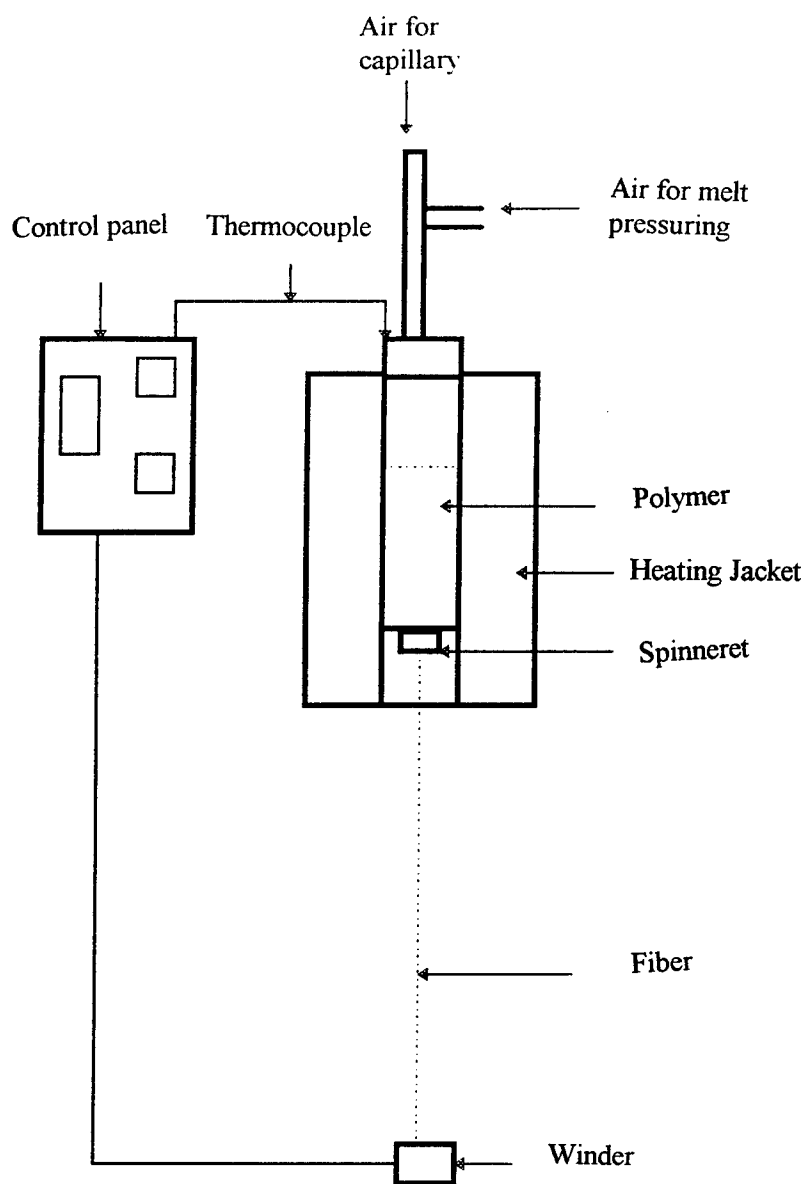


Figure 2. Melt Spinning Set-Up Used for Hollow Fiber Spinning.

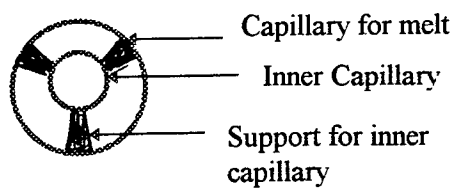


Figure 3. Capillary Design for Hollow Fiber Formation.

RESULTS AND DISCUSSION

Melt Spinning of Ultem

Melt spinning of the polymer was done using a home-built spinning unit described in the previous section. The important variables in spinning are, melt temperature, melt pressure, quenching conditions and winding speed. In this study, melt temperature, melt pressure, and winding speed were varied. There was no positive feeding of the melt and thus the flow rate could not be positively controlled, but was determined by melt temperature and pressure. Quenching was done by ambient air with no special air flow attachments.

Although fibers were collected, spinning was not without any problems. Obviously the temperature of the melt to achieve flow through the spinneret was very high. It is because of the very high viscosity of the polymer, as the resin was not made for fiber spinning, but for molding applications. Another problem was that of air bubbles coming with the melt. To overcome this problem, in later trials, vacuum was used during melting. This helped the flow of bubble free melt at least for the initial period. It appears that as the polymer melts, in the presence of vacuum, the melt in the bottom part of the pot is void free and in the upper part there are still air bubbles. However, for the amount of material to be spun, use of vacuum served the purpose.

SEM pictures of the material as it comes out of the spinneret and the hollow fibers spun at different wind-up speeds are shown in Figures 4 and 5. It is evident from the pictures that the fibers are fairly circular and have a large hole and a small annulus. The annulus is so small that it becomes difficult to handle the fibers as can be seen from figure 5 which shows the tip coming together and appearing as though it is not circular. All these fibers were spun with a very low flow rate of air in the inner capillary. Figures 6 and 7 show the effect of too high an air flow or not having any air in the capillary. Even a slight increase in the air flow through the capillary results in splitting of the fiber and providing no air leads to collapsing of the polymer without a visible hole in the fiber, at least in the processing conditions investigated. The mechanical properties and exact dimensions such as fiber diameter, hollow ratio need to be characterized.

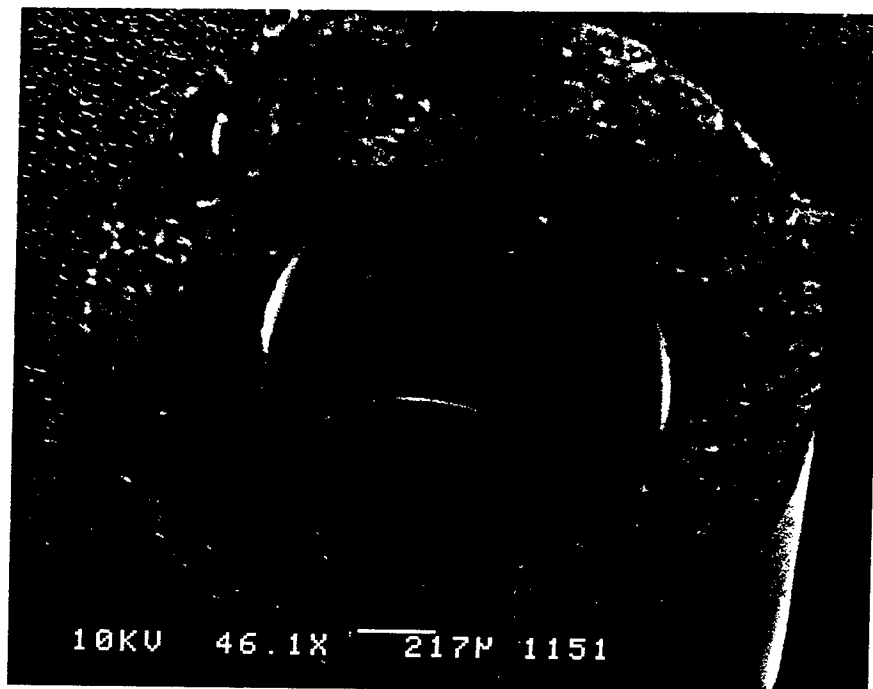


Figure 4. SEM Photograph of Hollow Fibers (immediately after extrusion).

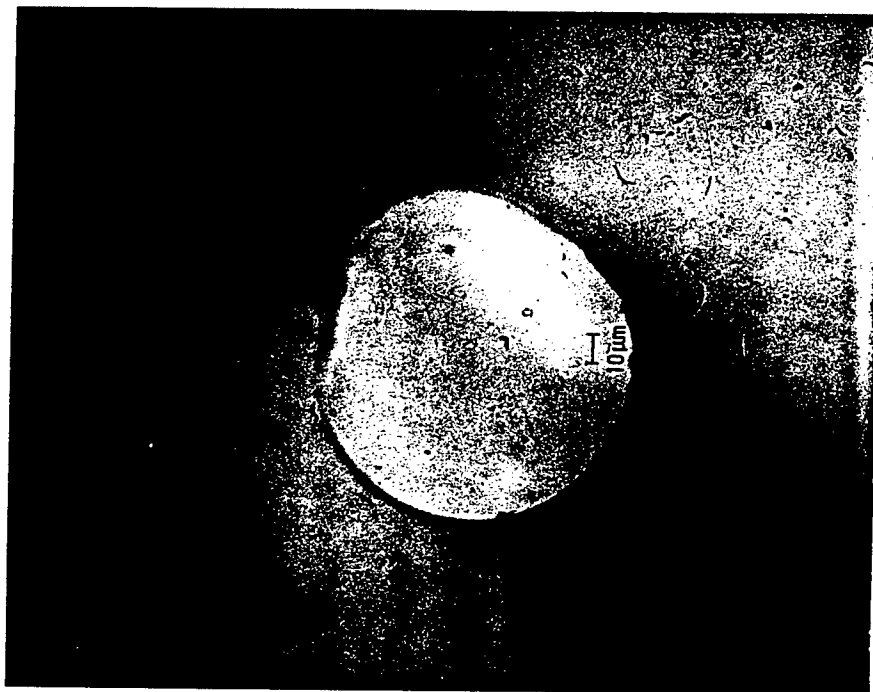


Figure 5. SEM Photograph of Hollow Fiber (wound at 360 ft/min).

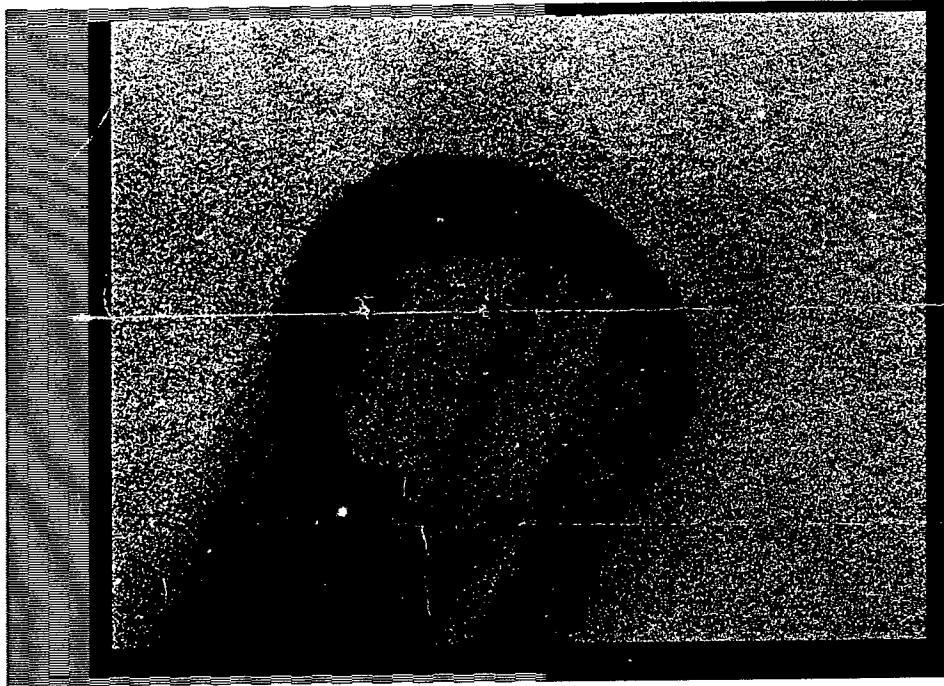


Figure 6. Photograph of Fiber spun With Higher Air Flow in the Capillary.

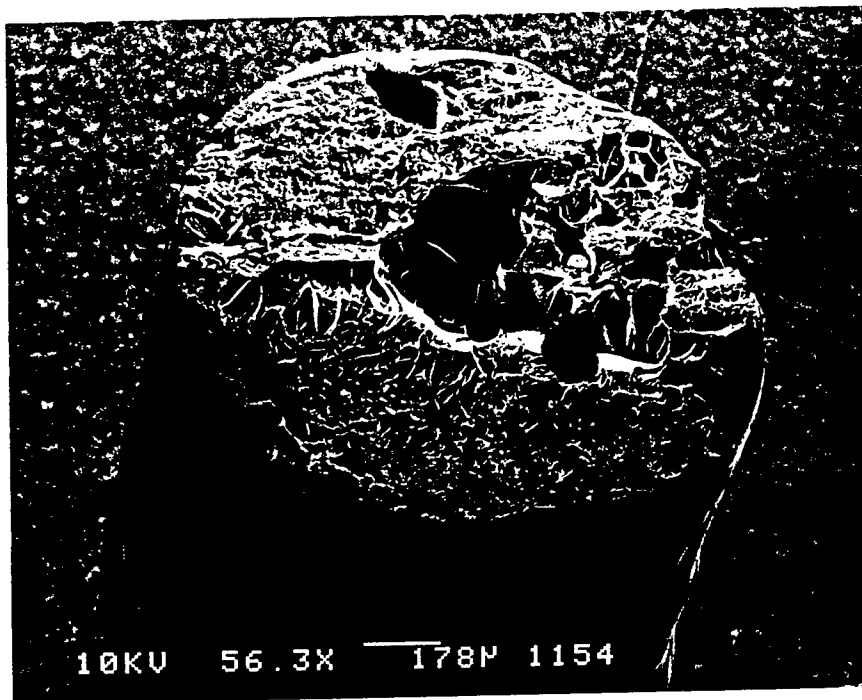


Figure 7. SEM Photograph of Fiber spun Without Air Flow in the Capillary.

Coating of Ultem

In addition to spinning hollow fibers, attempt was made to obtain a thick coating of Ultem on a copper wire by extruding the polymer on to it. Although coating of wires is a common process in the industry most of them are only a few microns thick. While thin coatings serve the purpose of achieving some desired surface properties such as conductivity or protection, thick coatings modify the bulk properties as well. To achieve thick coatings, instead of passing air through the inner capillary, the copper wire was continuously run as the polymer was being extruded through the annulus. Figure 8 shows a cross section of a coated wire. It is apparent that by choosing right conditions, one can coat Ultem onto a substrate to required thickness.

Melt Spinning of Mesophase Pitch

Two attempts were made to spin fibers from a mesophase (AR) pitch. As the reported spinning temperatures in the literature were in the range of 300-350 °C, initially heater was set to 340 °C. Once the temperature approached 330 °C the molten polymer was coming out with bead formation indicating the viscosity was very low. Then the temperature was reduced to 310 °C and a slight pressure of 50 psi was applied. Even under slight pressure, the material was flowing down very easily. Further lowering of the temperature did not help in achieving fiber formation as the material was almost over and spinning had to be stopped.

In the next batch, pitch was loaded and the heater was set only to a temperature of 290 °C. Under this condition when pressure was applied, there was flow of polymer with fiber formation, but the solidified fiber was very brittle and breaking apart. It was not possible to wind those fibers. Even fiber pieces collected were not easy to handle with. SEM pictures of the fiber formed from pitch are shown in Figure 9. Although the fiber looks hollow it has a lot of porosity as well. It is important to note that in this case fibers more than a few inches long could not be collected. Earlier studies have clearly indicated that spinning of mesophase pitch is not easy as they have a very narrow window of spinning conditions [13]. If the temperature is higher, they degrade and if lower, it is not possible to extrude into fibers. The conditions of spinning also depend on the properties of the pitch such as mesophase content and molecular weight. More work needs to be done to optimize the conditions of spinning before successfully spinning hollow fibers from pitch.

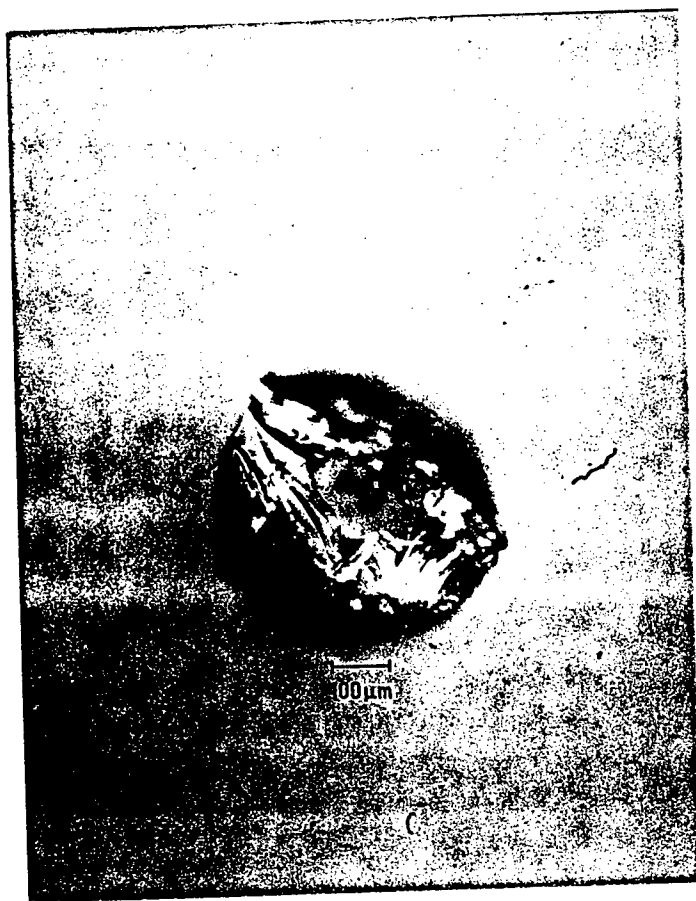


Figure 8. SEM Photograph of Ultem Coated Wire.

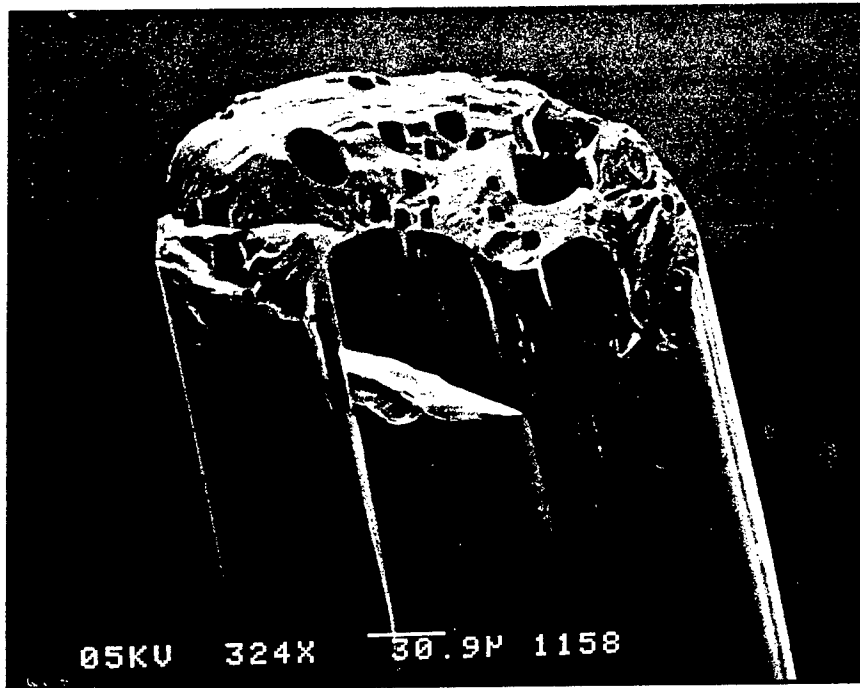


Figure 9. SEM Photographs of Melt Spun Pitch Fiber.

Solution Processing of Ultem

Since Ultem has a very high glass transition and softening temperatures melt processing is not easy. In addition to the difficulties in working with higher temperatures, there is also going to be degradation of the polymer under those conditions. As an alternative, solution processing of the polymer with methylene chloride as solvent was explored. The main interest being to find out whether viscous solutions of Ultem with high concentration of the polymer can be formed, and then is it possible to obtain thick coating on copper wires using such a solution.

Solutions were prepared with different concentrations of Ultem in methylene chloride. It was easy to dissolve upto 20 per cent (w/w). When the concentration was increased, it took longer to dissolve the material. In fact the mixture had to be left overnight or slightly warmed to increase the dissolution rate. Although viscosity of the dope was not checked, concentrations above 40 per cent formed thick dope which appeared to be suitable for extrusion through a capillary such as for spinning into fibers. Up to 50 per cent Ultem could be dissolved in methylene chloride solvent without much difficulty leading to formation of a viscous dope. Although fibers were not spun, copper wire was continuously passed through the spinneret achieving thick coating. Figure 10 shows the cross section of a wire coated from Ultem solution. As there was no attempt made to center the wire through the capillary, coating was not concentric. However, the results showed that solution processing is quite promising.

RECOMMENDATIONS FOR FUTURE WORK

Although hollow fibers were spun from Ultem they were not thoroughly characterized. Fiber structure and properties need to be characterized by microscopy, thermal analysis and tensile testing. Possibility of spinning fibers from the solution need to be investigated. It should be possible to dry spin the fiber. However care needs to be taken in designing the system so that evaporated solvent can be recovered. Another aspect which needs detailed investigation is the spinning of hollow fibers from mesophase pitch. Rheology of pitch, especially its viscosity change with temperature needs to be characterized so that the exact range of processing temperatures can be determined. Based on that data fibers can be spun from pitch. After that forming hollow fibers should be much easier.

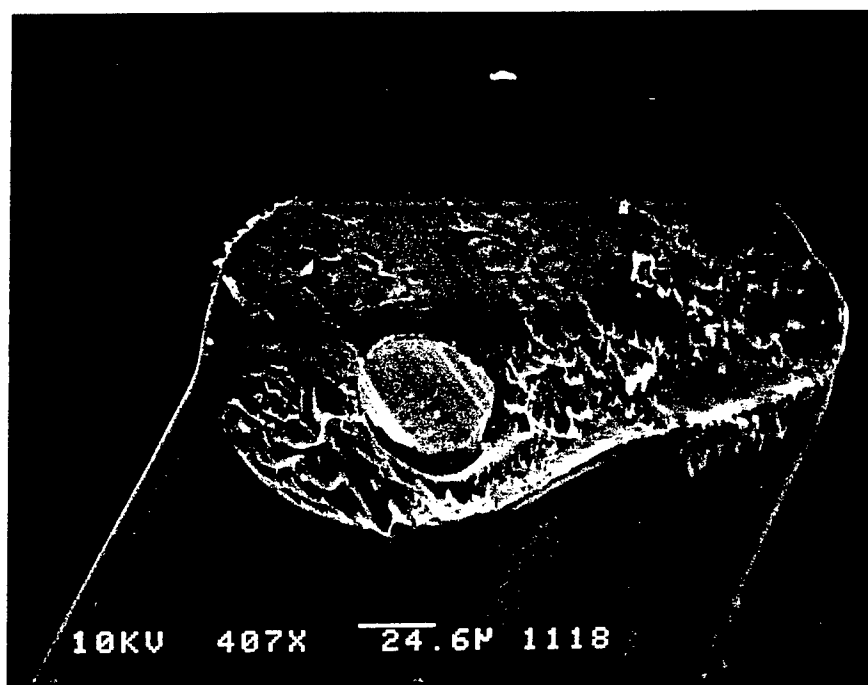


Figure 10. SEM Photograph of a wire coated with Ultem from Solution.

ACKNOWLEDGMENTS

Guidance and support from Drs. Phil Wapner and West Hoffman in this entire work is greatly acknowledged. Colleagues at the laboratory, especially Drs. Jones, Pollock and Ismail and Miss Marietta Fernadez, Hong Phan and Naomi are acknowledged for making my tour an enjoyable one. Financial support from AFOSR, which made this work possible is greatly appreciated. Staff of RDL for their cooperation is also acknowledged.

BIBLIOGRAPHY

1. H. H. yang, 'Aromatic high Strength Fibers,' John Wiley and Sons, New York (1989).
2. T. Kaneda, T. Katsura K. Nakagawa, H. Makino and M. Horio, *J. Appl. Polym. Sci.*, 2, 32, 3133; 32, 3151 (1986).
3. P-84 High Performance Products, Company literature, Lenzing AG.
4. G. V. Cekis, *Modern Plastics Encyclopedia*, mid October issue, 32 (1993).
5. H. R. Penton, *Modern Plastics Encyclopedia*, mid October issue, 87 (1993).
6. Ultem Polyetherimide Resin, Company literature, GE Plastics.
7. I. W. Serfaty, in *Polyimides*, ed. by K. L. Mittal, Plenum Press, New York (1988).
8. "Textile Applications of Performance Polymers," *Textile Month*, July, 20 (1991).
9. G. S. Bhat, AFOSR Summer Project Report, 1995.
10. O. E. Bruck, *Textile Institute and Industries*, 3, 118-121 (1965).
11. H. I. Mahon and B. J. Lipps, *Encyclopedia of Polymer Science and Technology*, Ed. H. F. Mark pp258-272 (1984).
12. Reinehr *et al.*, US Patent 4,457,885 (1984).
13. Y. Shi, Q. F. Zha and L. Liu, Proceedings of the European Carbon Conference "Carbon 96" - New Castle, UK 226-227 (1996).
14. G. J. Hays et al., Carbon 1992 Extended Abstracts, Germany, 813-815 (1992).
15. Reinehr *et al.*, US Patent 4,432,923 (1984).

BLACKHOLE ANALYSIS

**David B. Choate
Associate Professor
Department of Mathematics**

**Transylvania University
300 N. Broadway
Lexington, KY**

**Final Report for:
Summer Research Program
Phillips Laboratory**

**Sponsored by:
Air Force Office of Scientific Research
Bolling Air Force Base, Washington, DC**

And

Phillips Laboratory

August, 1997

BLACKHOLE ANALYSIS

David B. Choate
Associate Professor
Department of Mathematics
Transylvania University

Abstract

Blackhole space is a parallel universe to the complex plane in which some problems can be worked more easily and others with greater difficulty. The theorems of blackhole space are presented here and their application to superposition in signal processing. Parallel programs exist to any existing program, even some parallel machines.

BLACKHOLE ANALYSIS

1. BLACKHOLE ADDITION

Let $S = \{z = x + yj \mid x \text{ and } y \text{ real, } -\pi < y \leq \pi\}$ or equivalently, after an appropriate adjustment of the residue of y modulo 2π , let $S = \{z = x + y (\text{mod } 2\pi)j \mid x \text{ and } y \text{ real}\}$, a horizontal strip. Set $S_B = S \cup \{-\infty\}$.

Now let $z = x_1 + y_1j$ and $w = x_2 + y_2j \in S_B$. Define a *blackhole or B-multiplication* on S_B , denoted by \oplus , as

$$z \oplus w = (x_1 + x_2) + [(y_1 + y_2) \text{ mod } (2\pi)]j$$

provided both z and w are in S ; otherwise, $z \oplus w = -\infty$.

And if $z = re^{j\theta}$, then as usual define $\text{Log}(z) = \ln|r| + [\theta (\text{mod } 2\pi)]j$ again after the appropriate adjustment of the residue. Clearly

$$\text{Log}(zw) = \text{Log}(z) \oplus \text{Log}(w).$$

Now let $z, w \in S_B$. We define an operation called *blackhole addition* or *B-addition* on S_B , denoted by Γ , as

$$z \Gamma w = \text{Log}(e^z + e^w).$$

If we define $z \Gamma -\infty = z = z \Gamma -\infty$ for every z in S_B , then Γ is an operation on S_B .

And clearly

$$\text{Log}(z + w) = \text{Log}(z) \Gamma \text{Log}(w).$$

2. THE FIELD (S_B, \oplus, \lrcorner)

It is an easy exercise to show that (S_B, \oplus, \lrcorner) is a field. But for the purpose of illustration observe that the *B-additive identity* is $-\infty$ since

$$z \lrcorner -\infty = \text{Log}(e^z + e^{-\infty}) = z.$$

Also observe that if $z \in S$, then its *B-additive inverse* is $j\pi \oplus z$ since

$$\begin{aligned} z \lrcorner (j\pi \oplus z) &= \text{Log}(e^z + e^{j\pi \oplus z}) \\ &= \text{Log}[e^z(1 + e^{j\pi})] \\ &= \text{Log}(0) \\ &= -\infty. \end{aligned}$$

And certainly the B-additive inverse of $-\infty$ is $-\infty$. Therefore every element in S_B has a B-additive inverse. Furthermore, *B-division*, denoted by θ , may be defined as

$$z \theta w = z \oplus (j\pi \oplus w).$$

Furthermore, the distributive law of B-multiplication over B-addition can be established with the following calculation:

for $u, v, w \in S_B$

$$\begin{aligned} u \oplus (v \lrcorner w) &= \text{Log}(e^u) \oplus \text{Log}(e^v + e^w) \\ &= \text{Log}[e^u(e^v + e^w)] \\ &= \text{Log}(e^{u+v} + e^{u+w}) \\ &= \text{Log}(e^{u \oplus v} + e^{u \oplus w}) \\ &= (u \oplus v) \lrcorner (u \oplus w). \end{aligned}$$

Theorem 2.1 $(C, \cdot, +) \cong (S_B, \oplus, \lrcorner)$.

Proof. Define $\phi: C \rightarrow S_B$ by $\phi(z) = \text{Log}(z)$.

$$\begin{aligned} \text{Then} \quad \phi(z_1 z_2) &= \text{Log}(z_1 z_2) \\ &= \text{Log}(z_1) \oplus \text{Log}(z_2) \\ &= \phi(z_1) \oplus \phi(z_2). \end{aligned}$$

$$\begin{aligned} \text{Furthermore, } \phi(z_1 + z_2) &= \text{Log}(z_1 + z_2) \\ &= \text{Log}(z_1) \lrcorner \text{Log}(z_2) \\ &= \phi(z_1) \lrcorner \phi(z_2). \end{aligned}$$

If $w \in S$, then its preimage under ϕ , $w \in S$, is e^w . And since the preimage of $-\infty$ is 0, ϕ is onto.

If $\phi(z) = 0 \lrcorner$, then $\text{Log}(z) = -\infty$, or $z = 0$; so ϕ is one-to-one.

3. BLACKHOLE CALCULUS

Definition 3.1. The function f is said to be *B-differentiable at x* if the limit

$$\lim_{h \rightarrow -\infty} \{ [f(x \lrcorner h) \lrcorner (j\pi \oplus f(x))] \ominus h \} \quad ,$$

denoted by $(f)'_B(x)$, exists.

Theorem 3.2 Suppose f is differentiable. Then f is B-differentiable and

$$(f)'_B(x) = [\text{Log}(dy/dx)] \oplus y \ominus x.$$

Proof. By definition $(f)'_B(x) = \lim_{h \rightarrow \infty} \langle \{f[\text{Log}(e^x + e^h)] \text{ } \cap [j\pi \oplus f(x)]\} \theta h \rangle$

$$= \text{Log} [\lim_{h \rightarrow \infty} (\langle \exp\{f[\text{Log}(e^x + e^h)]\} - \exp(f(x)) \rangle / e^h)]$$

$$= \text{Log} (\lim_{h \rightarrow \infty} \{f[\text{Log}(e^x + e^h)] \exp\{f[\text{Log}(e^x + e^h)]\} / (e^x + e^h)\}) \quad (\text{by}$$

L'Hopital's Rule)

$$= \text{Log} [f(x)e^{f(x)\theta x}]$$

$$= \{\text{Log} [f(x)]\} \oplus f(x) \theta x . \quad \square$$

Corollary 3.3 Let c and p be constants. Then

$$i. (c)'_B = -\infty$$

$$ii. (px)'_B(x) = \text{Log}(p) \oplus (p \theta 1)x$$

$$iii. [\text{Log}(x)]'_B = \theta x$$

$$iv. (e^x \oplus c)'_B = e^x$$

$$v. [\text{Log}(px)]'_B = \text{Log}(p) \theta x$$

$$vi. [p\text{Log}(x)]'_B = \theta x \oplus \text{Log}(px^{p-1})$$

$$vii. (x^p)'_B = x^p \theta x \oplus \text{Log}(px^{p-1})$$

$$viii. (\sin x)'_B = \text{Log}(\cos x) \oplus \sin x \theta x$$

$$ix. (\cos x)'_B = \text{Log}(-\sin x) \oplus \cos x \theta x$$

$$x. (f)''_B(x) = \text{Log}\{f''(x) + [f'(x)]^2 - f'(x)\} \oplus f(x) \theta 2x .$$

Corollary 3.4. Let $f(x)$ be a real valued function in some interval I . Then $f(x)$ is increasing or decreasing in I if and only if $(f)'_B$ is real or purely imaginary in I .

Theorem 3.4.5 Let $f(x)$ be differentiable. Then $(f_B)'_B = (f')_B$.

Proof. By definition $f_B(x) = \text{Log}[f(e^x)]$.

$$\begin{aligned} \text{Then } [f_B(x)]'_B &= \text{Log}[e^x f(e^x)/f(e^x)] \oplus \text{Log}[f(e^x)] \ominus x = x \oplus \text{Log}[f(e^x)] \ominus x \\ &= [f(x)]_B . \quad \square \end{aligned}$$

The isomorphism in Theorem 2.1 is a portal into a parallel universe where we find

Theorem 3.5. Suppose that both f and g are both B -differentiable. Then

$$i. (c \oplus f)'_B(x) = [c \oplus (f)]'_B(x)$$

$$ii. (f \cap g)'_B = (f)'_B \cap (g)'_B$$

$$iii. (f \oplus g)'_B = [f \oplus (g)'_B] \cap [g \oplus (f)'_B]$$

To illustrate 3.5(iii) consider

Example 3.6. Let $f(x) = px$ and $g(x) = qx$. Then

$$\begin{aligned} [f \oplus (g)'_B] \cap [g \oplus (f)'_B] &= \{px \oplus [(\text{Log} q \oplus (q \ominus 1)x)]\} \cap \{qx \oplus [\text{Log} p \oplus (p \ominus 1)x]\} \\ &= \text{Log}\{qe^{[px + (q-1)x]} + pe^{[qx + (p-1)x]}\} \\ &= \text{Log}\{qe^{[px \oplus (q \ominus 1)x]} + pe^{[qx \oplus (p \ominus 1)x]}\} \\ &= \text{Log}(p \oplus q) \oplus [(p \oplus q) \ominus 1]x \\ &= (f \oplus g)'_B . \quad \square \end{aligned}$$

Definition 3.7 First set

$$\Gamma \sum_{i=1}^n a_i$$

$$= a_1 \Gamma a_2 \Gamma \dots \Gamma a_n$$

The *blackhole definite integral from a to b* is given by

$$\lim_{((\Delta x)_B \rightarrow -\infty} \langle \Gamma \sum_{i=1}^n [(f(x_i))_B \oplus (\Delta x)_B] \rangle$$

where $(\Delta x)_B = [b \Gamma (j\pi \oplus a)] \ominus n$. and x_i is in the i th subinterval.

For this limit we use the notation.

$$\Gamma \int_a^b [(f(x))_B \oplus (dx)_B]$$

$$\text{Theorem 3.8. } \Gamma \int_a^b [(f(x))_B \oplus (dx)_B] = \text{Log} \left[\int_a^b e^{[f(x)]_B + x} dx \right]$$

Proof. Set $x_0 = a$. Without loss of generality we may assume that $(\Delta x)_B = x_i \cap (j\pi \oplus x_{i-1}) =$

$\text{Log}[\exp(x_i) - \exp(x_{i-1})]$.

$$\text{By definition } \Gamma \int_a^b [f(x)_B \oplus (dx)_B]$$

$$= \lim_{(\Delta x)_B \rightarrow -\infty} \text{Log} [(e^{f(x_1)}) (e^{x_1} - e^{x_0}) + \dots + (e^{f(x_n)}) (e^{x_n} - e^{x_{n-1}})]$$

$$= \lim_{(\Delta x)_B \rightarrow -\infty} \text{Log} [e^{f(x_1) + x_1} + \dots + e^{f(x_n) + x_n} + e^{f(x_1) + x_0} + \dots + e^{f(x_n) + x_{n-1}}]$$

Set $\Delta x = (b - a)/n$. After multiplying the last n terms of the argument by $e^{\Delta x} / e^{\Delta x}$ and all terms by

$\Delta x / \Delta x$ we have

$$\Gamma \int_a^b [(f(x))_B \oplus (dx)_B]$$

$$= \text{Log} \left[\lim_{(\Delta x)_B \rightarrow -\infty} \frac{(e^{\Delta x} - 1)}{(\Delta x e^{\Delta x})} \right] \oplus \text{Log} \left[\int_a^b e^{f(x) + x} dx \right] = \text{Log} \int_a^b e^{f(x) + x} dx$$

$$= \text{Log} \left[\int_a^b e^{f(x) + x} dx \right]$$

by l'Hopital's Rule. \square

In order to get a feel for indefinite blackhole integrals consider

Example 3.9. Recall that $(\text{Log}x)'_B = \theta x$.

$$\begin{aligned}\int [(\theta x)_B \oplus (dx)_B] &= \text{Log} [\int e^0 dx] \\ &= \text{Log}\{x + e^c\} \\ &= (\text{Log}x) \int (c)\end{aligned}$$

Example 3.10. Recall that $(px)'_B = \text{Log}(p) \oplus (p \theta 1)x$.

$$\begin{aligned}\int [\text{Log}(p) \oplus (p \theta 1)x] \oplus (dx)_B &= \text{Log}(\int pe^{px} dx) \\ &= \text{Log}(e^{px} + e^c) \\ &= (px) \int (c).\end{aligned}$$

Example 3.11. Recall that $(e^x)'_B = e^x$.

$$\begin{aligned}\int [e^x \oplus (dx)_B] &= \text{Log} \{ \int [\exp(e^x + x)] dx \} \\ &= \text{Log} [\exp(e^x) + e^c] \\ &= (e^x) \int (c).\end{aligned}$$

Note 3.12. These examples indicate that

$$\begin{aligned}\int [(f(x))_B \oplus (dx)_B] \\ = [F_B(x) \int c]\end{aligned}$$

where $F_B(x)$ is the B- antiderivative of $f(x)$.

Other blackhole theorems are also immediate from Theorem 2.1 :

$$3.13 (i) \quad \Gamma \int_a^a [(f(x))_B \oplus (dx)_B] = -\infty$$

$$3.13. (ii) \quad \langle \Gamma \int_a^b [(f(x))_B \oplus (dx)_B] \rangle \Gamma \langle \Gamma \int_b^c [(f(x))_B \oplus (dx)_B] \rangle =$$

$$\langle \Gamma \int_a^c [(f(x))_B \oplus (dx)_B] \rangle$$

And clearly The blackhole version of the First Fundamental Theorem of Calculus is given by

$$\begin{aligned} 3.13. (iii) \quad & \Gamma \int_a^b [(f(x))_B \oplus (dx)_B] \\ & = [F_B(b)] \Gamma [(j\pi) \oplus F_B(a)] \end{aligned}$$

To illustrate 3.13. (iii) consider

Example 3.14. Let $f(x) = \text{Log}(p) \oplus (p \ominus 1)x$. Then, as we have seen $F_B(x) = (px) \Gamma (c)$.

Consequently,

$$\begin{aligned}
& \Gamma \int_a^b [(f(x))_B \oplus (dx)_B] \\
&= \text{Log} \left\langle \int_a^b e^{[\text{Log}(p) + (p-1)x + x]} dx \right\rangle \\
&= \text{Log} \left[\int_a^b p e^{px} dx \right] \\
&= \text{Log} (e^{pb} + e^c - e^{pa} - e^c) \\
&= [F_B(b)] \Gamma [(j\pi) + F_B(a)]
\end{aligned}$$

To argue the Second Fundamental Theorem of Blackhole Calculus let a be in an interval over which f(x) is continuous. Then certainly

$$\begin{aligned}
& (d/dx)_B \left\langle \Gamma \int_a^x [f(t)_B \oplus (dt)_B] \right\rangle \\
&= (d/dx)_B \left\langle \text{Log} \left[\int_a^x e^{f(t)+t} dt \right] \right\rangle \\
&= \text{Log} \frac{e^{[f(x)+x]}}{\int_a^x e^{f(t)+t} dt} \oplus \left\langle \text{Log} \left[\int_a^x e^{f(t)+t} dt \right] \right\rangle \theta x \\
&= f(x) \oplus x \theta x \\
&= f(x) \quad \square
\end{aligned}$$

Now observe that

Theorem 3.16 $(\iint f(x,y) dy dx)_B = \text{Log}(\iint \exp\{[f(x)]_B + x + y\} dy dx).$

$$\begin{aligned}
 \text{Proof. } (\iint f(x,y) dy dx)_B &= \{[\iint f(x,y) dy] dx\}_B \\
 &= (\iint [\text{Log}\langle \exp\{[f(x)]_B + y\} dy \rangle dx]_B \\
 &= (\text{Log}[\exp\langle \exp\{[f(x)]_B + y\} dy \rangle dx]_B \\
 &= \text{Log}\langle \iint \exp\{[f(x)]_B + x + y\} dy dx \rangle. \quad \square
 \end{aligned}$$

Example 3.17. Clearly $(\ln x + c_1)(\ln y + c_2) = \iint (dx dy)/xy$.

But observe that we can obtain this result through blackhole analysis. First descend to obtain

$$\begin{aligned}
 \iint (1/xy) \oplus (dx)_B \oplus (dy)_B &= \iint (\ominus x \ominus y) \oplus (dx)_B \oplus (dy)_B \\
 &= \text{Log}\{\iint \exp(-x - y + x + y) dx dy\} \\
 &= \text{Log}[(x + c_1)(x + c_2)]
 \end{aligned}$$

We now ascend to obtain

$$\exp\{\text{Log}[(\ln x + c_1)(\ln y + c_2)]\} = (\ln x + c_1)(\ln y + c_2). \quad \square$$

4. BLACKHOLE DIFFERENTIAL EQUATIONS

To understand how to apply blackhole calculus to ordinary space consider

Example 4.1 Let $dy/dx = y$

Solution. We now "descend" into the blackhole to obtain

$$(dy/dx)_B = (y)_B .$$

The left side can be calculated using Theorem 3.2 . The right term can be determined by "e-ing" each variable and then "Logging" the resulting expression. So we have

$$\text{Log}(dy/dx) \oplus y \theta x = y \quad (\text{ii}) ,$$

$$\text{or } dy/dx = e^x \text{ which implies}$$

$$y = e^x + \ln(c)$$

To "ascend" to ordinary space by "Logging" each variable and then "e-ing" the entire expression,

$$\text{or } \exp[\text{Log}(y)] = \exp[e^{\text{Log}(x)} + \text{Log}(c)] \text{ which gives}$$

$$y = ce^x . \quad \square$$

Example 4.2 $dy/dx = -x/y$.

Solution. We now descend to obtain

$$\text{Log}(dy/dx) \oplus y \theta x = (j\pi) \oplus x \theta y , \text{ or}$$

$$\text{Log}(dy/dx) = (j\pi) \oplus 2x \theta 2y \text{ which implies}$$

$$e^{2x}/2 + e^{2y}/2 = c .$$

We now ascend to obtain

$$\exp(x^2/2 + y^2/2) = e^c \text{ which implies}$$

$$x^2/2 + y^2/2 = c .$$

Example 4.3 $dy/dx = (y/x)\{1 - [\ln(y)]/[\ln(x)]\}$.

Solution. We descend to obtain

$$\text{Log}(dy/dx) \oplus y \theta x = y \theta x \oplus \text{Log}[1 - (y/x)] , \text{ or}$$

$$dy/dx + y/x = 1 .$$

whose solution is

$$y = x/2 + c/x.$$

We now ascend to obtain

$$y = \exp\{[\ln(x)/2] + [c/\ln(x)]\} , \text{ or}$$

$$y = (\sqrt{x})e^{[c/\ln(x)]} , \text{ the solution.}$$

Example 4.4. $dy/dx = (y/x)(\ln y/\ln x)[1 - (\ln x)(\ln y)] .$

Solution. We descend to

$$\text{Log}(dy/dx) \oplus y \ominus x = y \ominus x \oplus \text{Log}[(y/x)(1 - xy)] , \text{ or}$$

$$dy/dx + (-1/x)y = (-1)y^2$$

which is recognized at once as a Bernoulli differential equation whose solution is

$$y = [2x/(x^2 + 2c)] .$$

We now ascend to obtain

$$y = \exp\{2\ln x/[(\ln x)^2 + 2c]\} , \text{ the solution.}$$

Example 4.5. $d^2y/dx^2 = (dy/dx)^2/y .$

Solution. Descend to obtain

$$\{\text{Log}[y'' + (y')^2 - y']\} \oplus y \ominus 2x = 2[\text{Log}(y') \oplus y \ominus x] \ominus y , \text{ or}$$

$$y'' - y' = 0 , \text{ whose solution is}$$

$$y = c_1 + c_2 e^x .$$

We now ascend to obtain

$$y = c_1 \exp(c_2 x) , \text{ the solution.}$$

5. BLACKHOLE SIGNAL PROCESSING

All undefined and underdefined terms and symbols used in this section can be found in chapter 5 of [1]. In fact on p. 481 of [1] we are given a definition of a *superposition* H , a generalization of a system transformation, which must satisfy:

$$1. H[x_1(n) \square x_2(n)] = H[x_1(n) \circ x_2(n)]$$

$$2. H[c : x(n)] = c * H[x(n)] .$$

, where \square is an input operation and \circ is an output operation and where $:$ and $*$ represent scalar multiplication.

Now define $H: C \rightarrow S_B$ by $H(z) = \text{Log}(z)$.

If we let i. \square be $+$, ordinary addition in C ,

ii. \circ be Γ , or subaddition in S_B ,

iii. $:$ be scalar multiplication in C ,

and iv. $*$ be a scalar operation in S_B over C defined by

$$c * H[x] = \text{Log}(c) \oplus H(x) ,$$

then we have a generalized superposition H (where H stands for *homomorphism*.)

But by p.482 of [1] we can show that this homomorphic system can be written as a cascade of three systems provided that Γ is commutative and associative and that we can prove

Theorem 5.1. *The additive group S_B space under Γ is a vector space over C with scalar multiplication $*$.*

Proof. Let $\alpha, \beta \in C$ and $v, w \in S_B$. We can now easily establish the four properties of a vector space.

$$\text{i. } \alpha * (v \text{ } \Gamma \text{ } w) = \text{Log}(\alpha) \oplus (v \text{ } \Gamma \text{ } w)$$

$$= [\text{Log}(\alpha) \oplus v] \text{ } \Gamma \text{ } [\text{Log}(\alpha) \oplus w]$$

$$= (\alpha * v) \text{ } \Gamma \text{ } (\alpha * w) .$$

$$\text{ii. } (\alpha \oplus \beta) * v = \text{Log}(\alpha \text{ } + \text{ } \beta) \oplus v$$

$$= [\text{Log}(\alpha) \text{ } \Gamma \text{ } \text{Log}(\beta)] \oplus v$$

$$= [\text{Log}(\alpha) \oplus v] \text{ } \Gamma \text{ } [\text{Log}(\beta) \oplus w]$$

$$= (\alpha * v) \text{ } \Gamma \text{ } (\beta * w) .$$

$$\text{iii. } \alpha * (\beta * v) = \text{Log}(\alpha) \oplus [\text{Log}(\beta) \oplus v]$$

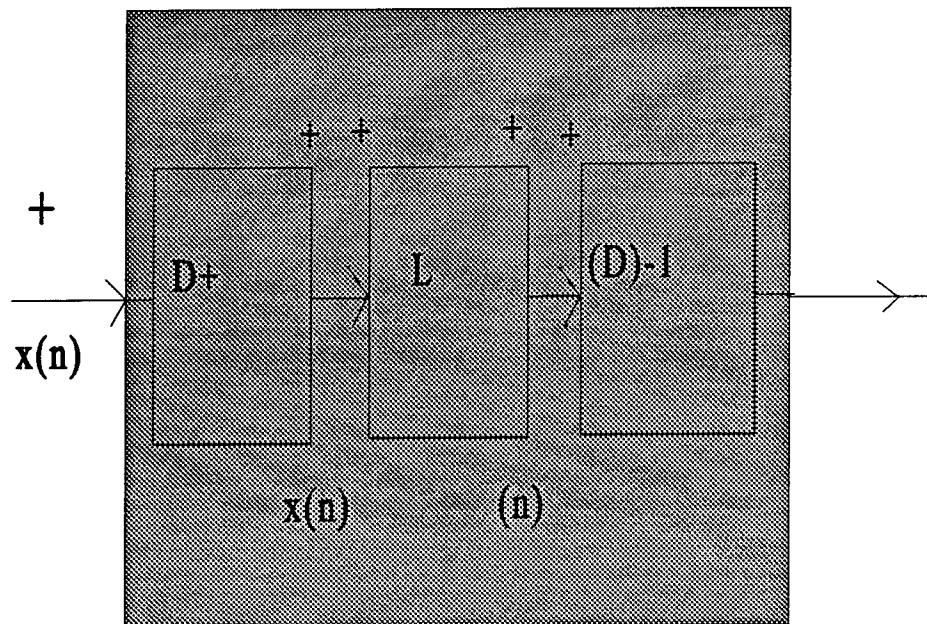
$$= \text{Log}(\alpha\beta) \oplus v$$

$$= (\alpha\beta) * v .$$

$$\text{iv. } 1 * v = \text{Log}(1) \oplus v$$

$$= v .$$

Again using [1] p. 482 , we know that since the system inputs constitute a vector space of complex numbers under addition and ordinary scalar multiplication and that the homomorphic system H outputs constitute a vector space under Γ , the blackhole addition, and $*$, the scalar multiplication, all systems of this class can be represented as a cascade of three systems



H

where the existence of D and L, a linear system, is guaranteed.

6. WHITEHOLE ANALYSIS

Set $S_w = S \cup \{+\infty\}$. We define an operation γ on S_w by

$z \gamma w = \text{Log}\{1/[(1/e^z) + (1/e^w)]\}$ if $z, w \in S$ and $+\infty$ otherwise. It is now easy to show

Theorem 6.1. $(C, +, \cdot) \cong (S_w, \gamma, \oplus)$.

Theorem 6.2. $(f)'_w(x) = f(x) \oplus x \oplus \text{Log}[f'(x)]$.

Corollary 6.3.

i. $(c)'_w = +\infty$

ii. $(x)'_w = 0$

iii. $(px)'_w = (p \oplus 1)x \oplus \text{Log}(p)$

iv. $(e^x)'_w = e^x \oplus 2x$

$$v. (-e^x)'_w = -e^x$$

$$vi. [Log(px)]'_w = [Log(x)] \theta x$$

$$vii. [pLog(x)]'_w = [Log(x/p)] \theta x$$

$$viii. [sin(x)]'_w = sin(x) \theta x \theta Log[cos(x)]$$

$$ix. [pLog(x)]'_w = cos(x) \theta x \theta Log[-sin(x)]$$

$$x. [f'']_w = y \theta 2x \theta Log[(y')^2 - y' - y''].$$

$$Theorem 6.4. [f(x)dx]_w = \theta Log \{ \theta [e^{-f(x)+x} dx] \}.$$

$$Theorem 6.5. (y)'_B \oplus (y)'_w = 2(y \theta x).$$

7. BLACKHOLE PROGRAMMING

We know, by Theorem 2.1, that every operation and function has a unique blackhole image. For example

$$1. f(x) \rightarrow Log[f(e^x)] \quad 2. d^2y/dx^2 \rightarrow \{Log[(d^2y/dx^2) \oplus (dy/dx)^2 \oplus dy/dx]\} \oplus y \theta 2x.$$

Consequently there exists a meta-blackhole algorithm which will accelerate any program in which multiplication and exponentiation dominate addition and subtraction.

Reference

1. Oppenheim, A. V., and R. W. Schaffer: "Digital Signal Processing," Prentice-Hall, Inc, 1975.

IMAGE RECOVERY USING PHASE DIVERSITY

Neb Duric
Professor
Department of Physics and Astronomy

University of New Mexico
800 Yale Bld. NE 87131

Final Report for:
Summer Faculty Research Program
Phillips Laboratory

Sponsored by:
Air Force Office of Scientific Research
Bolling Air Force Base, DC

And

Phillips Laboratory

October, 1997

IMAGE RECOVERY USING PHASE DIVERSITY

Neb Duric
Professor
Department of Physics and Astronomy
University of New Mexico

Abstract

The use of phase diversity to recover aberration-free images was the focal point of the research carried out under the Summer Faculty Research Program. Computer simulations were used to demonstrate that phase diversity can be used to remove aberrations from an image and that the Gonsalves error metric approach can be successfully implemented toward that goal. An experiment was designed to utilize a phase diversity camera for imaging aberrated wavefronts. It is proposed that such an experiment be carried out in order to determine the effectiveness of the phase diversity technique under "real life" conditions.

Image Recovery Using Phase Diversity

1 Introduction

The problem of imaging through the Earth's atmosphere can be addressed through a variety of well documented techniques. These techniques can be divided into "active" and "passive" categories. In the former, the optical elements of the imaging device (ie the camera) are adjusted in real time in order to counter the effects of the atmosphere as it varies spatially and temporally. In the latter case, no active components are used and the images are recovered through post-detection image processing.

The active method has the advantage that recording of faint signals can be achieved through integration of the signal on time scales much greater than the atmospheric coherence time. The Starfire Optical Range houses two active telescopes that operate this way. Stunning images approaching the diffraction limit have been recorded at SRO and represent the state-of-the art in active optics imaging through the Earth's atmosphere. The only drawback to this method is that it is technologically involved and therefore expensive.

The passive methods have met with more limited success. Their primary drawback is that post-detection processing requires a large number of pre-recorded images in order to time-resolve the coherence time of the atmosphere. Each recording of the image is therefore accompanied by detector noise. The combination of large numbers of image frames and noisy data make post-processing both difficult and time-consuming. The quality of the image cannot be assessed in real time. The major advantage, however, is that post-processing is inherently much cheaper than the construction of active optics and therefore presents greater availability to users.

The ideal passive technique, therefore, is one that minimizes the post-processing time and the detector noise limitations. One method that potentially bears such attributes is the Phase Diversity Technique. We report on the work we have performed, under the summer faculty program, relating to the phase diversity technique of image recovery. First, we describe the basic theoretical elements of this technique in the following section. Simulations we have performed are described in section 3. Section 4 describes an experimental setup for testing the phase diversity technique. Section 5 describes

future steps that need to be followed in order to recover images taken through the Earth's atmosphere.

2 Theoretical Basis of Phase Diversity

The Earth's atmosphere acts as an aberrator in which the aberrations vary spatially *and* temporally. For imaging objects at infinity one can consider the atmosphere as disturbing a wavefront which is initially plane-parallel, that is, surfaces of constant phases are planes oriented at right angles to the direction of propagation. As the plane wave travels through the Earth's atmosphere, different parts of the wavefront undergo different amounts of phase retardation resulting from the fact that different patches of the Earth's atmosphere have different indices of refraction. By the time the wavefront reaches the ground-based detector it is no longer plane-parallel. It has an overall tilt and the surfaces of constant phase are now corrugated. The corrugations represent phase variations (aberrations) imposed by the earth's atmosphere. For a wavefront incident on a circular aperture such as the aperture of a telescope, the aberrations can be expanded in a convenient series of functions called "Zernike Polynomials". Thus, any aberration can be, in principle, characterized by an appropriate set of Zernike polynomials. Any technique that can determine the coefficients of the Zernike polynomials can yield a characterization of the aberration and therefore can "undo" the aberration through an appropriate deconvolution.

The phase diversity technique takes advantage of the fact that the morphology of an image located at an arbitrary location with respect to the focal plane is a strong function of the aberrations that are present. Thus, the appearance of a defocused image, relative to an in-focus image, depends very much on the aberrations that the two images share. There are two basic methods by which the comparison of the defocused and focused images can be used to recover diffraction-limited images. We discuss them in turn.

2.1 The Gonsalves Error Metric

The passage of the wavefront through the atmosphere and the optical system of the instrument leads to distortions of the true wavefront and therefore the image that is recorded by the instrument. The relationship between the

true image (as would be obtained by a diffraction limited instrument in the absence of the atmosphere) and the recorded image is given by:

$$I'(x, y) = I(x, y) \star \zeta(x, y) \quad (1)$$

where, $I'(x, y)$, is the recorded image, $I(x, y)$ is the true, diffraction-limited (aberration-free) image and $\zeta(x, y)$ is the point-spread function of the complete optical system (atmosphere plus instrument). The point spread function is defined by the aberrations present in the optical system.

Taking the Fourier transform of both sides of equation 1 yields

$$\tilde{I}'(u, v) = \tilde{I}(u, v) \tilde{\zeta}(u, v)$$

where $\tilde{\zeta}(u, v)$ is commonly referred to as the *Optical Transfer Function* or OTF.

Consider now a second image that is produced by the same instrument at the same time. This image is defocused with respect to the first. Thus,

$$\tilde{I}'_d(u, v) = \tilde{I}_d(u, v) \tilde{\zeta}_d(u, v). \quad (2)$$

One can define an "error" as:

$$E = \sum_{u,v} |\tilde{I}'(u, v) - \tilde{I}(u, v) \tilde{\zeta}(u, v)|^2 + \sum_{u,v} |\tilde{I}'_d(u, v) - \tilde{I}_d(u, v) \tilde{\zeta}_d(u, v)|^2 \quad (3)$$

where the summation is over the pixels of the digitized image. This error arises from not knowing the exact form of the OTF, $\tilde{\zeta}(u, v)$. The goal, therefore, is to minimize E by choosing the appropriate OTF. The modeling of the OTF is performed by:

- (i) assuming $\tilde{\zeta}(u, v)$ can be described by a series of Zernike polynomials,
- (ii) satisfying the additional constraint that the defocused term of the error equation must be simultaneously minimized.

Differentiating equation 3 with respect to \tilde{I} , setting to 0, solving for \tilde{I} and plugging back into equation 3 yields,

$$E = \sum_{u,v} \frac{|\tilde{I}'(u, v) \tilde{\zeta}_d(u, v)|^2 - \tilde{I}'_d(u, v) \tilde{\zeta}(u, v)|^2}{|\tilde{\zeta}(u, v)|^2 + |\tilde{\zeta}_d(u, v)|^2}. \quad (4)$$

Further minimization of the above error equation can be achieved by choosing the appropriate OTF. The usual approach is to expand the OTF in terms of Zernike Polynomials and by varying the polynomial coefficients, minimize E . The method was first proposed by Gonsalves (1979, 1982).

2.2 The Transport Method

This technique is based on a description of the transport of light through the focal plane along the optical axis of the instrument (henceforth the z axis). Let us consider the amplitude and phase of the wavefront.

$$V = Ae^{i\omega t} = \sqrt{I}e^{i\delta}e^{i\omega t} \quad (5)$$

where V is the instantaneous electric field, I is the intensity, ω is the frequency (we are assuming monochromatic radiation) and δ is that portion of the phase of the signal that is produced by the aberrations.

The transport of the amplitude and phase along the z axis is normally described with the Helmholtz equation. If we assume that the wavefront can be described as a plane wave traveling in the z direction and if its amplitude varies slowly with z , the transport equation simplifies to

$$\left(i \frac{d}{dz} + \frac{\vec{\nabla}^2}{2k} + k \right) A_z = 0. \quad (6)$$

where k is the wave number. Substituting equation 5 into equation 6 yields:

$$-\frac{2\pi}{\lambda} \frac{\partial I}{\partial z} = \vec{\nabla} \cdot (I \vec{\nabla} \delta). \quad (7)$$

Equation 7 can be solved by numerical techniques such as the finite difference method. In general, δ is a function of x and y , coordinates that define a plane perpendicular to the z axis. A solution of equation 7 for $\delta(x, y)$ can be expressed in terms of Zernike polynomials and can therefore be used to correct the aberrations represented by the OTF. This method is described by Restaino (1992).

3 Simulations

To test the feasibility of the above ideas, we have performed numerical simulations. The simulations were performed under the summer faculty program during the summer of 1997. The Gonsalves error metric approach was implemented numerically by modifying a code originally written by Gordon Love (PL). A known image (the true image) was numerically convolved with a point spread function simulated by a finite series of Zernike terms, yielding the aberrated image.

A defocused image was also generated by numerically smoothing the aberrated image by a fixed amount of defocus, yielding the defocused image. Figure 1 shows the true image, the aberrated image and the defocused aberrated image, respectively.

The simulated images were manipulated in the IDL environment using both in-house programs and IDL programs. A test image was recorded onto a CCD camera by shining light through small apertures arranged in an approximate triplet pattern (figure 1a). This test image represents the “true” image, $I(x, y)$ introduced earlier. The image was degraded by numerically applying a phase screen described by the first seven terms of the Zernike expansion (figure 1b), yielding $I'(x, y)$. The defocused image, I'_d , was aberrated the same way but with an additional defocus term of 1 wave (figure 1c).

A program was applied to find the local minimum from equation 3. The resulting relationship between $\tilde{I}(u, v)$ and $\tilde{\zeta}(u, v)$ is given by,

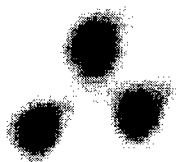
$$\tilde{I} = \frac{\tilde{I}\tilde{\zeta}^* + \tilde{I}_d\tilde{\zeta}_d^*}{|\tilde{\zeta}|^2 + |\tilde{\zeta}_d|^2}.$$

The above \tilde{I} represents the minimum error for a given OTF.

An initial guess of the OTF is used to begin the process of further minimization. This is achieved by setting the terms of the Zernike polynomial expansion of $\tilde{\zeta}(u, v)$ and finding the resulting E . The method of steepest descent was then used to find the combination of coefficients that yielded the minimum E . The resulting $\tilde{\zeta}(u, v)$ represents the recovered OTF.

With the recovered OTF and recorded image, $I'(x, y)$, in hand, the “true” image, $I(x, y)$ was recovered through a deconvolution (using equation 1). The recovered image is shown in figure 1d. Note that the true image and the recovered image are indistinguishable from each other.

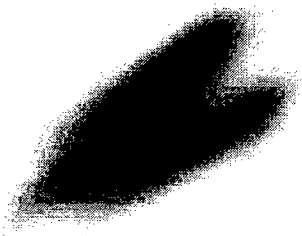
The main purpose of the simulation was to demonstrate that phase diversity works in principle. In recovering the image we have also demonstrated the robustness of the image recovery software and shown it to be accurate. What the simulation cannot tell us is how well this method works in practise. Finite detector noise and the time-varying aberrations of the atmosphere are two factors which cause deviations from the ideal case represented by the simulations. We therefore put together a laboratory experiment to test the feasibility of the phase diversity technique under “real-life” conditions.



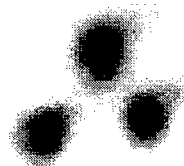
(a)



(c)



(b)

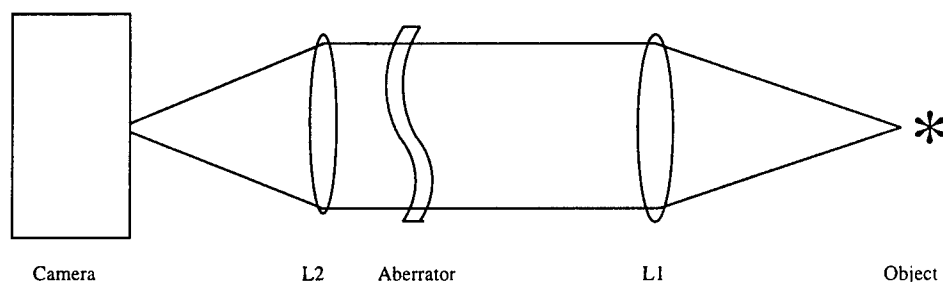


(d)

Figure 1: (a) The true image, taken before the introduction of aberrations. (b) The same image after aberrations are imposed. (c) The same image as (b) with defocus added. (d) The recovered image.

4 Experimental Setup

In order to test the above ideas, we proposed to set up a phase diversity camera and perform experiments aimed at recovering high-resolution images (see figure below). The basic setup was conceived last summer as part of the summer faculty research program but there was no time to carry out the experiment. We are therefore applying for a SREP in order to complete the experiment and to expand the scope of our phase diversity analysis. We begin with a brief description of the experimental setup, followed by a discussion of the specific steps needed to successfully complete an expanded analysis of phase diversity.



A system of lenses on an optical bench is used to focus images through the entrance pupil of the phase diversity camera. The camera was constructed by Lexitec Inc. A schematic of the camera is shown in figure 2.

In order to simulate astronomical observations, we use a re-imaging setup whereby all focused images appear as if they are at infinity relative to the camera. This is achieved by placing the object to be imaged at the focal point of the collimating lens, L1. An aberrator, consisting of a transparent plastic film is placed near the second converging lens, L2. In doing so we mimic the atmosphere as being a relatively local aberrator relative to the distant source of light such as a geostationary satellite or an astronomical object. With this experimental setup we propose to initiate a stepped approach toward the ultimate goal of recovering images of satellites and astronomical objects. The individual steps toward that goal are outlined in the next section.

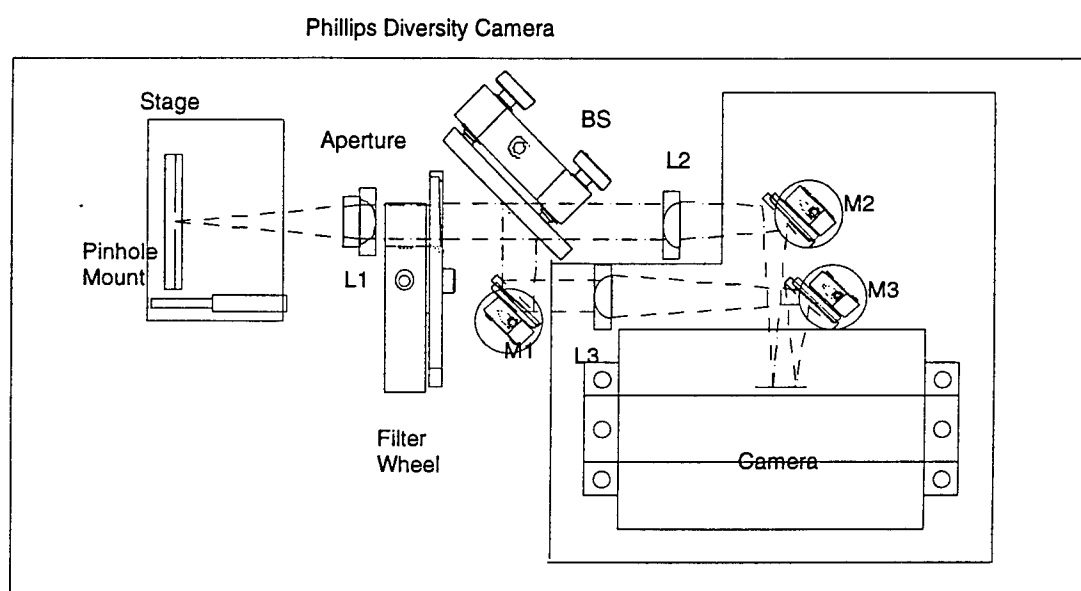


Figure 2: A schematic diagram of the phase diversity camera used in the experimental setup.

5 Future Work

5.1 Stationary Aberrations

The first element of a future, expanded analysis will be the implementation of the above experimental setup. The use of stationary aberrators will be used to determine the effectiveness of the phase diversity technique in recovering images of known morphology. This will be achieved through the experimental setup shown above, where collimated light from a known image will be passed through an aberrator before being focused onto the phase diversity camera. The recorded focused and defocused images contain phase errors imposed by the aberrator, which can be considered as a stationary phase screen. By varying the light level of the received signal and by varying the spectrum of aberrations the limitations of the phase diversity method can be explored.

5.2 Time Varying Aberrations

If, as the simulations suggest, the phase diversity technique proves successful in removing static aberrations from an image, the next step is to introduce time-varying aberrations into the imaging system to better replicate the turbulent nature of the earth's atmosphere. The atmosphere can also be thought of as a phase screen but one which changes its character on time scales of $\tau_0 \approx 1 - 100 \text{ ms}$. The phase diversity technique is therefore expected to work on images recorded over time scales shorter than the coherence time of the atmosphere. Time varying aberrations can be produced in the lab by using rotating pieces of aberrated glass or by generating turbulent motion of air with a localized heat source. The ultimate success of the image recovery will depend on two competing effects, the integration time, τ , used to record the signal, and the coherence time, τ_0 , of the aberrations. The former builds up the signal to levels needed for the phase diversity technique to operate optimally. The integration time is a critical parameter in observations of faint sources such as earth-orbit satellites and distant astronomical objects. Under those conditions, even observations with ideal noise-free detectors are subject to photon-statistical noise (referred to as shot noise or Poisson noise). Thus, it is desirable to use as large a τ as possible, in situations where the light level is low but at the same time, $\tau < \tau_0$ is the necessary requirement for optimal use of the phase diversity technique. For $\tau \gg \tau_0$, the phase diversity

technique fails. There is therefore a grey area, defined by $\tau \approx \tau_0$, where the phase diversity technique does not work optimally but may nevertheless provide significant corrections to the aberrations. It is therefore necessary to fully explore and document this regime because of its relevance to image recovery at low light levels.

5.3 Comparison of Post-Processing Techniques

In order to test the post-processing element of the phase diversity technique it is necessary to recover images using both the Gonsalves Error Metric approach (described in section 2.1) as well as the Transport approach (described in section 2.2). By using the two techniques under identical experimental conditions it is possible to compare them and determine their relative robustness.

5.4 Celestial Observations

Once the phase diversity technique is fully explored in the lab, observations of celestial objects can be undertaken. At the low light levels afforded by such objects it will be necessary to access a research-class astronomical telescope. The PI has access to a 0.61 meter telescope at the Capilla Peak Observatory. This observatory is operated by the University of New Mexico and is located at a dark high-altitude site, 9300 feet above sea level. Our long-term goal is to attach the phase diversity camera to the telescope and repeat the above analyses, this time with the Earth's atmosphere as the aberrator.

6 References

Gonsalves, R.A. and Childlow, R. 1979, SPIE, 207, 32.

Gonsalves, R.A. 1982, *Optical Engineering*, 829, 21.

Restaino, S. 1992, Appl. Opt. 31, 7442.

THEORY OF PROTONS IN BURIED OXIDES

**A. H. Edwards
Associate Professor
Department of Electrical Engineering**

**University of North Carolina at Charlotte
Charlotte, NC 28223**

**Final Report for:
Summer Research Program
Phillips Laboratory**

**Sponsored by:
Air Force Office of Scientific Research
Bolling Air Force Base, Washington, DC**

And

Phillips Laboratory

August, 1997

THEORY OF PROTONS IN BURIED OXIDES

Arthur H. Edwards
Associate Professor
University of North Carolina at Charlotte
Department of Electrical Engineering

Abstract

We have developed a model for electron capture at protons in α -SiO₂ under U-V illumination. The electrons are excited from the valence band to the gap level of the proton. The previously observed temperature dependence can result from competition between hydrogen motion away from the defect site and radiative recombination that would leave the proton as it was. At low temperature we argue that the latter dominates. At elevated temperatures, the system is vibrationally excited which leads to greater probability of hydrogen motion. This model not only explains previous observations, it predicts new results that can be readily tested experimentally. This model is buttressed by *ab initio* molecular orbital calculations and by a finite element analysis of vibrational spectra. Using the vibrational wave functions, we have completed a vibronic model for electron capture, including calculation of vibrational probability factors. This model is a work in progress. In an accompanying proposal we discuss our plans for completion of this work.

Theory of protons in buried oxides

Arthur H. Edwards

1 Introduction

Silicon on insulator (SOI) technologies have many important advantages, including large resistance to single event upset [1], absence of latch-up [1] and potential for dramatic decrease in scale of devices using current lithographic techniques [2]. SOI technologies include Separation by Implantation of Oxygen (SIMOX) and bond and etch-back SOI (BESOI), with SIMOX currently showing the greater promise. However, several studies have shown that all buried oxides have large densities of hole and electron traps [3]. In some technologies, there is evidence for silicon islands. These can be reduced by supplemental implants, but it is thought that very small silicon clusters (as small as two silicon atoms—a dimer) are left, and these can trap charge. Recently, Vanheusden and Stesmans showed that by annealing buried oxide structures in forming gas at elevated temperature and then cooling rapidly, they could produce large quantities of positive charge in the buried oxide. [4] Vanheusden *et al.* later showed that this charge was mobile: it could be moved back and forth across the oxide and that it was not annihilated at either Si-SiO₂ interface [5]. Through deuterium studies they have shown that the positive charge is associated with hydrogen [6]. For the balance of this section, we will refer to this positive charge as protons, even though this name is not really precise. There are several surprising features of this physical system that warrant study. First, the generation of positive charge by simply annealing in forming gas is remarkable. Currently, the mechanism is not understood. Second, the stability of the proton at the Si-SiO₂ interface is at apparent odds with the prevailing model of long-term build-up of interface states [7], in which an electrons tunnel from the silicon substrate and neutralize protons at room temperature. A third surprising observation is that electrons generated using 5.5 eV light are captured by protons through a temperature-activated process. We chose to study the last phenomenon as it seems completely counterintuitive for an attractive coulombic interaction. Furthermore, understanding this mechanism should lead to greater microscopic understanding of this technologically important defect.

2 Model for activated electron capture at protons

We show in Figs. 1 and 2 the principal results on electron capture [8]. The experiment consisted in shining 5.5 eV light on an exposed SIMOX layer. That is, a SIMOX layer that had been annealed in

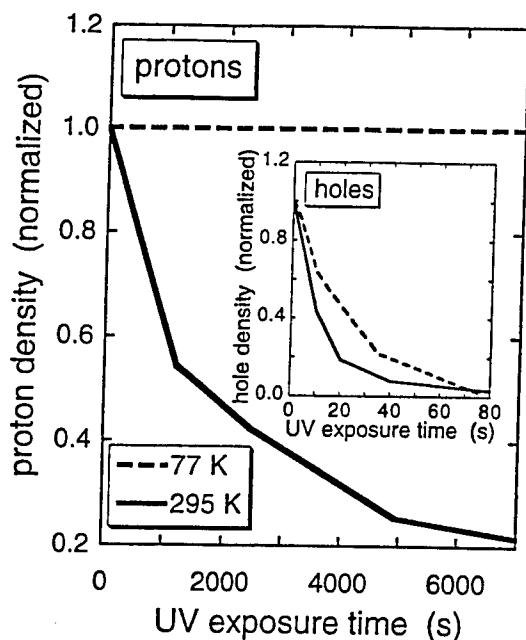


Figure 1: Results of isothermal illumination of protonated buried oxides. After Ref. [8]

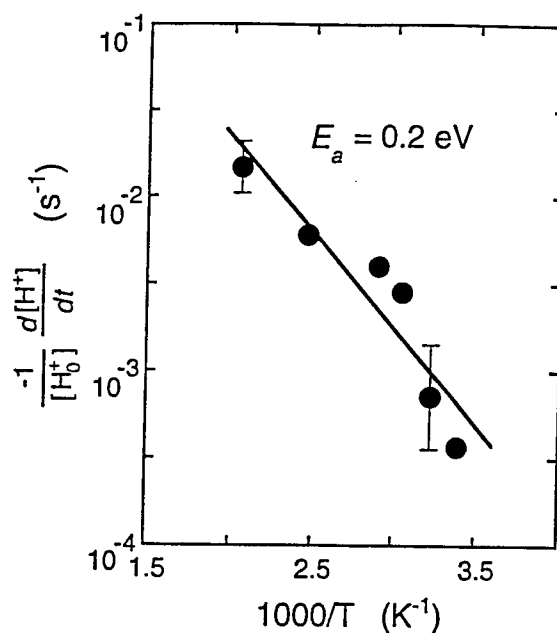


Figure 2: Arrhenius plot of the normalized initial rate of electron trapping at H⁺ sites in SiO₂ After Ref. [8]

forming gas was then exposed by removing the top layer of silicon. This system is then exposed to 5.5 eV light at fixed temperatures between 77K and 550 K. At the end of each isothermal illumination, the sample temperature was allowed to equilibrate rapidly to room temperature, at which point a mercury probe was used to measure a 1 MHz C-V curve. The hysteresis of this curve indicated motion of mobile charge (the direction of motion as a function of bias indicates the sign of the mobile charge). The magnitude of the shift is directly related to the areal density of the protons. If the illumination occurs at 77 K then there is approximately no change in the number of mobile protons, while at 295 K (room temperature) protons capture electrons at a rather modest rate. Fig. 2 shows that this process is thermally activated. With a limited data set, Vanheusden *et al.* obtained an approximate activation energy of 0.26 eV. This is a remarkable result considering that normal coulombic capture cross sections are 10^{-12} , which would predict rapid, athermal electron capture. We believe that this activation is the result of the method of generating the electrons. In the case of annihilation of trapped holes by UV light, Devine argued that the electrons were excited out of the SiO₂ valence band [9]. If the same mechanism applies here, we suggest that the observed activation arises because the optical activation energy (from the top of the SiO₂ valence band to the proton defect state) is very close to the UV photon energy (5.5 eV). To understand this, consider Figs. 3 and 4. These figures are configuration coordinate (CC) diagrams and deserve a general discussion.

The Hamiltonian for a many atom system (either a molecule or a solid) can be written

$$H_{tot} = H_{el} + H_{latt} + H_{el-latt} \quad (1)$$

where

$$H_{latt} = \sum_{\alpha=1}^{N_{atoms}} \frac{\hbar^2}{2M_{\alpha}} \nabla_{\alpha}^2 \quad (2)$$

$$H_{el} + H_{el-latt} = \sum_{i=1}^{n_e} \frac{\hbar^2}{2m_e} \nabla_i^2 - \sum_{\alpha=1}^{N_{atoms}} \frac{e^2 Z_{\alpha}}{|\vec{R}_{\alpha} - \vec{r}_i|} + \frac{1}{2} \sum_{\alpha, \beta=1}^{N_{atoms}} \frac{e^2 Z_{\alpha} Z_{\beta}}{|\vec{R}_{\alpha} - \vec{R}_{\beta}|} \quad (3)$$

Here, Greek subscripts refer to nuclear coordinates, Roman refer to electronic coordinates, n_e is the number of electrons, N_{atoms} is the number of atoms, $\{\vec{R}_{\alpha}\}$ is the set of all nuclear coordinates, and $\{\vec{r}_i\}$ is the set of all electronic coordinates. It is customary to consider $H_{el} + H_{el-latt}$ to be the electronic Hamiltonian, H_e . The total system wave function is assumed to have the form

$$\Psi_{tot}(\{\vec{r}_i\}, \{\vec{R}_{\alpha}\}) = \chi(\{\vec{R}_{\alpha}\}) \psi(\{\vec{r}_i\} : \{\vec{R}_{\alpha}\}) \quad (4)$$

where $\psi(\{\vec{r}_i\} : \{\vec{R}_{\alpha}\})$ is the wave function describing the electronic system, and is an eigenstate of H_e

$$H_e \psi(\{\vec{r}_i\} : \{\vec{R}_{\alpha}\}) = E_{tot}(\{\vec{R}_{\alpha}\}) \psi(\{\vec{r}_i\} : \{\vec{R}_{\alpha}\}). \quad (5)$$

The colon indicates that the set of nuclear coordinates, $\{\vec{R}_{\alpha}\}$, is held fixed to calculate $\psi(\{\vec{r}_i\} : \{\vec{R}_{\alpha}\})$. $E_{tot}(\{\vec{R}_{\alpha}\})$ is usually called the total energy of the system. This is only true in a semiclassical picture where the electrons are treated quantum mechanically and the lattice is treated classically. In the full Born-Oppenheimer theory, where the lattice is also treated quantum mechanically, $\chi(\{\vec{R}_{\alpha}\})$ is the wave function describing the nuclear or network motion and is an eigen state of the following Schrödinger equation

$$[H_{latt} + E_{tot}(\{\vec{R}_{\alpha}\})] \chi(\{\vec{R}_{\alpha}\}) = E_{vibronic} \chi(\{\vec{R}_{\alpha}\}) \quad (6)$$

Now, $E_{vibronic}$ is the true total energy. Note that $E_{tot}(\{\vec{R}_{\alpha}\})$ now acts as a potential energy for $\chi(\{\vec{R}_{\alpha}\})$. To calculate dipole matrix elements, we must evaluate

$$\langle \chi_i \psi_i | \vec{r} | \chi_f \psi_f \rangle = \langle \chi_i | \chi_f \rangle \langle \psi_i | \vec{r} | \psi_f \rangle \quad (7)$$

so that the overlap of vibrational wave functions will be as important as the electronic matrix element in determining the strength of an optical transition. This, of course, is the origin of Frank-Condon transitions.

In applying B-O theory, one usually simplifies dramatically the potential surface considered. In the problem at hand we consider only the motion of the central hydrogen. As we will show below, this is a reasonable assumption for the current system. Furthermore, we consider only one vibrational mode at a time allowing us to draw one-dimensional potential surfaces. The pertinent CC would be the stretch mode along the central OH bond direction. When multiple potential surfaces appear on the same CC diagram, we must be careful that each represents the system with the same number of electrons. The bottom curve in both figures 3 and 4 corresponds to a full valence band, an empty conduction band and a hole on the OH group. In short, the ground state of the system with one proton. The top curve corresponds to a hole in the valence band, an electron in the conduction band and a hole on the OH group. The vertical distance between the bottom and top curves must be the SiO₂ band gap. The middle curve corresponds to a hole in the valence band, an empty conduction band and a neutral OH group. Note that this is a repulsive potential curve. Thus, the bottom and top curves will give rise to true vibrational states, while the center curve will give vibrational wave functions that are free-particle-like. Furthermore, the energy spectrum along the center curve will be continuous.

In the first case, shown in Fig. 3, the photon energy is just below the Frank-Condon transition energy. At low temperatures, only the ground vibrational state is occupied, so the transition probability will be very small (small $|\langle \chi_i | \chi_f \rangle|^2$). At elevated temperatures, the excited vibrational states will be occupied. The most obvious effect is that the optical transition energy is smaller by a vibrational quantum, $\hbar\omega$. What may be more important is that excited vibrational states have maxima closer to the classical turning points. This can alter transition probabilities by altering $\langle \chi_i | \chi_f \rangle$ so that transitions to states lower and higher on the center potential surface are stronger. Because of the slope of this potential surface, the small change in energy ($\Delta E = \hbar\omega$) for the initial state can lead to a large decrease in energy of the final state, and hence to a larger change in the net excitation energy. Thus an increase in temperature could, as Fig. 3 indicates, lead to optical absorption and, hence to detachment, where none would be possible at low temperature.

Another related possibility is shown in Fig. 4. The Frank-Condon transition energy may be smaller than, but very close to, 5.5 eV. If an optical transition occurs in the ground vibronic state, the Frank-Condon condition will hold, implying that the most probable value for Q is indicated by the solid vertical arrow. In the excited state, at this point the kinetic energy of the hydrogen will be nearly zero. Also, the most probable value for momentum will be zero. Thus, if dissociation is to take place, the hydrogen must accelerate from nearly zero velocity. After optical absorption, it will clearly spend a finite amount of time in the vicinity of the defect. If this residence time is longer than the time scale for optical de-excitation, the hydrogen atom could lose its electron to

the valence band. In short, excitation could be followed rapidly enough by de-excitation so that the proton would be stable. At elevated temperatures, again, excited vibrational states would be occupied. Excitations from these states would again displace the most probable position of the hydrogen atom away from the adiabatic equilibrium, toward the turning points. This could lead to excitations as shown by the dashed vertical arrow in Fig. 4. At that point, the hydrogen atom would have additional kinetic energy. This could decrease considerably the residence time and make dissociation more probable relative to de-excitation.

We have so far offered only possibilities for a model. To make this model viable, we need to perform a variety of calculations. First, we need reliable potential surfaces to calculate vibrational energies and wave functions and, hence vibrational probability factors. We can also perform some classical calculations to estimate the residence time for different initial values of kinetic energy. Through calculating potential surfaces, we will obtain electronic wave functions and, hence, electronic optical matrix elements. To obtain reliable excitation energies, we will have to include electron correlation effects. It will turn out that straightforward configuration interaction will facilitate calculation of optical matrix elements. We report our results in Sect. 5. We discuss the experimental implications in Sect. 6. In Sect. 7 we discuss briefly our future plans.

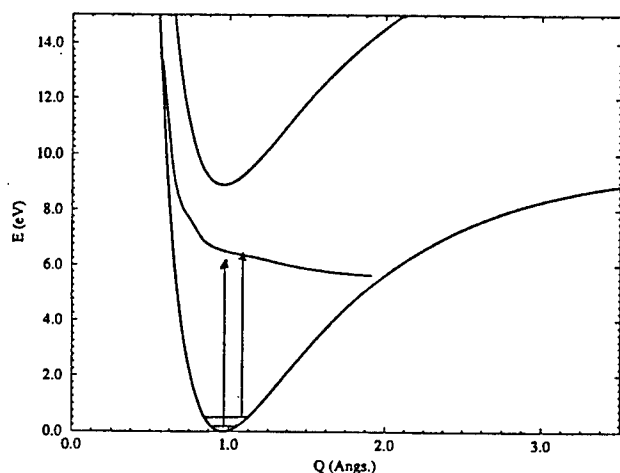


Figure 3: Model for temperature activated electron capture: Case 1.

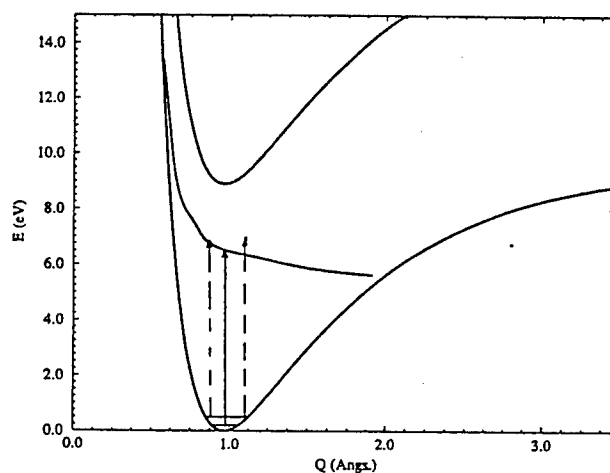


Figure 4: Model for temperature activated electron capture: Case 2.

3 Previous Theory

Several groups have studied protons in SiO₂. The earliest calculation was by Edwards *et al.* on the cluster shown in Fig. 5 [10]. Using a 6-31G** basis and second order perturbative Configuration Interaction (MP2), they performed a constrained optimization allowing the two silicon atoms and the central OH group to search for a minimum energy configuration subject to C_{2v} symmetry. They also calculated the binding energy, assuming that the reactants are the self-trapped hole and a neutral hydrogen atom, to be 1.2 eV. The geometrical parameters are given in Table 1. Note that in the

Table 1: Equilibrium geometry from previous calculations

	R _{Si-O*} (Å)	R _{O*-H} (Å)	∠ Si-O*-Si(°)
Ref. [10]	1.81	0.96	137.0
Ref. [11]	1.617	0.941	174

Edwards calculation, there is a very large but highly localized network relaxation: the two silicon atoms move 0.2 Å away from the central OH group. The motion is roughly along the original Si-O bond direction. Edwards *et al.* also calculated the changes in total charge for the proton compared to the reference system- a neutral hydrogen atom and neutral Cluster I without the central hydrogen atom. Only 0.6 *e* was removed from the hydrogen atom. Thus, the identification as a proton is only approximate.

Ferreira and coworkers have also studied the same system using similar techniques and have obtained similar, though not identical, results for the equilibrium geometry [11]. This is due in part to a different basis, and in part to the method of optimization. In addition, they obtained potential surfaces for the cluster in the neutral and positive charge states, which we show in Fig. 6. In the positive charge state, the hydrogen atom (proton) seems to be much more strongly bound than the 1.2 eV prediction of Edwards. This is the result of requiring that the proton dissociate along the OH stretch direction, thus retaining the symmetry of the system and forbidding a change in symmetry of the electronic state. If a change of symmetry were allowed, the lowest energy state would correspond to a self-trapped hole, and a neutral hydrogen atom. The result for the neutral charge state, that the OH interaction was completely repulsive, is expected, and is at odds with the results of Edwards and Germain based on MINDO/3 calculations.[12]

Finally, Yokozawa and Miyamoto have performed local density calculations on H⁺, H⁰ and H⁻ in β-cristobalite [13]. Their results were in essential agreement with the results of Edwards *et al.*[10] and of Ferreira *et al.* [11]

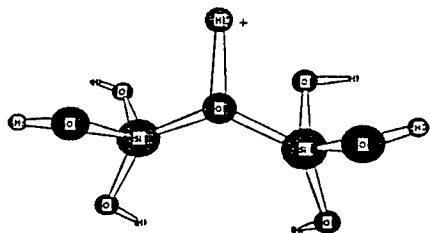


Figure 5: Cluster used in Refs. [10] and [11]

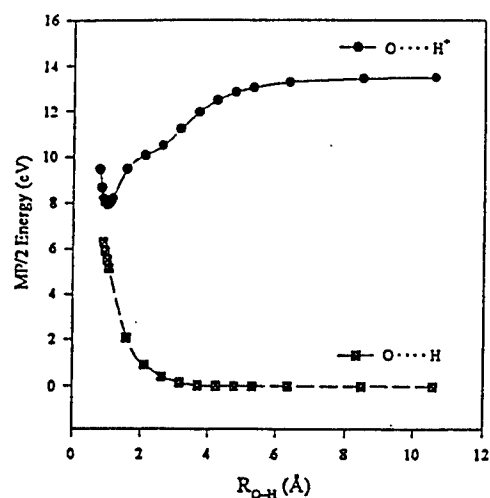


Figure 6: Potential surfaces obtained in Ref. [11]

4 Methods of Calculation

We used *GAMESS* [14], an *ab initio* molecular orbital program with the capability to calculate total energies, equilibrium geometries and Vibrational spectra in a variety of approximations. We applied this program to clusters shown in Fig. 7. In all cases the optimizations were constrained by keeping a set of the outer atoms fixed to simulate the reaction of the host solid. We used the following initial values to build the cluster and, hence, the constraining atomic cage: $R_{\text{Si-O}} = 1.61 \text{ \AA}$, $\angle \text{O-Si-O} = 109.47^\circ$, $\angle \text{Si-O-Si} = 144^\circ$. Note that clusters I and III have C_{2v} symmetry, while cluster II has C_1 (no) symmetry. In the former case, this places constraints on the dihedral angles we could use. In the latter case, we used a range to simulate the amorphous environment. In most of the calculations, we used the Stevens-Basch-Krauss (SBK) effective core potential (ECP) to reduce substantially the number of electrons in the system [15]. For the valence atomic states we used the basis associated with the SBK ECP. It turns out to be a 3-1 split valence set. We placed additional *d*-functions on all heavy atoms, and *p*-functions on the hydrogen atoms. We performed vibrational analyses in the positive charge state on all clusters, although for the larger clusters these were limited to one or two defect modes. For Cluster I, we used *GAMESS* to calculate the complete vibrational spectrum. For the cluster II, we used both the harmonic approximation and a finite element code applied to one-dimensional potential surfaces. In the latter case, we were able to evaluate the importance of

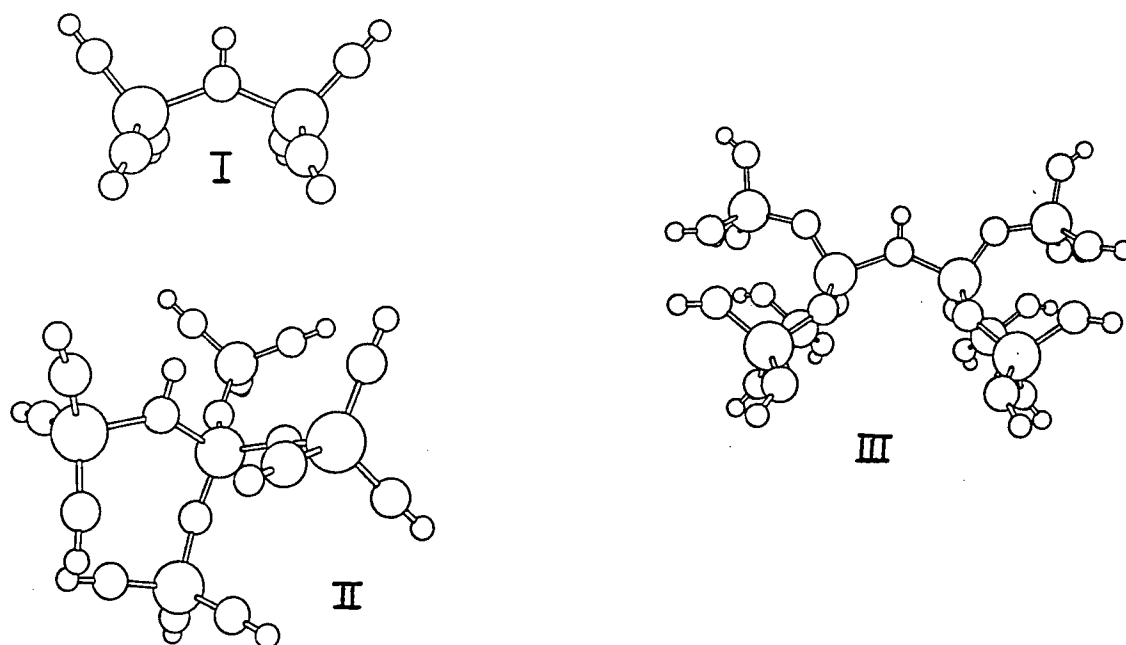


Figure 7: Clusters used in the current study

Table 2: Equilibrium Geometries for Clusters I, II, and III: SBK ECP and basis augmented with *p*- and *d*- functions.

	R_{Si-O^*}	$R_{O^*-H}(\text{\AA})$	$\angle Si-O^*-Si (^{\circ})$	
Cluster I	1.78	0.97	138.1	
Cluster I (MP2)	1.81	0.98	138.4	† average value
Cluster II	1.78†	0.96	140.0	
Cluster III	1.76	0.97	135.8	

anharmonic effects. We used several levels of configuration interaction to obtain optical excitation energies for the two smaller clusters.

5 Calculated results

5.1 Equilibrium geometries

In Table 2, we show the equilibrium geometries in the neutral charge state of all three clusters using the SBK ECP with the basis described in Sect. 4

For cluster II, the absence of symmetry means that the two Si-O* bonds need not be the same length. We would expect this because the geometrical constraints are more rigid for the outer Si-O*

Table 3: Changes in atomic charges for Clusters I, II, and III: SBK ECP and basis augmented with *p*- and *d*- functions. The two values are for Mulliken and (Löwdin) population analysis

	$\Delta Q_H (e)$	$\Delta Q_{O^*}(e)$
Cluster I	0.37 (0.30)	0.01 (0.11)
Cluster II	0.35 (0.28)	0.0 (0.15)
Cluster III	0.38 (0.31)	0.0 (0.17)

Table 4: Vibrational spectrum for the proton in SiO₂: Cluster I (all values in eV)

Mode	$\hbar\omega$	x_H	y_H	z_H
O-H stretch	0.338	0.0	0.0	0.94
in-plane rock	0.107	0.92	0.0	0.0
out-of-plane rock	0.108	0.0	0.96	0.0

bond. In this case the difference is 0.4 Å. Otherwise, the results are quite similar across clusters and compare well with the previous results using the 6-31G** basis. We show the differences of charge on each of the central atoms in Table 3. These differences were calculated by considering the isolated clusters in the neutral charge states without the extra hydrogen atom.

Even though this is called a proton, the calculated charges show clearly that the charge is delocalized significantly. In fact, the Löwdin population analysis indicates that the oxygen atom picks up more positive charge than the hydrogen atom. We should note, however, that charge assignments are somewhat arbitrary, and should only be used for qualitative arguments. In Fig. 9 we show the potential surfaces we obtained for H⁺ and H⁰ motion for clusters I and II. For all potential surfaces, the cluster is rigid; only R_{O-H} is altered. Note that for the H⁺ motion, the asymptotic state is a proton and a neutral Si₂O₇H₇ cluster, rather than the correct hydrogen atom and self-trapped hole. For our purposes, the calculation of the first three vibrational states, this will probably make no difference. (see Sect. 7.) For Cluster I, this result is in reasonable quantitative agreement with Ref. [11]. Our proton binding energy is actually larger by 3 eV. This is reduced dramatically in the MP2 approximation, leading to a surface that is very close to that of Ferreira *et al.* Furthermore, the surfaces for clusters I and II are almost identical. We obtain a better appreciation of this similarity from the vibrational analysis. In Table 4 we show the frequencies of the three principle proton vibrational modes involving the central hydrogen atom for cluster I. Because these were obtained from a full Hessian calculation, we obtained the components of the normal modes as well. These are also given in Table 4. Note the large components on the central hydrogen atom, justifying our claim that these are the principle proton modes. The most important

feature is that the out-of-plane O-H rock motion is a transition state for this cluster. That is to say, the C_{2v} minimum was really an unstable equilibrium. We have performed an optimization with no constraints and found the equilibrium configuration shown in Fig. 8. This is fundamentally different

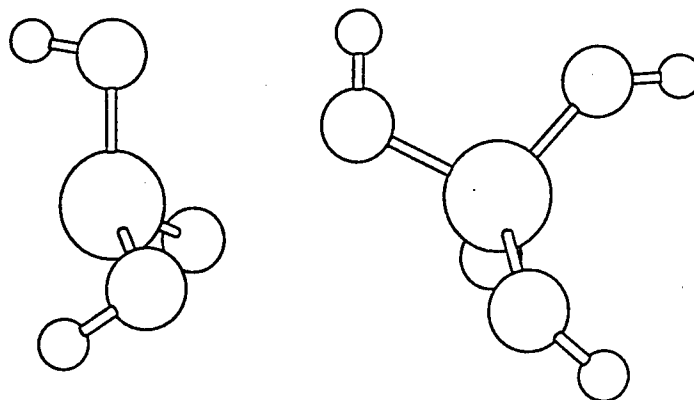


Figure 8: True minimum energy configuration for Cluster I

from the situation shown in Fig. 5. For the true equilibrium, the positive charge is primarily on the silicon atom. We have spent considerable effort verifying that this result is spurious. The best evidence comes from the calculations for Cluster II. Even though this cluster has C_1 symmetry, and the Si-O bondlengths are not equal, the electronic structure and geometry are qualitatively similar to the cases that include C_{2v} constraints. That is, the charge distribution is similar to the other two cases, there is no large silicon relaxation, and the proton lies in the Si-O-Si plane. Furthermore, we have calculated the out-of-plane rocking mode in the harmonic approximation for cluster II. While the frequency is small, it is real. (See Sect. 5.2) Thus, at the moment, we have fair confidence that the real equilibrium geometry for cluster I is spurious. However, full Hessian calculations under way will be definitive.

5.2 Vibrational analysis

In Table 5 we show the central OH stretching mode frequencies for cluster II in two different approximations. Case I is a parabolic fit to the potential surface for cluster II shown in Fig. 9. Case II is a complete finite element analysis of the same one-dimensional potential surface. In this case we used 400 linear elements, obtaining a precision of 0.1%. The vibrational frequencies are in good

Table 5: Vibrational spectrum for the proton in SiO₂: all values in eV

Cluster/aproximation	O-H stretch	in-plane rock	out-of-plane rock
Cluster I/harmonic	0.338	0.107	0.108 i
Cluster II/harmonic	0.34	—	0.02
Cluser II/finite element ($n=1$	0.34	—	—
$n=2$	0.31	—	—

agreement, indicating that the harmonic approximation is reasonable, although there is an observable anharmonicity. Also in this mode, the smaller and larger clusters give almost identical results. Note that the other two rocking frequencies are given in Table 5 for Cluster II in the harmonic

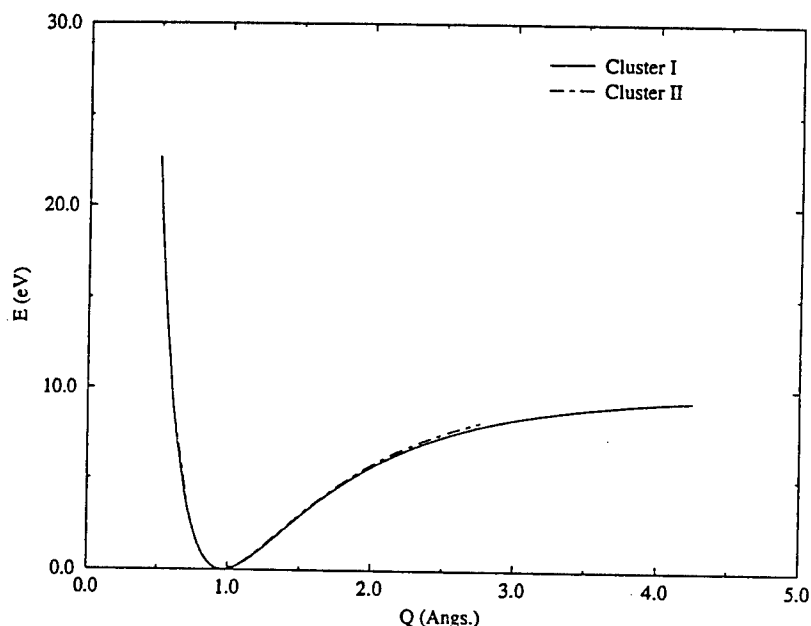


Figure 9: Potential surfaces for hydrogen motion along the OH direction

approximation. As mentioned above, the out-of-plane frequency is very small while the in-plane mode is intermediate.

To complete even a qualitative analysis of this problem, we need approximate excited vibrational states to calculate the appropriate vibrational overlaps. As we will discuss in Sect. 5.3, we only have single point estimates for the optical excitation energies. Here, we use a one-dimensional OH stretching mode potential surface from the neutral charge state of cluster II. Clearly, the over all shape will be very similar, so that the eigenfunctions will also be similar. It will be clear that the qualitative conclusions we draw will be independent of details. Because the curve is dissociative, we were required to use an infinite wall boundary condition at a large but arbitrary value of Q .

Having obtained these states, we performed the necessary overlap calculations, and show in Fig. 10 $10 | \langle \chi_i | \chi_f \rangle |^2$, the so-called Huang-Rhys factor [16], as a function of E_f for χ_i corresponding to the ground and first excited vibrational states. The results are illuminating. For the ground

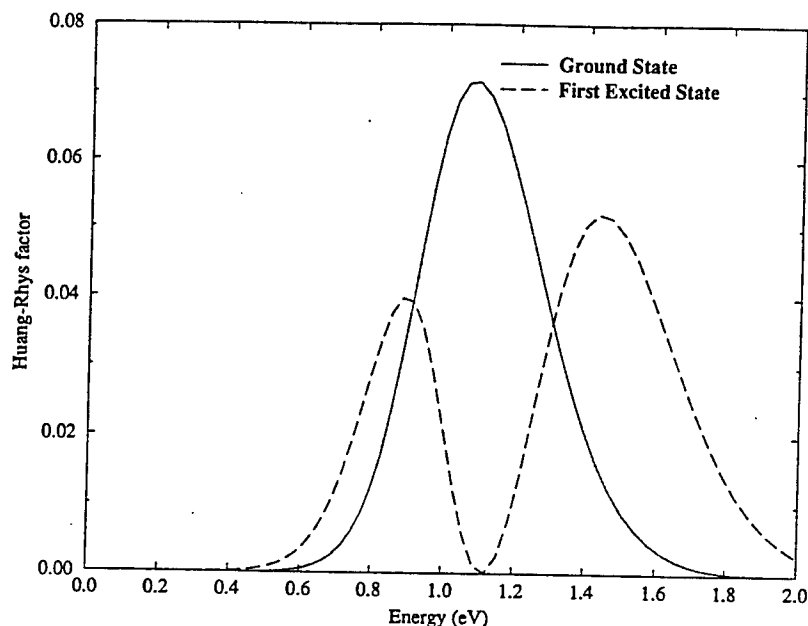


Figure 10: Huang-Rhys factors for transitions from the ground and first excited vibrational states of the Potential surfaces shown in Fig. 9

vibrational state, there is a single peak centered around the Frank-Condon transition, as expected. In the first excited state, there is a high and a low energy peak. To appreciate the significance of these two peaks, we show in Figs. 11 and 12 the initial and final vibrational states that give rise to them. We see that the overlap responsible for the low energy peak is with the first peak of the excited state, while for the high energy peak, the overlap is with the first two lobes. Here we have the two cases alluded to in Sect. 2. Recall that the photon energy required to reach the maximum probability transitions will be reduced by one vibrational quantum (in this case 0.34 eV). We see, then, that roughly the same energy photon will reach the high energy peak from the first excited vibrational initial state as will reach the Frank-Condon transition from the ground vibrational state. The difference is that in first excited vibrational state there will be higher probability of having a larger initial kinetic energy because the wave function of the initial state has larger spatial extent. We have been using a fairly classical picture of kinetic energy— the difference between the potential and total energies. We can also speak of dynamics in a classical picture. We can imagine starting the hydrogen at a given position with a given initial energy. We can then solve Newton's equations to follow time evolution of the position of the hydrogen atom. We have done this for a for Frank-

Condon-like transitions where we assume zero initial kinetic energy. Using the peak energies from Fig. 10 we found that starting the hydrogen atom at the classical turning point associated with the higher energy excited state peak decreased the residence time by a factor of 2. .

Our model predicts an activation energy of 0.34 eV, the first vibrational excitation. This is in fair agreement with the estimate given in Ref. [8]. Absent from this model is any mention of the

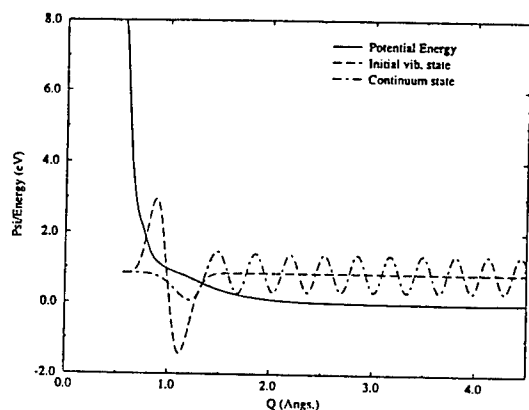


Figure 11: First excited state wave function and continuum wave function corresponding to low energy peak in fig. 10

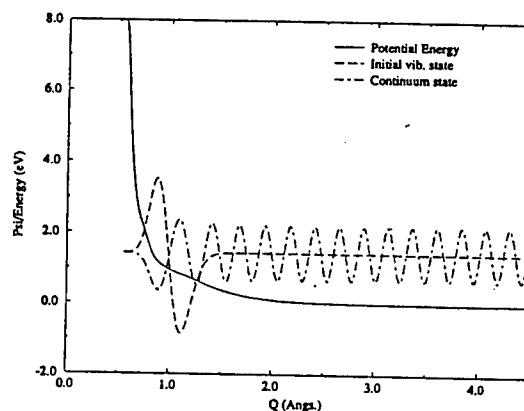


Figure 12: First excited state wave function and continuum wave function corresponding to high energy peak in fig. 10

rocking modes. Clearly, they will be occupied more readily and should be considered in a more detailed study. The difficulty is that we expect large amplitude vibrations that preclude the simple decoupled picture outlined here.

5.3 Optical Excitation

Optical excitation energies are consistently difficult to estimate accurately. We have performed excited state calculations for all of the clusters in a variety of approximations. We are again, looking for reasonable quantitative agreement. In Table 6 we summarize our current results.

Here, CIS 1 (2) is Configuration Interaction (CI) with all single excitations out of nine (one) initially doubly occupied state into a set of five (18) empty virtual states. These are actually the first and last in a series of CIS calculations in which we varied the number of initially doubly occupied

Table 6: Optical excitation energies for clusters I and II.

Cluster: Approximation	ΔE_{opt} (eV)
Cluster I: Triplet	12.06
Cluster I: CIS 1	13.16
Cluster I: CIS 2	12.57
Cluster II: Triplet	6.9
Cluster II: CIS	9.45
Cluster II: CISD	8.79

states and the number of available virtual states. Even in the case with many DOC's only the highest occupied molecular orbital (HOMO) had important contributions to the first excited state. On the other hand, eighteen virtual states led to a converged excited state energy. CISD is CI with all single and double excitations out of two DOC's and into eighteen virtual orbitals. All of these energies are significantly higher than the experimental value for $\hbar\omega$ 5.5 eV. There are two possible conclusions. First, we could assume that this speaks strongly against the model. Second, we could assume that the methods are too inaccurate. We note several obvious sources of error in this set of calculations. First, We are using a cluster to represent a solid. Several groups have shown that clusters can lead to excellent predictions of properties that are truly local to the defect [17,18,19]. These include lattice relaxations, spin densities, defect vibrational spectra, even transition energies. Furthermore, we would expect optical spectra to be fairly well represented if the initial and final states are strongly localized. However, for transitions involving nominally delocalized states, we might expect that the accuracy would be diminished. We should point out that there are calculations in the literature that obtain remarkably good band structure using clusters for both insulators [20] and semiconductors [21]. Second, there are questions about the quality of our basis set, and of the method of CI. Pacchioni *et al.* have presented a variety of optical energies for defects in SiO₂ that agree well with experiment [20,22]. Clearly these problems may be coupled. We intend to study this problem using the new periodic boundary condition code under development.

6 Discussion and Experimental Predictions

To summarize, we have investigated most of the important facets of the model presented in Sect. 2. The most compelling results are the harmonic analysis. They demonstrate that if the excitation energy is close to the photon energy, vibrational excitation can alter significantly the probability of hydrogen release. The results are fairly general. All dissociative curves have the same shape. Thus

the effects will differ quantitatively but not qualitatively. This quantitative difference could, of course be so large as to preclude practical observation of temperature activated capture. If, for example the ground state minimum were coincident with the flat section of the dissociative curve, then promotion to an excited vibrational state could have very little effect because there would be no state close to the excitation energy with significant vibrational overlap. We have performed deuterium studies with inconclusive results. We would predict small increases in activation energies, but no dramatic effects. However, we can make several experimental predictions that can be investigated immediately. First, any technique for introducing electrons into the SiO_2 conduction band should lead to proton annihilation at any temperature. A straightforward experiment would be avalanche electron injection. Second, we recommend a spectroscopic study of the excitation energy, as this could delineate between the kinetic and the energetic mechanism. If the photon energy is close to, but smaller than, the Frank-Condon transition energy, E_{F-C} , an increase in $\hbar\omega$ could well lead to an increase in low temperature proton annihilation. However, if the kinetic argument holds, and $\hbar\omega \approx E_{F-C}$, then increasing $\hbar\omega$ could have a variety of effects. One should be able to map the vibrational probability as a function of energy for the excited vibrational state.

7 Future extensions

In Sect. 1, we outlined several interesting problems in the protonated buried oxide system. We have reported here the progress made on one of them. Our future plans can be segregated into plans for completing the analysis of this model, and plans to study other interesting problems.

7.1 Electron capture: future studies

We have put forward and studied a model for electron capture under 5.5 eV light that relies on knowing both the vibrational spectrum and wave functions and the electronic spectrum to within 0.5 eV. We have finished the vibrational analysis for the case of an accurate positive charge state potential, and a model excited state potential—that for the neutral charge state. We plan to complete a careful study of the excited state going beyond the standard CI method to include multi-configuration SCF (MCSCF) calculations with a variety of sets of basis functions. To date, the best optical calculations from clusters are from Pacchioni and coworkers [20,22]. This group has used multi-reference singles and doubles CI (MRDCI). Part of our work will be to assess the need for such methods by repeating some of the Pacchioni calculations with MCSCF. When we are satisfied that we understand the calculational requirements for this system, we will obtain a complete excited

state potential surface. This, of course will be crucial for testing the model theoretically. If we obtain reliable excitation energies that disagree with the experimental values, we will be forced to abandon the cluster model. If the calculated energies are close to the experimental values, then we plan a careful calculation of the electronic part of the optical transition probability using the results from the CI calculations. We will be especially interested in the effect of hydrogen motion on the electronic transition strength. It may turn out that rocking motion will be especially important.

Another, possibly important, piece of this study will be the effect of local strain on the calculated potential surfaces. For many years Revesz has contended that local compressive strain should lead to higher reactivity. We will study clusters that have built in strain.

All of the work involving finite clusters should be finished over the five months. At the same time, we will be developing our periodic boundary condition-code to eliminate the effects of cluster termination. When this is available, we will use it on an α -quartz model of the proton problem. These calculations should lead to some definitive statements about the utility of our model.

7.2 Other proton-related problems

There are three very interesting and related problems we would like to pursue. We would like to understand the mechanism that transforms molecular hydrogen to protons in buried oxides. Specifically, we would like to study the possible cracking sites that would lead from H_2 to either H^0 or directly to the proton species. In the SERP, I will outline in detail, our ideas for these calculations. We also want to understand why this positively charged species is so stable. We are especially interested in why, in buried oxides, the proton does not acquire an electron from the substrate. Again, in the SERP, I will outline in detail our plans. Finally, Vanhuesden has shown recently that the formation of protons is very sensitive to the rate of cooling after the 600° anneal in forming gas. This last observation may well tie together the previous two questions. That is, the physics of proton formation and of proton stability will dictate the rate of annihilation as a function of cooling rate.

Acknowledgments

The author thanks Dr. K. Vanheusden for extremely useful discussions of the experiments prior to publication. He also thanks Dr. S. P. Karna and Profs. H. Kurtze, B. Kirtman, and W. B. Fowler for valuable comments and critiques during the course of this work. He gratefully acknowledges the support of Phillips Laboratory VT/MR branch, especially of Drs. Walter Shedd, R. Pugh and B. K. Singaraju, during his tenure as an AFOSR Summer Fellow. Finally, he acknowledges the use of the

computational resources at the Albuquerque Resource Center for many of the calculations presented herein.

REFERENCES

1. G. E. Davis, H. R. Hite, T. G. W. Blake, C. E. Chen, and H. W. Lam, IEEE Trans. Nuc. Sci. **NS-32**, 4432 (1985).
2. J. P. Colinge, Electron. Lett. **22**, 187 (1985).
3. R. E. Stahlbush, G. J. Campisi, J. B. McKitterick, W. P. Maszara, P. Roitman, and G. A. Brown, IEEE Trans. Nucl. Sci. **NS-39**, 2086 (1992).
4. K. Vanheusden, and A. Stesmans, Appl. Phys. Lett. **64**, 2575 (1994).
5. K. Vanheusden, W. L. Warren, R. A. B. Devine, D. M. Fleetwood, J. R. Schwank, M. R. Shaneyfelt, P. S. Winokur, and Z. J. Lemnios, Nature **386**, 587 (1997).
6. K. Vanheusden, W. L. Warren, and R. A. B. Devine, J. Non-Cryst. Solids **216**, 116 (1997).
7. D. L. Griscom, D. B. Brown, and N. S. Saks, in *The Physics and Chemistry of SiO₂ and the Si-SiO₂ Interface*, edited by C. R. Helms, and B. E. Deal, (Plenum, New York, 1988), p. 287.
8. K. Vanheusden, W. L. Warren, D. W. Fleetwood, S. P. Karna, A. M. Ferreira, R. D. Pugh, C. P. Brothers, B. K. Singaraju, R. A. B. Devine, and A. H. Edwards, Appl. Phys. *submitted*.
9. R. A. B. Devine, Private communication.
10. A. H. Edwards, J. A. Pickard, R. E. Stahlbush, J. Non-Cryst. Solids **179**, 148 (1994).
11. A. M. Ferreira, S. P. Karna, C. P. Brothers, R. D. Pugh, B. K. Singaraju, K. Vanheusden, W. L. Warren, and R. A. B. Devine, in *Amorphous and Crystalline Insulating Thin Films*, edited by W. L. Warren, R. A. B. Devine, M. Matsumura, S. Cristoloveanu, Y. Homma, and J. Kanicki, (Materials Research Society, Pittsburgh, 1997), p. 187.
12. A. H. Edwards, and G. Germann, Nucl. Instr. and Meth. in Phys. Res. **B 32**, 238 (1988).
13. A. Yokozawa, and Y. Miyamoto, Phys. Rev. B **55**, 13783 (1997).
14. M. W. Schmidt, K. K. Baldridge, J. A. Boatz, S. T. Elbert, M. S. Gordon, J. H. Jensen, S. Koseki, N. Natsunaga, K. A. Nguyen, S. J. Su, T. L. Windus, M. Dupuis, and J. A. Montgomery, J. Comput. Chem. **14**, 1347 (1993).
15. W. J. Stevens, H. Basch, and M. Krauss, J. Chem. Phys. **81**, 6026 (1984).
16. K. Huang, and A. Rhys, Proc. R. Soc. London Ser. **A 204**, 406 (1950).
17. A. H. Edwards, Phys. Rev. **B36**, 9638 (1987).
18. M. Cook, and C. T. White, Phys. Rev. Lett. **59**, 1741 (1987).
19. K. C. Snyder, and W. B. Fowler, Phys. Rev. **B48**, 13238 (1993).
20. G. Pacchioni, and G. Ierano, Phys. Rev. Lett. *in press* (1997).

21. A. Lizon-Nordstrom, and F. Yndurain, Solid State Commun. **94**, 335 (1995).
22. G. Pacchioni, and G. Ierano, Phys. Rev. **B56**, 1 (1997).

MODELING THE MAGNETOSPHERIC MAGNETIC FIELD

**Gary M. Erickson
Associate Professor
Center of Space Physics**

**Boston University
725 Commonwealth Avenue
Boston, MA 02215**

**Final Report for:
Summer Research Program
Phillips Laboratory**

**Sponsored by:
Air Force Office of Scientific Research
Bolling Air Force Base, Washington, DC**

And

Phillips Laboratory

August, 1997

MODELING THE MAGNETOSPHERIC MAGNETIC FIELD

Gary M. Erickson
Research Assistant Professor
Center for Space Physics
Boston University

Abstract

Following the formalism developed by Heinemann and colleagues, development of a numerical method for obtaining the three-dimensional, equilibrium, magnetospheric magnetic field has begun. Expressing the distributed currents of the magnetospheric plasma in terms of an effective magnetization M_{eff} , the magnetic scalar potential ψ is found as a solution of Poisson's equation. The magnetic field is $\mathbf{B} = \mu_0 (-\nabla\psi + \mathbf{M}_{eff})$ in MKS units, just as in an ordinary diamagnetic material. In this first stage of development, numerical solutions have been found in a closed rectangular geometry, with symmetry about the equatorial and noon-midnight meridian planes, and isotropic pressure with an assumed distribution in the equatorial plane.

MODELING THE MAGNETOSPHERIC MAGNETIC FIELD

Gary M. Erickson

Motivation

In support of spacecraft operations the Air Force has a long-term commitment to understand the near-Earth space environment. Energetic particles, both those trapped and energized within the magnetosphere and those arriving from the sun, have deleterious effects on space operations. Electron precipitation and Joule heating increases ionospheric densities and temperatures, which can interfere with radar, communications, and can result in increased drag on low-altitude spacecraft. Understanding the coupling between the solar wind, magnetosphere, and ionosphere is crucial if the time evolution of the near-Earth natural environment is to be specified or predicted.

There are two basic, complementary approaches to physics-based modeling of the near-Earth space environment: global MHD and regional-modular. Global MHD is very good at obtaining the global topology resulting from the flow of solar wind past Earth's magnetosphere. It can follow highly time-dependent (including shock propagation) evolution of the magnetosphere, whereas a regional-modular approach does not. However, MHD does not resolve boundary layers, the codes are diffusive, and simulations will wander rapidly away from reality during a simulation. Tuning is a difficult problem and data assimilation may be an unsolvable problem for MHD models.

For space weather operations the advantages of a regional-modular approach are in computational speed at higher spatial resolution, the ability to fine-tune the model to specific conditions, and, especially, data assimilation. For basic research the regional-modular approach complements global MHD by permitting higher resolution, incorporation of realistic boundary layers, and control of parameters external to the issue of investigation.

The central criticism of the regional-modular approach has concerned the "spine" or computational backbone; specifically, how does one get the various, often disparate, regional models to talk to each other? Heinemann and colleagues [*Heinemann and Pontius, 1990*,

1991; *Heinemann et al.*, 1994; *Heinemann and Erickson*, 1997] have derived expressions for the “effective magnetization” of the magnetospheric plasma, permitting solution for the global magnetospheric magnetic field from Ampere’s law using the magnetic scalar potential. Using this formulation, cross-module communication within the regional-modular approach is greatly simplified. The difficulty is that the effective magnetization depends explicitly on the magnetic field. An iterative, numerical approach is required to find the magnetospheric magnetic field and currents.

Development of a numerical method, based on the “effective magnetization” formulation, to obtain the three-dimensional, equilibrium, magnetospheric magnetic field has begun. In this first phase of development, solutions have been obtained in a rectangular, magnetospheric geometry. Vacuum solutions were obtained for various strengths of the normal component of the magnetic field through the tailward boundary of the modeling region. For non-zero normal component, these solutions contain a magnetic neutral line within the magnetotail. Non-vacuum solutions were obtained for zero normal component. Solutions were obtained with isotropic plasma pressures up to about one-quarter of that in Earth’s magnetotail. To proceed toward more realistic magnetospheric solutions, in the next phase of development the rectangular geometry must be abandoned for a more realistic magnetopause shape, and the tailward boundary condition must be constructed with finite plasma pressure and normal magnetic field component.

Methodology

For illustration of the “effective magnetization” formulation assume isotropic pressure and neglect inertial currents. The magnetic configuration at any instant will be in quasi-static equilibrium. In MKS units the magnetic field \mathbf{B} , plasma pressure P , and plasma current \mathbf{J} are related by

$$\mathbf{J} \times \mathbf{B} = \nabla P \quad (1)$$

where

$$\nabla \times \mathbf{B} = \mu_0 \mathbf{J} \quad (2)$$

and

$$\nabla \cdot \mathbf{B} = 0 \quad (3)$$

The procedure is to solve for \mathbf{J} in (1) in terms of \mathbf{B} . The solution for (1) is just *Vasyliunas'* [1970] formula (see *Heinemann and Pontius* [1990])

$$\mathbf{J}(\mathbf{x}) = \nabla \left[\int^{\mathbf{x}} \frac{ds}{B} \right] \times \nabla P \quad (4)$$

The integral is performed along \mathbf{B} from the equator to \mathbf{x} . The equatorial properties are determined from advection of the plasma. Since \mathbf{J} is divergence free, (4) can be written as a curl of an effective magnetization \mathbf{M}_{eff}

$$\mathbf{J} = \nabla \times \mathbf{M}_{eff} \quad (5)$$

where in the present case

$$\mathbf{M}_{eff}(\mathbf{x}) = -P \nabla \int^{\mathbf{x}} \frac{ds}{B} \quad (6)$$

and in analogy with ordinary diamagnetic media

$$\mathbf{B} = \mu_0 (-\nabla \psi + \mathbf{M}_{eff}) \quad (7)$$

where $\psi = \psi_{int} + \psi_M$; ψ_{int} is the magnetic scalar potential given by the multipole representation of the IGRF [*Barker et al.*, 1986]; and ψ_M is the contribution from the distributed (plasma) currents. Taking the divergence of (7), ψ satisfies

$$\nabla^2 \psi_M = \nabla \cdot \mathbf{M}_{eff} \quad (8)$$

noting that $\nabla^2 \psi_{int} = 0$ away from Earth's center.

Iterating between (6) and (8) yields the solution for \mathbf{B} , given by (7), consistent with the plasma currents, i.e., satisfying force balance. This illustrates the general approach we take to computing magnetic field configurations consistent with the plasma currents. The source terms (4)–(6) have been generalized for anisotropic pressure [*Heinemann and Pontius*, 1991], inclusion of steady-state inertial currents [*Heinemann et al.*, 1994], and finite-Larmour-radius

effects [Heinemann and Erickson, 1997]. Techniques are also provided for generalization to treat currents on open field lines. These generalizations permit modeling of the entire, open magnetospheric configuration, including its boundary layers.

Boundary conditions on (8) are given at the magnetopause and at a mid-tail cross-section. Boundary conditions along the magnetopause can be specified using the technique of *Toffoletto and Hill* [1993]. The plasma distribution within the magnetopause and tail boundary is self-consistently derived using an M-I coupled convection code such as the Rice Convection Model [e.g., *Erickson et al.*, 1991]. Following the techniques of *Onsager et al.* [1993] to obtain plasma distributions and *Heinemann and Erickson* [1997] to compute current associated with the plasma-sheet boundary layer, a convection model can be extended into the far tail. In principle, plasma transport can be modeled throughout the magnetosphere, including the boundary layers.

Describing plasma currents in terms of the plasma magnetization and solving directly for the magnetic scalar potential has several advantages over other methods. Lagrangian methods, such as developed for the fusion community and recently adapted for magnetospheric applications [Cheng, 1995], require specification of a flux surfaces as boundary conditions. Such specification is not possible when modeling the open magnetosphere. The “effective magnetization” approach includes field-aligned currents self-consistently. Eqns. (4)–(6), and thus (8), contain the current perpendicular and parallel to \mathbf{B} . Other methods, based on solution of the momentum equation (1), know only of the perpendicular current. Finally, non-MHD effects, such as finite-Larmour-radius effects [Heinemann and Erickson, 1997] can be incorporated into this formulation.

Numerical Approach

An alternating-directions-implicit (ADI) [e.g., *Varga*, 1959] is used to solve (8) for given $\nabla \cdot \mathbf{M}_{eff}(\mathbf{B})$. $\mathbf{M}_{eff}(\mathbf{B})$ is then recomputed, and (8) is solved again. This loop repeats until convergence is obtained.

For the first phase in the development of this approach to magnetospheric modeling, solutions of (8) were sought for a rectangular magnetospheric geometry. The normal magnetic field component $B_n = 0$ along the dayside face located at $10.5 R_E$ sunward of the Earth, and at the dawn, dusk, north and south faces making a square cross-section $40 R_E$ on a side. The tailward face was placed $60.5 R_E$ behind the Earth. (R_E is an Earth radius.) To test the basic logic of the code and ADI solver, vacuum ($M_{eff} = 0$) solutions were sought for various values of B_n along the tail boundary. (B_n into the simulation box in the northern hemisphere, and out in the southern hemisphere.) For non-vacuum solutions, the magnetic field was assumed closed within the rectangular boundary; $B_n = 0$ on all faces. The pressure was specified on the equatorial plane such as to be constant near Earth, fall off as $|x|^{-1.2}$ down the tail, and vanish at the dayside and tailward faces.

Results

Vacuum solutions were obtained for various values of B_n on the tailward face of the simulation box. For $B_n \neq 0$, the solution contained a magnetic neutral line within the simulation box. A neutral line must form in this case. As there is no north-south component of the field on the tailward face, Earth's magnetic field must close within the simulation box. At the same time, the boundary condition on the tailward face must be met. A neutral line is required to satisfy both conditions.

Non-vacuum solutions were obtained for varying amounts of plasma pressure up to about one-quarter of that in Earth's central plasma sheet. Solutions were sought for $B_n = 0$ on the tailward face. Adding pressure to the tail would normally cause the field to become more taillike. However, the $B_n = 0$ boundary condition does not permit this to happen. Instead, the field has to undergo an unnatural distortion in the tailward portion of the simulation box. Starting from the vacuum solution, convergence was fast as magnetic flux had nowhere to go. Unfortunately, as the pressure exceeded about one-quarter that in Earth's central plasma sheet, the distortions were becoming too large and the field-line tracer for computing M_{eff} had difficulties. Rather than adding additional overhead to the numerical code to deal with

this (unrealistic) behavior, the solver was declared to pass its first phase of development.

Conclusion

The first phase in the development of an equilibrium magnetospheric magnetic field solver based on the "effective magnetization" approach has been completed successfully. In this first phase of development, numerical solutions for (8) were obtained in a closed, rectangular, magnetospheric geometry. To proceed toward realistic magnetospheric solutions, the next phase of development will be to generalize the numerical code for realistic magnetopause shapes and $B_n \neq 0$ anywhere, as well as both nonzero pressure and B_n on the tailward boundary.

References

- Barker, F. S., D. R. Barraclough, V. P. Golovkov, P. J. Hood, F. J. Lowes, W. Mundt, N. W. Peddie, Qi Gui-zhong, S. P. Srivastava, R. Whitworth, D. E. Winch, T. Yukutake, and D. P. Zidarov, International geomagnetic reference field revision 1985, *EOS Tran. AGU*, 67, 523, 1986.
- Cheng, C. Z., Three-dimensional equilibrium with isotropic pressure, *Geophys. Res. Lett.*, 22, 2401, 1995.
- Erickson, G. M., R. W. Spiro, and R. A. Wolf, The physics of the Harang discontinuity, *J. Geophys. Res.*, 96, 1633, 1991.
- Heinemann, M., and G. M. Erickson, Field-aligned currents and parallel potential fields in the plasma sheet boundary layer, *J. Geophys. Res.*, submitted, 1997.
- Heinemann, M., and D. H. Pontius, Jr., Representation of currents and magnetic fields in isotropic magnetohydrostatic plasma, *J. Geophys. Res.*, 95, 251, 1990.
- Heinemann, M., and D. H. Pontius, Jr., Representation of currents and magnetic fields in anisotropic magnetohydrostatic plasma, 2. General theory and examples, *J. Geophys. Res.*, 96, 17,609, 1991.
- Heinemann, M., G. M. Erickson, and D. H. Pontius, Jr., Inertial currents in isotropic plasma,

- J. Geophys. Res.*, 99, 8635, 1994.
- Onsager, T. G., C. A. Kletzing, J. B. Austin, and H. MacKiernan, Model of magnetosheath plasma in the magnetosphere: cusp and mantle particles at low-altitudes, *Geophys. Res. Lett.*, 20, 479, 1993.
- Toffoletto, F. R., and T. W. Hill, A nonsingular model of the open magnetosphere, *J. Geophys. Res.*, 98, 1339, 1993.
- Varga, R. S., *Iterative Numerical Analysis*. University of Pittsburgh, Pittsburgh, Pa., 1959.
- Vasyliunas, V. M., Mathematical models of magnetospheric convection and its coupling to the ionosphere, in *Particles and Fields in the Magnetosphere*, edited by B. M. McCormac, D. Reidel, Hingham, MA, p. 60, 1970.

**FOCAL POINT ACCURACY ASSESSEMENT OF AN OFF-AXIS SOLAR
CONCENTRATOR**

**H. Ghoneim
Associate Professor
Department of Mechanical Engineering**

**Rochester Institute of Technology
One Lomb Memorial Drive
Rochester, NY 14623**

**Final Report for:
Summer Research Program
Phillips Laboratory**

**Sponsored by:
Air Force Office of Scientific Research
Bolling Air Force Base, Washington, DC**

And

Phillips Laboratory

August, 1997

FOCAL POINT ACCURACY ASSESSEMENT OF AN OFF-AXIS SOLAR CONCENTRATOR

H. Ghoneim
Associate Professor
Department of Mechanical Engineering
Rochester Institute of Technology

Abstract

A solar propulsion vehicle (SPV) consists of three principal components: thruster, concentrator, and support structure. An important function of the support structure is to maintain the reflected solar energy inside the thruster cavity during all on-orbit maneuvers and environmental conditions. A finite element analysis is conducted to assess the ability of support structures, of a 1574.8x1181.1 inches (40x30 meters) off-axis parabolic concentrator, to achieve this function. The combined effects of the thrust required to change orbit, the aerodynamic drag at low earth orbit, and the on-orbit thermally-induced deformations are considered in the investigation. Two kinds of support structure/concentrator arrangements are investigated: inflatable concentrator with a support torus, and a foam-rigidized concentrator with no torus. The analysis indicates that the inflatable concentrator arrangement satisfies the required focal point accuracy, and that the rigidized concentrator arrangement does not. The rigidized concentrator concept, though attractive and promising, is too flexible and needs a substantial stiffening. For a sound design, a rigidized concentrator with a support torus is suggested, and addition of a partial passive damping to the supporting struts is recommended.

FOCAL POINT ACCURACY ASSESSEMENT OF AN OFF-AXIS SOLAR CONCENTRATOR

H. Ghoneim

Introduction

The solar propulsion concept (SPC) is an attractive technique for orbital-transfer applications. Solar propulsion vehicles, in general, are efficient, relatively cheap, reusable and versatile {1}.

A solar propulsion vehicle (SPV) consists of three principal components (Fig. 1): concentrator, thruster (engine), and support structure. The concentrator gathers, focuses and concentrates the sun's energy into a thruster cavity. The thruster captures the solar energy and converts it into heat which expands a single hydrogen working fluid through a nozzle, producing the propulsive thrust. The support structure (tori and truss members) rigidly connects the concentrators to the thruster. The only relative motion allowed between the support structure and the thruster is the slewing motion about the z axis, in order to maintain the reflectors directed towards the sun. A turntable provides such slewing maneuver. An important function of the support structure which is vital to the success of the SPC is to maintain the reflected sun's rays focused inside the thruster cavity during all on-orbit maneuvers and environmental conditions.

The objective of this work is to investigate the ability of candidate support structures to achieve the above-mentioned function. The investigation is carried out using the ANSYS finite element software. The subject of the investigation is the SPV (Fig. 1) with two parabolic off-axis concentrators supported by three struts each (two long struts and one short). Two concentrator arrangements are examined: inflatable thin-film concentrator (reflector/canopy arrangement) with a support torus as shown in the Fig. 1, and a foam-rigidized concentrator. The latter is viewed as an alternative arrangement which overcomes the problem of the make-up gas needed to maintain inflation and which improves the optical quality of the concentrator. Three on-orbit loads are considered for the investigation: 1) the thrust due to firing the thruster to change orbit, 2) the aerodynamic drag force at low earth orbit (LEO), and 3) thermal load due to temperature differential with respect to earth temperature and temperature gradient across the struts and torus cross sections. The solar wind, plume impingement and the sun tracking control forces (roll and yaw torque) are not considered in the present investigation. Previous preliminary analyses suggest that these forces have little impact on the focal point accuracy {2}.

Characteristics of the Solar Propulsion Vehicle

Figure 2 shows the basic geometry, dimensions and coordinate system of the off-axis concentrator {2}, adopted for the current investigation. This concentrator gives a theoretical peak concentration ratio of 12,560 which satisfies the minimum required concentration ratio of 10,000. The concentrator also provides the desired 1 MWatt solar power.

Both the struts and tori of the support structure are made of inflated, rigidized, space-cured carbon-epoxy composite beams. These are thin-walled tubes consisting of unidirectional M40J carbon fibers composite prepreg with a lay-up of $[\pm 30/0/90/\pm 30]$. The carbon-fiber composites enjoy a near-zero coefficient of thermal expansion (CTE) and a high specific stiffness. The outside diameters of the tubular struts and torus are assumed to be 13 and 7 inches, respectively. A 0.015-inch wall thickness is assigned for both the torus and struts. The reflector as well as the canopy is constructed from a 0.0005-inch thin film polyimide material. Polyimide films have material properties that are superior to those of other film materials and they retain their properties over a wide range of temperature {3}. The rigidized concentrator is assumed to be made of a 0.0625-inch thick (LaRC-CP1) polyimide film foam-rigidized with EPON Resin 828 epoxy. It has excellent adhesive properties and consequently is viewed as a good material for this specific application. The relevant material properties adopted for the current analysis are shown in Table 1.

	Modulus of elasticity, $E \times 10^6$ (psi)	Poisson's ratio	CTE $\times 10^{-6}$ (in/in- $^{\circ}$ F)	Density (lb/ft 3)
Graphite-Epoxy composite	17.21	0.3	0.1	102
Polyimide (6FDA+APB)	0.4	0.4	27.5	60
polyimide (LaRC-CP1)	0.315	0.4		90
Foam Epoxy (with glass fillers)	0.15	0.35		50

Table 1 Relevant Material Parameters

As mentioned before, three combined loads are considered in the current study: thrust, aerodynamic drag, and thermal loads. It is assumed that the maximum output of the thruster is a 100-lb force. This force will be used to transfer the fully-loaded SPV, with a total mass of 50,000

lb, from LEO at 200 nautical miles to GEO. On returning from GEO to LEO, a smaller thrust will be needed as the total weight of the vehicle is reduced. For the current investigation, we assume that the thrust can be minimized such that the engendering acceleration level is less than that produced during orbit (0.002 g). Consequently, a thrust of 100 lb acting on the full-loaded vehicle is assigned for the current investigation. At 200 nautical miles, the effect of the aerodynamic drag force is significant, given the large diameter and relative light weight of the reflector. Drag forces of 0.246 and 0.05 lb per reflector are estimated when the SPV travels along the Y-direction and X-direction, respectively. The estimation is based on the following assumptions {4}: drag coefficient = 2, atmospheric density = 3×10^{-14} slug/ft³, and velocity = 33,000 ft/sec. Approximate projected reflector areas of 7600 ft² and 1530 ft² in the Y-direction and X-direction, respectively, are considered for the calculation. In general, during flight the support structure's members are exposed to the sun on one side and to a deep space on the other side, engendering a temperature gradient, ΔT , across the cross sections. This temperature gradient produces a thermally-induced bending moment. Also, a temperature differential between the bulk temperature, T_b , of each member and the initial earth temperature exists which stretches or contracts the member. The effect of the aforementioned thermal-loading scenario is taken into account. Two sets of temperature gradient and bulk temperature are adopted for the current investigation and are shown in Table 2. Both sets are approximate and based on the preliminary analyses done by Lockheed {2} and Marietta {4}.

	Lockheed		Marietta	
Temperature (°F)	Long strut	Short strut/ torus	Long strut	Short strut/ torus
Bulk, T_b	230	120	100	50
Gradient, ΔT	100	80	200	160

Table 2. Support Structure's Bulk Temperature and Temperature Gradient

Finite Element Analysis

The finite element model of the SPV is shown in Fig. 3. Taking advantage of symmetry, only one half of the vehicle is considered. The thruster, fuel tank and payload are all treated as concentrated masses (MASS21 elements) placed at the free ends of the struts. For the sake of clarity, the canopy is omitted from the Figure but it is included in the finite element analysis.

Beam (BEAM4) elements are adopted for the struts and torus, membrane (SHELL41) elements for the concentrator, and shell (SHELL63) elements for the foam-rigidized reflector. Six elements are assigned for the long strut, five for the short one, and sixty for the reflector as well as the canopy.

It should be pointed out that the objective of this study is to investigate the ability of the support structure to maintain the focal point of the reflected sun's rays inside the thruster cavity under the effect of the aforementioned three loads. That is, to check the ability of the support structure to keep the focal point deflection within a certain envelope. It is assumed that the maximum allowable deflection in any direction is 6 inches {2}. It is also assumed that the deflection of the focal point is dominated by two factors: the translation of the center of gravity of the torus, ΔX_G , and the angular rotation of the torus' plane, $\Delta \theta$. The total deflection ΔX_d is the sum of the deflections due to translation and rotation, i.e.; $\Delta X_d = \Delta X_G + 2 \Delta \theta \times R$, where R is the "reflected sun's ray" vector between the center of gravity of the torus and the theoretical focal point at $X, Y, Z = 0, 0, 12$ inches. It is understood that the focal spot deflection and dispersion due to the deformation of the reflector surface is a better measure of the pointing accuracy {5}. However, analysis of the focal spot deflection and dispersion is beyond the scope of this study.

Before the analysis of the focal point deflection due to the combined loading effects, a preliminary investigation is conducted. The purpose of the preliminary investigation is two folds: to examine the effect of using an equivalent static analysis instead of a transient one, and to estimate the impact of ignoring the reflector geometry on the focal point deflection. For the preliminary investigation, a modal analysis is performed first, in order to assess the dynamic characteristics of the system. Then, the transient response due to a thrust of 50 lb (only half the system is considered) as well as the static response due to an equivalent inertia load (0.002 g) is determined and the results are compared. The preliminary analysis is done for both cases when the reflector geometry is ignored and replaced by concentrated masses (MASS21 elements) distributed along the torus, and when the geometry is considered. In addition, the thrust (50 lb) is applied along the Y-direction as well as along the X-direction in order to determine which is more critical. Therefore, the finite element analysis is accomplished in three phases: preliminary investigation, analysis of the inflatable concentrator arrangement, and analysis of the foam-rigidized concentrator arrangement.

Results and Discussion

(1) Preliminary Investigation:

Table 3 presents the six first natural frequencies of the support structure for two cases: 1) when the concentrator geometry is ignored, and 2) when it is considered. Samples of the results are shown in Figures 4 and 5. They display the second mode shape (1st lateral bending mode in the Y-Z plane) of the former case and the sixth mode shape (1st vibration mode of the torus) of the latter case, respectively.

Case No.	Mode No.	Freq. (Hz)	Period (sec)	Mode Shape Description
1	1	0.083	12.00	1 st lateral bending mode in the X-Z plane
1	2	0.103	9.727	1 st lateral bending mode in the Y-Z plane
1	3	0.168	5.951	1 st Torsional mode around the Z-axis
1	4	0.836	1.196	Torsional mode, with plane distortion of torus
1	5	0.856	1.168	1 st vibration mode (bending) of the torus
1	6	1.017	0.983	1 st bending mode of the long strut
2	1	0.085	11.73	1 st lateral bending mode in the X-Z plane
2	2	0.103	9.672	1 st lateral bending mode in the Y-Z plane
2	3	0.181	5.514	1 st Torsional mode around the Z-axis
2	4	1.399	0.715	1 st bending mode of the long strut
2	5	1.500	0.667	1 st bending mode of the short strut
2	6	1.714	0.583	1 st vibration mode (bending) of the torus

Table 3. Natural Frequencies of The Concentrator/Support Structure

The following observations and comments can be stated:

- The first three fundamental modes are the same for both cases. These three modes pertain to the vibration of the torus about the thruster, with no significant deformation to the torus. Also, these fundamental frequencies are quite separated from the rest of the natural frequencies. Consequently, it is expected that the transient response of the SPV due to the

combined loads will be dominated by these modes and that ignoring the reflector's geometry in the analysis will have little effect on the response.

- Amongst these three fundamental modes, only the second mode undergoes motion predominantly along the Y-direction. Consequently, it is expected that the transient response due to the applied thrust in the Y-direction will be dominated by this mode, and there will be no significant difference between the transient and static results. On the other hand, both the first and third modes experience motion primarily along the X-direction and both will affect the transient response, when the thrust is applied along the X-direction. Consequently, in this case, it is expected that the transient response will be different from the corresponding static one. Keep in mind that the static response due to an equivalent inertia force captures the fundamental (first) mode shape only.
- The second three modes are noticeably higher for the second case. In particular, the first vibration (bending) mode of the torus is doubled when the concentrator geometry is included. This indicates that the concentrator does stiffen up the torus/concentrator system.

Loading condition	ΔX	ΔY	ΔZ
No concentrator, Thrust along X-direction, Static	-2.838	0.013	-0.004
No concentrator, Thrust along X-direction, Transient	-3.214	0.007	~ 0.0
No concentrator, Thrust along Y-direction, Static	-0.010	3.007	0.056
No concentrator, Thrust along Y-direction, Transient	0.0	3.044	0.062
With Concentrator, Thrust along Y-direction, Static	~ 0.0	3.078	0.043
With Concentrator, Thrust along Y-direction, Transient	~ 0.0	3.067	0.057

Table 4. Focal Point Deflection due to Thrust Under Different Conditions (units in inches)

The predicted focal point deflections, ΔX_d , under different loading conditions are given in Table 4. Notice that for the preliminary investigation only the 50-lb thrust is considered. As expected, when the thrust is applied along the Y-direction, neither inclusion of the concentrator geometry nor performing transient, versus static, analysis significantly affect the predicted focal point deflection. When the thrust is applied along the X-direction, however, the equivalent static analysis predicts a smaller deflection than the transient. This difference is engendered because two mode shapes contribute to the response.

(2) Analysis of the Inflatable Concentrator Arrangement:

The focal point deflection due to the different types of loading are presented in Table 5. A transient analysis is performed for the case when the aerodynamic drag force is applied along the X-direction. All other cases are simulated via static analyses. Since the preliminary investigation indicates that neglecting the concentrator geometry does not significantly influence the focal point results, the geometry is ignored in this analysis. It is assumed that the superposition principle is applicable in the current elastic, small deformation analysis. Consequently, the total focal point deflection due to a combined loading can be determined by simply summing the deflections due to the different loads.

Loading type	ΔX	ΔY	ΔZ
Aerodynamic drag force along the X-direction	-0.337	0.002	~ 0.0
Aerodynamic drag force along the Y-direction	0.0	1.618	0.033
Thermal load (Lockheed)	0.0	0.460	0.031
Thermal load (Marietta)	0.0	0.850	0.025
Inflating pressure	~ 0.0	-0.167	0.061

Table 5. Focal Point Deflections due to Different Loads (units in inches)

For the pressure effect analysis, an inflating pressure of 3×10^{-4} psi is applied. This pressure produces a minimum effective stress of 650 psi, needed to remove packing wrinkles {6}, in the thin-film material of concentrator. Calculation of the pressure is based on the stress formulas developed in {7}. The analysis predicts that the applied pressure causes a negligible focal point deflection, yet substantially distorts the reflector. Consequently, it is imperative that the pressure effect to be pre-considered in the design of the thin-film concentrator.

Assuming that the pressure effect will be pre-considered in the design of the concentrator, the results in Table 5 indicate:

- The aerodynamic drag force produces a significant focal point deflection when the SPV travels along the Y-direction. This is because of the large projected area and relative light weight of the concentrator. When the SPV travels along the X-direction, the projected area of the concentrator is much smaller rendering a less significant focal point deflection.

- The focal point deflection due to thermal loading is small. It should be pointed out, however, that the struts and torus are made of a near-zero CTE material. A material with CTE close to or more than 10^{-6} in/in- $^{\circ}$ F would exhaust the 6-inch maximum allowed deflection.
- The total focal point deflection due to the combined thrust, aerodynamic drag along the Y-direction and thermal loading (Marietta case) is approximately 5.5 inches. The deflection, though close to, is smaller than the maximum allowable. Since this combination of loading represents the worse loading scenario that renders the maximum focal point deflection, we may claim that the inflatable concentrator arrangement is safe but not comfortably.

(3) Analysis of the Foam-Rigidized Concentrator Arrangement:

The first six natural frequencies of the foam-rigidized concentrators are shown in Table 6. As a sample, the second "cambering" mode shape is displayed in Fig. 6.

Mode No.	Freq. (Hz) $\times 10^{-3}$	Period (sec)	Mode Shape Description
1	4.568	218.9	"Hoop twist" of the lower portion of the concentrator
2	5.203	192.2	Bending about the minor axis, "Cambering"
3	5.547	180.3	Bending about the major axis, "Flapping"
4	5.731	174.5	"Hoop twist"
5	7.773	128.6	"Flapping" of the upper portion of the concentrator
6	8.411	118.9	"Hoop twist" of the upper portion of the concentrator

Table 6. Natural Frequencies of the Rigidized-Reflector/Support Structure

Notice that all the natural frequencies are less than 0.01 Hz and that all the modes pertain to the concentrator alone, i.e., the struts' deformation is not involved. These observations indicate that, without the torus support, the 0.0625-inch thick rigidized reflector is too flexible. Also, the fact that all these modes cluster within a very narrow band of frequencies suggests that a static analysis, which takes into account the dominant mode only, will be erroneous. The transient response of the foam-rigidized concentrator system due to the 50-lb thrust is determined. Fig. 7 shows the deformation pattern at 108 second from firing the thrust. The evolution of the Y-displacement, relative to the thruster, of two points on the reflector is displayed in Fig. 8. These

two points are the connection points between the reflector and the long strut (UYRL), and between the reflector and the short strut (UYRS). Notice the prohibitively large displacement and severe distortion experienced by the reflector. Obviously, the rigidized-concentrator is too flexible to preserve its geometric integrity against the inertial effect of the applied thrust.

Conclusion

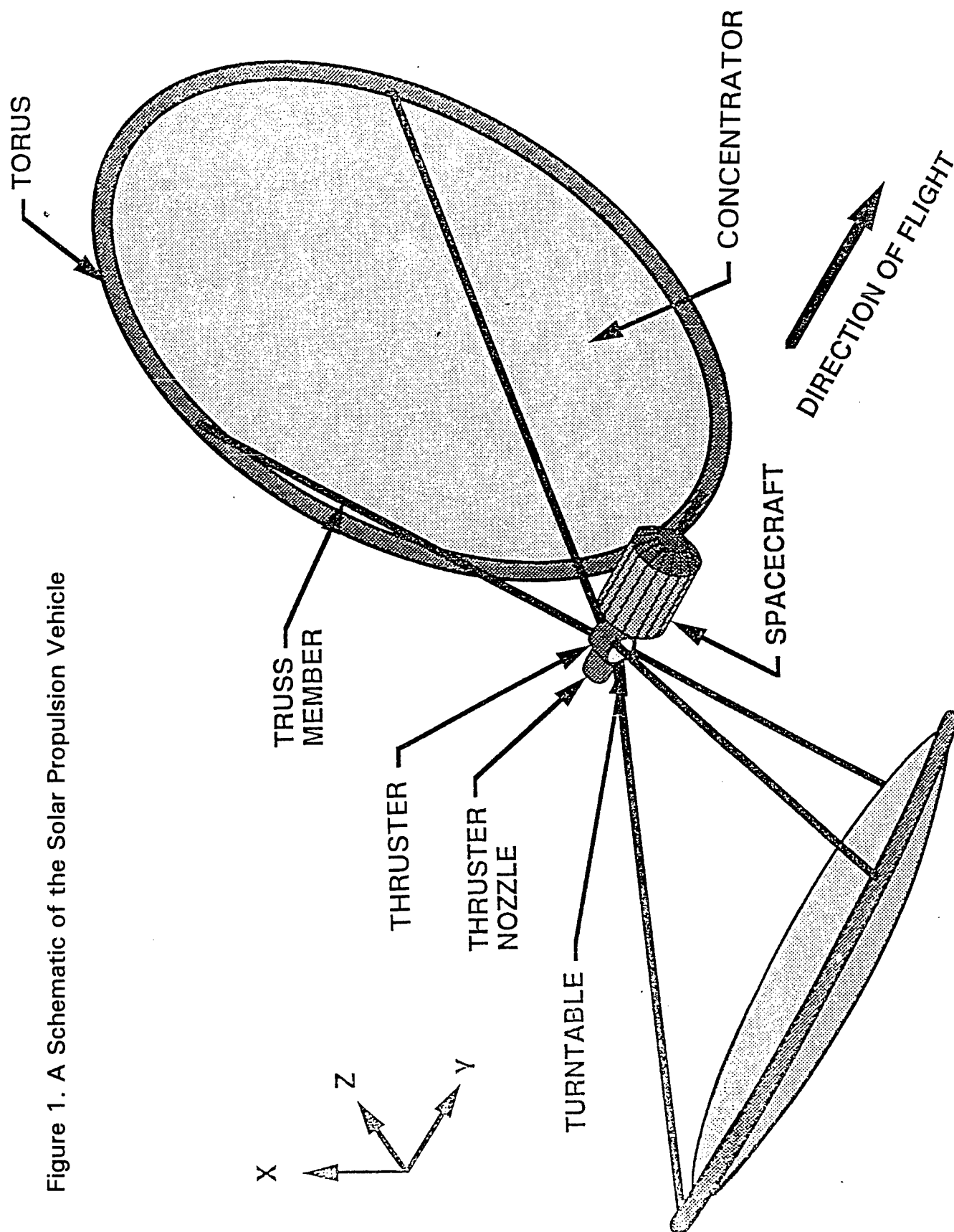
A finite element investigation of the SPV with the 1574.8x1181.1 inches off-axis parabolic concentrator is conducted. Two concentrator arrangements are examined: inflatable thin-film concentrator with a support torus and a foam rigidized-concentrator without the torus. The combined effect of the thrust, aerodynamic drag, and thermally-induced deformation on the focal point accuracy is assessed. Presuming that the struts and tori are made of a near-zero CTE material and that the pressure effects on the reflector is pre-considered, the inflatable thin-film concentrator fulfills the required accuracy of the focal point deflection. The foam-rigidized concentrator, on the other hand, severely fails to satisfy this required accuracy.

The above-mentioned conclusions suggest that a combination of both arrangements would be the most effective. A vehicle with a rigidized concentrator and a smaller torus would have sufficient stiffness to comfortably achieve the needed focal point accuracy. In addition, this arrangement will purge the vehicle from the canopy. Thereby, it will improve the optical quality of the reflector and overcome the problems associated with maintaining the inflation of the concentrator. More over, in order to further reduce the focal point deflection, adding some damping to the support structure is recommended. This damping will also attenuate the developed oscillatory motion and prevent multiplication of this oscillation upon repeated firing. Since the inflatable concentrator arrangement already satisfies the required deflection point accuracy, passive damping is considered adequate for this support structure. The constrained layer damping {8}, shunted piezoelectric {9}, and electromechanical surface damping {10} are passive, economical and reliable techniques that we recommend to be considered for this application.

References

1. K.K. Laug, "The Solar Propulsion Concept is Alive and Well at the Astronautics Laboratory," 1989 JANNAF Propulsion Meeting, 23-25 May 1989, CPIA Publication 515, Vol. 1, pp. 289-324.
2. G.L. Ritchie, D.M. Chisessi, and J.F. Wilson, "Solar Astromast Torus," Final Report No. AFRPL-TR-93-3034, Lockheed Missiles and Space Company, August 1993.
3. J. Paxton, and C. Hawk, "Material Property Effects on a Thin Solar Concentrator for Solar Thermal Propulsion," 30th AIAA/ASME/SAE/ASEE Joint Propulsion Conference, 1994/Indianapolis, IN, AIAA Publication 94-3029, 1994, pp. 1-12.
4. J.L. Draper, R.N. Gehling, R.R. Hanson, D.F. Shepard, and J.L. Summers, "Graphite/KelvarTM Strings Truss," Final Report No. AFRPL-TR-93-3032, Martin Marietta Astronautics Group, September 1993.
5. M.R. Holmes, "Ideal Performance of Off-Axis Paraboloid Concentrators for Solar-Thermal Propulsion," The 1996 International Solar Energy Conference, ASME Publication, edit. J.H. Davidson, 1996, pp. 443-449.
6. G.R. Veal, "Highly Accurate Inflatable Reflectors, Phase II," L'Garde, Inc. Final Report No. AFRPL-TR-86-089, March 1987.
7. G. Grossman, "Analysis of Rim Supports for Off-Axis Inflatable Reflectors. I: Loads," Journal of Aerospace Engineering, Vol. 4, 1991, pp.47-66.
8. G.R. Tomlinson, "The use of Constrained Layer Damping in Vibration Control," International Journal of Mechanics and Sciences, Vol. 32, 1990, pp. 233-242.
9. N.W. Hagood, and A. von Flotow, "Damping of Structural Vibrations With Piezoelectric Materials and Passive Electrical Networks," Journal of Sound and Vibration, Vol. 146, 1991, pp. 243-268.
10. H. Ghoneim, "Application of the Electromechanical Surface Damping to the Vibration Control of a Cantilever Plate," ASME Journal of Vibration and Acoustics, Vol. 118, 1996, pp. 551-557.

Figure 1. A Schematic of the Solar Propulsion Vehicle



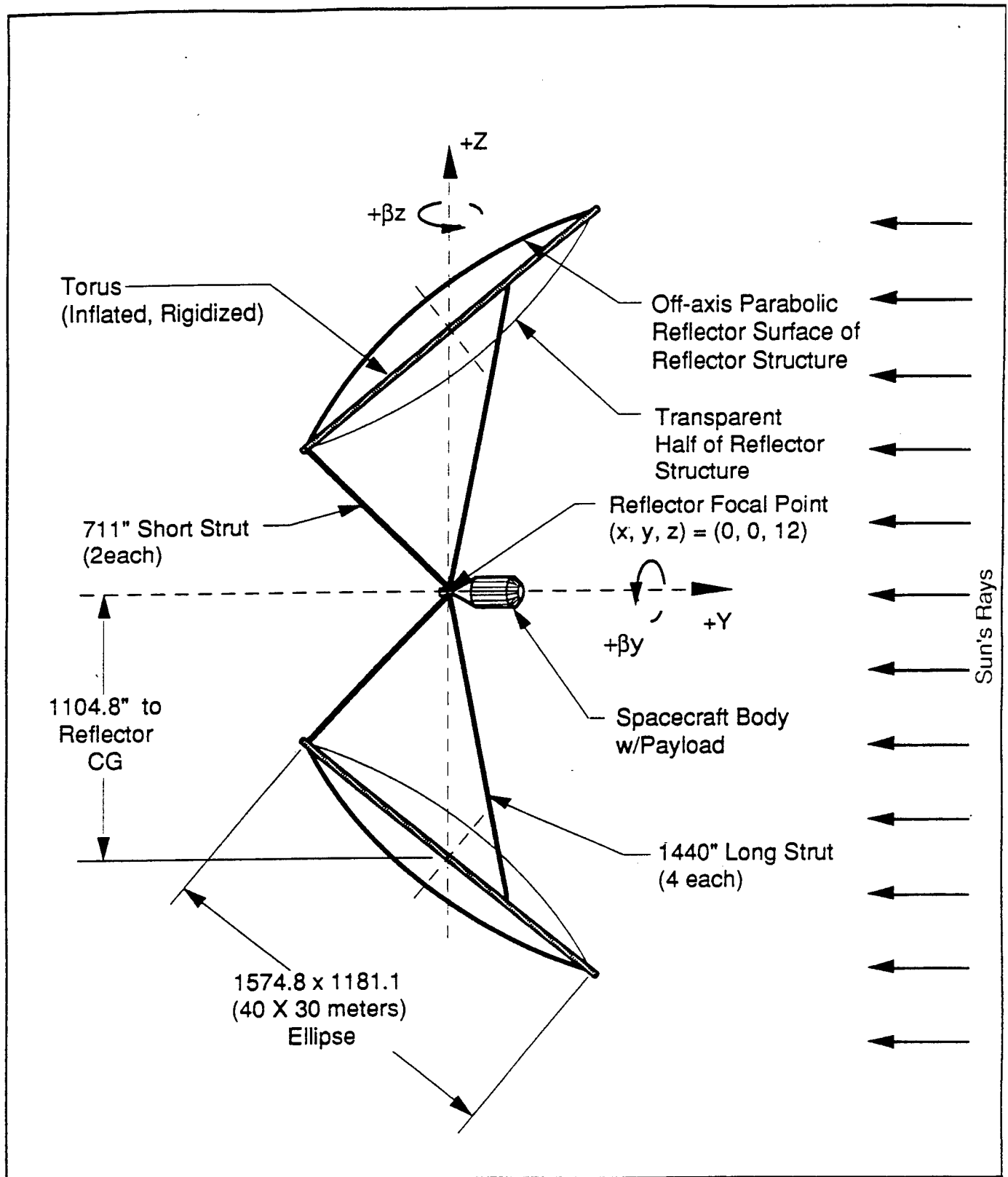


Figure 2. Solar Concentrator Coordinate System and Geometry

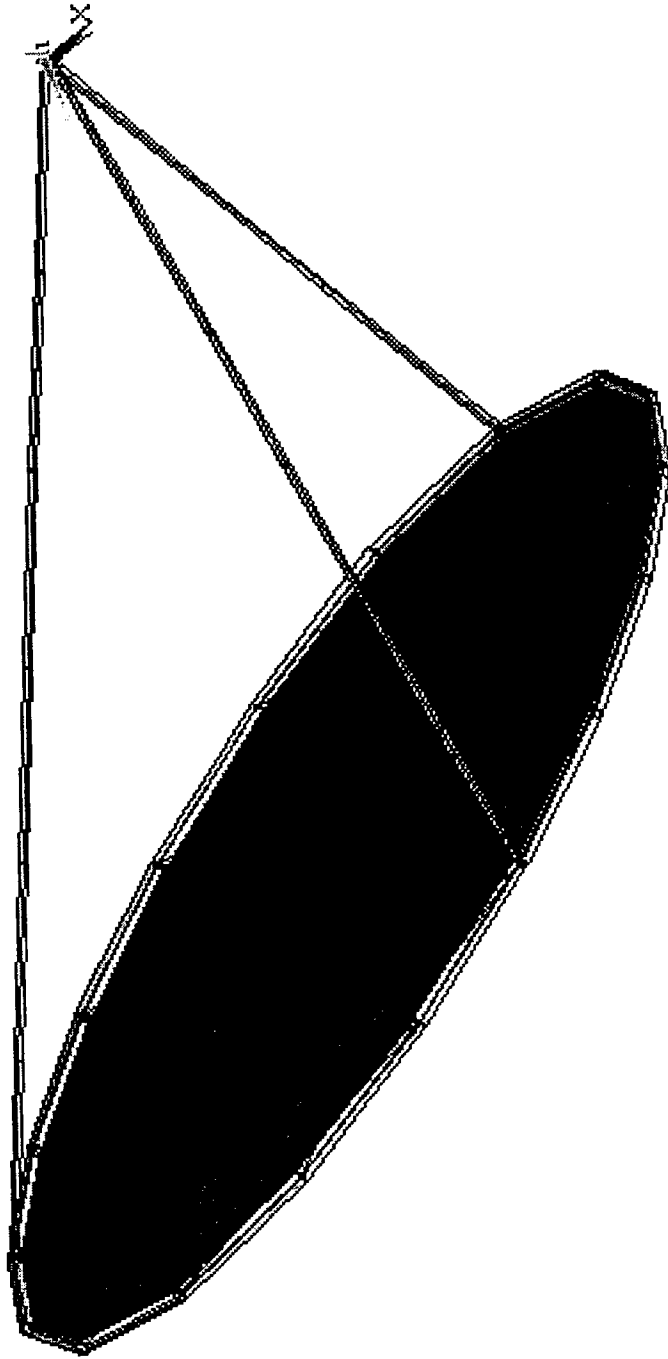


Figure 3. Finite Element Model of the Support Structure/ Reflector System

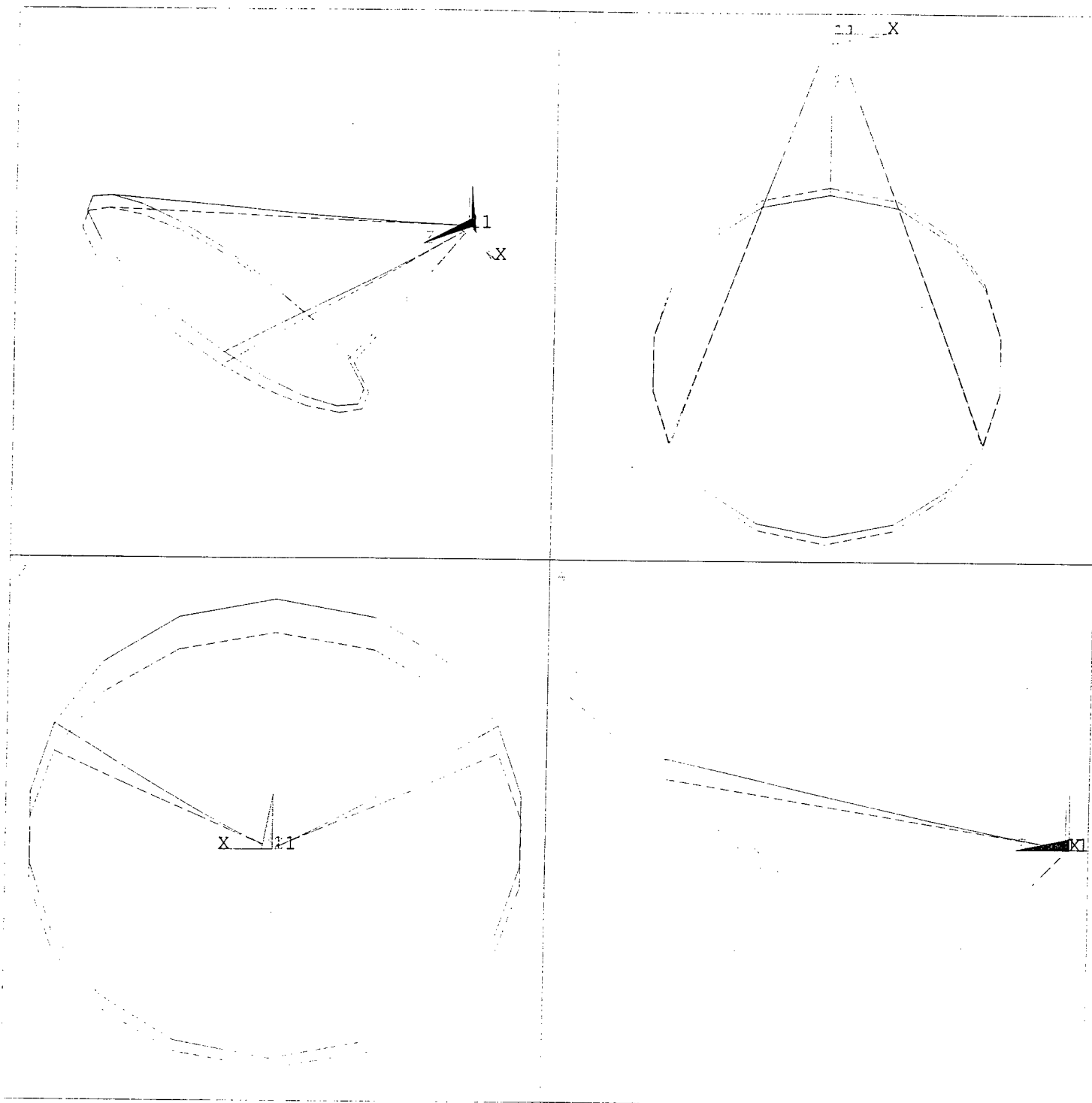


Figure 4. Second Mode Shape of the Inflatable Concentrator/Support Structure With the Concentrator's Geometry Ignored (Dashed Line Represents the Undeformed Shape)

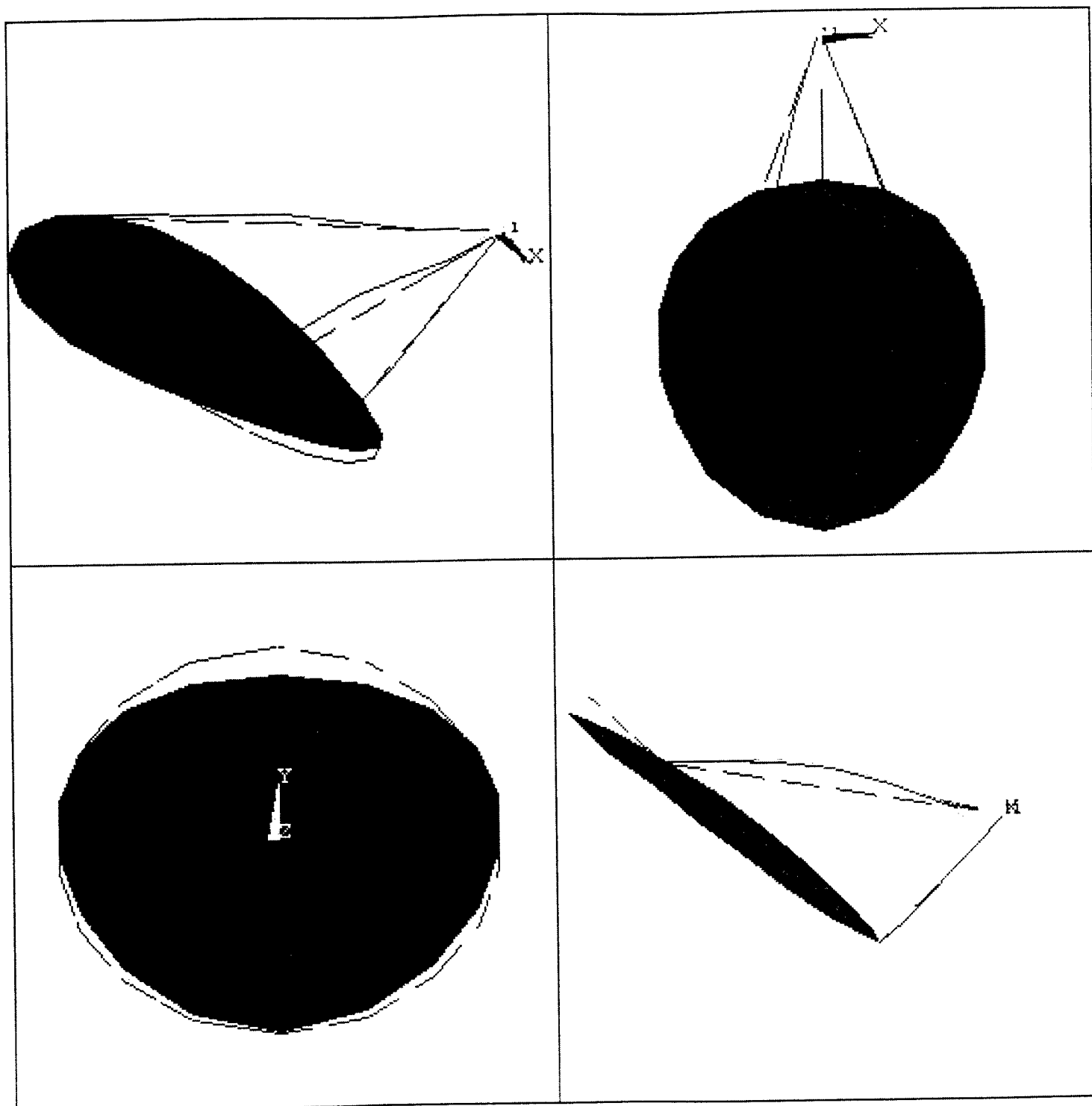


Figure 5. Sixth Mode Shape of the Inflatable Concentrator/Support Structure (Dashed Line Represents the Undeformed Shape)

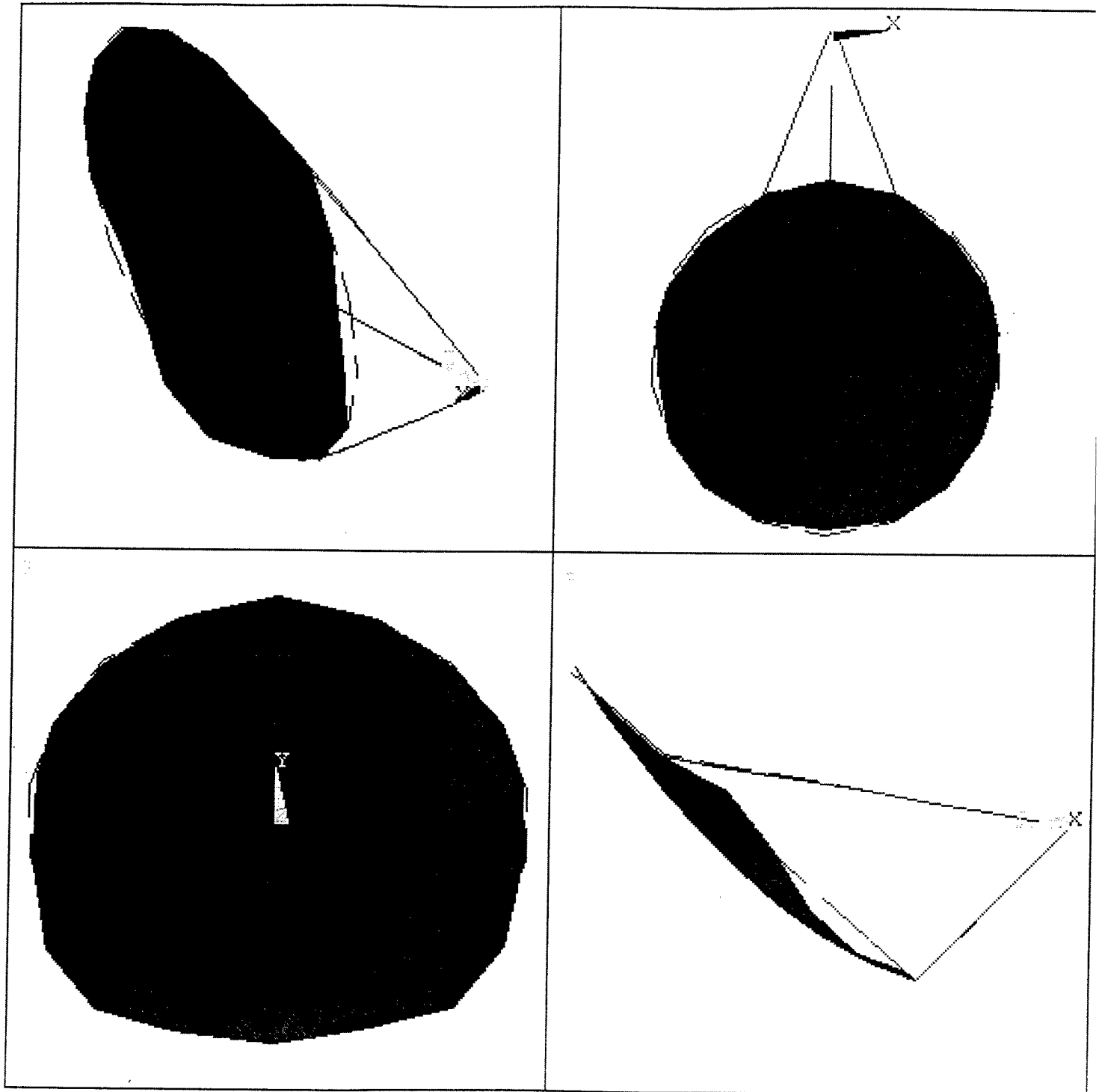


Figure 6. Second Mode Shape of the Foam-Rigidized
Concentrator/Support Structure
(Dashed Line Represents the Undeformed Shape)

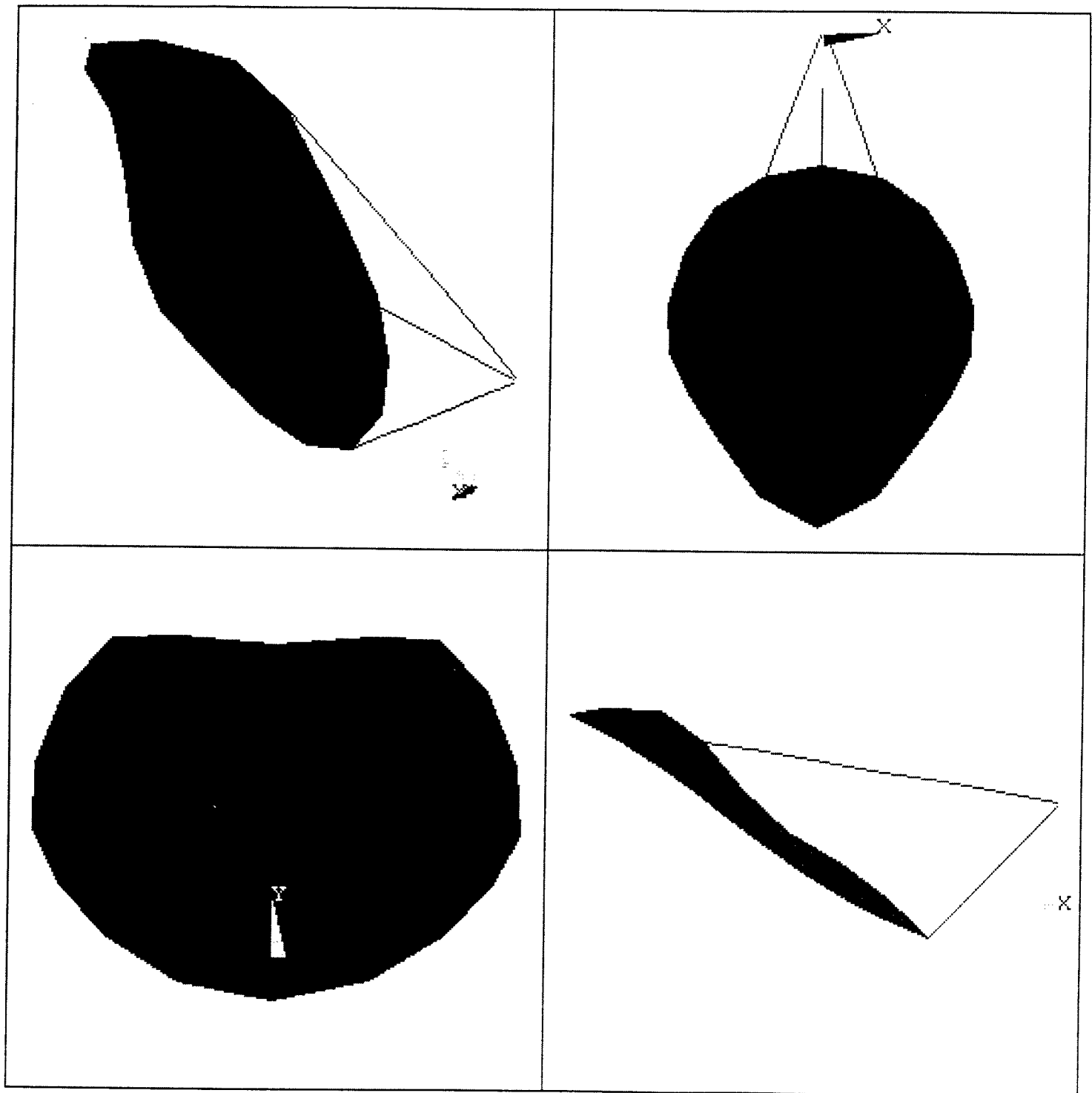


Figure 7. Deformed Shape of the Foam-Rigidized concentrator due to a 50-lb Thrust Acting Along the Y-Direction (at 108 Second)

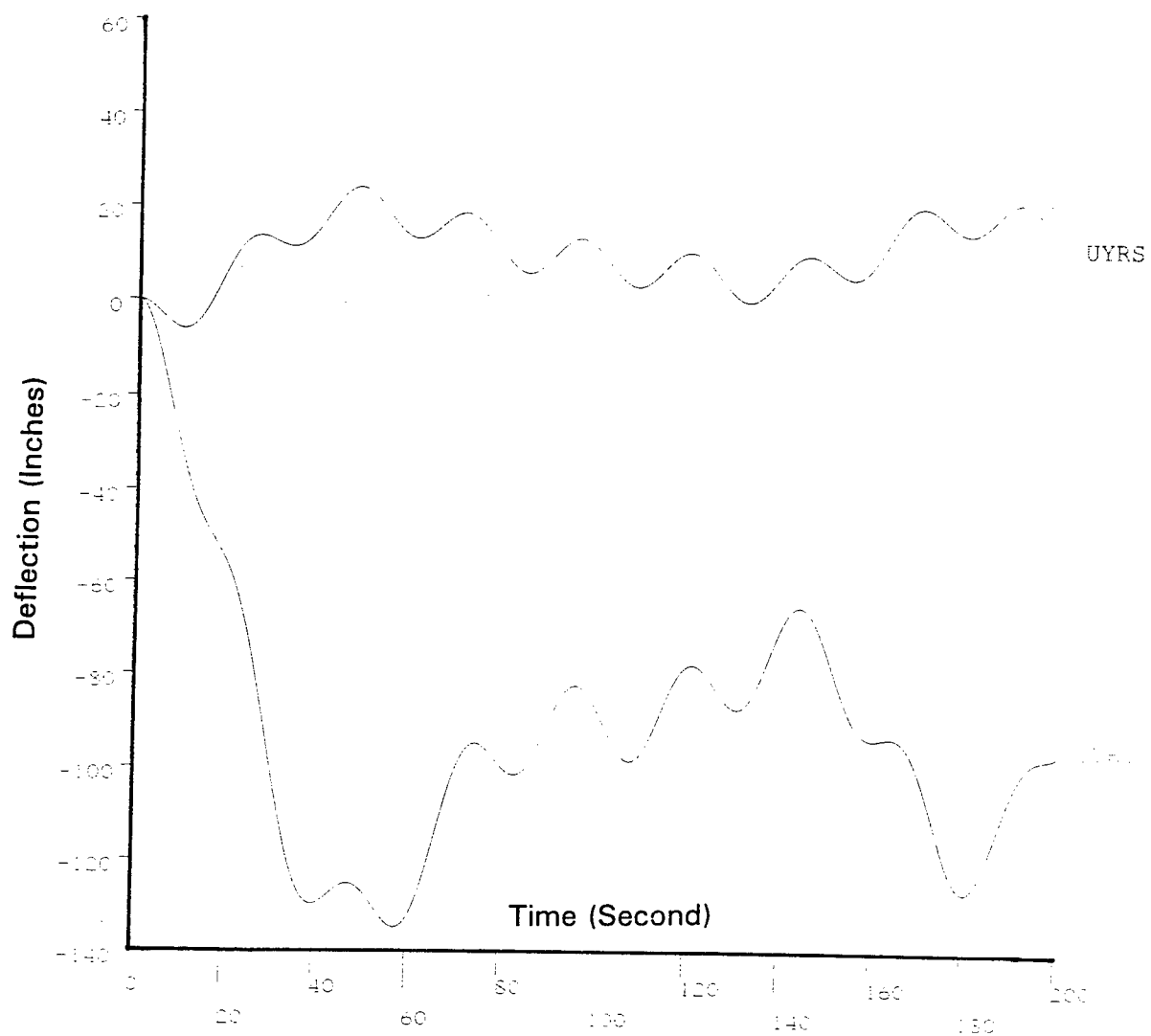


Figure 8. Evolution of the Relative Y-Deflection due to the 50-lb Thrust (UYRL \equiv The Connection Point Between the Reflector and Long Strut, UYRS \equiv The Connection Point Between the Reflector and Short Strut)

DESIGNING PROPULSION REALIABILITY OF SPACE LAUNCH VEHICLES

**Subir Ghosh
Associate Professor
Department of Statistical Engineering**

**University of California
Riverside, CA 92521**

**Final Report for:
Summer Research Program
Phillips Laboratory**

**Sponsored by:
Air Force Office of Scientific Research
Bolling Air Force Base, Washington, DC**

And

Phillips Laboratory

September, 1997

DESIGNING PROPULSION RELIABILITY OF SPACE LAUNCH VEHICLES

Subir Ghosh

Professor

Department of Statistics

University of California, Riverside

Abstract

The propulsion reliability of a thrust-augmented Single Stage to Orbit (SSTO) space launch vehicle depends on the number of solid boosters, the number of liquid engines, the reliability per solid booster, and the reliability per liquid engine. We give mathematical expressions of such dependence when the reliability does or does not depend on time. We present numerical results and corresponding figures demonstrating the relationship between the propulsion cluster reliability and the motor/engine reliabilities of both solid booster and liquid engines. This paper shows how the propulsion cluster reliability can be tailored to match a desired vehicle reliability.

DESIGNING PROPULSION RELIABILITY OF SPACE LAUNCH VEHICLES

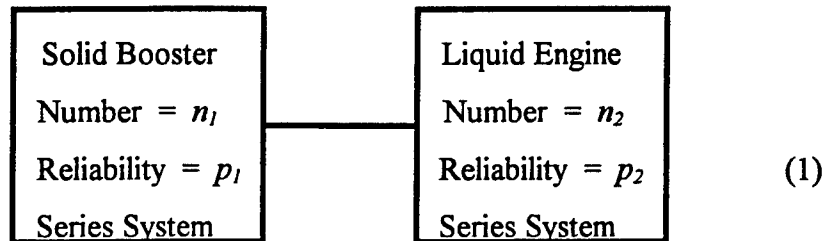
Subir Ghosh

Introduction

Single Stage to Orbit (SSTO) launch vehicle reliability is an important part of the performance evaluation of this class of vehicles. Our research is concerned with the propulsion reliabilities of space vehicles for catastrophic failures. Four methods are developed for calculating the propulsion reliability of such a vehicle. Launch vehicles with different combinations of solid booster and liquid engines are considered. The dependence of the propulsion cluster reliability on the numbers of solid boosters and liquid engines is studied. Specific recommendations are made for designing an SSTO vehicle with respect to the desired solid booster and liquid engines reliabilities as well as the cluster propulsion reliability of the vehicle. Historical data are used for defining representative reliabilities. A literature search does not find much published work available on vehicle reliability formulation. The work presented here presents new thinking in vehicle design.

Propulsion Reliability Models: Blocked Series System

In a blocked series system, solid boosters and liquid engines are considered as two blocks with series system in each. We first present the formula for calculating the non-time dependent propulsion reliability of an SSTO. Let



We assume that all solid boosters have the same reliability p_1 and all liquid engines have the same reliability p_2 . The failures of propulsion, solid or liquid, are assumed to be independent and furthermore, a failure of any propulsion unit, solid or liquid, results in the

catastrophic failure of the propulsion system and consequently, the catastrophic failure of the space vehicle. This is known as a *series system* for both solid boosters and liquid engines. The probabilistic setup is called a *Binomial Experiment*. The non-time dependent cluster reliability R_1 of the space vehicle can be expressed as

$$R_1 = 1 - [n_1(1 - p_1^{n_1}) + n_2(1 - p_2^{n_2})] . \quad (2)$$

Note that we want $0 \leq R_1 \leq 1$, which in turn sets constraints on n_1, p_1, n_2 and p_2 for reasonable values.

We now present the formula for calculating the time dependent propulsion reliability of an SSTO. We assume an Exponential Model with

$$\begin{aligned} p_1 &= e^{(-t/\theta_1)}, 0 \leq t \leq 90, \\ p_2 &= e^{(-t/\theta_2)}, 0 \leq t \leq 500, \end{aligned} \quad (3)$$

where θ_1 and θ_2 are unknown parameters. Note that the expressions of p_1 and p_2 given in (3) are time dependent. The operation time of solid boosters is assumed to be the first 90 seconds and the operation time of liquid engines is assumed to be the period of 500 seconds. The time dependent cluster reliability R_2 of the space vehicle can be expressed as

$$\begin{aligned} R_2 &= 1 - [n_1 \{1 - (e^{(-t/\theta_1)})^{n_1}\} + n_2 \{1 - (e^{(-t/\theta_2)})^{n_2}\}], 0 \leq t \leq 90, \\ R_2 &= 1 - [n_2 \{1 - (e^{(-t/\theta_2)})^{n_2}\}], 90 < t \leq 500. \end{aligned} \quad (4)$$

Non-Time Dependent Reliability : Blocked Series System

In this section, we study the dependence of R_1 , defined in (2), on n_1 and n_2 . Table 1 presents the overall reliability (R_1) values for $p_1 = 0.9999$ and $p_2 = 0.9990$ and 0.9999 , Table 2 presents the R_1 values for $p_1 = 0.999$ and $p_2 = 0.992$ and 0.999 . Figures 1.1 and

1.2 display R_I curves for $(n_1, n_2) = (0, 2), (2, 4), (3, 6)$ and $p_I = 0.9999$ and 0.999 , respectively.

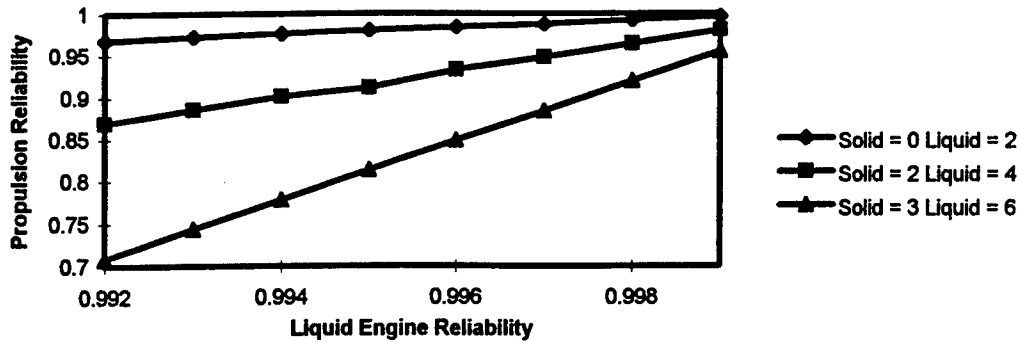


**Figure 1.1 : Propulsion Reliability by Liquid Engine Reliability
when Solid Booster Reliability = 0.999 : Blocked Series**

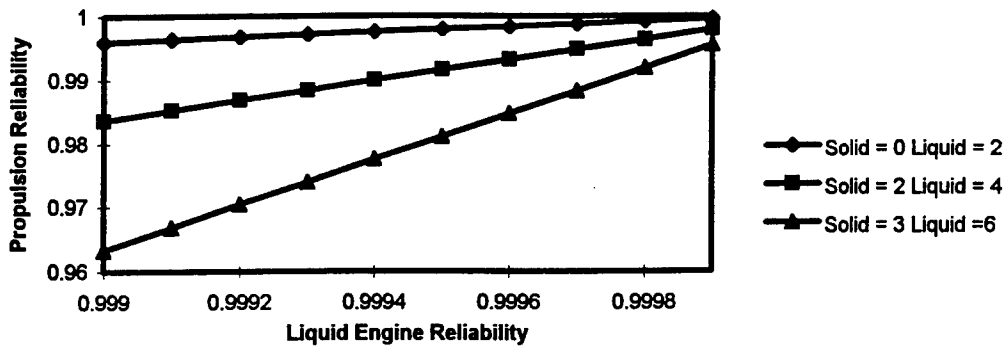


**Figure 1.2 : Propulsion Reliability by Liquid Engine Reliability
when Solid Booster Reliability = 0.9999 : Blocked Series**

Figures 2.1 - 2.4 display contour plots of R_I values. These graphs are useful for the purpose of reliability design. For designing a space vehicle with $p_I = 0.9999$ and $p_2 = 0.9999$, the problem is to find the values of n_1 and n_2 so that the desired propulsion reliability R_I is 0.999. The possible values of (n_1, n_2) are $(2, 2), (2, 3), (1, 2), (1, 3), (0, 2)$. Considering the desired performance and cost analyses, one could come up with the optimum choice of (n_1, n_2) . If the desired propulsion reliability

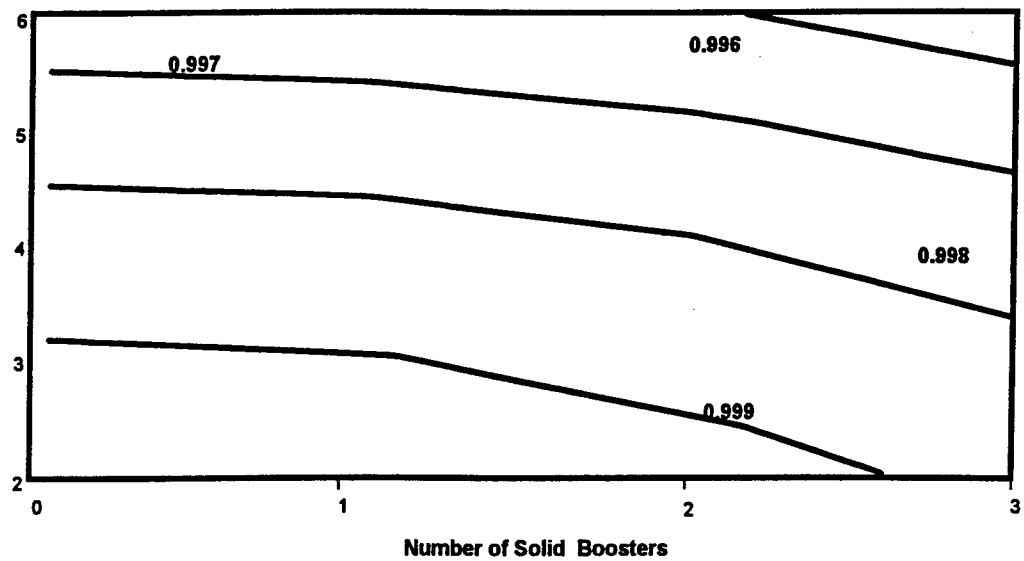


**Figure 2.1 : Propulsion Reliability Contour : Solid = 0.9999, Liquid = 0.9999
Blocked Series**

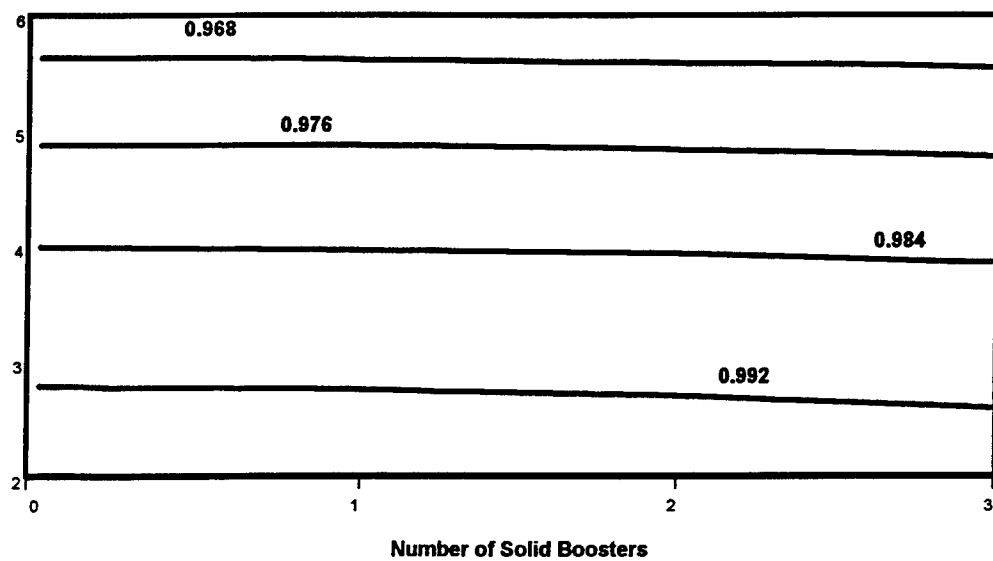


**Figure 2.2 : Propulsion Reliability Contour : Solid = 0.9999, Liquid = 0.999
Blocked Series**

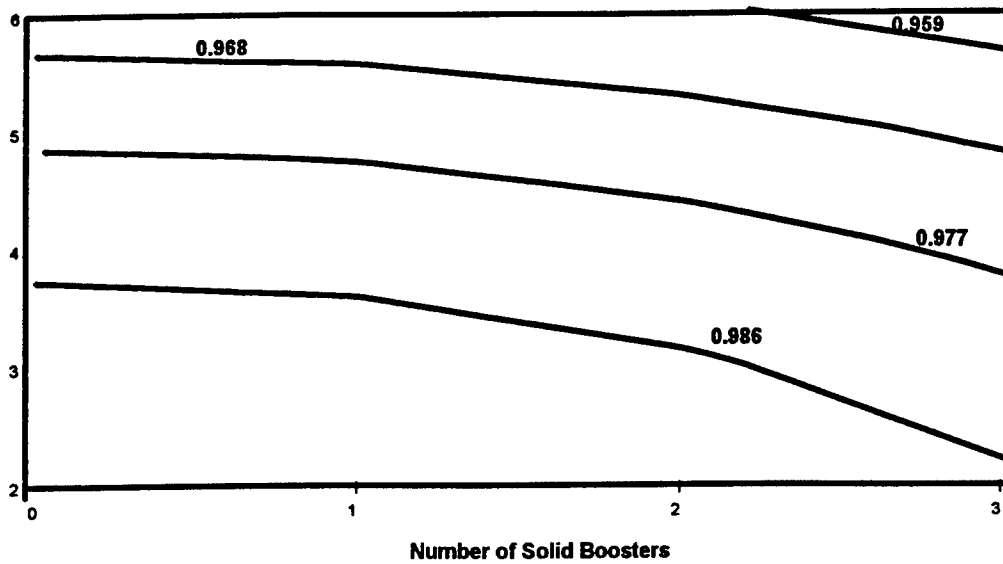


**Figure 2.3 : Propulsion Reliability Contour : Solid = 0.999, Liquid = 0.999
Blocked Series**

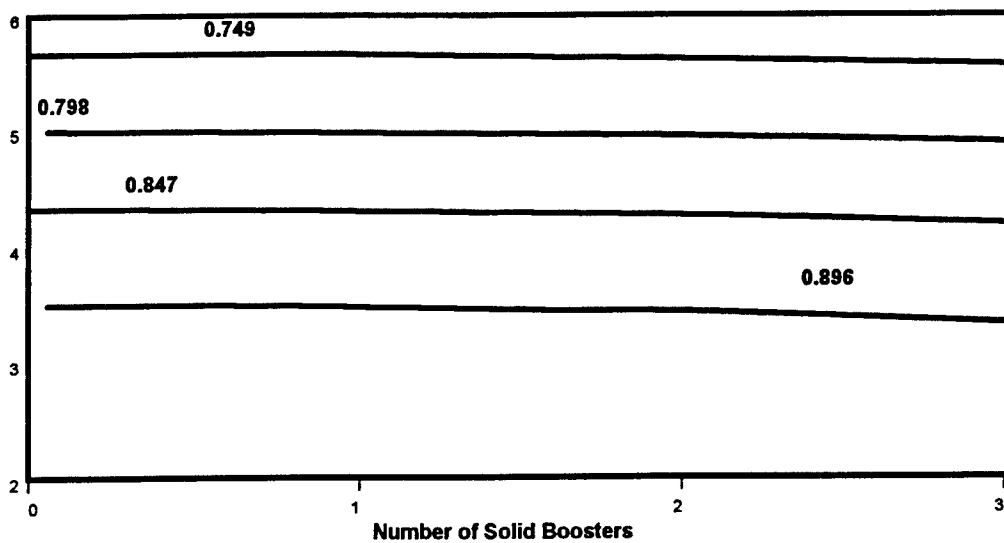


**Figure 2.4 : Propulsion Reliability Contour : Solid = 0.999, Liquid = 0.992
Blocked Series**

Table 1. Non-Time Dependent Propulsion Reliability, R_1 , when $p_1 = 0.9999$, $p_2 = 0.9990$ and 0.9999

		$p_2 = 0.9990$			
		n_1			
		0	1	2	3
n_2	2	0.9960	0.9959	0.9956	0.9951
	3	0.9910	0.9909	0.9906	0.9901
	4	0.9840	0.9839	0.9836	0.9831
	5	0.9751	0.9750	0.9747	0.9742
	6	0.9641	0.9640	0.9637	0.9632

		$p_2 = 0.9999$			
		n_1			
		0	1	2	3
n_2	2	0.9996	0.9995	0.9992	0.9987
	3	0.9991	0.9990	0.9987	0.9982
	4	0.9984	0.9983	0.9980	0.9975
	5	0.9975	0.9974	0.9971	0.9966
	6	0.9964	0.9963	0.9960	0.9955

Tables 2. Non-Time Dependent Propulsion Reliability, R_1 , when $p_1 = 0.999$, and $p_2 = 0.992$ and 0.999

		$p_2 = 0.992$			
		n_1			
		0	1	2	3
n_2	2	0.9681	0.9671	0.9641	0.9591
	3	0.9286	0.9276	0.9246	0.9196
	4	0.8735	0.8725	0.8695	0.8645
	5	0.8032	0.8022	0.7992	0.7942
	6	0.7177	0.7167	0.7137	0.7087

		$p_2 = 0.999$			
		n_1			
		0	1	2	3
n_2	2	0.9960	0.9950	0.9920	0.9870
	3	0.9910	0.9900	0.9870	0.9820
	4	0.9840	0.9830	0.9800	0.9750
	5	0.9751	0.9741	0.9711	0.9661
	6	0.9641	0.9631	0.9601	0.9551

R_1 is 0.995 (one catastrophic failure in 200 attempts), then with $(n_1 = 2, n_2 = 4)$, we need $p_2 = 0.9997$ for $p_1 = 0.9999$ as it can be seen from Figure 1.1. Similarly with $(n_1 = 3, n_2 = 6)$, we need $p_2 = 0.9999$ for $p_1 = 0.9999$. However, with neither $(n_1 = 2, n_2 = 4)$ nor $(n_1 = 3, n_2 = 6)$, we can achieve the cluster reliability $R_1 = 0.995$ for $p_1 = 0.999$. This can be done for $(n_1 = 0, n_2 = 2)$ with $p_2 = 0.999$. For an experimental SSTO with 1/200 catastrophic failure rate, a propulsion cluster of two liquid engines with each of 0.999 reliability is required. More liquid engines or strap-on solid boosters lower the overall vehicle reliability. Current Space Shuttle Main Engines (SSME) have demonstrated close to 0.999 reliability after approximately 2,000 full-duration tests since 1979 (Biggs (1997)).

Time Dependent Reliability : Blocked Series System

We now study the dependence of R_2 , defined in (4), on t , n_1 , and n_2 . For $n_1 = 1, 2$, and $n_2 = 2, 3, 4$, we determine θ_1 and θ_2 so that $R_2 = 0.995$ for $t = 90$ sec and $t = 500$ sec. For $n_1 = 0$ and $n_2 = 2, 3, 4$, we find θ_2 so that $R_2 = 0.995$ for $t = 500$ sec. As a result, with our determined values of θ_1 and θ_2 , $R_2 \geq 0.995$ for $0 \leq t \leq 500$. Figures 3.1 - 3.3 demonstrate the change in the cluster reliability R_2 with time t for $n_1 = 0, 1$, and 2. For $n_1 = 2$, we observe that after 90 sec the R_2 values stay at 0.995. For $n_1 = 1$, $R_2 = 0.995$ at $t = 90$ sec, jumps to $R_2 = 0.999$ at $t = 91$ sec, and finally becomes $R_2 = 0.995$ at $t = 500$ sec. For $n_1 = 0$, R_2 decreases from 1 to 0.995 for $t = 0$ sec to $t = 500$ sec. Figures 4.1 - 4.3 display the change in reliability per liquid engine over time for 2, 3, and 4 liquid engine vehicles. In order to achieve the cluster reliability of at least 0.995 during the 500 sec, the reliability per liquid engine drops to 0.998751 for a 2 liquid engines vehicle compared to 0.999687 for a 4 liquid engines vehicle with 2 solid boosters for both. For a vehicle with $n_1 = 2, n_2 = 2$, the reliability per liquid engine at 500 sec is 0.99875. If we calculate the cluster reliability at 500 sec by $(0.99875)^2$, we get 0.997502 which is much higher than 0.995 obtained from the time-dependent exponential model.

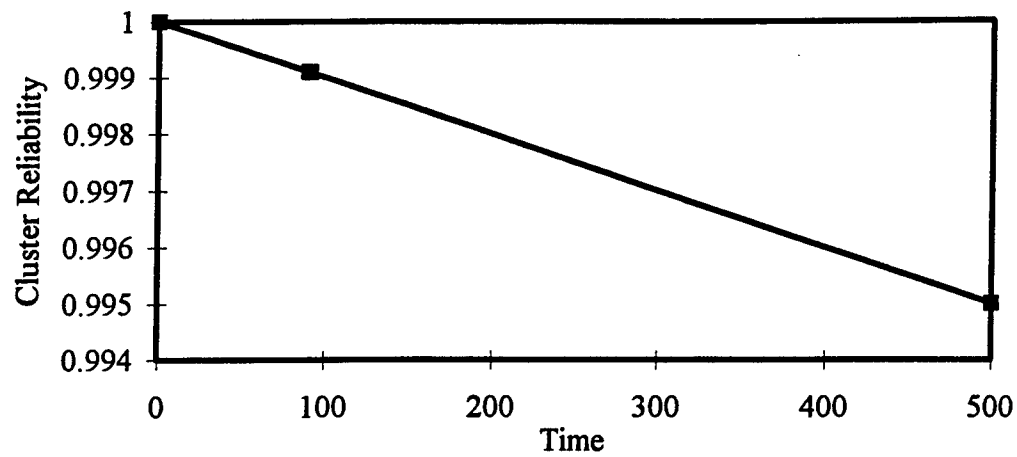


Figure 3.1. Cluster Reliability versus Time when Solid = 0 : Blocked Series

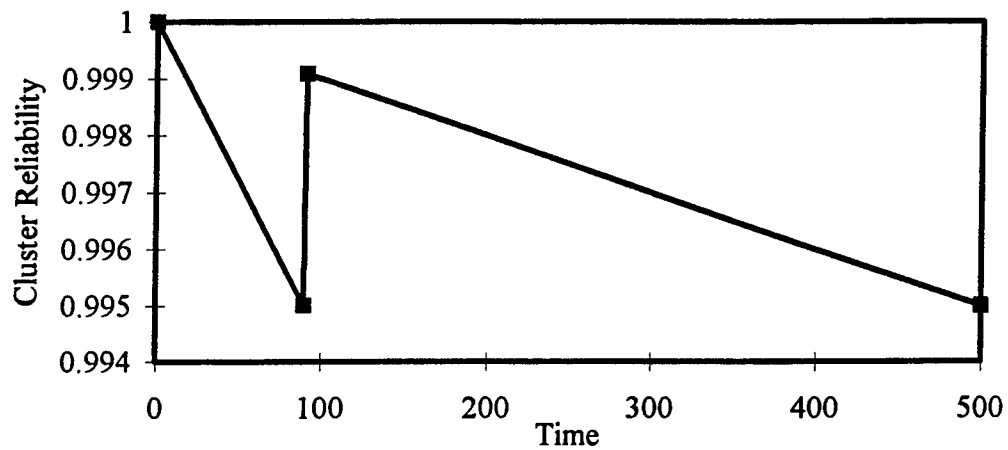


Figure 3.2. Cluster Reliability versus Time when Solid = 1 : Blocked Series

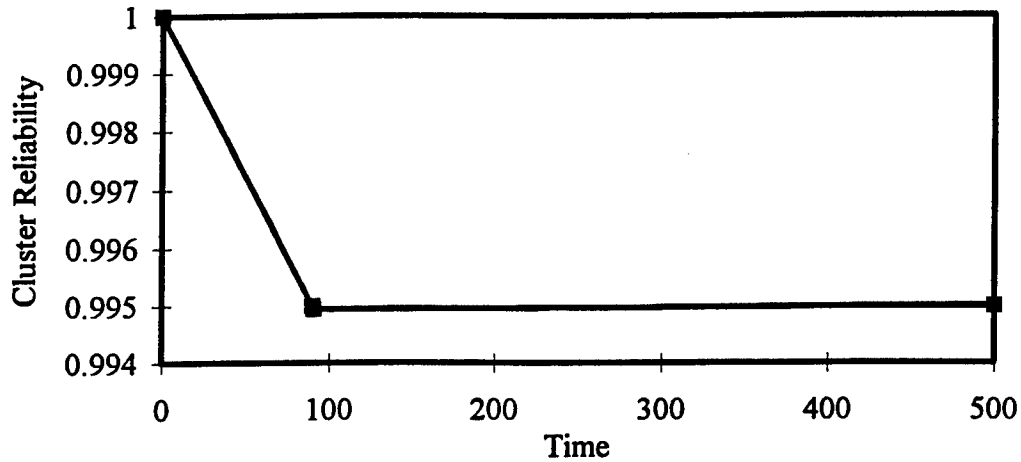
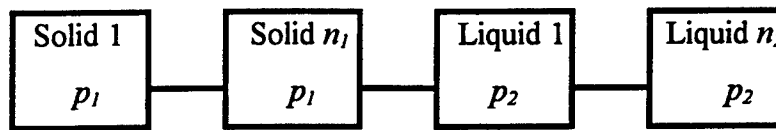


Figure 3.3. Cluster Reliability versus Time when Solid = 2 : Blocked Series

Propulsion Reliability Models: Series System

We now present the formula for calculating the non-time dependent propulsion reliability of a space vehicle. We assume that the whole system with solid boosters and liquid engines is working in a serial manner without any blocking as follows:



Series System

Then the non-time dependent cluster reliability R_3 of the space vehicle can be expressed as

$$R_3 = p_1^{n_1} p_2^{n_2} . \quad (5)$$

Notice that it is always true that R_3 , defined in (5), satisfies $0 \leq R_3 \leq 1$.

We now present the formula for calculation the time dependent propulsion reliability of a space vehicle under the assumption of the Exponential Model defined in (3).

Considering the operation times of solid boosters and liquid engines, the time dependent

cluster reliability R_4 of the space vehicle can be expressed as

$$R_4 = (e^{(-t/\theta_1)})^{n_1} (e^{(-t/\theta_2)})^{n_2}, 0 \leq t \leq 90,$$

$$R_4 = (e^{(-t/\theta_2)})^{n_2}, 90 < t \leq 500. \quad (6)$$

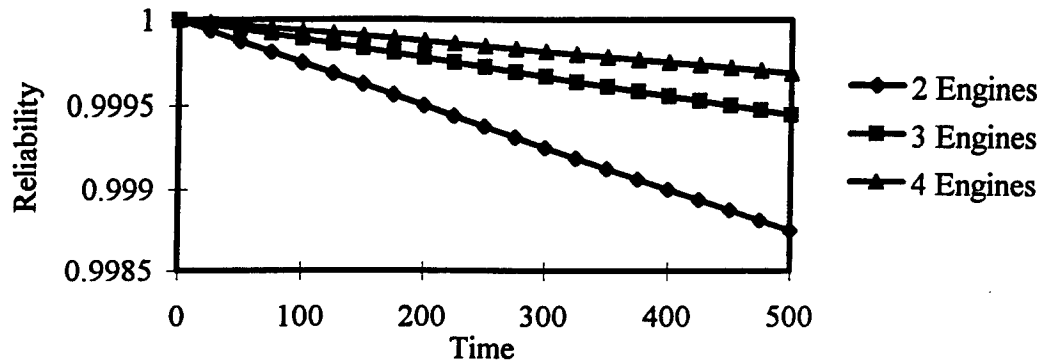


Figure 4.1. Reliability per Liquid Engine : Liquid = 2,3,4, Solid = 0 : Blocked Series

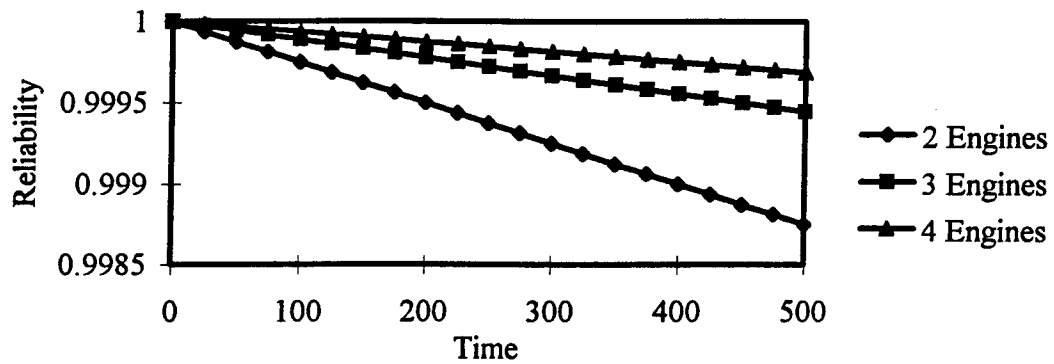


Figure 4.2. Reliability per Liquid Engine : Liquid = 2,3,4, Solid = 1 : Blocked Series

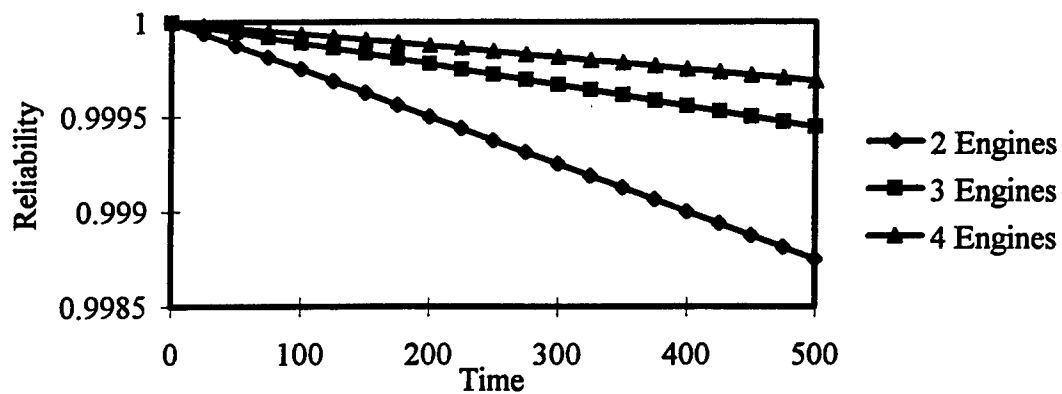


Figure 4.3. Reliability per Liquid Engine : Liquid = 2,3,4, Solid = 2 : Blocked Series

Non-Time Dependent Reliability: Series System

We now study the dependence of R_3 , defined in (5), on n_1 and n_2 . Figures 5.1 and 5.2 display R_3 lines for $(n_1, n_2) = (0, 2), (2, 4), (3, 6)$ and $p_1 = 0.9999$ and 0.999 , respectively.

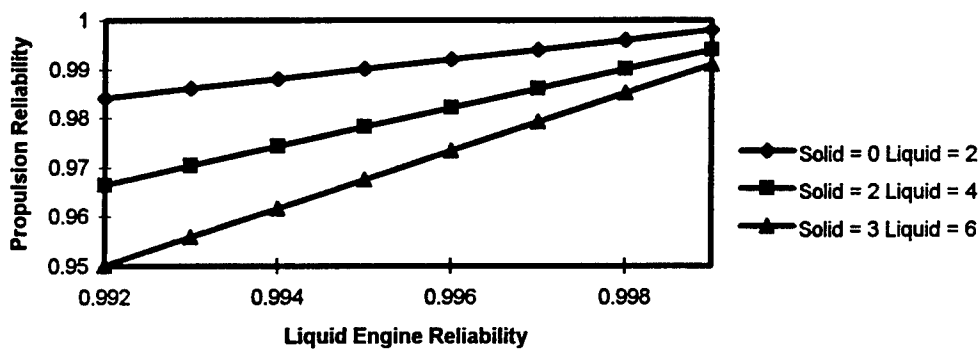
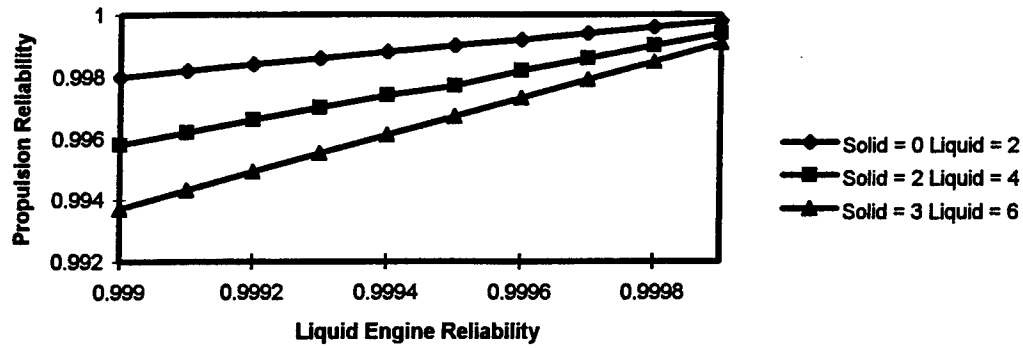


Figure 5.1: Propulsion Reliability by Liquid Engine Reliability when Solid Booster Reliability = 0.999 : Series



**Figure 5.2 : Propulsion Reliability by Liquid Engine Reliability
when Solid Booster Reliability = 0.9999 : Series**

Figures 6.1 - 6.4 display contour plots of R_3 values. We observe that the contour plots of R_3 for Methods 1 and 2 are different when $p_1 = p_2$ as can be seen in Figures 2.1 and 6.1 as well as in Figures 2.3 and 6.3. However, the contour plots of R_3 for Methods 1 and 2 are very similar when p_1 and p_2 differ widely as can be seen in Figures 2.2 and 6.2 as well as in Figures 2.4 and 6.4.

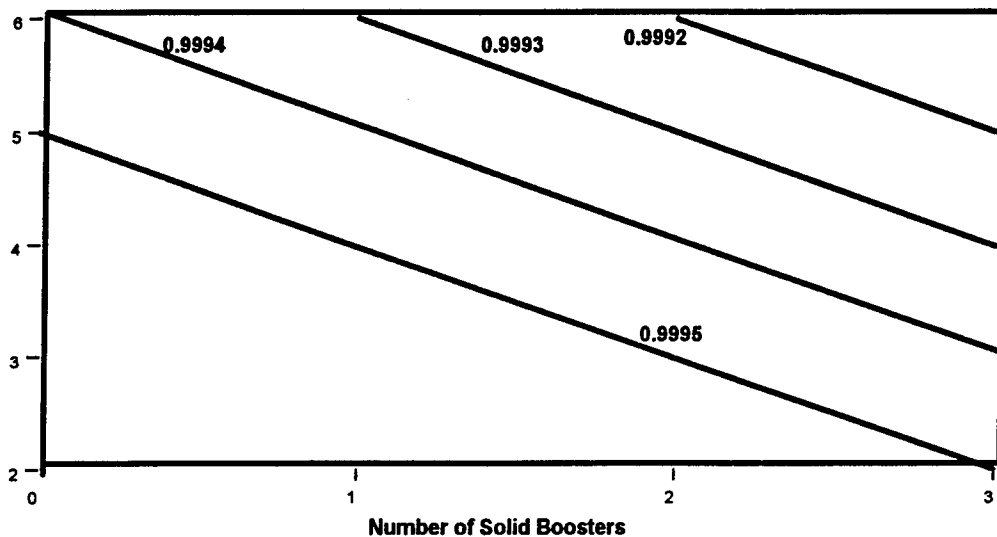


Figure 6.1. Propulsion Reliability Contour : Solid = 0.9999, Liquid = 0.9999 : Series

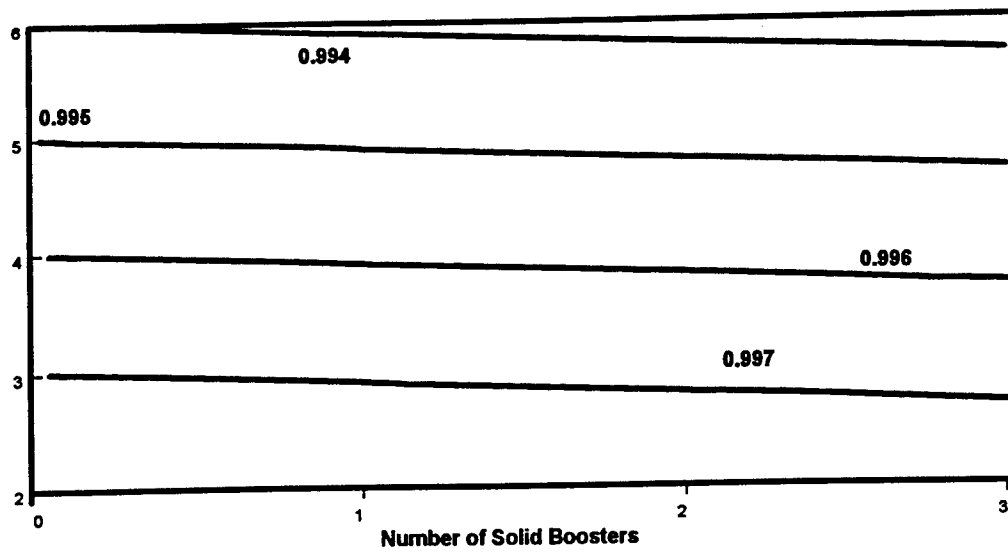


Figure 6.2. Propulsion Reliability Contour : Solid = 0.9999, Liquid = 0.999 : Series

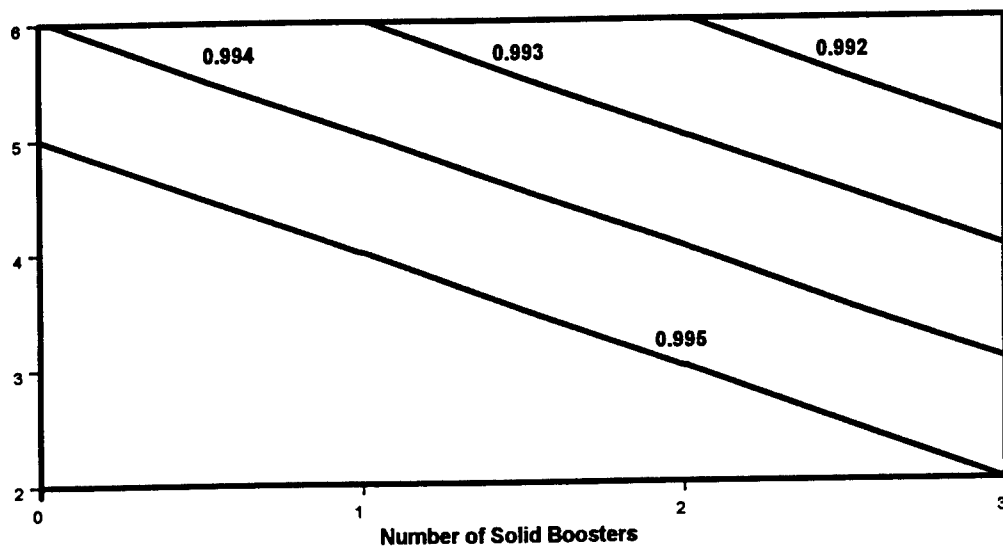


Figure 6.3. Propulsion Reliability Contour : Solid = 0.999, Liquid = 0.999 : Series

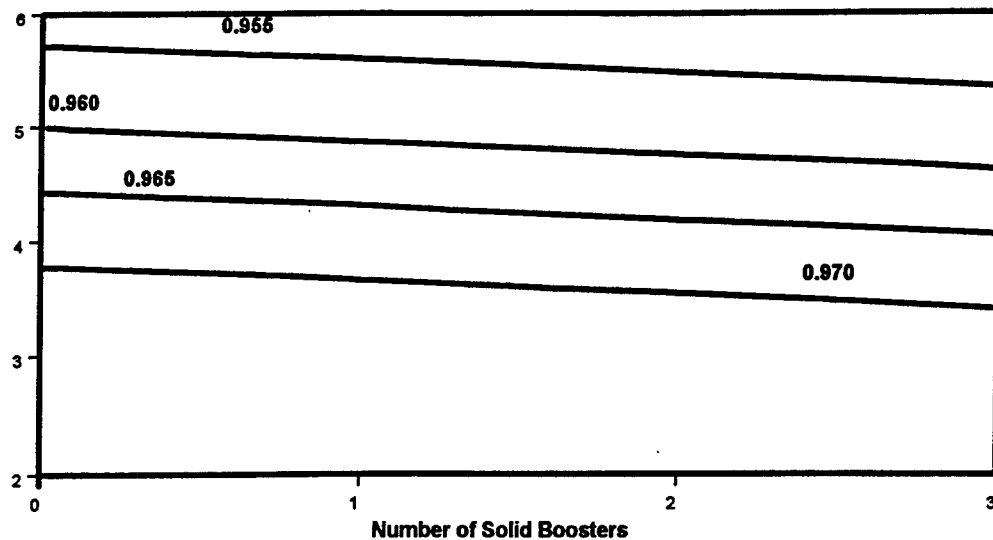


Figure 6.4. Propulsion Reliability Contour : Solid = 0.999, Liquid = 0.992 : Series

Time Dependent Reliability: Series System

We now study the dependence of R_4 , defined in (6), on t , n_1 , and n_2 . Figures 7.1- 7.3 show the change in the cluster reliability R_4 with time t for $n_1 = 0, 1$, and 2 . The comparison of R_4 values from Methods 1 and 2 can be made from Figures 3.1-3.3 and Figures 7.1-7.3. The R_4 values are very similar except for $n_1 = 2$ as can be seen from Figures 3.3 and 7.3. In Method 1, the R_4 values stay at 0.995 for $n_1 = 2$ for $t \geq 90$ but ,in Method 2, the R_4 value jumps from 0.995 to 0.999 for $t = 90$ to the immediately higher t and drops linearly to 0.995 at $t = 500$. Figures 8.1-8.3 display the change in reliability per liquid engine, under Method 2, over time for 2,3, and 4 liquid engine vehicles. Methods 1 and 2 resemble each other with respect to the change in reliability per liquid engine as can be seen from Figures 4.1-4.3 and 8.1-8.3.

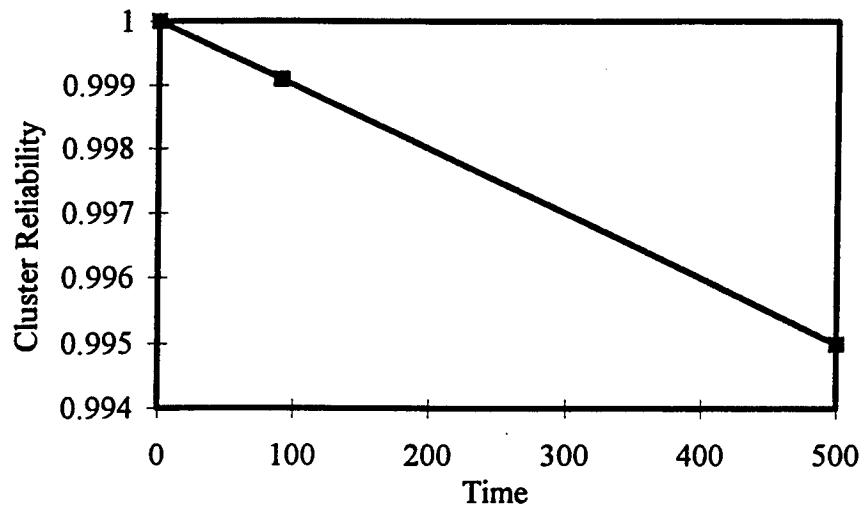


Figure 7.1. Cluster Reliability versus Time when Solid = 0 : Series

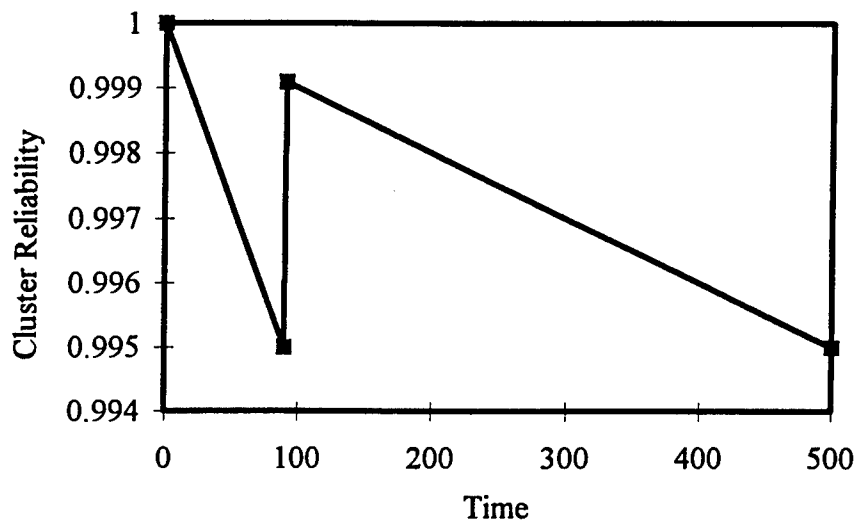


Figure 7.2. Cluster Reliability versus Time when Solid = 1 : Series

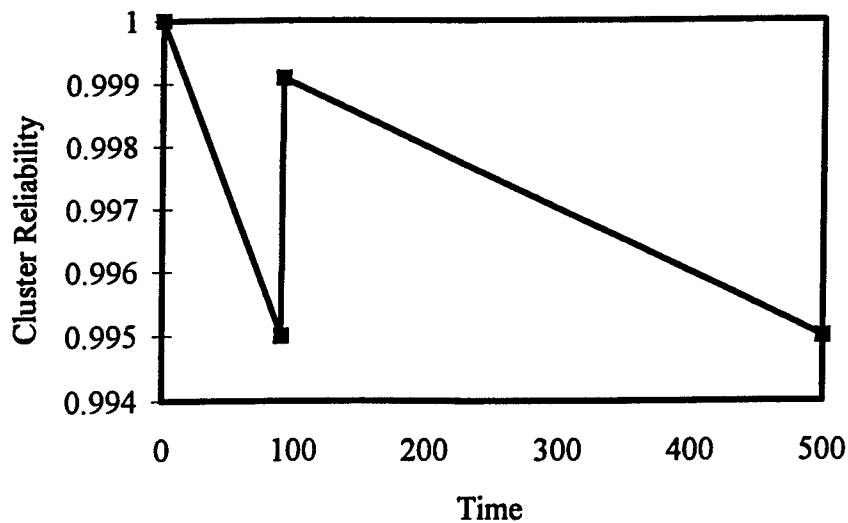


Figure 7.3. Cluster Reliability versus Time when Solid = 2 : Series

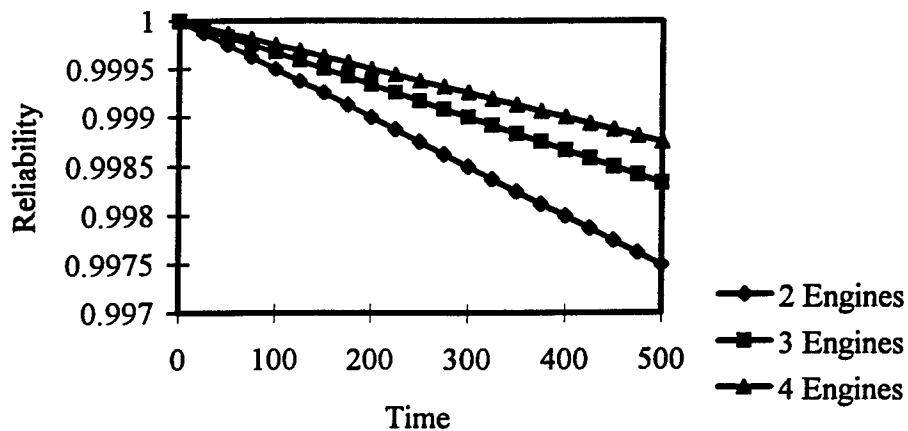


Figure 8.1. Reliability per Liquid Engine : Liquid = 2,3,4, Solid = 0 : Series

Conclusions

This study is on the propulsion reliability (R) of an SSTO vehicle as a function of the number of solid boosters (n_1), the reliability per solid booster (p_1), the number of liquid engines (n_2), and the reliability per liquid engines (p_2). Both time dependent and non-time dependent models are considered for p_1 and p_2 . Two models, series and blocked series, are considered for R . Our findings for non-time dependent

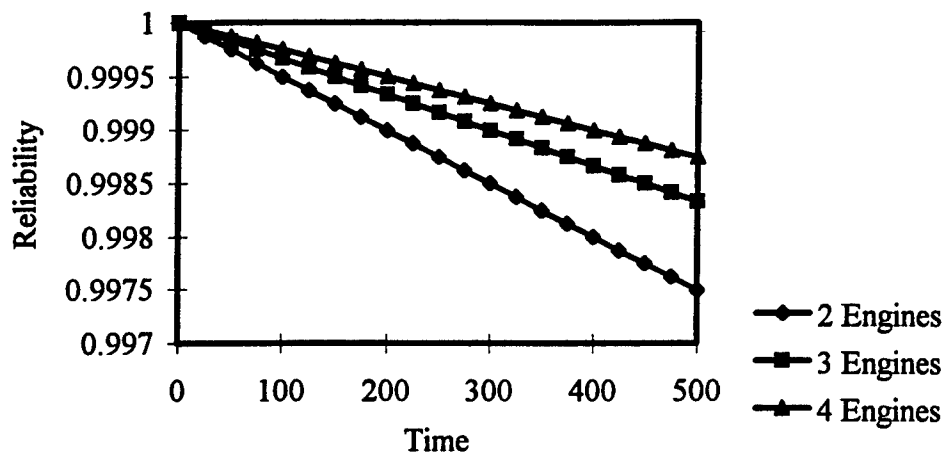


Figure 8.2. Reliability per Liquid Engine : Liquid = 2,3,4, Solid = 1 : Series

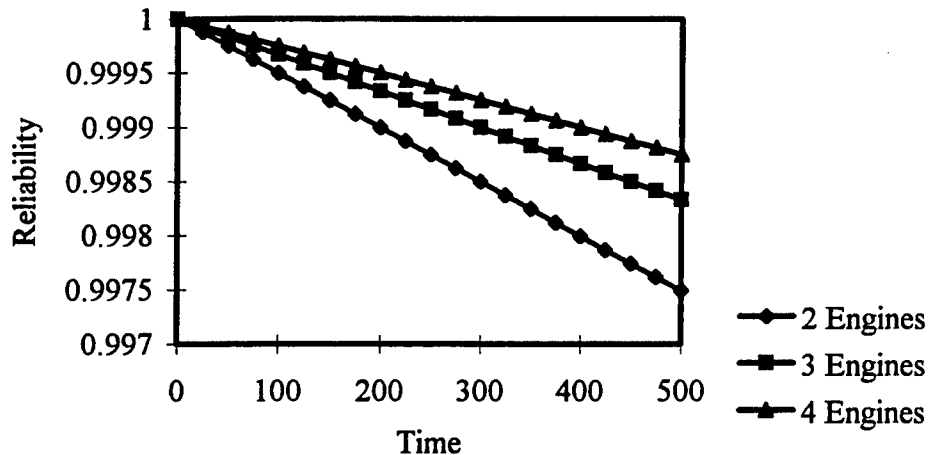


Figure 8.3. Reliability per Liquid Engine : Liquid = 2,3,4, Solid = 2 : Series

blocked series reliability model with $R \geq 0.995$ are summarized in Table 3. Table 3 describes the number of solid boosters and liquid engines to choose for targeting the propulsion reliability at 0.995. The number of liquid engines is recommended to be two or three and the number of solid boosters is recommended to be zero or one if their reliabilities are in between 0.9990 and 0.9995. In order to have more solid boosters and liquid engines with the same desired propulsion reliability 0.995, we need their reliabilities to be higher than 0.9995. Our findings for series model are similar to block series model. For the time dependent model, the propulsion cluster reliability drops rapidly over time in

presence of solid boosters but then after 90 seconds it jumps higher and decays at a much slower rate or remains the same. Moreover, for maintaining the propulsion reliability at 0.995 or higher over 500 seconds, the reliability per liquid engine drops more rapidly over time for four liquid engines than two or three liquid engines.

Table 3. Solutions for n_1 and n_2 to have at least 0.995 for R in the non-time dependent case

Model	p_1 Solid	p_2 Liquid	n_1 Solid	n_2 Liquid
Blocked Series	0.9990	0.9990	0,1	2
		0.9995	0	2,3
			1	2
		0.9999	0,1	2,3,4,5,6
			2	2,3
	0.9995	0.9990	0,1	2
		0.9995	0,1	2,3
			2	2
		0.9999	0,1	2,3,4,5,6
			2	2,3,4,5
			3	2
	0.9999	0.9990	0,1,2,3	2
		0.9995	0,1,2	2,3
			3	2
		0.9999	0,1,2,3	2,3,4,5,6

Acknowledgments

I would like to thank Terence Galati for the valuable discussions, guidance, and information. I am grateful to Francis McDougall for all his help and kindness. My sincere thanks also to Dr. Ray Moszee and to the Air Force Office of Scientific Research for making this possible.

References

- Biggs, B. (1997). *SSME Flight Reliability Determination*. Rocketdyne.
- Elsayed, E. A. (1996). *Reliability Engineering*. Addison Wesley Longman, Inc., Massachusetts.
- Lloyd, D. K., and Lipow, M. (1984). *Reliability: Management, Methods, and Mathematics*. The American Society for Quality Control, Milwaukee, Wisconsin.
- Report of the *Presidential Commission on the Space Shuttle Challenger Accident*. (1986) : Prepared by W. P. Rogers et al., Washington, D. C.

ASYMPTOTIC ANALYSIS OF THE NATURAL SYSTEM
MODES OF COUPLED BODIES IN THE LARGE
SEPARATION, LOW-FREQUENCY REGIME

George W. Hanson
Associate Professor
Department of Electrical Engineering and Computer Science

University of Wisconsin-Milwaukee
3200 N. Cramer Street
Milwaukee, Wisconsin 53211

Final Report for:
Summer Faculty Research Program
Phillips Laboratory

Sponsored by:
Air Force Office of Scientific Research
Bolling Air Force Base, DC

and

Phillips Laboratory

July 1997

ASYMPTOTIC ANALYSIS OF THE NATURAL SYSTEM
MODES OF COUPLED BODIES IN THE LARGE
SEPARATION, LOW-FREQUENCY REGIME

George W. Hanson
Associate Professor
Department of Electrical Engineering and Computer Science
University of Wisconsin-Milwaukee

Abstract

In this report we examine the natural electromagnetic system modes (characteristic frequencies and currents) of two coupled bodies in the limit of large separation. It is known that when objects are situated such that they may interact electromagnetically, natural modes of the coupled system occur. These modes differ from the natural modes of the isolated bodies, but may be related to the isolated body modes for some situations. Here we treat an N-body scattering problem in the limit of large separation by replacing the bodies with equivalent dipole moments. The natural frequencies are obtained as singular points in the scattering solution. For the special case of two coupled objects, a simple equation for the natural system frequencies is obtained which shows that the real radian system frequency approaches the origin as $1/r$, independent of the relative orientation and type of the two bodies. The damping coefficient approaches the origin approximately logarithmically, as a function of the body orientation and type. This simple equation leads to classification and ordering of some system modes based on their behavior in the limit of large separation. Using this formulation, the natural system modes of two coupled wires are investigated for large separation between the wires, and compared to an integral equation solution.

ASYMPTOTIC ANALYSIS OF THE NATURAL SYSTEM MODES OF COUPLED BODIES IN THE LARGE SEPARATION, LOW-FREQUENCY REGIME

George W. Hanson

I. Introduction

The electromagnetic response of coupled bodies is of interest in many applications, including target detection and identification. In this note we consider the frequency (s-plane) behavior of the system resonances of coupled objects in the limit of large separation.

In an early paper relating to the singularity expansion method (SEM) it was observed that the SEM frequencies of an isolated thin wire scatterer can be grouped in layers in the s-plane nearly parallel to the $j\omega$ axis [1]. These resonances are further identified by their position within these layers. This observation naturally leads to the notation for the complex frequencies $s_{n,l}^0$, where n denotes the n th pole as measured from the $\text{Re}(s)$ axis in the l th layer, measured from the $j\omega$ axis. Similar groupings can be identified for other objects, but to illustrate the effect considered here the situation for thin wires will be described.

Shortly after the above observations were made concerning isolated wires, the natural system frequencies of coupled wires were studied. It was found that these system resonances exhibited some interesting characteristics as wire separation was varied [2]. To simplify the discussion, consider two identical wires, for which the system resonances can be divided into symmetric ($s_{n,l}^s$) and antisymmetric ($s_{n,l}^a$) modes [14]. As observed in [2] for two thin wire scatterers, the low-order system resonances ($s_{1,1}^{a,s}$) tended to spiral around the dominant isolated body resonance ($s_{1,1}^0$) as spacing between the objects was varied over some intermediate distance. As separation was further increased, the system resonances moved off towards the origin in the complex frequency plane, and other system modes from another layer moved in to take their place, again spiraling around $s_{1,1}^0$. Subsequent to [2], other papers further considered coupled wire scatterers [3]-[4].

The fact that the system frequencies eventually tended towards the origin as spacing is increased beyond some intermediate distance, rather than tending towards the isolated body resonances, was discussed in [2], and explained from a time-domain perspective in [5]. It was observed that the SEM system modes are global quantities for the coupled body system, and have no clear physical interpretation

prior to times when global modes can be established. Hence, in a two-body system the time period after which the scattered field from each body has interacted with the other body is designated as late time. During late time, the two objects interact electromagnetically, and global system modes are established. As spacing between the objects becomes large relative to the largest linear dimension of each body, the system resonances tend towards low frequencies since the time for a wave to travel between the two bodies becomes long. Eventually the spacing tends towards infinity, and the system resonances tend toward zero.

Since the resonances of a coupled system are rigorously obtained from a complicated (usually integral) system of equations, simple approximate formulas which describe the system resonance behavior as a function of body separation are of interest. For intermediate separations, perturbation formulas have been obtained which relate the natural system frequencies to the natural frequencies of the isolated bodies. Two related classes of perturbation solution have been obtained, both based upon the exact integral-operator description of the coupled system. The first method yields a quasi-analytic formula for the system frequencies of an object and a mirror object, separated by some intermediate distance. The resulting formula involves a numerically computed coefficient which only depends upon the isolated object's characteristics, multiplied by an exponential term which is a function of the separation between the objects [6]. The second method is more numerical in nature, yet represents a considerable simplification of the exact IEs and is applicable to a more general system of coupled bodies [7]. The formulation described in [7] was subsequently applied to a variety of coupled objects [5], [8]-[9].

In this note, we present a scattering formulation for N coupled objects valid in the limit of large separation between all objects. The system of scatterers are replaced by interacting dipole moments, which is a suitable approximation for large separations (which lead to low system frequencies). A simpler formulation is provided for two objects coupled in a mirror symmetric configuration. Singularities of the scattering solution are identified as natural frequencies, leading to the characteristic equation for natural frequencies of the coupled system. The example of two coupled wires is considered to demonstrate the accuracy of the asymptotic method, where the natural system frequencies from the asymptotic formulation are compared to those generated from a full-wave integral equation solution. The system modes are classified according to their behavior for large separation between the bodies, and some results for the natural currents are provided to examine their behavior in the corresponding limit.

II. Preliminary Relations

Consider Maxwell's curl equations for free space in the two-sided Laplace transform domain

$$\begin{aligned}\nabla \times \vec{E}(\vec{r}, s) &= -s \vec{B}(\vec{r}, s) - \vec{J}^m(\vec{r}, s) \\ \nabla \times \vec{H}(\vec{r}, s) &= s \vec{D}(\vec{r}, s) + \vec{J}^e(\vec{r}, s).\end{aligned}\quad (1)$$

The relationships between fields and currents are given in terms of four Green's dyadics as [10]

$$\begin{aligned}\vec{E}(\vec{r}, s) &= -s \mu_0 \langle \vec{G}_{e,e}(\vec{r}|\vec{r}', s); \vec{J}^e(\vec{r}', s) \rangle \\ &\quad + \langle \vec{G}_{e,m}(\vec{r}|\vec{r}', s); \vec{J}^m(\vec{r}', s) \rangle \\ \vec{H}(\vec{r}, s) &= -s \epsilon_0 \langle \vec{G}_{h,m}(\vec{r}|\vec{r}', s); \vec{J}^m(\vec{r}', s) \rangle \\ &\quad + \langle \vec{G}_{h,e}(\vec{r}|\vec{r}', s); \vec{J}^e(\vec{r}', s) \rangle\end{aligned}\quad (2)$$

where the bracket notation indicates a real inner product with integration over common spatial coordinates (typically volume or surface integration). The Green's dyadics are

$$\vec{G}_{e,e}(\vec{r}|\vec{r}', s) = PV [\vec{1} - \gamma^{-2} \nabla \nabla] G(\vec{r}|\vec{r}', s) + \gamma^{-2} \vec{L}(\vec{r}) \delta(\vec{r} - \vec{r}') \quad (3)$$

$$\vec{G}_{e,m}(\vec{r}|\vec{r}', s) = -\nabla G(\vec{r}|\vec{r}', s) \times \vec{1} \quad (4)$$

$$\vec{G}_{h,e}(\vec{r}|\vec{r}', s) = -\vec{G}_{e,m}(\vec{r}|\vec{r}', s) \quad (5)$$

$$\vec{G}_{h,m}(\vec{r}|\vec{r}', s) = \vec{G}_{e,e}(\vec{r}|\vec{r}', s) \quad (6)$$

where $G(\vec{r}|\vec{r}', s) = \frac{\gamma e^{-\xi}}{4\pi\xi}$ is the free-space scalar Green's function, with $\gamma = \frac{s}{c}$, $\xi = \gamma R$,

$c = (\epsilon_0 \mu_0)^{-1/2}$, and $R = |\vec{r} - \vec{r}'|$. The first term in (3) can be written as

$$\begin{aligned}[\vec{1} - \gamma^{-2} \nabla \nabla] G(\vec{r}|\vec{r}', s) &= \frac{\gamma e^{-\xi}}{4\pi} \{ [-2\xi^{-3} - 2\xi^{-2}] \vec{1}_R \vec{1}_R + [\xi^{-3} + \xi^{-2} + \xi^{-1}] [\vec{1} - \vec{1}_R \vec{1}_R] \} \\ &= -\frac{\gamma e^{-\xi}}{4\pi} \{ [3\vec{1}_R \vec{1}_R - \vec{1}] (\xi^{-3} + \xi^{-2}) + [\vec{1}_R \vec{1}_R - \vec{1}] \xi^{-1} \}\end{aligned}\quad (7)$$

where $\vec{1}_R = \frac{\vec{r} - \vec{r}'}{|\vec{r} - \vec{r}'|}$, and $\vec{1} = \vec{1}_x \vec{1}_x + \vec{1}_y \vec{1}_y + \vec{1}_z \vec{1}_z$ is the identity dyadic. For later convenience, define

$$\vec{F}_{e,e}(\vec{r}|\vec{r}',s) \equiv \frac{e^{-\gamma R}}{4\pi} \left\{ [3\vec{1}_R\vec{1}_R - \vec{1}] \left(\frac{1}{\epsilon_0 R^3} + \frac{sZ_0}{R^2} \right) + [\vec{1}_R\vec{1}_R - \vec{1}] \frac{s^2\mu_0}{R} \right\} \quad (8)$$

with $Z_0 = \sqrt{\frac{\mu_0}{\epsilon_0}}$, such that the $\vec{G}_{e,e}$ term can be expressed as

$$\vec{G}_{e,e}(\vec{r}|\vec{r}',s) = PV \frac{-1}{s^2\mu_0} \vec{F}_{e,e}(\vec{r}|\vec{r}',s) + \gamma^{-2} \vec{L}(\vec{r}) \delta(\vec{r} - \vec{r}') . \quad (9)$$

The magnetic Green's dyadic, $\vec{G}_{e,m}$, can be expressed as

$$\vec{G}_{e,m}(\vec{r}|\vec{r}',s) = -\nabla G(\vec{r}|\vec{r}',s) \times \vec{1} = \frac{e^{-\gamma R}}{4\pi} \left[\frac{1}{R^2} + \frac{s}{RC} \right] \vec{1}_R \times \vec{1} \quad (10)$$

where upon defining for later convenience

$$F_{e,m}(\vec{r}|\vec{r}',s) \equiv \frac{e^{-\gamma R}}{4\pi} \left(\frac{s\mu_0}{R^2} + \frac{s^2\mu_0}{RC} \right) \quad (11)$$

the magnetic Green's dyadic can be written as

$$\vec{G}_{e,m}(\vec{r}|\vec{r}',s) = \frac{1}{s\mu_0} F_{e,m}(\vec{r}|\vec{r}',s) \vec{1}_R \times \vec{1} . \quad (12)$$

In (3), the PV notation indicates that the corresponding term should be integrated in the principal value sense [10], where

$$\vec{L}(\vec{r}) = \frac{1}{4\pi} \int_{S_b} \frac{\vec{1}_S(\vec{r}') \vec{1}_{R'}(\vec{r}|\vec{r}')}{|\vec{r} - \vec{r}'|^2} dS' \quad (13)$$

is the depolarizing dyadic integral, evaluated over the surface S_b of the exclusion volume V_b excluded in the PV integration. In (13), $\vec{1}_{R'}(\vec{r}|\vec{r}') = -\vec{1}_R(\vec{r}|\vec{r}') = \vec{1}_R(\vec{r}'|\vec{r})$, and $\vec{1}_S(\vec{r})$ is the unit normal vector to S at \vec{r} . Note that the $\vec{G}_{\{h,m\}}^{(e,e)}$ terms are properly interpreted as distributions.

III. Scattering formulation

Consider a N-body scattering problem which can be analyzed by formulating a coupled set of integral equations for the current (surface or volume polarization) induced on/in the objects by an incident field. When the separation between all objects becomes large compared to the largest linear dimension of each object, and in the limit of low frequency, the formulation can be considerably simplified by replacing each object with equivalent dipole moments. This follows from the fact that the electric and magnetic dipole moment terms dominate the fields due to a given current (as in a multipole expansion of the current) for large distances and low frequencies [12]. To formulate the desired set of equations, the scatterers, which are assumed to reside in free space, are replaced with dipole moments $\vec{P}^{(\beta)}, \vec{m}^{(\beta)}$ for $\beta = 1, 2, \dots, N$ corresponding to object 1, 2, ..., N, respectively, as shown in Fig. 1. The dipoles are considered to be generated by fields via polarizability dyadics as

$$\begin{aligned}\vec{P}^{(\beta)}(s) &= \epsilon_0 \vec{P}^{(\beta)}(s) \cdot \vec{E}(\vec{r}_\beta, s) \\ \vec{m}^{(\beta)}(s) &= \vec{M}^{(\beta)}(s) \cdot \vec{H}(\vec{r}_\beta, s)\end{aligned}\tag{14}$$

where the fields (\vec{E}, \vec{H}) are the total fields due to all dipoles not located at \vec{r}_β , plus any externally impressed field. The polarizability dyadics are symmetrical for reciprocal media,

$$\begin{aligned}\vec{P}^{(\beta)\top}(s) &= \vec{P}^{(\beta)}(s) \\ \vec{M}^{(\beta)\top}(s) &= \vec{M}^{(\beta)}(s)\end{aligned}\tag{15}$$

and as $s \rightarrow 0$ [12]

$$\begin{aligned}\vec{P}^{(\beta)}(s) &= \vec{P}_0^{(\beta)} + O(s) \\ \vec{M}^{(\beta)}(s) &= \vec{M}_0^{(\beta)} + O(s).\end{aligned}\tag{16}$$

The currents associated with the dipole moments are

$$\begin{aligned}\vec{J}_e^{(\beta)} &= s \vec{P}^{(\beta)} \delta(\vec{r} - \vec{r}_\beta) \\ \vec{J}_m^{(\beta)} &= s \mu_0 \vec{m}^{(\beta)} \delta(\vec{r} - \vec{r}_\beta).\end{aligned}\tag{17}$$

Inserting (17) into (2) leads to the fields at \vec{r}_α maintained by electric and magnetic dipoles located at \vec{r}_β as

$$\begin{aligned}
\vec{E}^{(\alpha, \beta)}(\vec{r}_\alpha, s) &= \vec{F}_{e, e}(\vec{r}_\alpha | \vec{r}_\beta, s) \cdot \vec{P}^{(\beta)}(s) + F_{e, m}(\vec{r}_\alpha | \vec{r}_\beta, s) (\vec{l}_{R_{\alpha, \beta}} \times \vec{l}) \cdot \vec{m}^{(\beta)}(s) \\
\vec{H}^{(\alpha, \beta)}(\vec{r}_\alpha, s) &= -\frac{1}{\mu_0} F_{e, m}(\vec{r}_\alpha | \vec{r}_\beta, s) (\vec{l}_{R_{\alpha, \beta}} \times \vec{l}) \cdot \vec{P}^{(\beta)}(s) + \epsilon_0 \vec{F}_{e, e}(\vec{r}_\alpha | \vec{r}_\beta, s) \cdot \vec{m}^{(\beta)}(s)
\end{aligned}
\tag{18}$$

where

$$\begin{aligned}
\vec{F}_{e, e}(\vec{r}_\alpha | \vec{r}_\beta, s) &= \frac{e^{-\gamma R_{\alpha, \beta}}}{4\pi} \left\{ [3\vec{l}_{R_{\alpha, \beta}}\vec{l}_{R_{\alpha, \beta}} - \vec{l}\vec{l}] \left(\frac{1}{\epsilon_0 R_{\alpha, \beta}^3} + \frac{sZ_0}{R_{\alpha, \beta}^2} \right) + [\vec{l}_{R_{\alpha, \beta}}\vec{l}_{R_{\alpha, \beta}} - \vec{l}\vec{l}] \frac{s^2 \mu_0}{R_{\alpha, \beta}} \right\} \\
F_{e, m}(\vec{r}_\alpha | \vec{r}_\beta, s) &= \frac{e^{-\gamma R_{\alpha, \beta}}}{4\pi} \left\{ \frac{\mu_0 s}{R_{\alpha, \beta}^2} + \frac{\mu_0 s^2}{R_{\alpha, \beta} c} \right\}
\end{aligned}
\tag{19}$$

with $\vec{l}_{R_{\alpha, \beta}} = \frac{\vec{r}_\alpha - \vec{r}_\beta}{|\vec{r}_\alpha - \vec{r}_\beta|}$ being the unit vector from \vec{r}_β to \vec{r}_α , and $R_{\alpha, \beta} = |\vec{r}_\alpha - \vec{r}_\beta|$. The total field

at \vec{r}_α due to N-1 dipoles located at \vec{r}_β , $\beta=1, 2, \dots, N$, $\beta \neq \alpha$ is

$$\begin{aligned}
\vec{E}(\vec{r}_\alpha, s) &= \sum_{\substack{\beta=1 \\ \beta \neq \alpha}}^N \vec{E}^{(\alpha, \beta)}(\vec{r}_\alpha, s) \\
\vec{H}(\vec{r}_\alpha, s) &= \sum_{\substack{\beta=1 \\ \beta \neq \alpha}}^N \vec{H}^{(\alpha, \beta)}(\vec{r}_\alpha, s) .
\end{aligned}
\tag{20}$$

Considering the scatterers to be as shown in Fig. 1, a coupled system of equations for the induced dipole moments can be written down as

$$\begin{aligned}
\vec{P}^{(\alpha)}(s) &= \epsilon_0 \vec{P}_0^{(\alpha)} \cdot \left[\vec{E}^{(inc)}(\vec{r}_\alpha, s) + \sum_{\substack{\beta=1 \\ \beta \neq \alpha}}^N \vec{E}^{(\alpha, \beta)}(\vec{r}_\alpha, s) \right] \\
\vec{m}^{(\alpha)}(s) &= \vec{M}_0^{(\alpha)} \cdot \left[\vec{H}^{(inc)}(\vec{r}_\alpha, s) + \sum_{\substack{\beta=1 \\ \beta \neq \alpha}}^N \vec{H}^{(\alpha, \beta)}(\vec{r}_\alpha, s) \right]
\end{aligned}
\tag{21}$$

$\alpha = 1, 2, \dots, N$

where the fields $(\vec{E}^{(inc)}, \vec{H}^{(inc)})$ are externally impressed fields. Defining

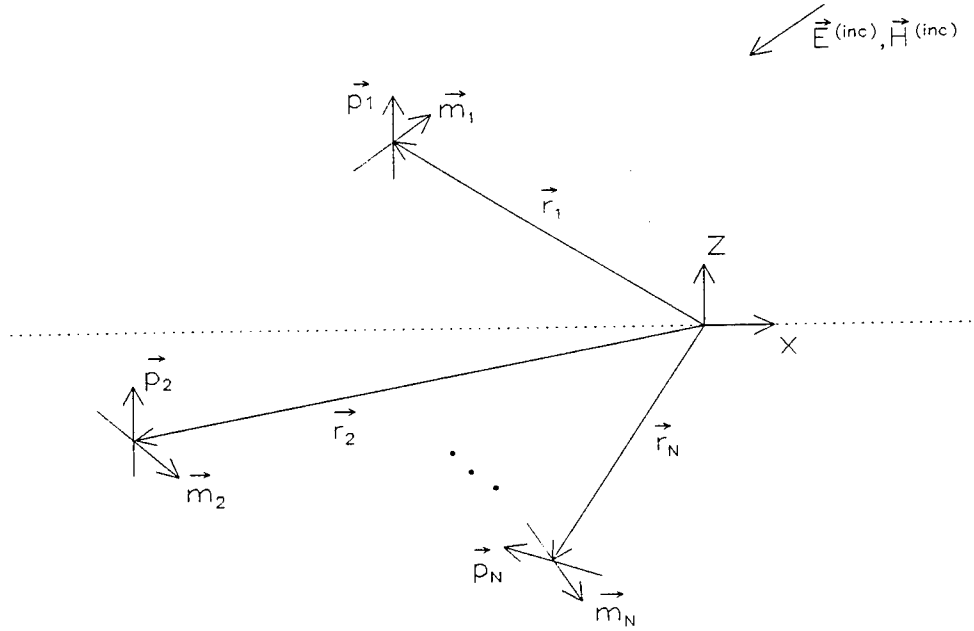


Fig. 1. Configuration of N interacting dipoles.

$$\begin{aligned}\vec{F}_{e,e}^{(\alpha,\beta)} &\equiv \vec{F}_{e,e}(\vec{r}_\alpha | \vec{r}_\beta, S) \\ F_{e,m}^{(\alpha,\beta)} &\equiv F_{e,m}(\vec{r}_\alpha | \vec{r}_\beta, S) = F_{e,m}(\vec{r}_\beta | \vec{r}_\alpha, S)\end{aligned}\quad (22)$$

the set of equations (21) can be written as

$$\begin{aligned}\vec{P}^{(\alpha)}(S) - \epsilon_0 \vec{P}_0^{(\alpha)} \cdot \sum_{\substack{\beta=1 \\ \beta \neq \alpha}}^N \left[\vec{F}_{e,e}^{(\alpha,\beta)} \cdot \vec{P}^{(\beta)} + F_{e,m}^{(\alpha,\beta)} (\vec{1}_{R_{\alpha,\beta}} \times \vec{1}) \cdot \vec{m}^{(\beta)} \right] &= \epsilon_0 \vec{P}_0^{(\alpha)} \cdot \vec{E}^{(inc)}(\vec{r}_\alpha, S) \\ \vec{m}^{(\alpha)}(S) - \vec{M}_0^{(\alpha)} \cdot \sum_{\substack{\beta=1 \\ \beta \neq \alpha}}^N \left[-\frac{1}{\mu_0} F_{e,m}^{(\alpha,\beta)} (\vec{1}_{R_{\alpha,\beta}} \times \vec{1}) \cdot \vec{P}^{(\beta)} + \epsilon_0 \vec{F}_{e,e}^{(\alpha,\beta)} \cdot \vec{m}^{(\beta)} \right] &= \vec{M}_0^{(\alpha)} \cdot \vec{H}^{(inc)}(\vec{r}_\alpha, S) \\ \alpha &= 1, 2, \dots, N\end{aligned}\quad (23)$$

It is convenient to write the above in block dyadic form

$$\begin{bmatrix} \tilde{\mathbf{I}}_{2 \times 2} & \tilde{\mathbf{Q}}_{2 \times 2}^{(1,2)}(s) & \tilde{\mathbf{Q}}_{2 \times 2}^{(1,3)}(s) & \dots & \tilde{\mathbf{Q}}_{2 \times 2}^{(1,N)}(s) \\ \tilde{\mathbf{Q}}_{2 \times 2}^{(2,1)}(s) & \tilde{\mathbf{I}}_{2 \times 2} & \tilde{\mathbf{Q}}_{2 \times 2}^{(2,3)}(s) & \dots & \tilde{\mathbf{Q}}_{2 \times 2}^{(2,N)}(s) \\ \tilde{\mathbf{Q}}_{2 \times 2}^{(3,1)}(s) & \tilde{\mathbf{Q}}_{2 \times 2}^{(3,2)}(s) & \tilde{\mathbf{I}}_{2 \times 2} & \dots & \tilde{\mathbf{Q}}_{2 \times 2}^{(3,N)}(s) \\ \vdots & \vdots & \vdots & \vdots & \vdots \\ \tilde{\mathbf{Q}}_{2 \times 2}^{(N,1)}(s) & \tilde{\mathbf{Q}}_{2 \times 2}^{(N,2)}(s) & \tilde{\mathbf{Q}}_{2 \times 2}^{(N,3)}(s) & \dots & \tilde{\mathbf{I}}_{2 \times 2} \end{bmatrix} \cdot \begin{bmatrix} \vec{\mathbf{d}}_{2 \times 1}^{(1)}(s) \\ \vec{\mathbf{d}}_{2 \times 1}^{(2)}(s) \\ \vec{\mathbf{d}}_{2 \times 1}^{(3)}(s) \\ \vdots \\ \vec{\mathbf{d}}_{2 \times 1}^{(N)}(s) \end{bmatrix} = \begin{bmatrix} \vec{\mathbf{F}}_{2 \times 1}^{(1)}(s) \\ \vec{\mathbf{F}}_{2 \times 1}^{(2)}(s) \\ \vec{\mathbf{F}}_{2 \times 1}^{(3)}(s) \\ \vdots \\ \vec{\mathbf{F}}_{2 \times 1}^{(N)}(s) \end{bmatrix} \quad (24)$$

where

$$\tilde{\mathbf{Q}}_{2 \times 2}^{(\alpha, \beta)}(s) \equiv \begin{bmatrix} -\epsilon_0 \vec{\mathbf{P}}_0^{(\alpha)} \cdot \vec{\mathbf{F}}_{e,e}^{(\alpha, \beta)} & -\epsilon_0 F_{e,m}^{(\alpha, \beta)} \vec{\mathbf{P}}_0^{(\alpha)} \cdot (\vec{\mathbf{I}}_{R_{\alpha, \beta}} \times \vec{\mathbf{I}}) \\ \frac{1}{\mu_0} F_{e,m}^{(\alpha, \beta)} \vec{\mathbf{M}}_0^{(\alpha)} \cdot (\vec{\mathbf{I}}_{R_{\alpha, \beta}} \times \vec{\mathbf{I}}) & -\epsilon_0 \vec{\mathbf{M}}_0^{(\alpha)} \cdot \vec{\mathbf{F}}_{e,e}^{(\alpha, \beta)} \end{bmatrix} \quad (25)$$

$$\tilde{\mathbf{I}}_{2 \times 2} \equiv \begin{bmatrix} \vec{\mathbf{I}} & \vec{\mathbf{0}} \\ \vec{\mathbf{0}} & \vec{\mathbf{I}} \end{bmatrix}, \quad \vec{\mathbf{d}}_{2 \times 1}^{(\alpha)}(s) \equiv \begin{bmatrix} \vec{\mathbf{P}}^{(\alpha)}(s) \\ \vec{\mathbf{M}}^{(\alpha)}(s) \end{bmatrix}, \quad \vec{\mathbf{F}}_{2 \times 1}^{(\alpha)}(s) \equiv \begin{bmatrix} \epsilon_0 \vec{\mathbf{P}}_0^{(\alpha)} \cdot \vec{\mathbf{E}}^{(inc)}(\vec{\mathbf{r}}_{\alpha}, s) \\ \vec{\mathbf{M}}_0^{(\alpha)} \cdot \vec{\mathbf{H}}^{(inc)}(\vec{\mathbf{r}}_{\alpha}, s) \end{bmatrix}. \quad (26)$$

Providing that the left-hand dyadic matrix is non-singular, (24) can be inverted to yield

$$\begin{bmatrix} \vec{\mathbf{d}}_{2 \times 1}^{(1)}(s) \\ \vec{\mathbf{d}}_{2 \times 1}^{(2)}(s) \\ \vec{\mathbf{d}}_{2 \times 1}^{(3)}(s) \\ \vdots \\ \vec{\mathbf{d}}_{2 \times 1}^{(N)}(s) \end{bmatrix} = \begin{bmatrix} \tilde{\mathbf{I}}_{2 \times 2} & \tilde{\mathbf{Q}}_{2 \times 2}^{(1,2)}(s) & \tilde{\mathbf{Q}}_{2 \times 2}^{(1,3)}(s) & \dots & \tilde{\mathbf{Q}}_{2 \times 2}^{(1,N)}(s) \\ \tilde{\mathbf{Q}}_{2 \times 2}^{(2,1)}(s) & \tilde{\mathbf{I}}_{2 \times 2} & \tilde{\mathbf{Q}}_{2 \times 2}^{(2,3)}(s) & \dots & \tilde{\mathbf{Q}}_{2 \times 2}^{(2,N)}(s) \\ \tilde{\mathbf{Q}}_{2 \times 2}^{(3,1)}(s) & \tilde{\mathbf{Q}}_{2 \times 2}^{(3,2)}(s) & \tilde{\mathbf{I}}_{2 \times 2} & \dots & \tilde{\mathbf{Q}}_{2 \times 2}^{(3,N)}(s) \\ \vdots & \vdots & \vdots & \vdots & \vdots \\ \tilde{\mathbf{Q}}_{2 \times 2}^{(N,1)}(s) & \tilde{\mathbf{Q}}_{2 \times 2}^{(N,2)}(s) & \tilde{\mathbf{Q}}_{2 \times 2}^{(N,3)}(s) & \dots & \tilde{\mathbf{I}}_{2 \times 2} \end{bmatrix}^{-1} \cdot \begin{bmatrix} \vec{\mathbf{F}}_{2 \times 1}^{(1)}(s) \\ \vec{\mathbf{F}}_{2 \times 1}^{(2)}(s) \\ \vec{\mathbf{F}}_{2 \times 1}^{(3)}(s) \\ \vdots \\ \vec{\mathbf{F}}_{2 \times 1}^{(N)}(s) \end{bmatrix} \quad (27)$$

Equation (27) provides a formal solution to the scattering problem for configurations and frequencies such that the dipole moment approximation is valid. Scattered fields are obtained by substituting (27) into (20).

Each dyadic block, with the exception of the identity blocks, is a function of complex frequency s . In this note we are primarily interested in determining the natural frequencies such that the left-hand block-dyadic matrix is singular. At a natural frequency,

$$\det \begin{bmatrix} \tilde{\mathbf{I}}_{2 \times 2} & \tilde{\mathbf{Q}}_{2 \times 2}^{(1,2)}(s) & \tilde{\mathbf{Q}}_{2 \times 2}^{(1,3)}(s) & \dots & \tilde{\mathbf{Q}}_{2 \times 2}^{(1,N)}(s) \\ \tilde{\mathbf{Q}}_{2 \times 2}^{(2,1)}(s) & \tilde{\mathbf{I}}_{2 \times 2} & \tilde{\mathbf{Q}}_{2 \times 2}^{(2,3)}(s) & \dots & \tilde{\mathbf{Q}}_{2 \times 2}^{(2,N)}(s) \\ \tilde{\mathbf{Q}}_{2 \times 2}^{(3,1)}(s) & \tilde{\mathbf{Q}}_{2 \times 2}^{(3,2)}(s) & \tilde{\mathbf{I}}_{2 \times 2} & \dots & \tilde{\mathbf{Q}}_{2 \times 2}^{(3,N)}(s) \\ \vdots & \vdots & \vdots & \vdots & \vdots \\ \tilde{\mathbf{Q}}_{2 \times 2}^{(N,1)}(s) & \tilde{\mathbf{Q}}_{2 \times 2}^{(N,2)}(s) & \tilde{\mathbf{Q}}_{2 \times 2}^{(N,3)}(s) & \dots & \tilde{\mathbf{I}}_{2 \times 2} \end{bmatrix} = 0 \quad (28)$$

which forms the fundamental characteristic equation for natural system frequencies of N interacting objects in the large separation, low frequency regime.

For the special case of two interacting dipoles,

$$\begin{bmatrix} \vec{\mathbf{d}}_{2 \times 1}^{(1)}(s) \\ \vec{\mathbf{d}}_{2 \times 1}^{(2)}(s) \end{bmatrix} = \begin{bmatrix} \tilde{\mathbf{I}}_{2 \times 2} & \tilde{\mathbf{Q}}_{2 \times 2}^{(1,2)}(s) \\ \tilde{\mathbf{Q}}_{2 \times 2}^{(2,1)}(s) & \tilde{\mathbf{I}}_{2 \times 2} \end{bmatrix}^{-1} \cdot \begin{bmatrix} \vec{\mathbf{F}}_{2 \times 1}^{(1)}(s) \\ \vec{\mathbf{F}}_{2 \times 1}^{(2)}(s) \end{bmatrix} \quad (29)$$

where [13]

$$\begin{bmatrix} \tilde{\mathbf{I}}_{2 \times 2} & \tilde{\mathbf{Q}}_{2 \times 2}^{(1,2)} \\ \tilde{\mathbf{Q}}_{2 \times 2}^{(2,1)} & \tilde{\mathbf{I}}_{2 \times 2} \end{bmatrix}^{-1} = \begin{bmatrix} \tilde{\mathbf{A}}_{2 \times 2} & \tilde{\mathbf{B}}_{2 \times 2} \\ \tilde{\mathbf{C}}_{2 \times 2} & \tilde{\mathbf{D}}_{2 \times 2} \end{bmatrix} \quad (30)$$

with

$$\begin{aligned} \tilde{\mathbf{A}}_{2 \times 2} &= [\tilde{\mathbf{I}}_{2 \times 2} - \tilde{\mathbf{Q}}_{2 \times 2}^{(1,2)} \cdot \tilde{\mathbf{I}}_{2 \times 2}^{-1} \cdot \tilde{\mathbf{Q}}_{2 \times 2}^{(2,1)}]^{-1} \\ \tilde{\mathbf{B}}_{2 \times 2} &= -[\tilde{\mathbf{I}}_{2 \times 2} - \tilde{\mathbf{Q}}_{2 \times 2}^{(1,2)} \cdot \tilde{\mathbf{I}}_{2 \times 2}^{-1} \cdot \tilde{\mathbf{Q}}_{2 \times 2}^{(2,1)}]^{-1} \cdot \tilde{\mathbf{Q}}_{2 \times 2}^{(1,2)} \cdot \tilde{\mathbf{I}}_{2 \times 2}^{-1} \\ &= -\tilde{\mathbf{A}}_{2 \times 2} \cdot \tilde{\mathbf{Q}}_{2 \times 2}^{(1,2)} \\ \tilde{\mathbf{D}}_{2 \times 2} &= [\tilde{\mathbf{I}}_{2 \times 2} - \tilde{\mathbf{Q}}_{2 \times 2}^{(2,1)} \cdot \tilde{\mathbf{I}}_{2 \times 2}^{-1} \cdot \tilde{\mathbf{Q}}_{2 \times 2}^{(1,2)}]^{-1} \\ \tilde{\mathbf{C}}_{2 \times 2} &= -[\tilde{\mathbf{I}}_{2 \times 2} - \tilde{\mathbf{Q}}_{2 \times 2}^{(2,1)} \cdot \tilde{\mathbf{I}}_{2 \times 2}^{-1} \cdot \tilde{\mathbf{Q}}_{2 \times 2}^{(1,2)}]^{-1} \cdot \tilde{\mathbf{Q}}_{2 \times 2}^{(2,1)} \cdot \tilde{\mathbf{I}}_{2 \times 2}^{-1} \\ &= -\tilde{\mathbf{D}}_{2 \times 2} \cdot \tilde{\mathbf{Q}}_{2 \times 2}^{(2,1)} \end{aligned} \quad (31)$$

For two interacting dipoles, (28) becomes

$$\det \begin{bmatrix} \tilde{\mathbf{I}}_{2 \times 2} & \tilde{\mathbf{Q}}_{2 \times 2}^{(1,2)} \\ \tilde{\mathbf{Q}}_{2 \times 2}^{(2,1)} & \tilde{\mathbf{I}}_{2 \times 2} \end{bmatrix} = \det [\tilde{\mathbf{I}}_{2 \times 2}] \det [\tilde{\mathbf{I}}_{2 \times 2} - \tilde{\mathbf{Q}}_{2 \times 2}^{(2,1)} \cdot \tilde{\mathbf{I}}_{2 \times 2}^{-1} \cdot \tilde{\mathbf{Q}}_{2 \times 2}^{(1,2)}] \quad (32)$$

$$= \det [\tilde{\mathbf{I}}_{2 \times 2} - \tilde{\mathbf{Q}}_{2 \times 2}^{(2,1)} \cdot \tilde{\mathbf{Q}}_{2 \times 2}^{(1,2)}] = 0$$

IV. Characteristic equation for thin wires

At this point it is instructive to examine a special case of (32). Consider two non-identical objects with $\tilde{\mathbf{M}}^{(1)} = \tilde{\mathbf{M}}^{(2)} = \tilde{\mathbf{O}}$. In this case the two non-trivial block-dyadics are

$$\tilde{\mathbf{Q}}_{2 \times 2}^{(\alpha, \beta)} = \begin{bmatrix} -\epsilon_0 \tilde{\mathbf{P}}_0^{(\alpha)} \cdot \tilde{\mathbf{F}}_{e,e}^{(\alpha, \beta)} & \tilde{\mathbf{O}} \\ \tilde{\mathbf{O}} & \tilde{\mathbf{O}} \end{bmatrix} \quad (33)$$

leading to

$$\det [\tilde{\mathbf{I}} - \epsilon_0^2 \tilde{\mathbf{P}}_0^{(2)} \cdot \tilde{\mathbf{F}}_{e,e}^{(2,1)} \cdot \tilde{\mathbf{P}}_0^{(1)} \cdot \tilde{\mathbf{F}}_{e,e}^{(1,2)}] = 0. \quad (34)$$

As an example, consider thin, perfectly conducting wires oriented along the α -direction, for which $\tilde{\mathbf{P}}_0 = P_0 \tilde{\mathbf{I}}_\alpha \tilde{\mathbf{I}}_\alpha$ and the magnetic polarizability dyadic is negligible. A prolate spheroid model of a wire, with semi-major axis $L/2$ and semi-minor axis a , results in [14]

$$P_0 = \frac{4}{3} \pi \left(\frac{L}{2} \right)^3 \left[1 - \left(\frac{2a}{L} \right) \right] \left\{ \frac{1}{2} \left[1 - \left(\frac{2a}{L} \right)^2 \right]^{-1/2} \ln \left[\frac{1 + \left[1 - \left(\frac{2a}{L} \right)^2 \right]^{1/2}}{1 - \left[1 - \left(\frac{2a}{L} \right)^2 \right]^{1/2}} \right] - 1 \right\}^{-1} \quad (35)$$

$$= \frac{4}{3} \pi \left(\frac{L}{2} \right)^3 \left[\ln \left(\frac{L}{a} \right) - 1 \right]^{-1} \quad \text{as } \frac{a}{L} \rightarrow 0.$$

Now, consider three different orientations of the wires. For simplicity, in each case the wires will be located at $\tilde{\mathbf{r}}_1 = x_0 \tilde{\mathbf{I}}_x + y_0 \tilde{\mathbf{I}}_y \pm \frac{L}{2} \tilde{\mathbf{I}}_z$, such that $\tilde{\mathbf{F}}_{e,e}^{(2,1)} = \tilde{\mathbf{F}}_{e,e}^{(1,2)}$.

Case a. parallel wires:

Consider the wires to be oriented parallel to the x-axis of Fig. 1., such that $\tilde{\mathbf{P}}_0^{(\alpha)} = \tilde{\mathbf{I}}_x \tilde{\mathbf{I}}_x P_0^{(\alpha)}$ with $P_0^{(\alpha)}$ defined by (35). The governing equation (34) becomes

$$\begin{aligned} & \det [\vec{1} - \epsilon_0^2 \vec{P}_0^{(2)} \cdot \vec{F}_{e,e}^{(2,1)} \cdot \vec{P}_0^{(1)} \cdot \vec{F}_{e,e}^{(1,2)}] \\ & = 1 - \epsilon_0^2 P_0^{(2)} P_0^{(1)} \left[\left(\frac{e^{-\gamma r}}{4\pi} \right) \left(\frac{1}{r^3 \epsilon_0} + \frac{Z_0 S}{r^2} + \frac{\mu_0 S^2}{r} \right) \right]^2 = 0 . \end{aligned} \quad (36)$$

Making the substitution $\Gamma = \gamma r$, yields

$$e^{-\Gamma}(1 + \Gamma + \Gamma^2) = \pm \frac{r^3 4\pi}{\sqrt{P_0^{(2)} P_0^{(1)}}} \quad (37)$$

which is the characteristic equation for the natural system frequencies of two non-identical, parallel wires in the large-separation limit. The solution of (37) for the special case of two identical wires will be considered in Sec. VII and in the appendix. If we further assume the same length-to-radius ratio for both wires, $L^{(1)}/a^{(1)} = L^{(2)}/a^{(2)} = L_a$, then $P_0^{(1,2)} = K[L^{(1,2)}]^3$ with $K = \frac{\pi}{6} [\ln(L_a) - 1]^{-1}$, (37) can

be written more directly in terms of the three parameters $r, L^{(1)}, L^{(2)}$ as

$$e^{-\Gamma}(1 + \Gamma + \Gamma^2) = \pm \left(\frac{r}{L^{(2)}} \right)^{\frac{3}{2}} \left(\frac{r}{L^{(1)}} \right)^{\frac{3}{2}} \frac{4\pi}{K} . \quad (38)$$

Case b. collinear wires:

Consider two collinear wires aligned parallel to the z-axis of Fig. 1, such that $\vec{P}_0^{(\alpha)} = \vec{1}_z \vec{1}_z P_0^{(\alpha)}$

with $P_0^{(\alpha)}$ defined by (35). The governing characteristic equation (34) becomes

$$\begin{aligned} & \det [\vec{1} - \epsilon_0^2 \vec{P}_0^{(2)} \cdot \vec{F}_{e,e}^{(2,1)} \cdot \vec{P}_0^{(1)} \cdot \vec{F}_{e,e}^{(1,2)}] \\ & = 1 - \epsilon_0^2 P_0^{(2)} P_0^{(1)} \left[\left(\frac{e^{-\gamma r}}{2\pi} \right) \left(\frac{1}{r^3 \epsilon_0} + \frac{Z_0 S}{r^2} \right) \right]^2 = 0 \end{aligned} \quad (39)$$

resulting in

$$e^{-\Gamma}(1+\Gamma) = \pm \frac{r^3 2\pi}{\sqrt{P_0^{(2)} P_0^{(1)}}} \quad (40)$$

which is the characteristic equation for the natural system frequencies of two non-identical, collinear wires in the large-separation limit. The solution of (40) for the special case of two identical wires will be considered in the appendix. For $L^{(1)}/a^{(1)} = L^{(2)}/a^{(2)} = L_a$, such that $P_0^{(1,2)} = K[L^{(1,2)}]^3$ with k as defined previously, (40) can be written as

$$e^{-\Gamma}(1+\Gamma) = \pm \left(\frac{r}{L^{(2)}} \right)^{\frac{3}{2}} \left(\frac{r}{L^{(1)}} \right)^{\frac{3}{2}} \frac{2\pi}{k}. \quad (41)$$

Case c. perpendicularly-oriented wires:

To analyze two wires oriented perpendicularly to each other, one may take, for instance, $\vec{P}_0^{(1)} = \vec{1}_x \vec{1}_x P_0^{(1)}$ and $\vec{P}_0^{(2)} = \vec{1}_z \vec{1}_z P_0^{(2)}$. The characteristic equation (34) becomes

$$\det[\vec{1} - \epsilon_0^2 \vec{P}_0^{(2)} \cdot \vec{F}_{e,e}^{(2,1)} \cdot \vec{P}_0^{(1)} \cdot \vec{F}_{e,e}^{(1,2)}] = \det[\vec{1} - \vec{0}] = 1 \quad (42)$$

so that no frequency exists to yield a singular matrix.

Additional details can be found in [15], where a separate formulation is provided for two objects configured in a mirror-symmetric fashion.

VII. Numerical results

In order to demonstrate the accuracy of the presented formulation, the example of two identical, thin, perfectly conducting parallel wires separated by a distance $r=d$ is considered, as depicted in the insert of Fig. 2. The wires are in a mirror-symmetric configuration, which admits pure symmetric and antisymmetric modes. In all results to follow, both wires have $L/a=200$, and the natural frequencies in the upper-half s -plane will be considered. For one such wire when isolated, the dominant resonance is

at $\frac{s_{1,1}^0 L}{c\pi} = -0.0865 + j0.9386$, computed from a rigorous electric-field integral equation (IE) using a

pulse basis and point matching [16]. Other resonances are available in the literature, e.g. [1].

For the coupled wire configuration described above, the asymptotic formulation (37) becomes for $L/a=200$. The migration of the lowest-order anti-symmetric and symmetric mode as a function of

$$e^{-\Gamma(1+\Gamma+\Gamma^2)} = \mp 103.1596 \left(\frac{d}{L} \right)^3 \quad (43)$$

spacing d/L is shown in Fig.'s, 2 and 3, respectively. The solid line is the solution from the integral equation [16], the dashed line is from the perturbation solution formulated in [6], while the dotted line is the solution of (43). The solid box is the location of the isolated body resonance, $\frac{S_{1,1}^0 L}{C\pi}$. It can

be seen that the spiraling behavior is essentially well described by the perturbation solution for intermediate spacings, and the asymptotic solution agrees very well for larger spacings, as expected.

Fig.'s 4-7 show the radian frequency and damping coefficient for the lowest-order anti-symmetric and symmetric mode versus spacing d/L . For the modes considered in these figures, the asymptotic formulation (43) agrees very well with the exact solution for $d/L > 10$. For all of the IE solutions presented, 20 pulses were used to generate the natural frequencies.

VI. Conclusion

In this report we have examined the natural system frequencies of coupled bodies in the limit of large separation between all bodies. The general N-body problem is treated in the limit by replacing the bodies with equivalent dipole moments and solving the relevant scattering problem. Singular solutions of the scattering formulation lead to a transcendental equation which may be solved to obtain the natural system frequencies of the coupled bodies. It has been found for two coupled wires that the real radian system frequency approaches the origin as $1/r$, independent of the relative orientation and type of the two bodies, and that the damping coefficient approaches the origin approximately logarithmically, as a function of the body orientation and type. The asymptotic formulation is applied to the example of two parallel-coupled wires, and a comparison between the asymptotic formulation and an integral equation solution is made, indicating the accuracy of the asymptotic formulation in the appropriate range.

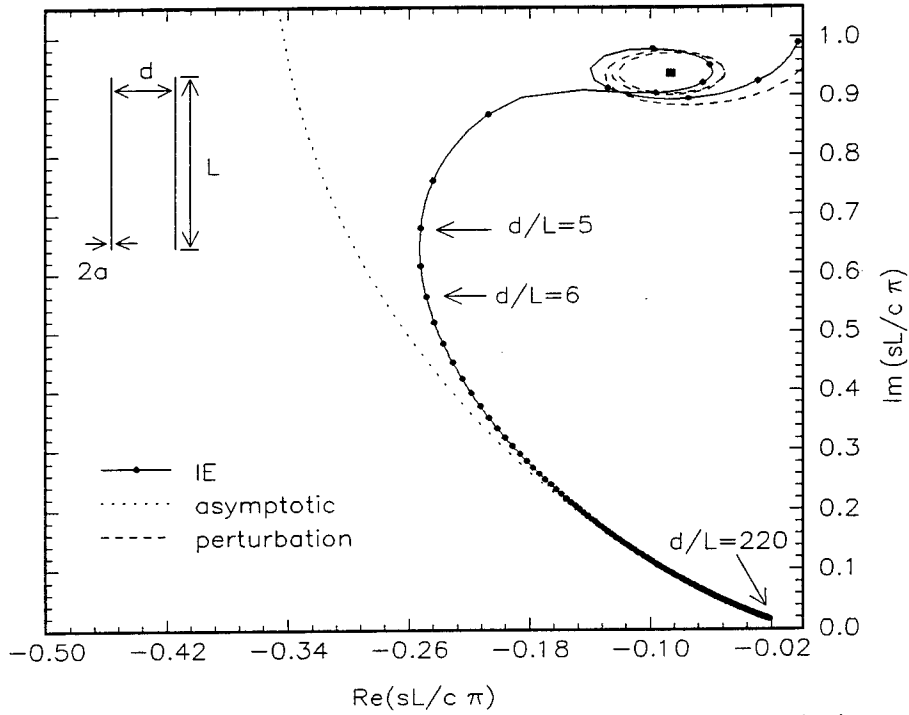


Fig. 3. Trajectory of lowest order anti-symmetric mode of two identical parallel wires parameterized by separation distance, which varies from $d/L=220$ to $d/L=0.01$. Solid box is the location of the isolated-wire dominant natural resonance.

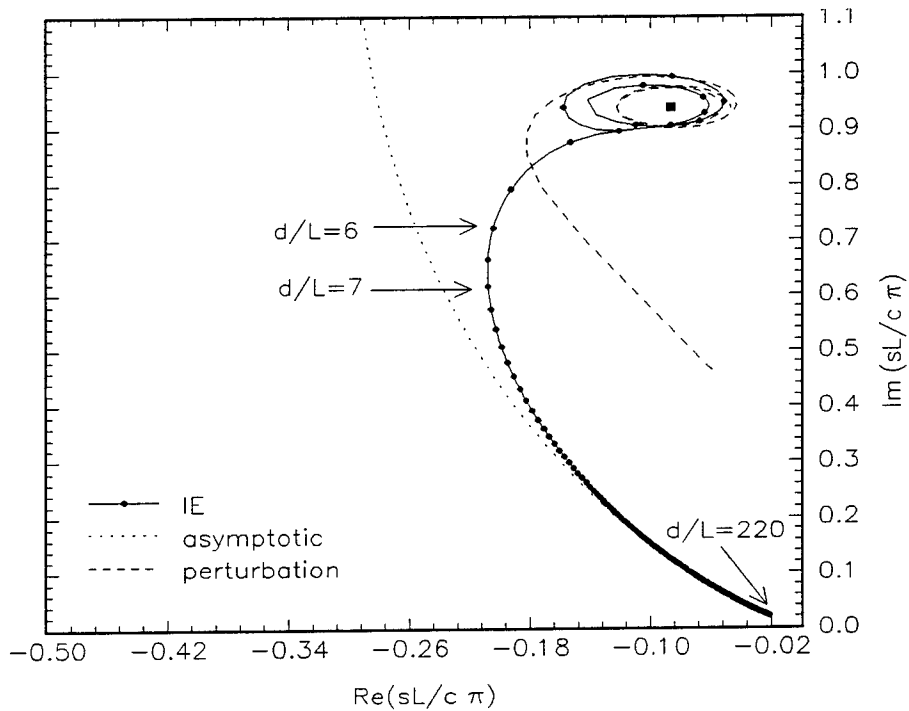


Fig. 4. Trajectory of lowest order symmetric mode of two identical parallel wires parameterized by separation distance, which varies from $d/L=220$ to $d/L=0.01$. Solid box is the location of the isolated-wire dominant natural resonance.

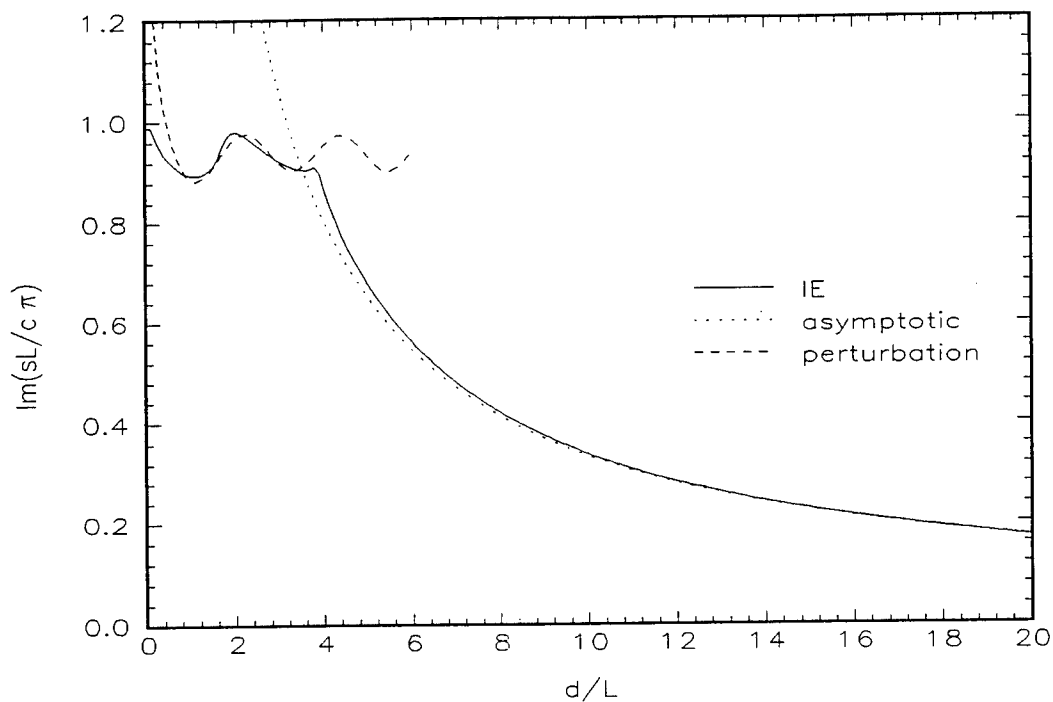


Fig. 5. Radian frequency of lowest order anti-symmetric mode of two identical parallel wires versus separation distance.

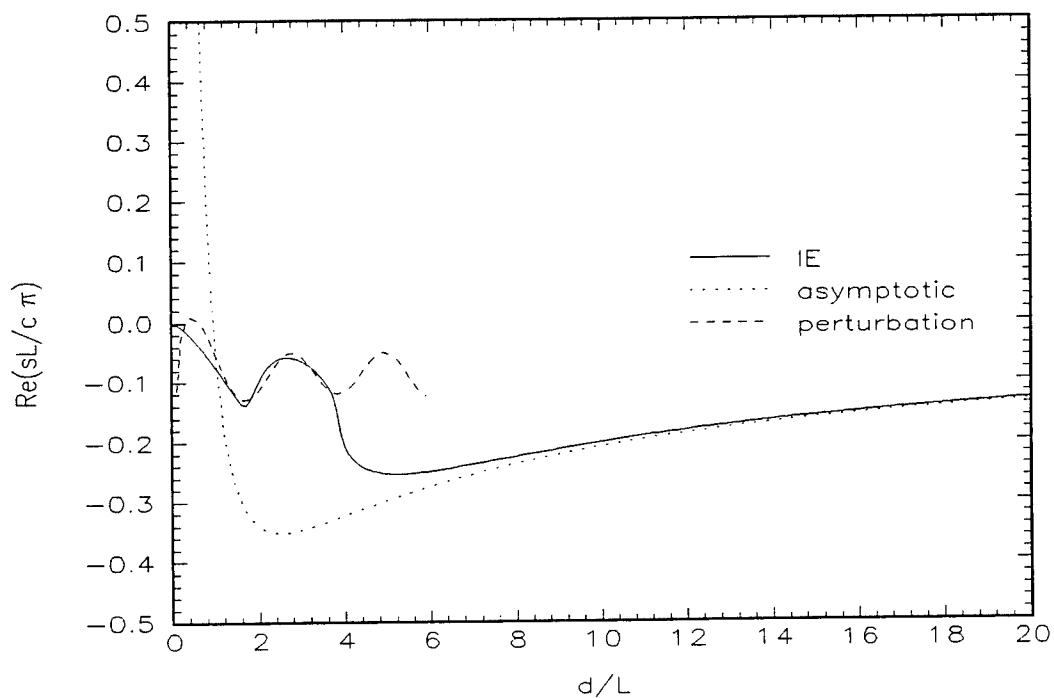


Fig. 6. Damping coefficient of lowest order anti-symmetric mode of two identical parallel wires versus separation distance.

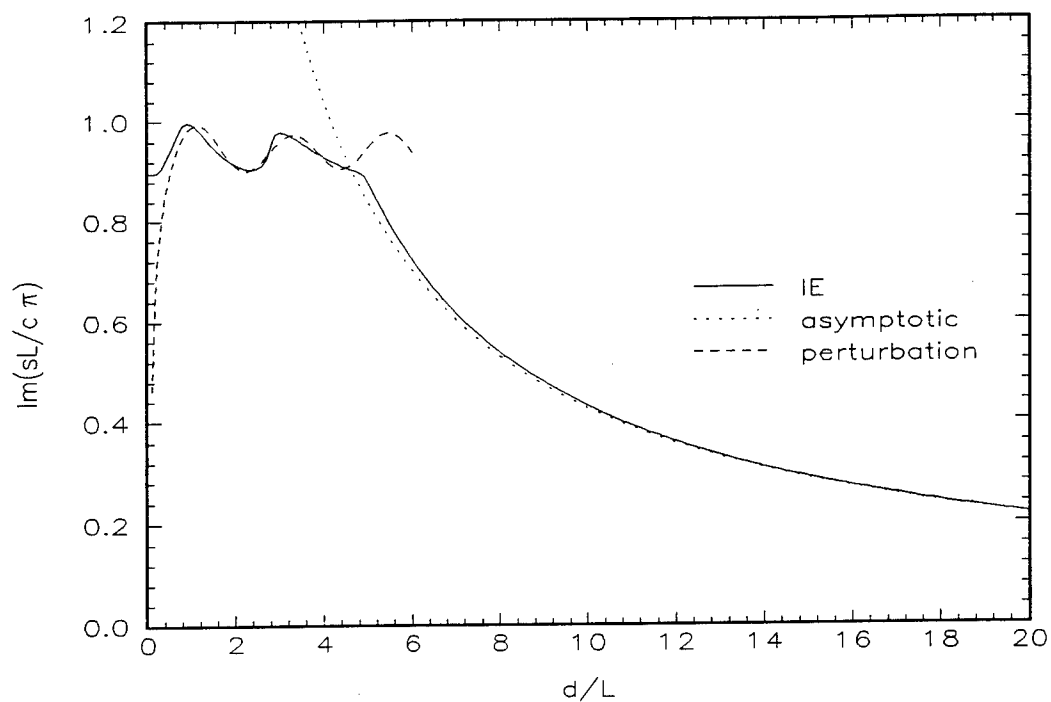


Fig. 7. Radian frequency of lowest order symmetric mode of two identical parallel wires versus separation distance.

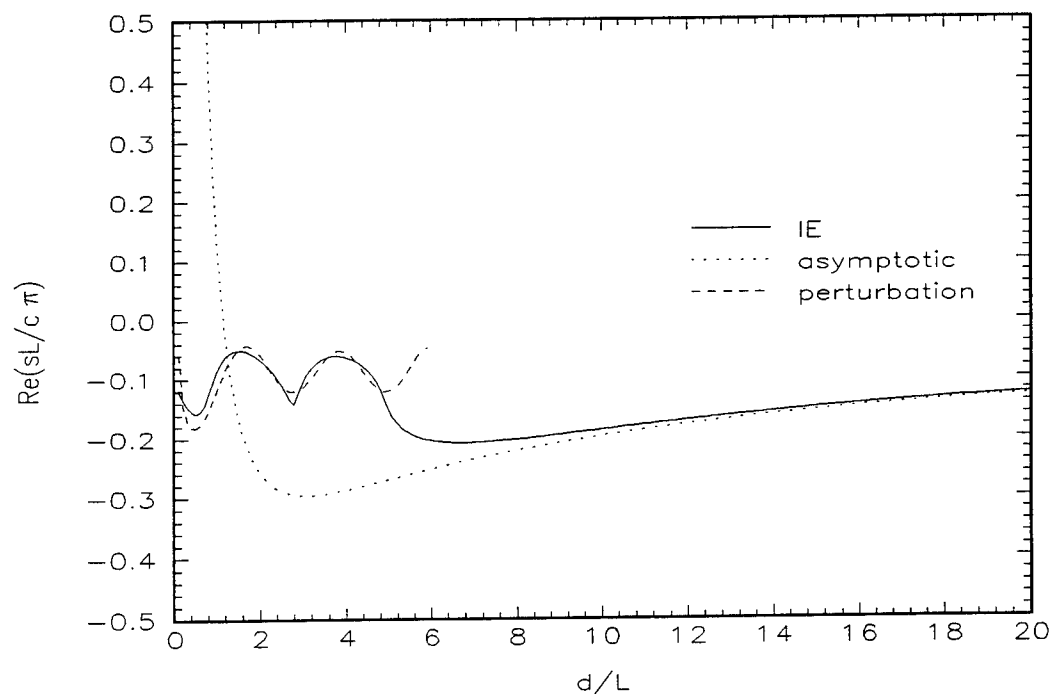


Fig. 8. Damping coefficient of lowest order symmetric mode of two identical parallel wires versus separation distance.

References

- [1] F.M. Tesche, "On the analysis of scattering and antenna problems using the singularity expansion technique," *IEEE Trans. Antennas Propagat.*, vol. AP-21, pp. 53-62, Jan. 1973. Also, F.M. Tesche, "On the singularity expansion method as applied to electromagnetic scattering from thin-wires," *Interaction Note 102*, April 1972.
- [2] K.R. Umashankar, T.H. Shumpert, and D.R. Wilton, "Scattering by a thin wire parallel to a ground plane using the singularity expansion method," *IEEE Trans. Antennas Propagat.*, vol. AP-23, pp. 178-184, Mar. 1975.
- [3] T.H. Shumpert and D.J. Galloway, "Finite length cylindrical scatterer near perfectly conducting ground. A transmission line mode approximation," *IEEE Trans. Antennas Propagat.*, vol. AP-26, pp. 145-151, Jan. 1978.
- [4] L.S. Riggs and T.H. Shumpert, "Trajectories of the singularities of a thin wire scatterer parallel to a lossy ground," *IEEE Trans. Antennas Propagat.*, vol. AP-27, pp. 864-868, Nov. 1979.
- [5] J.E. Ross, E.J. Rothwell, D.P. Nyquist, and K.M. Chen, "Approximate integral-operator methods for estimating the natural frequencies of coupled objects," *Radio Science*, vol. 29, pp. 677-684, 1994.
- [6] C.E. Baum, T.H. Shumpert, and L.S. Riggs, "Perturbation of the SEM-pole parameters of an object by a mirror object," *Electromagnetics*, vol. 8, pp. 169-186, 1989. Also, C.E. Baum, T.H. Shumpert, and L.S. Riggs, "Perturbation of the SEM-pole parameters of an object by a mirror object," *Sensor and Simulation Note 309*, Sept. 1987.
- [7] C.I. Chuang and D.P. Nyquist, "Perturbational formulation for nearly degenerate coupling," *1984 National Radio Science Meeting*, Boulder, CO., Jan. 1984.
- [8] Y. Yuan and D.P. Nyquist, "Full-wave perturbation theory based upon electric field integral equation for coupled microstrip transmission lines," *IEEE Trans. Microwave Theory Tech.*, vol.

38, pp. 1576-1584, Nov. 1990.

- [9] G.W. Hanson and D.P. Nyquist, "Full-wave perturbation theory for the analysis of coupled microstrip resonant structures," *IEEE Trans. Microwave Theory Tech.*, vol. 40, pp. 1774-1779, Sept. 1992.
- [10] J. Van Bladel, *Singular Electromagnetic Fields and Sources*, Oxford Univ. Press, New York, 1991.
- [11] A.D. Yaghjian, "Electric dyadic Green's functions in the source region," *Proc. IEEE*, vol. 68, pp. 248-263, Feb. 1980.
- [12] C.E. Baum, "Some characteristics of electric and magnetic dipole antennas for radiating transient pulses, " *Sensor and Simulation Note 125*, Jan., 1971.
- [13] C.E. Baum, T.K. Liu, and F.M. Tesche, "On the analysis of general multiconductor transmission-line networks, " *Interaction Note 350*, Nov, 1978.
- [14] K.S.H. Lee, "Electrically-small ellipsoidal antennas, " *Sensor and Simulation Note 193*, Feb., 1974.
- [15] G.W. Hanson and C.E. Baum, "Asymptotic Analysis of the Natural System Modes of Coupled Bodies in the Large Separation, Low-Frequency Regime, " *Interaction Note 528*, July, 1997.
- [16] J.E. Ross, private communication.

BLIND BAYESIAN RESTORATION OF ADAPTIVE OPTICS IMAGES
USING GENERALIZED GAUSSIAN MARKOV RANDOM FIELD
MODELS

Brian D. Jeffs
Associate Professor
Department of Electrical and Computer Engineering

Brigham Young University
459 CB
Provo, UT 84602

Final Report for:
Summer Faculty Research Program
Phillips Laboratory

Sponsored by:
Air Force Office of Scientific Research
Bolling Air Force Base, DC

And

Phillips Laboratory

September, 1998

BLIND BAYESIAN RESTORATION OF ADAPTIVE OPTICS IMAGES USING GENERALIZED GAUSSIAN MARKOV RANDOM FIELD MODELS

Brian D. Jeffs
Associate Professor
Department of Electrical and Computer Engineering
Brigham Young University

Abstract

This report introduces a blind method based on Bayesian maximum a posteriori (MAP) estimation theory for restoring images corrupted by noise and blurred by one or more unknown point-spread-functions (psf). The paper addresses post processing for resolution enhancement of sequences of short exposure (2-10 ms) adaptive optics (AO) images of space objects. In the problem formulation, both the true image and the unknown blur psf's are represented by the flexible generalized Gaussian Markov random field (GGMRF) model. The GGMRF probability density function provides a natural mechanism for expressing available prior information about the image and blur. Incorporating such prior knowledge in the deconvolution optimization is crucial for the success of blind restoration algorithms. For example, space objects often contain sharp edge boundaries and geometric structures, while the residual blur psf in the corresponding partially corrected AO image is spectrally band limited, and exhibits smoothed, random, texture-like features on a peaked central core. By properly choosing parameters, GGMRF models can accurately represent both the blur psf and the object, and serve to regularize the deconvolution problem. These two GGMRF models also serve as discriminator functions to separate blur and object in the solution. Algorithm performance is demonstrated with examples from AO images collected at the Starfire Optical Range, USAF Phillips Laboratory. Results from both real and synthetic data indicate significant resolution enhancement when applied to partially corrected AO images. An efficient computational algorithm is described.

BLIND BAYESIAN RESTORATION OF ADAPTIVE OPTICS IMAGES USING GENERALIZED GAUSSIAN MARKOV RANDOM FIELD MODELS¹

Brian D. Jeffs

1 Introduction

This report introduces a blind method based on Bayesian maximum a posteriori (MAP) estimation theory for restoring images corrupted by noise and blurred by one or more unknown point-spread-functions (psf). A major advantage of this MAP approach is that it provides a natural (rather than ad-hoc) mechanism for incorporating prior information about the image and blur. Use of this prior knowledge is crucial for the success of blind algorithms. This information is expressed in the form of an image probability density function model, and serves as a regularizing term in the associated inverse problem.

The term "blind" as used in this paper refers to a wide variety of uncertainty levels regarding the blur psf's. For example, the available psf prior information may consist of high quality blur estimates or parametric analytical models. At the other extreme, blur knowledge may be limited to simply knowing the psf is non-negative and spectrally band limited. The proposed method permits a natural representation of any of these degrees of psf uncertainty in the blur model, and permits refining the blur estimate to be consistent with each frame observation.

Though the algorithm presented here may be used in a wide variety of blind deconvolution applications, we are particularly interested in high resolution restoration of multiframe adaptive optics (AO) telescopic images. AO systems can remove much of the atmospheric-turbulence-induced blur in astronomical and orbiting space objects imagery, but there is typically some adaptation error [1] [2] [3] [4]. Thus, a residual time-varying blur below the theoretical aperture cutoff resolution limit remains. Though the general structure of this residual blur is known [5] [6], the detail is not, and varies significantly over a period of milliseconds.

It is often impractical to acquire an accurate sample of the true residual psf by observing a nearby star. This residual blur is spatially varying, so a natural guide star may not be in the same isoplanatic patch as the object, and in the case of tracking space objects, no natural reference stars which follow the object are available. When observing bright objects, it is possible to acquire a sequence of high SNR, closely spaced (in time) frames with significant blur variation from frame to frame. This scenario is ideally suited to multi-frame blind deconvolution methods which exploit the blur diversity to solve the difficult blind problem.

As is usually the case, the blind restoration problem addressed here is complicated by the ill-posed nature of the associated inverse problem [7], and by the fact that blur psf, H , and the true object image, F can only be identified in combination ($H * F$) unless distinguishing prior information is available. This solution ambiguity is due to the commutative property of convolution which will yield the same observation regardless of whether a given image feature is contained in H or F . Therefore, the blind restoration problem is hopeless without a well formed method of expressing and imposing prior information on the solution. A number of authors have successfully applied various "hard" and "soft" constraints on the object and blur solutions as a means of incorporating prior information into the blind multiframe solution [2] [3] [1] [4] [8] [9] [10] [6].

The method presented here includes a new approach for incorporating image prior information in the blind problem. Probability density functions are used to statistically model available prior information about the structure of both the true image, F , and the blurring psf, H . We will show that adopting appropriate image and blur pdf models serves as a powerful discriminating constraint that leads to realistic estimates for both H and F . We will use the generalized Gaussian Markov random field model [11] because of its ability to represent a wide range of practical image types [12] [13]. It can accurately model both structured, hard edged fields typical of the true image, and smooth, "low pass" or "band limited" images typical of blurring psf's.

The availability of multiple observations with different but unknown blur psf's, H_i , can be a great aid in estimating F . The multiple frame observation reduces convolutional ambiguity because any image component that

¹Sponsored by the Air Force Office of Scientific Research, Bolling Air Force Base, DC. The author acknowledges the contributions to this work from Dr. Julian C. Christou and Dr. Robert Fugate, Starfire Optical Range, USAF Phillips Laboratory.

is not common to all frames cannot be a component of the F . The method presented below will be developed to exploit this fact, and will be applicable for both single and multiple frame cases.

We adopt the following familiar linear image observation model

$$G_i = H_i * F + \eta_i, \quad i = 1 \cdots M \quad (1)$$

where G_i is the i^{th} observed image frame, η_i is additive noise, and '*' denotes 2-D convolution. G_i , H_i , F , and η_i are all assumed to be realizations of 2-D random fields, but F remains constant between observation frames. It will also be convenient to use the vector-matrix form of equation (1)

$$\mathbf{g}_i = \mathbf{H}_i \mathbf{f} + \eta_i, \quad i = 1 \cdots M \quad (2)$$

where \mathbf{g}_i , \mathbf{f} , and η_i are now vectors formed by column scanning the corresponding 2-D images, and \mathbf{H}_i is the doubly block Toeplitz convolution matrix corresponding to \mathbf{h}_i [14].

The frame blur psf's may be statistically correlated, so the optimal solution requires that the joint pdf across all frames be considered. For this case, when the \mathbf{H}_i are not independent, equation (2) must be augmented as

$$\begin{aligned} \bar{\mathbf{g}} &= \mathcal{H} \mathbf{f} + \bar{\eta}, \quad \text{where} \\ \bar{\mathbf{g}} &= [\mathbf{g}_1, \mathbf{g}_2, \cdots, \mathbf{g}_M]^T, \quad \bar{\eta} = [\eta_1, \eta_2, \cdots, \eta_M]^T, \\ \mathcal{H} &= \begin{bmatrix} \mathbf{H}_1 \\ \vdots \\ \mathbf{H}_M \end{bmatrix} \end{aligned} \quad (3)$$

2 Problem Formulation

Assuming \mathbf{f} and \mathcal{H} are statistically independent (a reasonable assumption in practice), the blind MAP restoration problem may be stated as

$$\begin{aligned} \hat{\mathbf{f}}, \hat{\mathcal{H}} &= \arg \max_{\mathbf{f}, \mathcal{H}} p_{f,h|g}(\mathbf{f}, \mathcal{H} | \bar{\mathbf{g}}) \\ &= \arg \max_{\mathbf{f}, \mathcal{H}} p_{g|f,h}(\bar{\mathbf{g}} | \mathbf{f}, \mathcal{H}) p_f(\mathbf{f}) p_h(\mathcal{H}) \end{aligned} \quad (4)$$

In order to solve equation (4), we adopt the following density function models. Assuming the noise is zero mean, white Gaussian, the noise density is given by

$$p_\eta(\bar{\eta}) = \frac{1}{\sqrt{2\pi}^{MN} \sigma_\eta} e^{-\frac{1}{2\sigma_\eta^2} \bar{\eta}^t \bar{\eta}} \quad (5)$$

where N is the total number of pixels in the image field. The following development could also be easily adapted to a Poisson distribution noise model. This approach is favored by some authors in Adaptive Optics restoration because it more accurately characterizes photon noise in short exposure images [8]. Assuming that the noise is statistically independent from both the true image and the blur, the conditional probability of $\bar{\mathbf{g}}$ given \mathbf{f} and \mathcal{H} can be trivially shown to be

$$\begin{aligned} p_{g|f,h}(\bar{\mathbf{g}} | \mathbf{f}, \mathcal{H}) &= p_\eta(\bar{\mathbf{g}} - \mathcal{H} \mathbf{f}) \\ &= \frac{1}{\sqrt{2\pi}^{MN} \sigma_\eta} e^{-\frac{1}{2\sigma_\eta^2} (\bar{\mathbf{g}} - \mathcal{H} \mathbf{f})^t (\bar{\mathbf{g}} - \mathcal{H} \mathbf{f})} \end{aligned} \quad (6)$$

The image is modeled as a generalized Gaussian Markov random field (GGMRF), with joint pdf given by the Gibbs distribution [11]

$$p_f(\mathbf{f}) = \frac{1}{Z_f} \exp \left\{ -\beta \left[\sum_{\langle s,t \rangle \in \mathcal{C}_f} b_{s,t} |f_s - f_t|^p + \sum_{s \in S_f} a_s |f_s|^p \right] \right\} \quad (7)$$

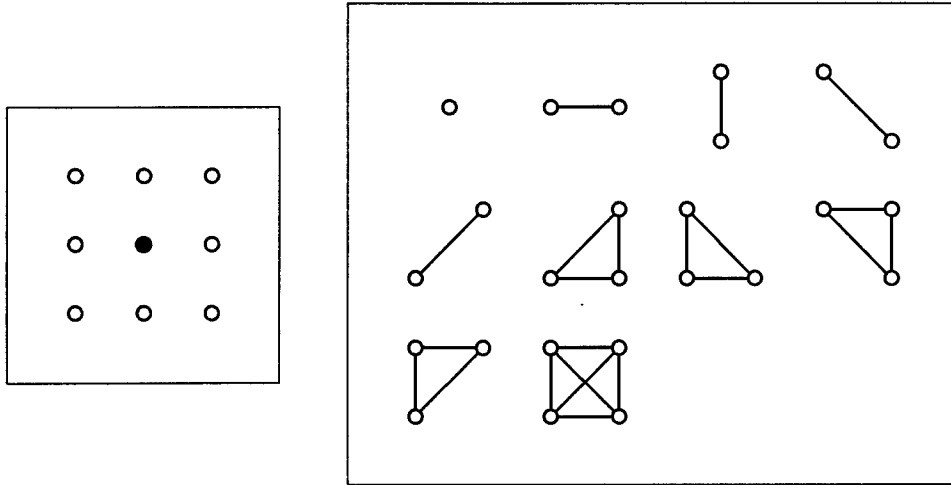


Figure 1: a) [left] A second order neighborhood. b) [right] The cliques associated with a second order neighborhood.

where \mathcal{C}_f is the set of all cliques of pixels invoked by the specified neighborhood system, p is the GGMRF shape parameter, S_f is the set of all pixels in the image lattice, f_s denotes the s^{th} pixel in \mathbf{f} , and $b_{s,t}$ and a_s are potential weights. β is the scale parameter (controlling variance) and Z_f is the partition function, which is simply the scale constant required to insure the pdf integrates to 1.0.

The neighborhood clique system is a critical part of defining a Markov random field, and it controls local pixel interactions. Figure 1a illustrates all the neighbors for a single pixel (the center darkened dot) in a second order neighborhood. A clique is defined as any set of pixels which are all mutual neighbors. Figure 1b shows all possible geometric configurations of cliques permitted in a second order neighborhood. \mathcal{C}_f contains all such cliques over the entire image, i.e. the union (non repeating) over all pixels of the set of cliques containing each pixel.

A first order neighborhood is defined as containing only left, right, up and down neighbors. The circles in Figure 1a located diagonally from the center dot would be excluded from a first order neighborhood. Likewise, only the first three cliques shown in Figure 1b would be defined in a first order neighborhood.

The GGMRF model is a particularly flexible and useful for image restoration problems because it is capable of representing a wide variety of statistical image classes using just a few parameters. Equation (7) can be viewed as a definition for a random texture field. Parameters p , $b_{s,t}$ and a_s control the structure of this texture. p is known as the shape parameter, and controls the “edginess,” or transition structure in the image. $b_{s,t}$ and a_s jointly control the correlation structure between neighboring pixels. With appropriate value selections, the model can be parameterized to generate fields that look like the detail in any desired visual texture, such as gravel, cork, grass, clouds, sand, waves, natural animal coat coloring, or geometric blocky structures.

Figure 2 shows an example of how shape parameter p affects this texture field. The images shown were generated as synthetic Markov random fields using Chen’s algorithm to express the model of equation (7) [15]. A first order uniform neighborhood was used in each example, and only p was varied. We propose that Figure 2a, with $p = 0.5$, is a better statistical match for the blocky geometric structures of man-made objects, like satellites, than are the other three fields. Thus the GGMRF model with p values near 0.5 can serve as a powerful image prior to influence as restoration solution away from overly smoothed results typical of many other algorithms. This regularization is accomplished without detailed geometric descriptions of unknown object, but with a simple statistical preference for the desired texture-like pixel relationships.

For $.5 < p < 1.5$ (approximately) a MAP restoration using this GGMRF image prior preserves edge detail and regional structure found in most images of interest. The structural information contained in $p_f(\mathbf{f})$ is key

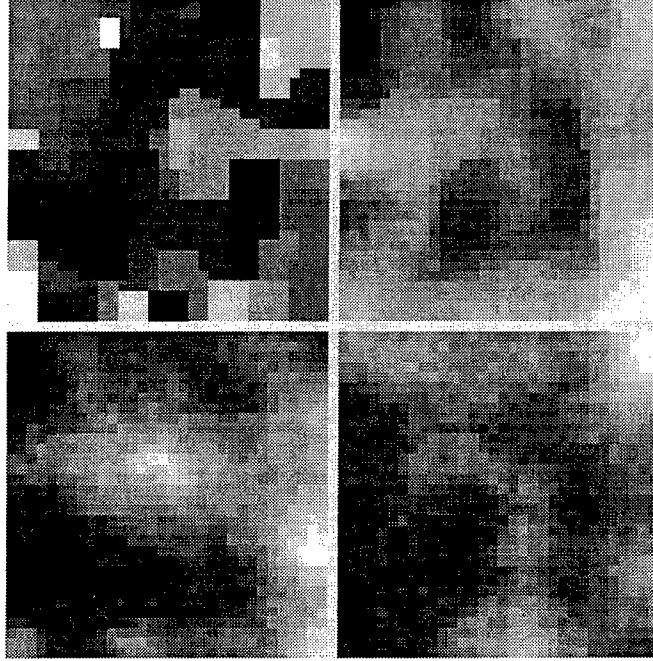


Figure 2: Synthetic GGMRF images. a) [top left] $p = 0.5$, b) [top right] $p = 1.0$, c) [bot. left] $p = 2.0$, d) [bot. right] $p = 3.0$.

to overcoming the convolutional ambiguity between \mathbf{f} and \mathbf{H} in blind restoration. Further, due to the Markov properties inherent in Gibbs distributions, the pdf of any single pixel depends only on the value of its neighbors as defined in the clique system, \mathcal{C} . This greatly simplifies the MAP optimization algorithm because updates need only consider local neighbor data rather than the entire image at each iteration.

The appropriate blur pdf model is application dependent, and two different approaches will be discussed in the following sections.

3 Solutions for GGMRF Blur

When the blur function cannot be described by a low order parametric model, or is too random, we must use a more general pdf model. The GGMRF is again well suited to this task because it can be adapted to favor the smoother, band-limited image types usually encountered as blur operators. Our notions of what a blur field should look like are conveyed by specifying a few neighbor potential weights, the GGMRF shape parameter (q will be used to distinguish it from the object shaper parameter, p) and a mean value, μ_h . This in turn defines a texture class used to penalize the optimization objective function if a candidate blur differs significantly from the model.

The GGMRF blur model is given by

$$p_h(\mathcal{H}) = \frac{1}{Z_h} \exp \left\{ -\alpha \left[\sum_{\langle s,t \rangle \in \mathcal{C}_h} c_{s,t} |(h_s - \mu_{h,s}) - (h_t - \mu_{h,t})|^q + \sum_{s \in S_h} d_s |h_s - \mu_{h,s}|^q \right] \right\} \quad (8)$$

where \mathcal{C}_h is the set of all cliques of pixels invoked by the specified neighborhood system, q is the GGMRF shape parameter, S_h is the set of all points in blur the lattice over all frames (set of every pixel in every frame), and $c_{s,t}$ and d_s are potential weights.

Equation (8) is flexible enough to not only represent a wide variety of blur types, but to also quantify the degree of uncertainty in the model relative to observation $\tilde{\mathbf{g}}$. Including a mean in the $p_h(\mathcal{H})$ model (which was not needed in $p_f(\mathbf{f})$) allows us to incorporate prior information from previous experiments. For example, in astronomical imaging, isolated stars in a nearby field, or even from frames acquired on different experiments, can be averaged to

serve as the reference mean. An analytic model can also be used as a mean. The Lorentzian function model may be used for residual AO blur [5] [6], or a simple Gaussian function for atmospheric turbulence. The GGMRF scale parameter, α , controls variance, and can be adjusted to match the degree of confidence in the GGMRF model as a whole. If the mean is a very good estimate of the actual blur, we set the scale parameter high (for low variance), and keep d_s fairly large (positive) relative to $c_{s,t}$. If the mean estimate is very poor, d_s is kept small, or zero, and all μ_h terms are dropped from equation (8). The model can then still impose the desired texture structure in \mathcal{H} . If the blur is known to be spectrally band limited (e.g. bounded by the pupil cut off frequency), then the corresponding values of $b_{s,t}$ are large (relative to a_s), nearly uniform, and are all positive. It has been shown that for $1.75 < q < 3.0$ and \mathcal{C}_h corresponding to a first or second order uniformly weighted neighborhood, this model produces a random field with smoothed structures typical of many blur operators [13] [12].

Substituting equations (8),(7) and (6) into (4), and performing a little algebra yields

$$\begin{aligned} \hat{\mathbf{f}}, \hat{\mathcal{H}} = & \arg \min_{\mathbf{f}, \mathcal{H}} \sum_{i=1}^M \|\mathbf{g}_i - \mathbf{H}_i \mathbf{f}\|^2 + \gamma \left[\sum_{\langle s,t \rangle \in \mathcal{C}_f} b_{s,t} |f_s - f_t|^p + \sum_{s \in S_f} a_s |f_s|^p \right] \\ & + \lambda \left[\sum_{\langle s,t \rangle \in \mathcal{C}_h} c_{s,t} |(h_s - \mu_{h,s}) - (h_t - \mu_{h,t})|^q + \sum_{s \in S_h} d_s |h_s - \mu_{h,s}|^q \right] \end{aligned} \quad (9)$$

where we have taken the logarithm of the r.h.s. (which does not change the maximization due to monotonicity) and have dropped additive constants. γ and λ control the relative influence, as regularizing terms, that the image and blur pdf's have respectively on the solution. If the neighborhood clique system, \mathcal{C}_h does not include cliques that cross frame boundaries, then the \mathbf{H}_i are mutually independent, and equation (9) simplifies slightly to

$$\begin{aligned} \hat{\mathbf{f}}, \hat{\mathcal{H}} = & \arg \min_{\mathbf{f}, \mathcal{H}} \sum_{i=1}^M \left(\|\mathbf{g}_i - \mathbf{H}_i \mathbf{f}\|^2 + \lambda \left[\sum_{\langle s,t \rangle \in \mathcal{C}_{hi}} c_{s,t} |(h_s - \mu_{h,s}) - (h_t - \mu_{h,t})|^q + \sum_{s \in S_{hi}} d_s |h_s - \mu_{h,s}|^q \right] \right) \\ & + \gamma \left[\sum_{\langle s,t \rangle \in \mathcal{C}_f} b_{s,t} |f_s - f_t|^p + \sum_{s \in S_f} a_s |f_s|^p \right] \end{aligned} \quad (10)$$

where now \mathcal{C}_{hi} and S_{hi} contain only cliques and pixels in the single frame, \mathbf{H}_i .

The theoretical values γ and λ are functions of p , q , and the SNR, though exact expressions for are difficult to derive. Therefor, these parameters are usually manually adjusted for most desirable results. The following proportionality relationships give some guidance on how to set γ and λ .

$$\gamma \propto 2\beta\sigma_\eta^2, \quad \lambda \propto 2\alpha\sigma_\eta^2 \quad (11)$$

Examples of restorations using the above formulation are presented in Section 6.

4 Solutions for Parametric Blur Models

In this section we develop a restoration solution for cases where significant detailed prior information regarding blur structure is available. This problem may be referred to as "semi-blind" or "myopic" restoration. Many common blurring functions, such out-of-focus and motion blurs, are well understood and can be accurately described using analytical psf models with one or two parameters [16] [17]. For example, if it is known a priori that blur is due to linear motion, the estimation problem can be reduced to simply finding the direction and extent of the motion. Rather than independently estimating every pixel in the psf, this two parameter estimation dramatically reduces the difficulty of blind restoration. Drummond has proposed a low order analytical model for AO residual blur based on a 2-D elliptic rotation of a Lorentzian function [5] [6]. This model requires only six parameters to fully describe the AO blur remaining in a partially corrected observation frame, and is a promising model for the AO space object restoration problem of interest.

For MAP restoration with parametric blur models we treat the parameters as random variables with an associated pdf, $p_\theta(\theta_i)$, where θ_i is the vector of blur model parameters for the i^{th} frame. Applying this expression to equation

(4) and assuming \mathbf{f} is independent of θ_i yields

$$\begin{aligned}\hat{\mathbf{f}}, \hat{\theta} &= \arg \max_{\mathbf{f}, \theta} p_{f, \theta | g}(\mathbf{f}, \theta | \bar{\mathbf{g}}) \\ &= \arg \max_{\mathbf{f}, \theta} p_{g | f, \mathcal{H}}(\bar{\mathbf{g}} | \mathbf{f}, \mathcal{H}(\bar{\theta})) p_f(\mathbf{f}) p_\theta(\bar{\theta})\end{aligned}\quad (12)$$

where $\bar{\theta} = [\theta_1, \theta_2, \dots, \theta_M]^T$ and $\mathcal{H}(\bar{\theta})$ is a known deterministic matrix function of blur parameters, $\bar{\theta}$.

For polar parameters (e.g. orientation angle) we have used a uniform pdf model, $p_\theta(\theta_i) = U(0, 2\pi)$. For most other parameters a Gaussian pdf model with a suitable mean value has proven adequate, though this choice is clearly arbitrary in many cases. Adopting a Gaussian blur parameter model and the GGMRF image prior distribution leads to the solution

$$\begin{aligned}\hat{\mathbf{f}}, \hat{\theta} &= \arg \min_{\mathbf{f}, \theta} \sum_{i=1}^M \|\mathbf{g}_i - \mathbf{H}_i(\theta_i) \mathbf{f}\|^2 + \gamma \left[\sum_{\langle s, t \rangle \in \mathcal{C}_f} b_{s, t} |f_s - f_t|^p + \sum_{s \in S_f} a_s |f_s|^p \right] \\ &\quad + \lambda (\bar{\theta} - \bar{\mu}_\theta)^T \mathbf{R}_\theta^{-1} (\bar{\theta} - \bar{\mu}_\theta)\end{aligned}\quad (13)$$

where $\mathbf{R}_\theta = E\{(\bar{\theta} - \bar{\mu}_\theta)^T (\bar{\theta} - \bar{\mu}_\theta)^*\}$ and $\bar{\mu}_\theta$ is the multiframe vector of parameter means specified by the operator. Examples of restoration using this formulation are presented in Section 6.

5 Optimization Algorithms

5.1 Metropolis Algorithm Implementation

Equation (4) is in general very difficult to solve since for most realistic pdf's it is highly non-linear and has many local minima. This suggests that a stochastic optimization approach with randomized search strategy, such as the Metropolis algorithm for simulated annealing, is called for. The following procedural description adapts the Metropolis algorithm for use in blind, multiframe, GGMRF image restoration. The particular form shown has assumed both \mathbf{f} and \mathcal{H} are distributed GGMRF, but the algorithm is trivially modified to handle the parametric blur model of Section 4.

1. Choose an initial image, \mathbf{f}^0 and initial blur frames, \mathbf{h}_i^0 (e.g. $\mathbf{f}^0 = \mathbf{g}_1$ and $\mathbf{h}_i^0 = \mu_h$).
2. Set initial temperature, T_0 .
3. Repeat for $k = 1$ to N , the total number of iterations.
 - (a) Repeat for the total number of pixels in \mathbf{f} .
 - i. Randomly choose a pixel site, s , without repeating.
 - ii. Generate a random variate, z_s uniformly on Λ_f , the set of allowed gray levels for \mathbf{f} .
 - iii. Assign $y_s = z_s$ and $y_t = f_t^k \forall t \neq s$.
 - iv. Assign $w = \min \left\{ 1, \frac{p_{g | f, h}(\bar{\mathbf{g}} | \mathbf{y}, \mathcal{H}^k) p_f(y_s | y_t \forall t \neq s)}{p_{g | f, h}(\bar{\mathbf{g}} | \mathbf{f}^k, \mathcal{H}^k) p_f(f_s^k | f_t^k \forall t \neq s)} \right\}$.
 - v. Replace \mathbf{f}^k with \mathbf{y} with probability w , otherwise set $\mathbf{f}^{k+1} = \mathbf{f}^k$.
 - (b) Repeat for $i = 1$ to M .
 - i. Repeat for the total number of pixels in \mathbf{h}_i .
 - A. Randomly choose a pixel site, s , without repeating.
 - B. Generate a random variate, z_s uniformly on Λ_h , the set of allowed gray levels for \mathcal{H} .
 - C. Let $\mathcal{V} = [\mathbf{v}_1, \dots, \mathbf{v}_M]^T$, where $\mathbf{v}_i = [v_{i,1}, \dots, v_{i,N}]^T$. Assign $v_{i,s} = z_s$ and $v_{i,t} = h_{i,t}^k \forall t \neq s$. Assign $\mathbf{v}_j = \mathbf{h}_j^k \forall j \neq i$.
 - D. Assign $w = \min \left\{ 1, \frac{p_{g | f, h}(\bar{\mathbf{g}} | \mathbf{f}^{k+1}, \mathcal{V}) p_h(v_{i,s} | v_{j,t} \forall j, t \neq s)}{p_{g | f, h}(\bar{\mathbf{g}} | \mathbf{f}^k, \mathcal{H}^k) p_h(h_{i,s}^k | h_{j,t}^k \forall j, t \neq s)} \right\}$.
 - E. Let $\mathcal{H}^{k+1} = \mathcal{V}$ with probability w , otherwise set $\mathcal{H}^{k+1} = \mathcal{H}^k$.

(c) Reduce temperature, $T_{k+1} = \frac{\log(1+k)}{\log(2+k)} T_k$.

Due to the Markov property of Gibbs distributions, the conditional probability densities in the above algorithm have a particularly simple form which depends only on the neighbors of pixel s . Additionally, since only ratios of density functions are considered, we may neglect all leading scale (partition function) terms.

$$p_f(f_s^k | f_t^k \forall t \neq s) = p_f(f_s^k | f_t^k t \in \delta_s) \propto e^{\gamma \left[\sum_{t \in \delta_f} b_{s,t} |f_s^k - f_t^k|^p + a_s |f_s^k|^p \right]} \quad (14)$$

$$p_h(h_{i,s}^k | h_{j,t}^k \forall j, t \neq s) = p_h(h_{i,s}^k | h_t^k t \in \delta_s) \propto e^{\lambda \left[\sum_{t \in \delta_s} c_{s,t} |(h_s - \mu_{h,s}) - (h_t - \mu_{h,t})|^q + d_s |h_s - \mu_{h,s}|^q \right]} \quad (15)$$

where δ_s is the small set of pixels neighboring pixel s as defined by the clique system \mathcal{C} . Examples of restorations using this algorithm are presented in Section 6.

5.2 Steepest Descent Algorithm

For certain choices of the GGMRF parameters, equations (9) and (10) represent optimizations of convex functionals, and can therefore be solved using the much more efficient gradient descent techniques. Sufficient conditions for the model parameters to insure convex optimization are: $q, p > 1$, $a_s, d_s \geq 0 \forall s$, and $b_{s,t}, c_{s,t} \geq 0 \forall s, t$. If $p = 2$, then a necessary and sufficient condition for the image prior term to be convex is that \mathbf{B} be a non-negative definite matrix with elements B_{st} related to equation (7) by $B_{st} = -b_{s,t}$, $a_s = \sum_{t \in \delta_s} B_{st}$, and $B_{st} = 0$ for $s \notin \delta_s$. δ_s is the set of neighboring pixels in all cliques containing f_s . Similar constraints hold for $c_{s,t}$ and d_s if $q = 2$. These conditions are not overly restrictive. We have found that with $p = 1.1$ and $q \geq 2$ the image model preserves edge features, and the blur model imposes sufficient smoothness to separate \mathbf{f} from \mathcal{H} .

In order to simplify gradient computation, the objective function of equation (10) can be expressed as

$$J(\mathbf{f}, \mathcal{H}) = (\bar{\mathbf{g}} - \mathcal{H}\mathbf{f})^T (\bar{\mathbf{g}} - \mathcal{H}\mathbf{f}) + \gamma \text{Trace}\{\text{Diag}\{\sum_{t \in \delta_f} b_t |\mathbf{f} - \mathbf{P}_t \mathbf{f}|^p\}\} + \lambda \text{Trace}\{\text{Diag}\{d |\mathbf{h} - \mu_h|^q + \sum_{t \in \delta_h} c_t |(\mathbf{h} - \mu_h) - \mathbf{P}_t (\mathbf{h} - \mu_h)|^q\}\} \quad (16)$$

where $|\cdot|^p$ indicates element-wise exponentiation of the magnitude and $\text{Diag}\{\cdot\}$ forms a diagonal matrix from a vector. We have assumed $a_s = 0$ (a common choice [11]), and that $b_{s,t}$, $c_{s,t}$, and d_s are constant with respect to s . This assumption restricts the model to homogeneous (spatially stationary) random fields. \mathbf{P}_t is a permutation matrix which shifts \mathbf{f} to align f_t with f_s . δ_f and δ_h are sets of indices used to select shifts consistent with the neighborhood structure of \mathcal{C} . Since the field is stationary, these sets are independent of s . For example, in the case of a first order neighborhood, δ_f would contain four indices to select up, down, left, and right neighbors. Neglecting edge effects, an example of \mathbf{P}_t where $t = \text{"nearest neighbor down"}$ would be as follows:

$$\mathbf{P}_t = \begin{bmatrix} 0 & 1 & 0 & \cdots & 0 \\ & \ddots & \ddots & & \\ 0 & \cdots & 0 & 1 & 0 \\ 0 & \cdots & & 0 & 1 \\ 0 & \cdots & & & 0 \end{bmatrix} \quad \text{when } t \text{ is the index for 1 row down.} \quad (17)$$

The derivative of equation (16) with respect to \mathbf{f} is readily computed. However, to compute the derivative with respect to the i^{th} frame blur, \mathbf{h}_i , the first term of (16) is replaced with the equivalent expression $\sum_{i=1}^M (\bar{\mathbf{g}} - \mathbf{F}\mathbf{h}_i)^T (\bar{\mathbf{g}} - \mathbf{F}\mathbf{h}_i)$, where \mathbf{F} is the block Toeplitz convolution matrix formed from \mathbf{f} .

$$\frac{d}{d\mathbf{f}} J(\mathbf{f}, \mathcal{H}) = -2 \sum_{i=1}^M \mathbf{H}_i^T (\mathbf{g}_i - \mathbf{H}_i \mathbf{f}) + \alpha p \sum_{t \in \delta_f} b_t \mathbf{Q}_t^T |\mathbf{Q}_t \mathbf{f}|^{p-1} \odot \text{sign}\{\mathbf{Q}_t \mathbf{f}\} \quad (18)$$

$$\frac{d}{d\mathbf{h}_i} J(\mathbf{f}, \mathcal{H}) = -2\mathbf{F}^T(\mathbf{g}_i - \mathbf{F}\mathbf{h}_i) + \lambda q \left(\sum_{t \in \delta_h} c_t \mathbf{Q}_t^T |\mathbf{Q}_t(\mathbf{h}_i - \mu_h)|^{q-1} \odot \text{sign}\{\mathbf{Q}_t(\mathbf{h}_i - \mu_h)\} + d |\mathbf{h}_i - \mu_h|^{q-1} \odot \text{sign}\{\mathbf{h}_i - \mu_h\} \right) \quad (19)$$

where $\mathbf{Q}_t = \mathbf{I} - \mathbf{P}_t$, \odot is the Schur matrix product, and $\text{sign}\{\cdot\}$ is the signum function.

Having used matrix-vector notation to facilitate evaluating the gradients, we now note that the conventional matrix vector products in equations (18) and (19) involve huge matrices, and are extremely computationally inefficient. Fortunately, each product corresponds to either 2-D convolution or 2-D deterministic correlation in the image domain, which can be computed directly with far lower computational burden.

A simple and efficient iterative steepest descent algorithm based on the gradient expressions given above is

$$F^{k+1} = F^k + \alpha \sum_{i=1}^M H_i^k \star (G_i - H_i^k \star F^k) - \alpha \gamma p \sum_{t \in \delta_f} b_t Q_t \star |Q_t \star F^k|^{p-1} \odot \text{sign}\{Q_t \star F^k\} \quad (20)$$

$$H_i^{k+1} = H_i^k + \alpha F^k \star (G_i - F^k \star H_i^k) - \alpha \lambda q \sum_{t \in \delta_h} c_t Q_t \star |Q_t \star (H_i^k - \mu_h)|^{q-1} \odot \text{sign}\{Q_t \star (H_i^k - \mu_h)\} - \alpha d |(H_i^k - \mu_h)|^{q-1} \odot \text{sign}\{H_i^k - \mu_h\} \quad (21)$$

where all upper case variables represent 2-D images (rather than the column scanned images), superscripts, k , indicate the iteration number, ' \star ' represents 2-D deterministic correlation, ' \ast ' indicates 2-D convolution, and α is the iteration step size. The convolutions and correlations in equations (20) and (21) involving F and H_i can be computed efficiently in the frequency domain using a 2-D FFT based algorithm. Since \mathbf{Q}_t was formed as the sum of permutation and identity matrices, it is seen that convolutions and correlations involving Q_t are computationally trivial, involving just a simple shift and add, i.e.

$$\begin{aligned} Q_t \star F &= F[m, n] - F[m - m_t, n - n_t], \quad [m - m_t, n - n_t] \in \{\text{the region of support for } F\} \\ Q_t \ast F &= F[m, n] - F[m + m_t, n + n_t], \quad [m + m_t, n + n_t] \in \{\text{the region of support for } F\} \end{aligned} \quad (22)$$

where m_t and n_t are the row and column distances to the neighbor indexed by t . Restorations results using this algorithm are presented in the following section.

6 Preliminary Experimental Results

This section presents examples of results for the algorithms introduced above, processing both synthetic and real data sets.

6.1 Algorithm Evaluation

This section presents some experiments which demonstrate algorithm performance for a variety of model parameters and operational conditions using synthetically generated image data. The purpose of these experiments is to provide insight into how various parameter values affect the solution, and to validate both the Metropolis and steepest descent algorithms.

Figure 3 presents a single frame conventional (non-blind) application of GGMRF MAP restoration using the Metropolis algorithm. The 5 by 5 pixel uniform blur psf is assumed known. Figure 3a shows the true object, which is a simple geometric pattern intended to exhibit the sharp edged and constant intensity valued regions expected in space objects images. Figures 3c and 3d show restorations using p values of 1.1 and 3.0 respectively. The two results have the same error residual level. Note that the $p = 1.1$ result much more sharply resolves edges, while $p = 3.0$ as an image prior parameter favors smooth edges. These results confirm the applicability of the GGMRF model for this class of images when $p \approx 1.0$.

Figures 4 - 6 present a simple demonstration case for multiframe fully blind restoration using the GGMRF model for both image and blur. The Metropolis algorithm was used to solve equation 10. Figure 4 shows the two frames of observed data, and the corresponding residual error between the observation and the forward projected image

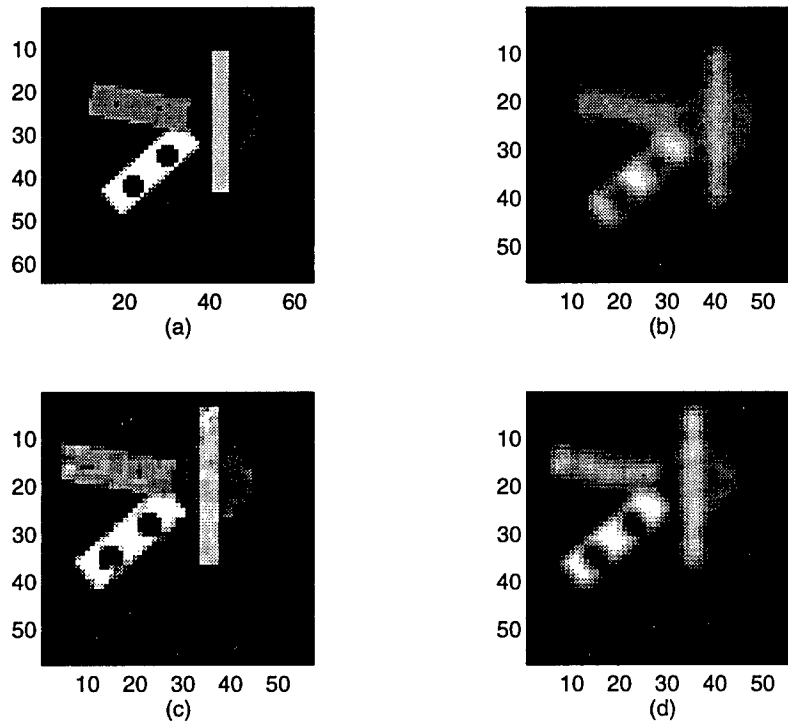


Figure 3: GGMRF MAP restoration of test figure 1 blurred with a 5 by 5 uniform psf, and 35 dB peak SNR. The psf is assumed known. Results shown are for 500 iterations of the Metropolis algorithm with $\gamma = 0.3$ and $\lambda = 0.001$. a) Original image, b) Observation c) Restoration with $p = 1.1$, d) Restoration with $p = 3.0$. Note how $p = 3.0$ causes over smoothing while $p = 1.1$ sharply resolves edges.

estimate using the estimated blur psf's. The lack of structure in this residual error is an indication that convergence was achieved. Figure 5a shows the simple true object (again designed to emphasize sharp edge boundaries and flat regions as in space objects) and 5b shows the blind restoration. Note that sharp edges were preserved, and all the major features except one of the black dots were recovered. The true psf's used to generate \tilde{g} and the corresponding estimates are shown in figure 6. The true psf's were designed to accurately model the residual blur in a partially corrected AO system. These psf's consist of elliptical rotations of Lorentzian functions with different orientations, with spatially low pass filtered Gaussian random fields added to create a random texture. The mean blur psf, μ_H , used in the restoration was a circular Lorentzian function with full-width-half-max of 1.25 pixels. The blur estimates show some error due to observation noise, but have captured all of the major structural features of the true blur.

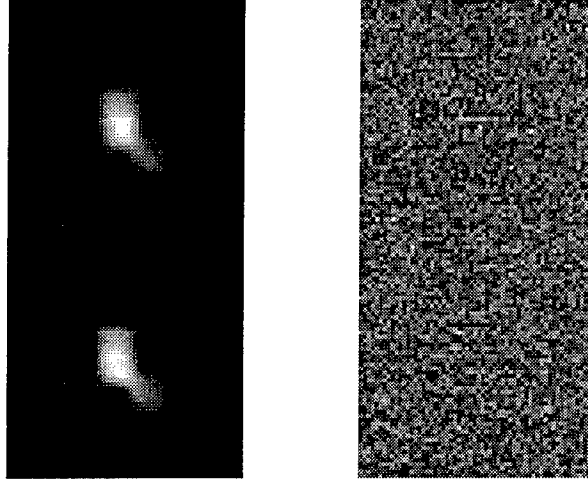


Figure 4: Observation used for fully blind GGMRF MAP Restoration. a) [left] Observation frames 1 (upper half), and 2 (lower half). Noise was i.i.d. Gaussian with peak SNR of 53.5 dB (46.1 dB average SNR). The original true image is shown in Figure 5a, and the blurring psf's for each frame are in Figure 6a. b) [right] Residual error for restoration, $G - H * \hat{F}$, for both frames. Note the lack of structure indicates convergence was achieved.

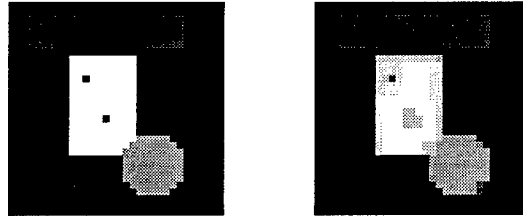


Figure 5: Fully blind GGMRF MAP Restoration of the observed data shown in Figure 4a. GGMRF models were used for both F and H . For F , $p = 0.8$. For H , $q = 2.5$. Both used first order symmetric neighborhoods. a) [left] True image. b) [right] Restoration with 3000 iterations, $T0 = 1$, $\lambda = 10.0$, and $\gamma = 1.0$.

Figure 7 shows an experiment to compare the two algorithms, Metropolis and steepest descent. A single frame was used in fully blind restoration with first order GGMRF models used for both F and H . Figure 7a is the true image, and 7b is the blurred, noise corrupted observation. A 5 by 5 pixel uniform blur was used, and noise is added for 35 dB peak SNR. The other images in Figure 7 are restorations using various image prior model and algorithm parameter settings. The top row, ((c), (e), (g)) contains steepest descent results, while the bottom row, ((d), (f), (h)) was generated with the Metropolis algorithm. The obvious similarity between results from the two algorithms serves as a validation of both techniques. The Metropolis results however are somewhat more random (pixel noise), which is to be expected with a finite duration randomized search method. Figure 7 also provides insight into the effect of parameters p and γ . Comparing (b) and (c) with (g) and (h) shows how values of p near 1.0 emphasizes

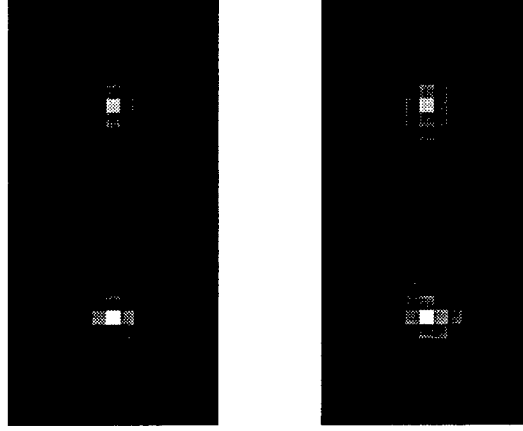


Figure 6: Blind blur psf estimates of the observed data shown in Figure 4. a) [left] True blur psf's for frame 1 (top) and frame 2, (bot.). The blurs were 2-D ellipsoidal Lorentzian functions added to a Gaussian random field generated by low pass filtering white Gaussian noise. The Lorentzian major and minor axis full-width-half-max dimensions (in pixel units) and rotation angle were $[1.5, 1.0, \pi/2]$ and $[1.5, 1.0, -\pi/8]$ for frames 1 and 2 respectively. b) [right] Estimated blur psf/s.

sharp edges in the restoration, while $p = 2.0$ introduces significant edge smoothing. Comparing (e) and (f) with (g) and (h) we note that a value of $\gamma = 3$ produces an under-regularized solution with significant noise amplification when $p = 2.0$.

6.2 Simulated Space Objects Restoration Examples

This section presents examples of GGMRF blind restoration of synthetic and actual AO images of satellites. These results demonstrate the potential of the new method for high resolution recovery of space objects in partially corrected AO multiframe sequences.

Figure 8 shows the observed image frames for a high noise case with a synthetic satellite image and blur psf's taken from actual AO data. A series of 5 partially corrected AO star images were used as the blurring psf's, and noise was added at a level of 20 dB peak SNR. Each observed frame is 64 by 64 pixels. Figure 9 shows the true image at high resolution (128 by 128 pixels), a single observed frame for reference, and the steepest descent algorithm result. GGMRF models were used for both the object and the psf's, with $p = 1.1$ and $q = 2.5$. The object model was first order, while the blur psf model was second order to impose more smoothness in blur estimates. Note that though the solution is noisy, due to low observation SNR, much of the satellite structure is recovered. Figure 10 shows the blur estimates corresponding to Figure 9. It is notable that the central peak structure of the psf's are correctly estimated, though there is noticeable random structure in the halo's due to the low SNR. The low level structure has been emphasized in this figure by using a logarithmic grayscale.

Figure 11 shows results for a similar synthetic satellite case, but with higher peak SNR of 60 dB. Again the data set included five frames blurred with actual AO system psf's, but in this case the Metropolis algorithm was used. Note that the result is significantly smoothed, due to strong regularization imposed by the high value of $\gamma = 1.0$. Even with this over regularization, the bands around the main body, the top antenna, the darker disk at the center of the four panels, and the diagonal crossing bar are resolved.

6.3 Restoration of Real AO Satellite Images

The next experiment uses real AO data, collected at the Starfire Optical Range (SOR) of Phillips Laboratory. The SOR AO system includes a 1.5 meter telescope with a (approximately) 200 cell fully adaptive deformable mirror and a Shack-Hartmann wavefront detector of corresponding size in a closed loop control configuration. The data presented here is from a pass of a METEOR-1 satellite, collected in July or 1995. Partial AO correction was obtained using the object image itself at the wavefront detector, without the use of a guide star. Figure 12 is a sketch of the configuration of the METEOR-1 satellite class.

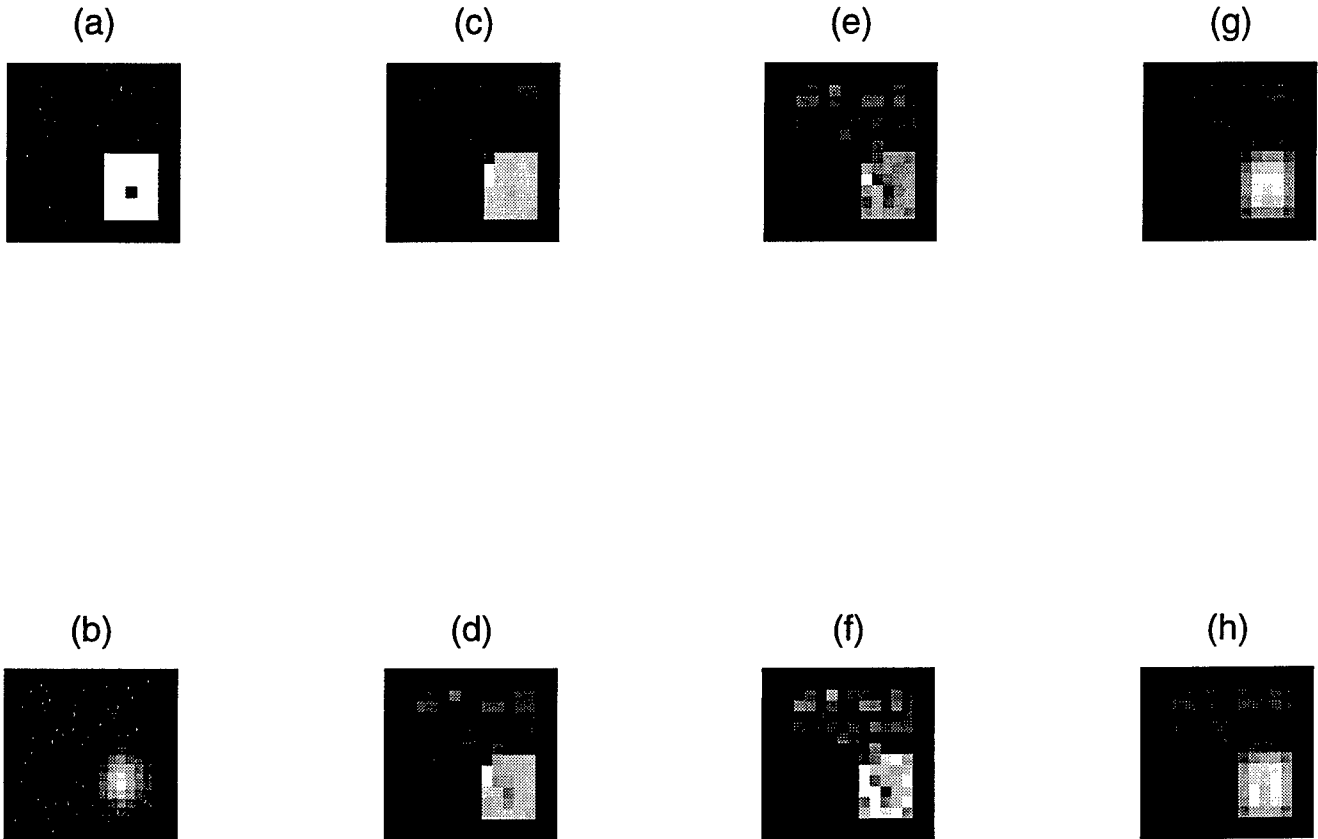


Figure 7: Comparison between the Metropolis and steepest descent algorithms. a) True image. b) Observed image, corrupted by a 5 by 5 uniform blur with 35 dB peak SNR. c) Steepest descent restoration with $p = 1.1$ and $\gamma = 3$. d) Metropolis restoration with $p = 1.1$ and $\gamma = 3$. e) Steepest descent restoration with $p = 2.0$ and $\gamma = 3$. f) Metropolis restoration with $p = 2.0$ and $\gamma = 3$. g) Steepest descent restoration with $p = 2.0$ and $\gamma = 50$. h) Metropolis restoration with $p = 2.0$ and $\gamma = 50$.

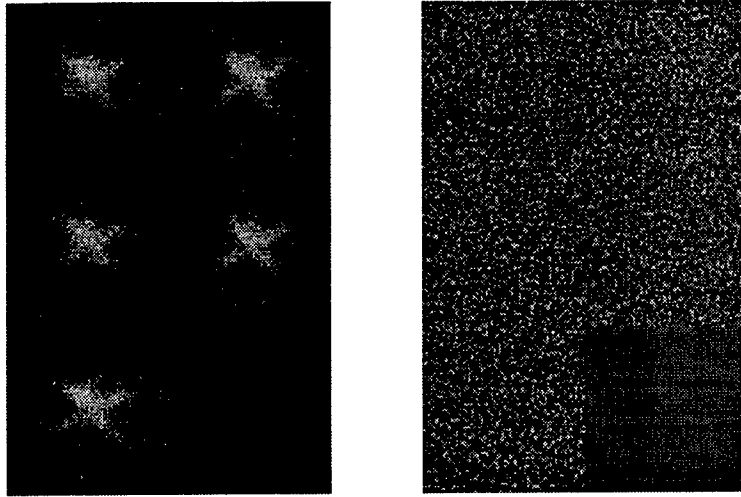


Figure 8: Synthetic Satellite observation used for Fully blind GGMRF MAP Restoration. Each of the 5 frames was blurred with a different actual psf taken from an AO observation of an isolated star. a) [left] Observation frames, with 20 dB peak SNR b) [right] Reconstruction residual error resulting from the solution of Figure 9. Note that lack of structure in the residual indicates the restoration has converged.

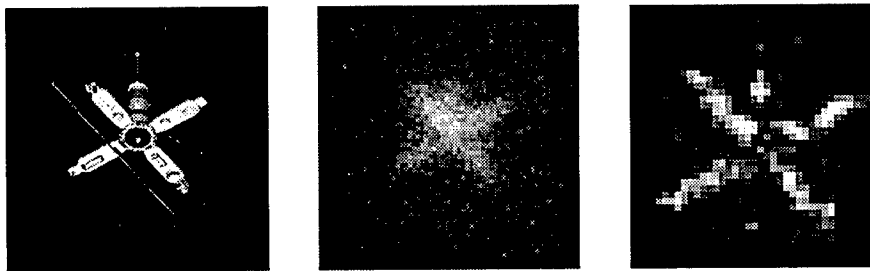


Figure 9: Steepest descent GGMRF restoration of synthetic Satellite data shown in Figure 8. a) [left] High resolution (128×128) true object. b) [middle] An example observation frame (64×64). c) [right] Restored image, 40×40 pixel window. Parameter settings were $p = 1.1$, $q = 2.5$, $\gamma = 0.2$, $\lambda = 200$, $\alpha = 0.001$, and 1,000 iterations.

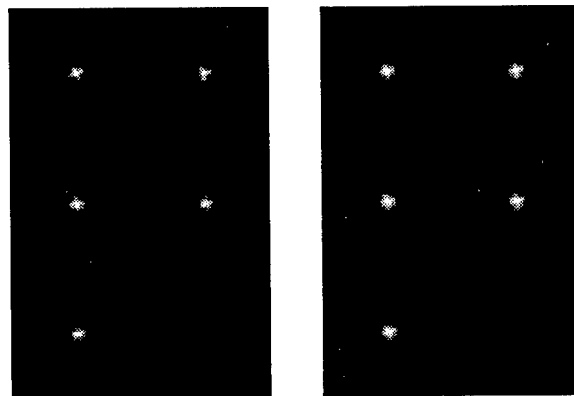


Figure 10: Blur estimates for synthetic Satellite data shown in Figure 8. a) [left] True blur psf's. b) [right] Blur estimates.

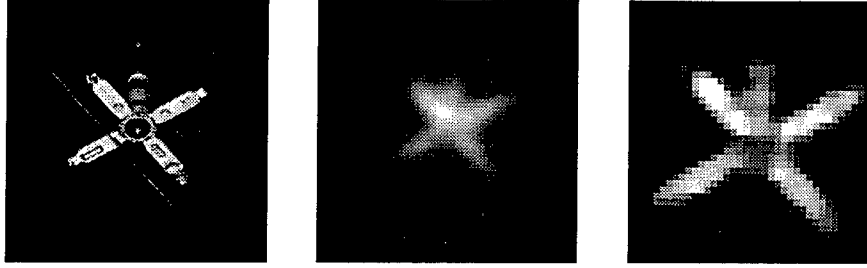


Figure 11: Metropolis GGMRF restoration of synthetic Satellite data with 60 dB peak SNR. a) [left] High resolution (128×128) true object. b) [middle] An example single observation frame (64×64). c) [right] Restored image, 40×40 pixel window. Parameter settings were $p = 1.1$, $q = 2.5$, $\gamma = 1.0$, $\lambda = 50$, and 2,000 iterations.

Figure 13 shows the data set used to compute the restoration. Each of the 10 frames shown is the average (without alignment correction) of 16 consecutive frames of the original data.

collected with a frame exposure time of 5 ms. This averaging increases SNR, albeit at the expense of the desired blur diversity. Figure 14 presents the steepest descent restoration achieved using GGMRF models for object and blur. Note that the solar panels are clearly resolved, and that shadowing at the junction of the lower panel and main body is evident. Figure 14b shows the result that would be obtained with no object regularization, i.e. without the GGMRF image prior term. This result is equivalent to the commonly used Maximum Likelihood solution. It is apparent that without the image prior model, the solution converges to an overly thinned, unrealistic region of support. Figure 14a is consistent with phase diversity processing of this data reported by Paxman et al [4], and with results using the algorithm of Jefferies and Christou [1] [2].

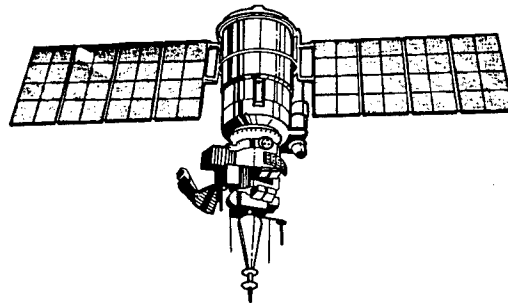


Figure 12: Diagram of the METEOR-1 satellite class. Drawing courtesy of USAF Phillips Laboratory [18].

6.4 Parametric Blind Restoration Results

This section presents a synthetic data example of the effectiveness of parametric blur GGMRF MAP restoration as introduced in Section 4. Figure 15 shows a two frame restoration problem where the blur was known to uniform rectangular, but the extent in the x and y directions was unknown. The blur parameter vector, θ , is defined with $\theta_1 = 'x \text{ direction blur half width}'$, and $\theta_2 = 'y \text{ direction blur half width}'$. The Metropolis algorithm was used to compute the results shown, and the object GGMRF was first order with $p = 0.8$. As shown in Figure 15, the object is restored with significant resolution improvement, and the blur parameters are accurately estimated.

7 Conclusions

This report has detailed the progress made in multiframe blind restoration for AO systems by the author during the AFOSR Summer Faculty Research Program. A new theory for maximum a-posteriori blind image restoration has

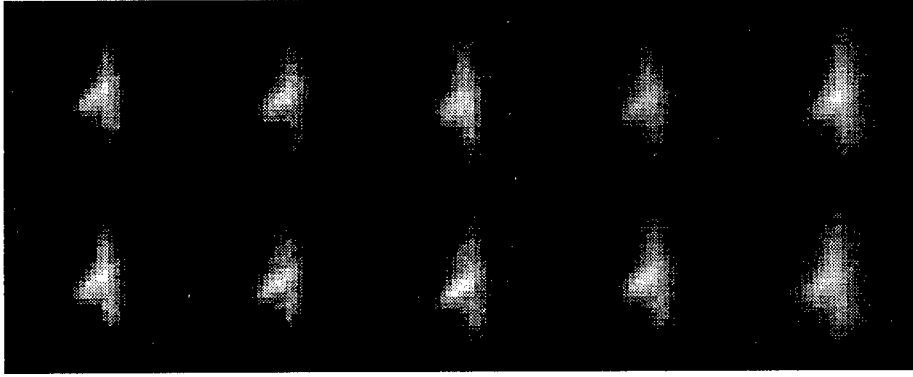


Figure 13: Observed data for catalog number 4419, METEOR-1 satellite. Each of the 10 frames consists of the average over 16 sequential original 5 ms exposure frames. Frames are 32×32 pixels. Note the shift in alignment and blur extent from frame to frame.

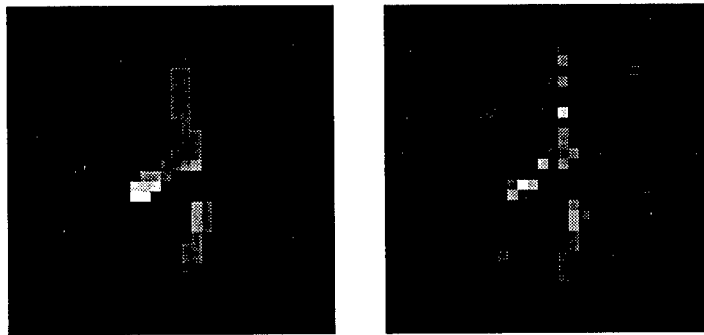


Figure 14: Restoration of the data in Figure 13. A logarithmic grayscale is used to emphasize low level detail. 6,000 iterations of the steepest descent algorithm were used, with $p = 1.1$, $q = 2.5$, first order GGMRF object model, and second order blur model. a) [left] Solution with $\gamma = .4$. b) [right] Solution with $\gamma = 0$, i.e. using no image prior model. This is equivalent to the Maximum likelihood solution, and is seen in this example to overly thin the solution.

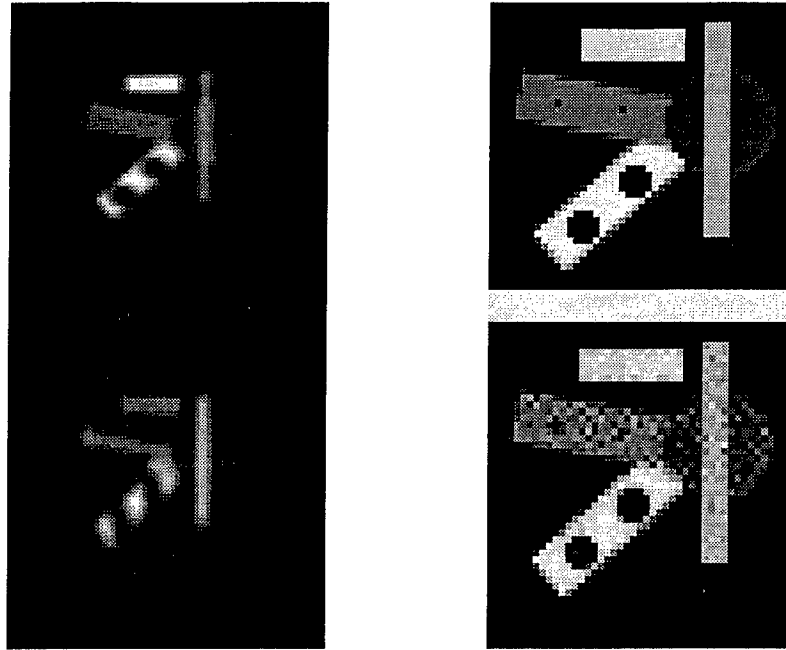


Figure 15: Parametric blind GGMRF MAP Restoration with 2 observation frames. Peak SNR was 40 dB. a) [left] Top: Observation frame 1 . Rectangular blur psf with parameters $\theta = [1.5, 3]$. Bottom: Observation frame 2. Rectangular blur psf with parameters $\theta = [4, 1.75]$, b) [top right] True image, c) Restoration with $\mu_{\Theta} = [3, 3]$, $\gamma = .2$, and $p = 0.8$. Estimated blur parameters were $\hat{\theta} = [1.45, 2.94]$ and $\hat{\theta} = [3.96, 1.73]$ for frames 1 and 2 respectively.

been developed and its application to reducing the error residual in adaptive optics images has been investigated. Two new algorithms, and associated computational computer codes have been developed. In particular, these new algorithms have been shown to be useful in resolution enhancement of space object images collected as a sequence of short exposure frames in an AO environment.

It is anticipated that the new theory and algorithms presented here will be developed into practical tools for space objects imaging at US Air Force facilities. This will be particularly useful because in most space object imaging applications the AO correction is only partial at best. This can be due to difficulty in keeping the object in the same isoplanatic patch as the LASER guide star, or due to the non-point-like size of the extended object when using AO without a guide star. With multiframe data, and the methods presented above, it is possible to recover significant additional edge detail, and in some cases to achieve resolution beyond the cutoff frequency limit of the telescope aperture.

Experimental restoration results using both synthetic and actual AO data are promising. The preliminary results presented here are a strong indication that continued effort will be beneficial to the space objects observation mission of Starfire Optical Range.

References

- [1] S.M. Jefferies and J.C. Christou, "Restoration of astronomical images by iterative blind deconvolution", *Astrophysical Journal*, vol. 415, pp. 862-874, Oct. 1993.
- [2] J.C. Christou, D. Bonaccini, and Nancy Ageorges, "Deconvolution of adaptive optics images using the object autocorrelation and positivity", *Proceedings of the SPIE*, vol. 3126: Conference on Adaptive Optics and Applications, July 1997.

- [3] J.M. Conan, L. Laurent, T. Fusco, V. Michau, and G. Rousset, "Deconvolution of adaptive optics images using the object autocorrelation and positivity", *Proceedings of the SPIE*, vol. 3126: Conference on Adaptive Optics and Applications, July 1997.
- [4] R.B. Paxman, J.H. Seldin, B.J. Thelen, M.F. Reiley, and D.A. Carrarra, "Focused-beam scoring techniques, volume i", Tech. Rep. 278140-9-F(V.I), SOR, Air Force Phillips Laboratory, Kirtland AFB, 1997.
- [5] J.D. Drummond, "Sizes, shapes and rotational poles of ceres and vesta from adaptive optics images", *Bulletin of the American Astronomical Society*, vol. 27, pp. 16, 1996.
- [6] J.D. Drummond, R.Q. Fugate, J.C. Christou, and E.K. Hege, "Full adaptive optics images of asteroids ceres and vesta: Rotational poles and triaxial ellipsoid dimensions", *to appear in ICARUS*, 1998.
- [7] R. L. Lagendijk and J. Biemond, *Iterative Identification and Restoration of Images*, Kluwer, Boston, 1991.
- [8] P.J. Sementilli, M.S. Nadar, and B.R. Hunt, "Poisson map super-resolution estimator with smoothness constraint", *Proceedings of the SPIE*, vol. 2032, July 1993.
- [9] Y. Yang, N.P. Galatsanos, and H. Stark, "Projection-based blind deconvolution", *Journal of the Optical Society of America A*, vol. 11, no. 9, Sept. 1994.
- [10] Z. Mou-yan and R. Unbehauen, "New algorithms of two-dimensional blind deconvolution", *Optical Engineering*, vol. 34, no. 10, pp. 2945-2956, Oct. 1995.
- [11] C. Bouman and K. Sauer, "A generalized Gaussian image model for edge-preserving MAP estimation", *IEEE Transactions on Image Processing*, vol. 2, no. 3, pp. 296-310, July 1993.
- [12] Wai Ho Pun, *Parametric Model-Adaptive Image Restoration*, PhD thesis, Brigham Young University, 1995.
- [13] W. H. Pun and B. D. Jeffs, "Shape parameter estimation for generalized gaussian markov random field models used in map image restoration", in *Conference Record, 29th Asilomar Conf. Signals, Syst., Comp.*, Oct. 1995, pp. 1472-1476.
- [14] A. K. Jain, *Fundamentals of Digital Image Processing*, Prentice Hall, Englewood Cliffs, 1989.
- [15] C. C. Chen, *Markov random field models in image analysis*, PhD thesis, Michigan State University, East Lansing, 1988.
- [16] R.C. Gonzalez and R.E. Woods, *Digital Image Processing*, Addison-Wesley, Reading, Massachusetts, 1992.
- [17] J.W. Goodman, *Fourier Optics*, McGraw-Hill, New York, 1964.
- [18] N.L. Johnson and D.M. Rodvold, "Europe and asia in space, 1993-1994", Tech. Rep., USAF Phillips Laboratory/XPF, Kirtland AFB, NM, 1994.

MECHANICS OF SURFACE PRECISION FOR MEMBRANE REFLECTORS

Dr. Christopher H. M. Jenkins, P. E.
Associate Professor
Department of Mechanical Engineering

South Dakota School of Mines and Technology
501 E. Saint Joseph Street
Rapid City, SD 57701

Final Report for:
Summer Research Program
Phillips Laboratory

Sponsored by:
Air Force Office of Scientific Research
Bolling Air Force Base, Washington, DC

And

Phillips Laboratory

September, 1997

MECHANICS OF SURFACE PRECISION FOR MEMBRANE REFLECTORS

Dr. Christopher H. M. Jenkins, P.E.
Associate Professor
Director, Compliant Structures Laboratory
Mechanical Engineering Department
South Dakota School of Mines and Technology

Abstract

The seminal application of membrane structures for space-based communications occurred over four decades ago with the Echo series of satellites. Today, a resurgence of interest in membrane structures for extraterrestrial use is developing, due to their potential for reduced launch mass and stowed volume. Applications for such structures range from planar configurations in solar sails, concentrators, and shields, to inflatable lenticulars for radar, radio, and optical uses. The performance of this latter class of applications is studied, with particular emphasis on the precision of the reflector surface.

MECHANICS OF SURFACE PRECISION FOR MEMBRANE REFLECTORS

Christopher H. M. Jenkins

INTRODUCTION

The seminal application of membrane structures for space-based communications occurred over four decades ago with the Echo series of satellites [Shortal, 1978]. Today, a resurgence of interest in membrane structures for extraterrestrial use is developing, due to their potential for reduced launch mass and stowed volume. Applications for such structures range from planar configurations in solar sails, concentrators, and shields, to inflatable lenticulars for radar, radio, and optical uses.

Three key factors are paramount for the success and user acceptance of this technology: manufacture, deployment, and performance. Performance hinges critically on the precision of the membrane surface. The amount of precision is highly mission dependent, and may entail one or more of the following issues: surface smoothness, deviation from desired surface profile, and slope error.

A range of precision requirements exist. At one end are the solar sails and planar concentrators which require maximum exposed surface area and/or flatness. At the other extreme, membrane optical reflectors may require ratios of aperture diameter to figure error (rms) around 10^6 to 10^7 or more [Rapp, 1996].

For example, the AF Phillips Laboratory has recently undertaken the task of creating a large optical quality membrane telescope. The membranes on these telescopes will range in thickness from 10 - 150 micrometers. The maximum acceptable peak-to-peak figure error over the entire surface will range from 10 - 20 micrometers. (This value assumes that a certain amount of secondary adaptive optics will be used to correct image errors.)

THEORETICAL BASIS

Background

The problem of the inflation of an initially plane membrane with circular boundary begins with Hencky [1915]. Earlier, Föppl [1907] had arrived at equilibrium equations for a membrane plate. These equations were essentially modified von Kármán plate equations [1910] with the bending rigidity set to zero. Figure 1 represents a plane elastic sheet with circular boundary of

radius a . The geometry is rotationally symmetric (axisymmetric); we also assume the loading to be a symmetric pressure p . The sheet has modulus E , thickness h , and Poisson's ratio ν

The von Kármán plate equations are based upon strains which have nonlinearity introduced through rotations (squares of slope):

$$\varepsilon_r = \frac{du}{dr} + \frac{1}{2} \left(\frac{dw}{dr} \right)^2 \quad (1)$$

$$\varepsilon_\theta = \frac{u}{r} \quad (2)$$

where u and w are displacements in the r and z directions, respectively.

The von Kármán plate equations in axisymmetric form can be written as:

$$D \left(\frac{d^2}{dr^2} + \frac{1}{r} \right)^2 w - \frac{h}{r} \frac{d}{dr} \left(\frac{d\Phi}{dr} \frac{dw}{dr} \right) = p \quad (3)$$

$$r \frac{d}{dr} \left(\frac{d^2 \Phi}{dr^2} + \frac{1}{r} \frac{d\Phi}{dr} \right) + \frac{E}{2} \left(\frac{dw}{dr} \right)^2 = 0 \quad (4)$$

where $D = Eh^3/12(1-\nu^2)$ is the bending rigidity, and Φ is a stress function to which the stress resultants in the radial and circumferential direction are related respectively by:

$$N_r = \frac{1}{r} \frac{d\Phi}{dr}, N_\theta = \frac{d^2 \Phi}{dr^2} = \frac{d}{dr} (r N_r) \quad (5)$$

Linear elastic constitutive relations are assumed. It is important to note that the above equations are not *geometrically exact*, in that several assumptions have been made.

Hencky provided a solution of the above for the case of zero boundary displacements ($u = 0 = w$ at $r = a$) and $D = 0$ by assuming power series for stresses and transverse displacement. Little interest in the Hencky problem seems to have taken place until the 1940's, when, in conjunction with a study on air-supported roofs, Stevens [1944] performed an experimental investigation on a 10 inch radius by 0.014 inch thick cellulose acetate butyrate inflated circular membrane. Stevens compared his results for the deflected membrane shape (which were apparently empirical in nature) with Hencky's. Apparently Chien [1948] provided slight corrections to Hencky's solutions for maximum values of stress and transverse deflection [see also Kao and Perrone, 1971].

Cambell [1956] allowed an arbitrary initial tension in the membrane. Dickey [1967] re-examined the Hencky problem, this time using a nonlinear integral equation formulation. Dickey provided a plot of $u(r)$ for various values of the Poisson's ratio. Weil and Newmark [1955] provide some experimental evidence that validate Dickey's predictions. We discuss later the important relationship of $u(r)$ with the surface precision.

Kao and Perrone [1971] used a relaxation method, developed earlier by Shaw and Perrone [1954], to solve the Hencky problem [see also Kao and Perrone, 1972]. Schmidt and DaDeppo [1974] and Schmidt [1974] used a perturbation analysis based on odd powers of r (actually r/a), in conjunction with the Marguerre shallow shell equations (which collapse to the von Kármán plate equations when there exists no initial curvature), to determine the maximum values of the stress and transverse displacement in the Hencky problem. In a series of articles, Storakers [1983] uses a power series in even powers of r (or r/a) for stresses and transverse displacement (odd powers of r for $u(r)$).

Föppl-Hencky-von Kármán from Shallow Shell Theory

Inherent in the Föppl-Hencky-von Kármán (FHvK) theory are a number of assumptions which must be understood if this is to be a predictive tool for precision membrane reflectors. This large deflection theory is an extension of linear plate theory, in which no distinction is made between the reference (plane) configuration and the deformed configuration. Hence we find FHvK describing a non-planar deformed configuration in terms of reference configuration variables $u(r)$, $w(r)$, N_r , etc.

Questions immediately arise: Is N_r the tangential or meridional stress, or its radial component? In the case of uniform distributed loading, does the load remain always in the same initial direction, transverse to the reference plane of the membrane, or is it a "follower" load, i.e., a true pressure?

A more rational approach to deriving a large deformation membrane plate theory begins by writing equilibrium equations in the deformed configuration. This puts us in the domain of shell equations, and we need only ignore the initial curvature and related effects to collapse back to plate theory. Although many shell theories exist with different levels of complexity, an excellent starting point for our purposes can be found in the so-called "simplified Reissner

nonlinear axisymmetric shell equations,” or SRE for convenience. We follow here Libai and Simmonds [1988], and Weinitschke and Grabmüller [1992].

We take a cylindrical-polar coordinate system with basis \mathbf{e}_r , \mathbf{e}_θ and \mathbf{e}_z . The SRE can be written as:

$$C \left(rF'' + F' \cos \phi_0 - \frac{1}{r} F \right) + \cos \phi_0 - \cos(\phi_0 + \phi) + C \left[(r^2 p_H)' + \nu r p_T \right] = 0 \quad (6)$$

$$D \left(r\phi'' + \phi' \cos \phi_0 - \frac{1}{r} \sin \phi \right) - F \sin(\phi_0 + \phi) + rV \cos(\phi_0 + \phi) = 0 \quad (7)$$

where $C = 1/Eh$, $D = Eh^3/12(1-\nu^2)$, ϕ_0 is the initial orientation of the meridional tangent (measured from the base plane of the surface of revolution), ϕ measures the rotation of the meridional tangent during deformation, ν is Poisson's ratio, ' denotes derivatives with respect to meridional arc length, p_T is the meridional component of load, p_H is the r component of load, V is the z component of the meridional stress resultant N_ϕ , $F = rH$, and H is the r component of the meridional stress resultant N_ϕ .

To collapse to the circular membrane, we let differentiation with respect to arc length be replaced by differentiation with respect to the radial coordinate r , and set ϕ_0 and D equal to zero. Then we get:

$$C \left(rF'' + F' \cos \phi - \frac{1}{r} F \right) + 1 - \cos \phi + C \left[r^2 p_H' + (2 + \nu \cos \phi) r p_H + \nu r p_V \sin \phi \right] = 0 \quad (8)$$

$$-F \sin \phi + rV \cos \phi = 0 \quad (9)$$

where

$$(r^2 p_H)' = r^2 p_H' + 2r p_H \quad (10)$$

and

$$p_T = p_H \cos \phi + p_V \sin \phi \quad (11)$$

From (10),

$$F = \frac{rV}{\tan \phi} = \frac{rN_\phi \sin \phi}{\tan \phi} = rN_r \cos \phi \quad (12)$$

Now substituting (13) into (9), and noting that $p_H = 0$ for the plane membrane problem, we get

$$C\left(rF'' + F' - \frac{1}{r}F\right) + 1 - \cos\phi + Crp_v \sin\phi = 0 \quad (13)$$

After performing the indicated operations and some algebra, we get

$$C\left(r^2 N_\phi'' \cos\phi + 3rN_\phi' \cos\phi + 2rN_\phi \cos'\phi + r^2 N_\phi \cos''\phi\right) + 1 - \cos\phi + Crp_v \sin\phi = 0 \quad (14)$$

Note that no assumptions have been made up to this point on the smallness of the meridional tangent angle ϕ

Now, to arrive at the FHvK equation corresponding to (4), we assume that ϕ is small such that $\cos\phi \rightarrow 1$, $\sin\phi \rightarrow \phi \approx dw/dr$, and that $\cos'\phi = 0 = \cos''\phi$. Then expanding $1 - \cos\phi$ and keeping only quadratic terms

$$- \cos\phi = 1 - \left(1 - \frac{\phi^2}{2} + \dots\right) \approx \frac{1}{2}\phi^2 \approx \frac{1}{2}\left(\frac{dw}{dr}\right)^2 \quad (15)$$

we get

$$r^2 N_\phi'' + 3rN_\phi' = -\frac{Eh}{2}\left(\frac{dw}{dr}\right)^2 \quad (16)$$

which is precisely the FHvK result, when (5) is substituted into (4), and N_r is replaced by N_ϕ . (In (17), the term $Crp_v \phi$ is neglected since the error associated with this term is roughly the same order of magnitude as that inherent in shallow shell theory; see Libai and Simmonds, 1988, p. 222.)

This exercise makes clear a number of issues left unresolved from the FHvK formulation.

1. There is no need to make an assumption that the loading is other than normal to the membrane *always*, i.e., the loading is indeed a *pressure* loading.

Various authors have suggested that the loading in FHvK is *transverse*, i.e. the loading is not a *follower* load like pressure, but always maintains its original orientation. Fichter [1997] in fact includes an additional force term not included in the original FHvK formulation to account for pressure loads. There is no way to determine the exact nature of the loading from the original FHvK formulation, due to its lineage from plate theory. Ultimately, it will take careful

experimentation to resolve this question, but the result of the above exercise suggest that the loading is indeed a follower or pressure load.

2. Stress resultants are indeed “in-plane” or tangential resultants.

Various authors confuse the FHvK problem by describing stress and displacement in terms of the undeformed configuration. That is, *radial* stress and displacement are used where meridional stress and displacement are called for. Again, the distinction cannot be made from the plate-based FHvK theory itself.

3. The order of approximation error inherent in the FHvK formulation is exposed. The error between the SRE and FHvK results ought to be of the same order as the error in assuming the cosine of a small angle is approximately unity. FHvK makes this assumption relative to the deformed membrane slope (dw/dr) and membrane slope angle (ϕ). That is,

$$\tan \phi = \frac{dw}{dr} \approx \sin \phi \quad (17)$$

Hence, approximating $\sin \phi$ by ϕ itself is like approximating $\tan \phi$ with $\sin \phi$. It is easy to show that this is identical to approximating $\cos \phi$ by unity (except for a negative sign):

$$\frac{\tan \phi - \sin \phi}{\sin \phi} = -\frac{\cos \phi - 1}{\cos \phi} \quad (18)$$

SURFACE PRECISION METRICS

General

Thomas and Veal [1984] report on surface precision measurements of membrane reflectors, with various gore/seaming configurations. They suggest that an “rms surface error” of 1 mm is suitable for membrane reflectors with frequency applications less than 15 Ghz; they do not define rms surface error. Plotting the deviation of the actual membrane surface from that of a true parabola results in a “W-shaped curve” or simply a “W-curve.”

One measure that categorizes curved reflector or imaging surfaces is the so-called f/D ratio or “f-number”, where f is the focal length of the surface and D its diameter. Values of f/D around 1 or 2 are typical for an optical imaging surface, while solar concentrators might be in the 15 - 35 range; note that the lower the f/D , the greater the surface curvature. Murphy [1986, 1987] studied “stretched membrane heliostats” (large, nearly flat, concentrating solar reflectors) which are inflated into a doubly-curved surface with f/D around 14. The surface profile was assumed to be parabolic,

and initial tension was considered. Palisoc and Thomas [1995] suggest that the variation of elastic modulus with strain over the membrane surface can be large, and may be a major cause of surface inaccuracies.

Surface rms

From a structural perspective, a common surface precision metric is the rms measure of surface deviation. This metric has had a long tradition in the antenna community [see, e.g., Ruze (1966), Zarghamee (1967), Fichter (1984), and Meyer (1985)]. The mean of the square of the surface deviation δ of the current configuration relative to a reference configuration is found from

$$\langle \delta^2 \rangle = \frac{\iint_A \delta^2 \psi dA}{\iint_A \psi dA} \quad (19)$$

where ψ is an “illumination function”; for uniform illumination, $\psi = 1$, which we assume in what follows.

If the reference surface is a sphere, the calculation is relatively straightforward. The element of surface area of a spherical cap is $dA = \rho^2 \sin \phi d\phi d\theta$, where ρ is the radius of the sphere, ϕ is the polar angle, and θ is the azimuthal angle. In this case, the denominator of (29) is easily shown to be equal to $2\pi\rho w_0$, where w_0 is the “height” of the cap as measured from its base plane. Note that for the axisymmetric cases of interest here, geometry, kinematics, and kinetics are independent of θ , and we conveniently use the 2-dimensional surface *profiles* and cylindrical-polar coordinates. In that case, the integral of $d\theta$ merely provides a factor of 2π to both numerator and denominator, and can henceforth be disregarded.

In order to evaluate the numerator of (29), it is most convenient to write the equations of both reference surfaces relative to a cylindrical-polar coordinate system having origin at the center of the sphere (circle profile). This is trivial for the surface of the sphere, but requires a translation of coordinates for the membrane surface as it is usually described, where the origin of coordinates usually resides in the base plane.

Consider for example the so-called Stevens’ equation for the circular membrane profile:

$$w(r) = w_0 \left(1 - 0.9 \frac{r^2}{a^2} - 0.1 \frac{r^5}{a^5} \right) \quad (20)$$

where w and z are used interchangeably. We translate coordinates to the center of the sphere (\sim coordinates) whose great circle passes through $w(0)$ and $w(a)$. Then a little geometry shows that

$$\tilde{w}(r) = w(r) + \sqrt{\rho^2 - a^2} \quad (21)$$

Now δ can be written as:

$$\delta = \rho - \tilde{R} = \rho - \sqrt{r^2 + \tilde{w}^2} \quad (22)$$

Then using the fact that integration takes place from $\phi = 0$ to

$$\phi = \phi_{\max} = \cos^{-1} \left(\frac{\sqrt{\rho^2 - a^2}}{\rho} \right), \quad (23)$$

$\langle \delta \rangle$ can be determined using (29).

However, if the reference surface is a paraboloid, one must resort to a formulation written in paraboloidal coordinates (ζ, ξ, θ) , with origin at the focus of the paraboloid and where θ is as above. The paraboloidal coordinates (overbar coordinates) are related to the cylindrical-polar coordinates through the complex relationship [Jeffreys and Jefferys (1972)]:

$$\zeta + i\xi = \sqrt{\bar{z} + ir} \quad (24)$$

where $i = \sqrt{-1}$. Then solving for the cylindrical-polar coordinates in terms of the paraboloidal coordinates gives

$$r = 2\zeta\xi, \quad \bar{z} = \zeta^2 - \xi^2 \quad (25)$$

As in the case of the sphere, we take the paraboloid that passes through $w(0)$ and $w(a)$. In this case it can be readily shown that $w_0 = a^2/4f$, where f is the focal length of the paraboloid. The surface area of the paraboloidal cap can be shown to be [Wilkes (1997)]:

$$\frac{8\pi}{3} f^2 \left[\left(1 + \frac{w_0}{f} \right)^{3/2} - 1 \right] \quad (26)$$

The coordinate transformation is then

$$\bar{w} = w + f - w_0 \quad (27)$$

and δ can be written as

$$\delta = \bar{\rho} - \bar{R} = \bar{\rho} - \sqrt{r^2 + \bar{w}^2} \quad (27)$$

Wavefront Error

The ideal parabolic reflector will image an axial (i.e., parallel to the paraboloid axis) bundle of monochromatic rays at a unique spot on the paraboloid axis, viz., the *focal point*. Any deviation of the surface from a true paraboloid will result in slightly different image distances for different annuli of the reflector. Hence the focal point becomes a focal “spot” in a two-dimensional plane perpendicular to the optical axis. Such imaging errors are called *spherical aberrations* [Walker, 1994].

Optical engineers characterize such aberrations in terms of *wavefront error*, or number of waves of optical path difference. In typical high-performance optical systems, wavefront errors are on the order of a small fraction of the wavelength of interest. Wavefront error may be specified as peak-to-valley (PTV) or as rms.

SURFACE PRECISION OF AN IDEAL INFLATED CIRCULAR MEMBRANE

An inflated membrane reflector was simulated using finite element methods (FEM). The reference configuration is a 0.005 inch thick plane circular membrane of diameter 42 inch and elastic modulus 500000 psi. In most cases, the membrane is inflated to F-numbers ($F\# = \text{ratio of focal length to aperture diameter}$) around unity. For example, with an inflation pressure of 0.75 psi and Poisson ratio of 0.4, the central deflection is about 2.46 inch, with resultant focal length of 44.9 inch, or $F\# = 1.07$. (One case uses a pressure of 0.075 psi, which clearly results in much larger $F\#$ s.)

The nonlinear FEM code ABAQUS was used to analyze a one-quarter symmetry model comprised of 288 2nd-order membrane elements. Due to the fact that the membrane has no stiffness to resist the initial pressure loading, some sort of starting scheme must be implemented. In the present case, elastic “springs” or rod elements were applied transversely to the undeformed membrane to provide the requisite transverse stiffness. After a small inflation increment, the springs are removed and full inflation is achieved.

FEM-generated surface profiles, in the form of nodal displacement data, are fit with n th-order polynomials by a Levenburg-Marquardt (nonlinear least-squares) procedure [Press et al., 1986]; typically $n = 7$ here. Equivalent parabolas are found in a similar manner, wherein the

parabolas are forced by limiting the polynomials to a form $y = a + bx^2$. The polynomials are then passed through surface rms and wavefront error estimators as described previously.

In Table 1, two pressure loadings are considered: $p = 0.75\text{psi}$ and 0.075psi . Note that the FEM results for either case “over predict” the center deflection relative to Hencky, particularly so for the 0.75psi case.

For the 0.075 psi case, the maximum slope angle is about 7 degrees, and for the 0.75 case it is about 15 degrees. (This was determined from the derivative of the 7th order polynomial curve fit to the FEM data, then evaluated at the boundary.) To get a rough estimate of the error at this time, we find the average slope angles are about 3 and 7 degrees, respectively. (These are found from taking the average of the derivative of the polynomial above.) Note that the errors are in the same direction, but under predict the central deflection data by about half. (Clearly, the angle approximation error should be more “cumulative” than the average slope angle would suggest.)

The point is this: the inflation case of 0.75 psi is pushing the limits of accuracy of the FHvK theory. (In this case, $w_0/a = 2.46/21 = 0.117$ and $w_0/h = 2.46/0.005 = 492!$) Note how much closer the FEM & FHvK results are for the lower pressure. As the cosine of the slope angle continues to deviate from unity, the error between FEM & FHvK increases, and the FHvK “under predicts” the “exact” deformation.

pressure	w0 Hencky	w0 fem	% diff.	max phi	avg phi	(cos phi-1)/cos phi
0.075	1.1269565	1.13	-0.27007	-6.938	3.09	-0.145719703
0.75	2.4279541	2.459	-1.27868	-15.057	6.7	-0.688187948

Table 1. Error in FHvK theory as a function of slope angle.

Table 2 provides results of precision metrics for FEM simulations. Both surface rms and wavefront error (PTV and rms) are given. Inflation pressure is a constant 0.75 psi for each case, while the Poisson ratio of the membrane material is varied. (Also shown is one case of pressure equal to 0.075 psi .) Wavefront errors were determined using on-axis 0.55 micron wavelength monochromatic light. Wavefront error is given both in number of waves (at 0.55 micron) and mm. Surface rms values are given in mm, thus allowing comparisons to be made.

pressure (psi)	Poisson	1/2 aperture (inch)	w0 (inch)	focal length (inch)	F#	PTV Wavefront (waves)	RMS Wavefront (waves)/(mm)	RMS surface (mm)
0.75	0.25	21.00826216	2.62	42.113	1.00229	9841.5	2738.7/1.51	1.721798
0.75	0.3	20.961742	2.569	42.759	1.01992	9202.4	2561.2/1.41	1.69584
0.75	0.35	20.901481	2.516	43.409	1.03841	8707.3	2441.98/1.34	1.59548
0.75	0.4	21.0072825	2.459	44.866	1.06786	7643.98	2141.4/1.18	1.433964
0.75	0.45	21.147018	2.398	46.622	1.10233	6513.97	1814.4/0.998	1.258159
0.75	0.49	20.9876	2.346	46.939	1.11825	6417.98	1814.9/0.998	1.215917
0.075	0.4	20.99010795	1.13	97.474	2.32190	3192.9	n/a	0.611973

Table 2. Comparison of precision metrics.

The minimum error is given with the highest Poisson ratio. This is to be expected given the physical arguments of Jenkins and Marker [1997], which explains why the inflated circular membrane is never a parabola. A plot of rms surface error versus Poisson ratio is shown in Figure 2.

CONTROL OF SURFACE PRECISION

Passive and active methods are possible for control of surface precision in membrane reflectors. The fundamental passive technique is to manufacture the reflector in such a way that it achieves as close to parabolic profile as possible upon inflation. Palisoc and Thomas [1995], and Palisoc and Huang [1997], report on a computer code that allows for flat gores to be cut to achieve such a construction.

Other possibilities for passive techniques include tailoring material parameters such as thickness, CTE, modulus, homogeneity, etc., to achieve the desired profile. Studies on varying the thickness distribution of the undeformed membrane to achieve either a parabolic [Vaughn, 1980] or spherical [Hart-Smith and Crisp, 1967] profile upon inflation have shown that, in both of these cases, thickness must initially increase from center to edge in order to achieve either of these desired shapes.

Concepts for active control include electrostatic, thermal, and boundary manipulations. Electrostatic forces can be used to deform metalized membrane reflectors, e.g., BY using a planar electrode with a planar membrane. A potential difference between the electrode and membrane causes an electrostatic attraction or repulsion, thus forming the reflector surface. Discrete control is possible. [See Rapp, 1996 for a summary.]

Application of temperature gradients to the reflector may be used to effect changes in the surface profile. Haftka and Adelman [1985] investigated such a scheme analytically for large space structures. Selective heating of the membrane surface via a laser is an intriguing possibility.

Manipulating the boundary (rim) of the reflector has been shown in simulations to be effective. Jenkins [1996], Jenkins and Marker [1997], and Marker and Jenkins [1997] have shown that the figure error in the inflated membrane profile can be reduced through judicious boundary displacements [see also Natori et al., 1989].

REFERENCES

- Cambell, J.D. (1956), "On the theory of initially tensioned circular membranes subjected to uniform pressure," *Q J Mech Appl Math* **9**, 84-93.
- Chien, W.Z. (1948), "Asymptotic behavior of a thin clamped plate under uniform normal pressure at very large deflection," *Sci. Rep. Natn. Tsing Hua Univ.* A5, 71-94.
- Dickey, R.W. (1967), "The plane circular elastic surface under normal pressure," *Arch Rational Mech Anal* **26**, 219-236.
- Fichter, W. B. (1984), "Reduction of root-mean-square error in faceted antennas," *AIAA J* **22**, 1679-1684.
- Fichter, W. B. (1997), "Some solutions for the large deflections of uniformly loaded circular membranes," *NASA Technical Paper* 3658.
- Föppl, A. (1907), "Vorlesungen über technische Mechanik," *B.G. Teubner*, Bd. 5., p. 132, Leipzig, Germany.
- Haftka, R. T., and Adelman, H. M. (1985), "An analytical investigation of shape control of large space structures by applied temperatures," *AIAA J* **23**, 450-457.
- Hart-Smith, L.J., and Crisp, J.D.C. (1967), "Large elastic deformations of thin rubber membranes," *Int J Eng Sci* **5**, 1-24.
- Hedgepeth, J.M. (1982), "Accuracy potentials for large space antenna reflectors with passive structures," *J Spacecraft* **19**(3), 211-217.
- Hencky, H. (1915), "Über den Spannungszustand in kreisrunden Platten," *Z. Math. Phys.* **63**, 311-317.
- Jeffreys, H., and Jeffreys, B. S. (1972), *Methods of mathematical physics*, Cambridge.

- Jenkins, C.H., Marker, D.K., and Wilkes, J.M. (1998a), "Improved surface accuracy of precision membrane reflectors through adaptive rim control," *ALAA Adaptive Structures Forum*, Long Beach, CA (to appear).
- Jenkins, C.H., Wilkes, J.M., and Marker, D.K. (1998b), "Surface accuracy of precision membrane reflectors," *Space 98*, Albuquerque, NM (to appear).
- Jenkins, C. H., and Marker, D. K. (1997), "Surface precision of inflatable membrane reflectors," *J Solar Energy Engr* (in review).
- Jenkins, C.H. (1996). *Shape Control of an Inflated Membrane Disk: Preliminary Investigation*. Summary Report, Phillips Laboratory, Kirtland AFB.
- Jenkins, C.H. (1996), "Nonlinear Dynamic Response of Membranes: State of the Art -- Update," *Appl Mech Rev* 49 (10), S41-S48.
- Jenkins, C.H., and Leonard, J.W. (1991), "Nonlinear Dynamic Response of Membranes: State of the Art," *Appl Mech Rev* 44, 319-328.
- Kao, R., and Perrone, N. (1971), "Large deflections of axisymmetric circular membranes," *Int J Solids Struct* 7, 1601-1612.
- Kao, R., and Perrone, N. (1972), "Large deflections of flat arbitrary membranes," *Comput Struct* 2, 535-546.
- Libai, A. and Simmonds, J.G. (1988), *"The nonlinear theory of elastic shells,"* Academic Press.
- Marker, D. K., and Jenkins, C. H. (1997), "On the systematic "W" profile error in uncompensated isotropic membrane reflectors," *25th Midwestern Mechanics Conf*, Rapid City, SD.
- Meyer, R. X. (1985), " Precision of mesh-type reflectors for large space-borne antennas," *J Spacecraft* 22,80-84.
- Mikulus, M. M. (1964), "Behavior of a flat stretch membrane wrinkled by the rotation of an attached hub, *NASA Technical Note TN D-2456*.
- Miller, R. K., Hedgepeth, J. M., Weingarten, VI, Das, , and Shahrzad K. (1985), "Finite element analysis of partly wrinkled membranes," *Computers Structures* 20, 631-639.
- Murphy, L.M. (1987), "Moderate axisymmetric deformations of optical membrane surfaces," *J Solar Energy Eng* 109, 111-120.

- Murphy, L.M. (1986), "Stretched-membrane heliostat technology," *J Solar Energy Eng* **108**, 230-238.
- Natori, M., Shibayam, Y., and Sekine, K. (1989), "Active accuracy adjustment of reflectors through change of element boundary," *AIAA paper no. 89-1332-CP*.
- Palisoc, A., and Thomas, M. (1995), "A comparison of the performance of seamed and unseamed inflatable concentrators," *Solar Engineering 1995: 1995 ASME/JSME/JSES Int Solar Energy Conf* **2**, 855-864.
- Palisoc, A. L., and Huang, Y. (197), "Design tool for inflatable space structures," *AIAA paper 97-1378*.
- Press, W. H., Flannery, B. P., Teukolsky, S. A., and Vetterling, W. T. (1986), *Numerical recipes*, Cambridge Univ. Press.
- Rapp, D. (1996), "Prospects and limitations of technical approaches for ultra lightweight space telescopes," *JPL Report D-13975*.
- Ruze, J. (1966), "Antenna tolerance theory - a review," *Proc. IEEE* **54**, 633-640.
- Schmidt, R. (1974), "On Berger's method in the non-linear theory of plates," *J Appl Mech* **41**, 521-523.
- Schmidt, R., and DaDeppo, D.A. (1974), "A new approach to the analysis of shells, plates, and membranes with finite deflections," *Int J Non-Linear Mech* **9**, 409-419.
- Shaw, F.S., and Perrone, N. (1954), "A numerical solution for the non-linear deflection of membranes," *J Appl Mech* **21**, 117-128.
- Shortal, J. A. (1978), "A new dimension: Wallops Island flight test range - the first fifteen years," *NASA Reference Publication 1028*.
- Stevens, H.H. (1944), "Behavior of circular membranes stretched above the elastic limit by air pressure," *Experimental Stress Analysis* **2**, 139-146.
- Stein, M., and Hedgepeth, J. M. (1961), "Analysis of partly wrinkled membranes, *NASA Technical Note D-813*.
- Storakers, B. (1983), "Small deflections of linear elastic circular membranes under lateral pressure," *J Appl Mech* **50**, 735-739.
- Thomas, M., and Veal, G. (1984), "Highly accurate inflatable reflectors," *AFRPL TR-84-021*.

- Vaughn, H. (1980), "Pressurizing a prestretched membrane to form a paraboloid," *Int J Eng Sci* **18**, 99-107.
- von Kármán, T. (1910), "Festigkeitsproblem im Naschinenbau," *Encyk D Math Wiss* **IV**, 311-385.
- Walker, B. H. (1994), *Optical engineering fundamentals*, McGraw-Hill.
- Weil, N.A., and Newmark, N.M. (1955), "Large plastic deformations of circular membranes," *J Appl Mech* **22**, 533-538.
- Wilkes, J.M. (1997), private communication.
- Zarghamee, M.S. (1967), "On antenna tolerance theory," *IEEE Trans Antennas Propagat.* **AP-15**, 777-781.

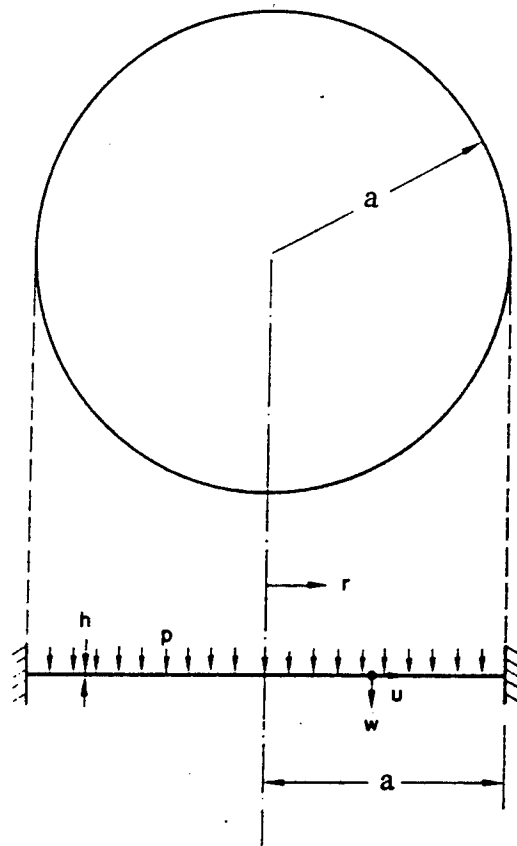


Figure 1. Definition sketch
13-18

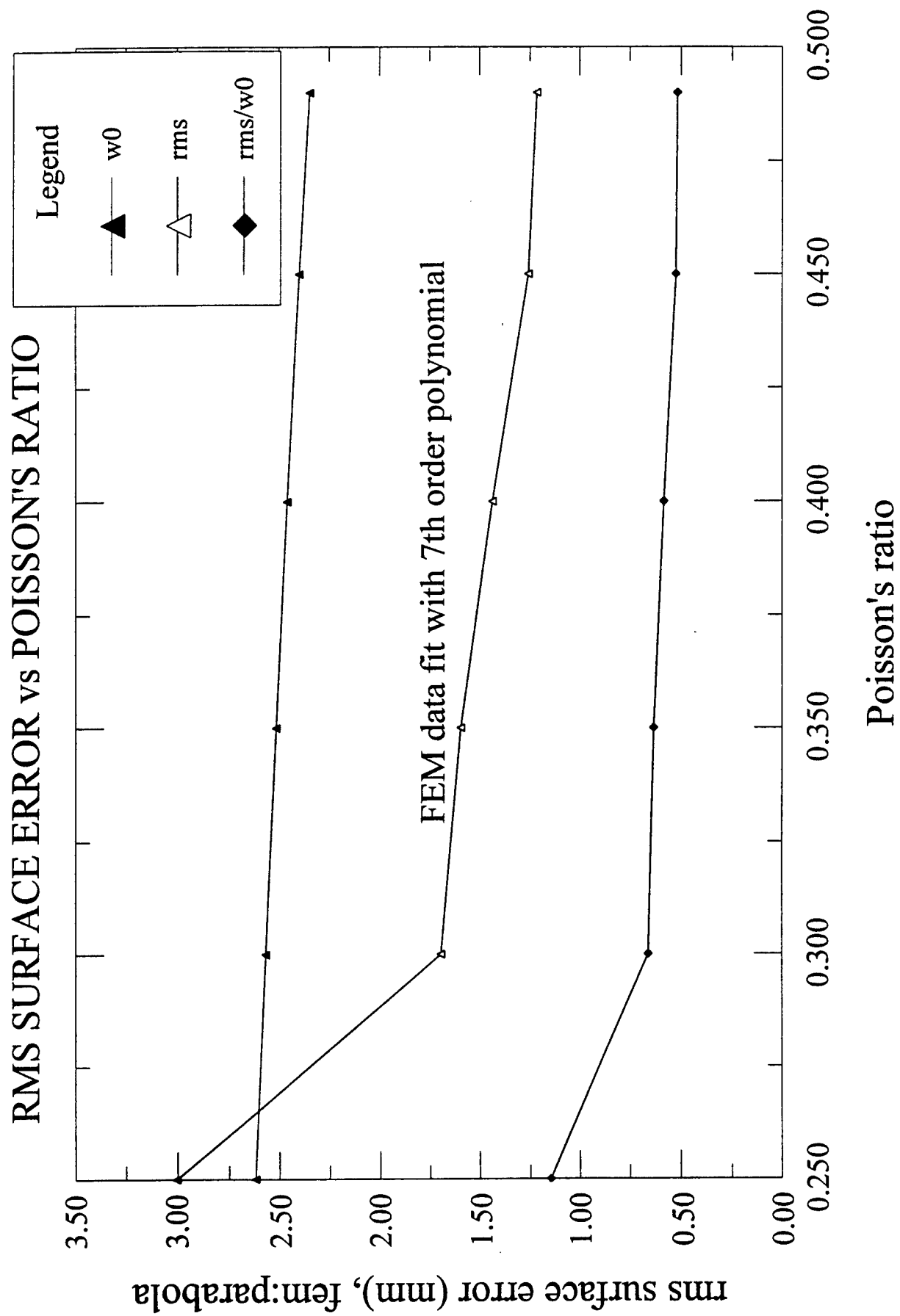


Figure 2. RMS surface error vs. Poisson's ratio.

MODE CONVERSION IN A TIME-VARYING MAGNETOPLASMA MEDIUM

Dikshitulu K. Kalluri
Professor
Department of Electrical Engineering

University of Massachusetts Lowell
One University Avenue
Lowell, MA, 08154, USA

Final Report for:
Summer Faculty Research Program
Phillips Laboratory / Geophysics Directorate

Sponsored by:
Air Force Office of Scientific Research
Bolling Air Force Base, DC

and

Phillips Laboratory /Geophysics Directorate

September 1997

Mode Conversion in a Time-varying Magnetoplasma Medium

Dikshitulu K. Kalluri
Professor
Department of Electrical Engineering
University of Massachusetts Lowell
Lowell, MA, 08154, USA

Abstract

The modification of frequency and field amplitudes of an extraordinary wave (X wave) by a time-varying magnetoplasma medium is considered. An explicit expression for the amplitude of the electric and magnetic fields in terms of the magnetoplasma parameters and the new frequency is obtained. Based on the qualitative results, one may conclude that the mode conversion takes place in the neighborhood of $\omega_b \approx \omega_o$.

Dikshitulu K. Kalluri

I. Introduction

The main effect of switching a magnetoplasma[1-17] is the splitting of the source wave into new waves whose frequencies are different from the frequency of the source wave. When the medium properties change slowly with time due to slow change of the electron density in the plasma, one of these waves whose initial frequency is the source frequency will be the dominant new wave in the sense that its field amplitudes will be significant. Other waves have field amplitudes of the order of the initial slope of the electron density profile. The case of longitudinal propagation is already discussed in [13, 16-17]. The case of transverse propagation involving X-waves[18] is the topic of this report. A more complete account of this research will be published elsewhere [19].

II Transverse Propagation

II.1 Development of the problem

The geometry of the problem is shown in Figure 1. Initially, for time $t < 0$, the entire space is considered to be free space. A uniform electromagnetic plane wave with a frequency ω_o propagating in the positive z direction and the electric field in the positive x direction is established over the entire space.

The fields of the source wave are given by:

$$\mathbf{E}(z, t) = \hat{x} E_o e^{j(\omega_o t - k_o z)}, \quad t < 0, \quad (1a)$$

$$\mathbf{H}(z, t) = \hat{y} H_o e^{j(\omega_o t - k_o z)}, \quad t < 0, \quad (1b)$$

where k_o is the free space wave number, $E_o = \eta_o H_o$, η_o is the intrinsic impedance of free space, and $j = \sqrt{-1}$. A static magnetic field \mathbf{B}_0 is present along the y -direction.

At time $t = 0$, the entire space is converted into a time varying plasma medium. The plasma medium is spatially homogeneous and unbounded. Therefore the wave number k_o remains constant[1]. The free electron density $N(t)$ is slowly increasing to a certain value N_o with zero initial value. Therefore the plasma medium has a time-varying plasma frequency $\omega_p(t)$ and an electron gyrofrequency ω_b given by

$$\omega_p(t) = \sqrt{\frac{N(t)q}{m\epsilon_o}}, \quad (2a)$$

$$\omega_b = \frac{B_o q}{m}, \quad (2b)$$

where q is the absolute value of the charge, m the mass of the electron, and B_0 the magnitude of \mathbf{B}_0 . With these assumptions, we can write the fields for $t > 0$ as follows:

$$\mathbf{E}(z, t) = [\hat{x}E_x(t) + \hat{z}E_z(t)]e^{-jk_0 z}, \quad t > 0, \quad (3a)$$

$$\mathbf{H}(z, t) = \hat{y}H_y(t)e^{-jk_0 z}, \quad t > 0, \quad (3b)$$

$$\mathbf{v}(z, t) = [\hat{x}v_x(t) + \hat{z}v_z(t)]e^{-jk_0 z}, \quad t > 0, \quad (3c)$$

where $\mathbf{v}(z, t)$ is the velocity of an electron. The differential equations for these fields can be obtained by using the Maxwell equations:

$$\nabla \times \mathbf{E} = -\mu_0 \frac{\partial \mathbf{H}}{\partial t}, \quad (4a)$$

$$\nabla \times \mathbf{H} = \epsilon_0 \frac{\partial \mathbf{E}}{\partial t} + \mathbf{J}. \quad (4b)$$

From (3) and (4) the following differential equations are obtained:

$$\eta_0 \frac{\partial H_y}{\partial t} = j\omega_0 E_x, \quad (5a)$$

$$\frac{\partial E_x}{\partial t} = j\omega_0 \eta_0 H_y - \frac{1}{\epsilon_0} J_x, \quad (5b)$$

$$\frac{\partial E_z}{\partial t} = -\frac{1}{\epsilon_0} J_z. \quad (5c)$$

Here J_x and J_z denote the current density components. The current density vectors are closely related to the motion of the electron charges.

II.2 Current Density Vector

In the previous section, we obtained three equations with five unknowns. Two more equations are needed to determine the five unknowns. The equation of motion of the electrons is given by the Lorentz force equation:

$$m \frac{d\mathbf{v}}{dt} = -q[\mathbf{E} + \mathbf{v} \times \mathbf{B}_0]. \quad (6)$$

The velocity vector may be related to the current density vector. When free space is slowly converted into plasma, it is necessary to impose the requirement that the electrons born at different times have zero initial velocity [12-13]. Applying these concepts to the case of transverse propagation [14] we obtain the equations for J_x and J_z given below:

$$\frac{dJ_x}{dt} = \epsilon_0 \omega_p^2 E_x + \omega_b J_z, \quad (7a)$$

$$\frac{dJ_z}{dt} = \varepsilon_o \omega_p^2 E_z - \omega_b J_x. \quad (7b)$$

II.3 Higher order differential equation

Equations (5) and (7) are the first order coupled differential equations that contain time-varying and complex coefficients. Generally, it is difficult to obtain exact solutions, but reasonable approximate solutions can be obtained. Equations (5) and (7) are manipulated by differentiation and substitution and a fifth order differential equation for E_x is obtained:

$$E_x^{(5)} + AE_x^{(3)} + BE_x^{(1)} + g[5E_x^{(2)} + (2\omega_o^2 + 3\omega_p^2)E_x] + \frac{dg}{dt}(3E_x^{(1)} + \omega_b E_z) + \frac{d^2g}{dt^2}E_x = 0, \quad (8)$$

where

$$A = \omega_o^2 + 2\omega_p^2 + \omega_b^2. \quad (9a)$$

$$B = \omega_o^2 \omega_b^2 + \omega_o^2 \omega_p^2 + \omega_p^4. \quad (9b)$$

$$g = \frac{d\omega_p^2}{dt}. \quad (9c)$$

We neglect $\frac{dg}{dt}$, $\frac{d^2g}{dt^2}$, and g^2 since $\omega_p^2(t)$ is a slowly varying function of time. The equation for E_x becomes simpler and is given by:

$$E_x^{(5)} + AE_x^{(3)} + BE_x^{(1)} + g[5E_x^{(2)} + (2\omega_o^2 + 3\omega_p^2)E_x] = 0. \quad (10)$$

II.4 Riccati equation

To solve (10), the WKB method can be applied [15]. A complex instantaneous frequency function, $p(t)$, is defined such that

$$\frac{dE_x}{dt} = p(t)E_x. \quad (11)$$

Then

$$E_x^{(2)} = (\dot{p} + p^2)E_x, \quad (12a)$$

$$E_x^{(3)} = (\ddot{p} + 3p\dot{p} + p^3)E_x, \quad (12b)$$

$$E_x^{(4)} = (\ddot{\ddot{p}} + 4p\ddot{p} + 6p^2\dot{p} + 3\dot{p}^2 + p^4)E_x, \quad (12c)$$

$$E_x^{(5)} = [(p^{(4)} + 5p\ddot{\ddot{p}} + 10(\dot{p} + p^2)\ddot{p} + 5(2p^3 + 3p\dot{p})\dot{p} + p^5)]E_x. \quad (12d)$$

Substitution of (12) into (10) gives

$$p^{(4)} + 5p\ddot{p} + 10(\dot{p} + p^2)\ddot{p} + 5(2p^3 + 3p\dot{p})\dot{p} + p^5 + A(\ddot{p} + 3p\dot{p} + p^3) + Bp + g[5(\dot{p} + p^2) + (2\omega_o^2 + 3\omega_p^2)] = 0. \quad (13)$$

This Riccati equation can be solved to zero order and the solution gives real frequencies of the new waves.

II.5 Frequencies of the new waves

We let $p = j\omega$ in (13) and neglect higher order terms (\dot{p} , \ddot{p} , $\ddot{\ddot{p}}$, $p^{(4)}$, g , and their powers), then we get

$$\omega^5 - A\omega^3 + B\omega = 0. \quad (14)$$

The solutions to this equation can be easily obtained as

for $\omega_b < \omega_o$,

$$\omega_1 = [\tfrac{1}{2}\{A + \sqrt{A^2 - 4B}\}]^{1/2}, \quad (15a)$$

$$\omega_2 = [\tfrac{1}{2}\{A - \sqrt{A^2 - 4B}\}]^{1/2}, \quad (15b)$$

$$\omega_3 = -\omega_1, \quad (15c)$$

$$\omega_4 = -\omega_2, \quad (15d)$$

$$\omega_5 = 0, \quad (15e)$$

for $\omega_b > \omega_o$,

$$\omega_1 = [\tfrac{1}{2}\{A - \sqrt{A^2 - 4B}\}]^{1/2}, \quad (16a)$$

$$\omega_2 = [\tfrac{1}{2}\{A + \sqrt{A^2 - 4B}\}]^{1/2}, \quad (16b)$$

$$\omega_3 = -\omega_1, \quad (16c)$$

$$\omega_4 = -\omega_2, \quad (16d)$$

$$\omega_5 = 0. \quad (16e)$$

We split the solutions into two regions given by (15) and (16) to obtain the same initial values at $t = 0$. Consequently, in both regions, the first wave has the same initial value ω_o and may be considered as the modified source wave (MSW). The other waves may be considered as new waves created by the switching action and are of the order of $g(0) = g_o$. Equations (15) and (16) are the same as those that can be obtained from the consideration of conservation of the wavenumber of the X wave in a time-varying, unbounded, and homogeneous plasma medium [15].

Equations (15) and (16) show that five new waves are generated when $t > 0$ as a result of the imposition of the magnetoplasma. The first two solutions are transmitted waves while the next two are reflected waves. Since ω_5 is zero, the fifth solution is not a wave.

II.6 Amplitudes of the Fields of the New Waves

Amplitudes of the fields of the new waves can be obtained by expanding the frequency function to include a real part. Let $p = \alpha + j\omega$. Neglecting higher order terms except α , $\dot{\omega}$, and g , we can get the relation for α :

$$\alpha_n = \frac{g(5\omega_n^2 - 2\omega_o^2 - 3\omega_p^2) - \dot{\omega}(10\omega_n^2 - 3A)\omega_n}{5\omega_n^4 - 3A\omega_n^2 + B}. \quad (17)$$

II.7 Complete Solution

The complete solutions to the problem can be represented by the linear combination of the five new modes. Let's suppose the field components have the following form:

$$E_x = E_o \sum_{n=1}^5 A_n \exp\left[\int_0^t (j\omega_n(\tau) + \alpha_n(\tau)) d\tau\right]. \quad (18)$$

To determine the unknown coefficients A_n , we can use the initial conditions at $t = 0$.

$$E_x(0) = E_o, \quad (19a)$$

$$E_z(0) = 0, \quad (19b)$$

$$H_y(0) = H_o, \quad (19c)$$

$$J_x(0) = 0, \quad (19d)$$

$$J_z(0) = 0. \quad (19e)$$

Symbolic manipulations [20] have been done to obtain the coefficients:

$$A_1 = 1 - jg_o \frac{\omega_b^4 + 14\omega_b^2\omega_o^2 + \omega_o^4}{8\omega_o(\omega_o^2 - \omega_b^2)^3}, \quad (20a)$$

$$A_2 = jg_o \frac{\omega_b}{2(\omega_o + \omega_b)(\omega_o - \omega_b)^3}, \quad (20b)$$

$$A_3 = jg_o \frac{1}{8\omega_o(\omega_o^2 - \omega_b^2)}, \quad (20c)$$

$$A_4 = -jg_o \frac{\omega_b}{2(\omega_o - \omega_b)(\omega_o + \omega_b)^3}, \quad (20d)$$

$$A_5 = 0. \quad (20e)$$

The above expressions become singular when $\omega_o = \omega_b$. The evaluation of the unknown constants using (18) makes it possible to describe the transmitted fields and the reflected fields completely in terms of their time-varying envelope functions and the frequency functions. The resulting expression is

$$E_x(z, t) = E_o \sum_{n=1}^4 A_n \exp[\beta_n(t)] \exp[j(\theta_n(t) - k_o z)], \quad (21)$$

where

$$\theta_n(t) = \int_0^t \omega_n(\tau) d\tau, \quad (22a)$$

$$\beta_n(t) = \int_0^t \alpha_n(\tau) d\tau. \quad (22b)$$

II.7 Explicit Expressions for the Amplitudes of the Fields

The expression for g in terms of ω may be obtained by differentiating (14):

$$g = \frac{2(2\omega^2 - A)\omega\dot{\omega}}{2\omega^2 - \omega_o^2 - 2\omega_p^2}. \quad (23)$$

From (17) and (23), $\alpha(t)$ can be expressed as

$$\alpha(t) = \frac{(\omega_o^2 A - 2(2\omega_b^2 + \omega_o^2)\omega^2)\dot{\omega}}{2\omega(2\omega^2\omega_b^2 - 3\omega_o^2\omega_b^2 + \omega_o^4 + 2\omega_b^2\omega_p^2)} = -\frac{2\omega\omega_b^2}{G(G - \omega_b^2)}\dot{\omega} - \frac{\omega_o^2}{2\omega G}\dot{\omega}. \quad (24)$$

where

$$G = \sqrt{4\omega^2\omega_b^2 - 4\omega_o^2\omega_b^2 + \omega_o^4}, \quad (25a)$$

$$\omega_p^2 = (2\omega^2 - \omega_o^2 - G)/2. \quad (25b)$$

We can integrate (24) to obtain $\beta(t)$:

$$\beta(t) = \int_0^t \alpha(\tau) d\tau = -\frac{1}{2} \ln(G - \omega_b^2) + \frac{\omega_b^2}{2\sqrt{\omega_o^4 - 4\omega_o^2\omega_b^2}} \ln \left. \frac{G + \sqrt{\omega_o^4 - 4\omega_o^2\omega_b^2}}{\omega} \right|_{\omega(0)}^{\omega(t)}. \quad (26)$$

II.8 Adiabatic Analysis of the Modified Source Wave

For the first wave, from (26),

$$F(t) = \exp[\beta_1(t)] = \sqrt{\frac{\omega_o^2 - \omega_b^2}{2\omega_1^2 - \omega_o^2 - 2\omega_p^2 - \omega_b^2}} \times \left(\frac{\omega_o}{\omega_1} \frac{2\omega_1^2 - \omega_o^2 - 2\omega_p^2 + \sqrt{\omega_o^4 - 4\omega_b^2\omega_o^2}}{\omega_o^2 + \sqrt{\omega_o^4 - 4\omega_b^2\omega_o^2}} \right)^{\frac{\omega_o^2}{2\sqrt{\omega_o^4 - 4\omega_b^2\omega_o^2}}}. \quad (27)$$

In (27) the factors including the last exponent are real for $\omega_o^2 > 4\omega_b^2$. For other ranges, some of these factors are complex but easily computed by using mathematical software [15]. For small g_o , and ω_o sufficiently different from ω_b , $A_1 \cong 1$ and the other A coefficients are negligible. Only the first wave has significant amplitude and it

may be labeled as the Modified Source Wave (MSW). Each of the fields of the MSW may be written as a product of an instantaneous amplitude function and a frequency function:

$$E_x(z, t) = E_o e_x(t) \cos[\theta_1(t) - k_o z], \quad (28a)$$

$$H_y(z, t) = H_o h_y(t) \cos[\theta_1(t) - k_o z], \quad (28b)$$

$$E_z(z, t) = E_o e_z(t) \cos\left[\theta_1(t) - k_o z + \frac{\pi}{2}\right], \quad (28c)$$

where the instantaneous amplitude functions are given by

$$e_x(t) = F(t), \quad (28d)$$

$$h_y(t) = \frac{\omega_o}{\omega_1(t)} F(t), \quad (28e)$$

$$e_z(t) = \frac{\omega_b \omega_p^2}{\omega_1(t) [\omega_1^2(t) - \omega_p^2(t) - \omega_b^2]} F(t), \quad (28f)$$

and the power density function $S(t)$ is given by

$$S(t) = \frac{\omega_o}{\omega_1(t)} [F(t)]^2. \quad (29)$$

For $\omega_b \ll \omega_o$ the amplitude functions reduce to

$$e_x(t) \cong \left(\frac{\omega_o^2}{\omega_o^2 + \omega_p^2(t)} \right)^{\frac{1}{4}} \left[1 + \frac{\left(2\omega_o^2(\omega_o^2 + \omega_p^2(t)) \ln \left(\frac{\omega_o^2}{\omega_o^2 + \omega_p^2(t)} \right) - \omega_p^2(t)(3\omega_o^2 + 2\omega_p^2(t)) \right) \omega_b^2}{4\omega_o^4(\omega_o^2 + \omega_p^2(t))} \right], \quad (30a)$$

$$e_z(t) \cong \left(\frac{\omega_o^2}{\omega_o^2 + \omega_p^2(t)} \right)^{\frac{1}{4}} \frac{\omega_b \omega_p^2(t)}{\omega_o^2 \sqrt{\omega_o^2 + \omega_p^2(t)}}. \quad (30b)$$

For $\omega_b \gg \omega_o$ and $\omega_b \gg \omega_p$

$$e_x(t) \cong 1 - \frac{3}{4} \frac{\omega_p^2(t)}{\omega_b^2}. \quad (30c)$$

$$e_z(t) \cong -\frac{\omega_p^2(t)}{\omega_b \omega_o}. \quad (30d)$$

Graphical results given in Section III are obtained by computing $F(t)$ from (27). The results are verified using (22b) involving a numerical integration routine.

III Graphical Illustrations and Results

An exponentially varying electron density profile is used for an illustrative example. The time-varying plasma frequency is considered as:

$$\omega_p^2(t) = \omega_{p_0}^2 [1 - \exp(-bt)]. \quad (31)$$

The results for the first wave are presented in a normalized form by taking $\omega_o = 1$. The parameter b is chosen as 0.01. Figures 2, 3, and 4 show the characteristics of the MSW. It has an upshifted frequency (Fig. 2) compared to the source wave frequency ω_o when $\omega_b < \omega_o$ and a downshifted frequency when $\omega_b > \omega_o$. The amplitude function $e_x(t)$ (Fig. 3) of the MSW decreases with the increase of ω_b as long as $\omega_b < \omega_o$. However, it increases with ω_b for $\omega_b > \omega_o$. The amplitude function $h_y(t)$ follows a similar pattern. The amplitude function $e_z(t)$ changes sign as ω_b value crosses $\omega_b = \omega_o$ (Fig. 4).

Figures 5, 6, 7, and 8 show the variation of the saturation values ($t \rightarrow \infty$) of the frequency and amplitude function of the MSW. The horizontal axis is ω_b . However, in the neighborhood of $\omega_b \approx \omega_o$, the assumptions $A_1 \approx 1$ and all other A 's are zero are not valid. The following validity condition is obtained by restricting the magnitude of the second term on the right hand side of (20a) to be less than 0.1. The validity condition is

$$\left| 1 - \frac{\omega_b^2}{\omega_o^2} \right| > \left(20 \frac{b\omega_{p_0}^2}{\omega_o^3} \right)^{1/3}. \quad (32)$$

From Figures 5-8, the following qualitative result may be stated: as the value of ω_b crosses ω_o , there will be a rapid change in the frequency and the fields of the source wave, signifying a mode conversion.

IV Conclusion

The creation of a time varying magnetoplasma medium splits the incident wave into four new waves having different frequencies in the case of transverse propagation. Two of the waves are transmitted waves and the other two are the reflected waves. The first wave whose initial frequency is that of the incident wave has the strongest intensity compared to the others and is labeled as the MSW. Based on the adiabatic analysis of the MSW, the following qualitative statement may be made: as the value of ω_b crosses ω_o , there will be a rapid change in the frequency and the fields.

We still have difficulty in quantifying the behavior of the fields in the neighborhood of $\omega_b \approx \omega_o$. The accuracy of the solution degrades since $\dot{\omega}$ at $t = 0$ tends to infinity as ω_b tends towards ω_o . In this neighborhood the higher order terms become important. The aspect of the effect at $\omega_b = \omega_o$ is currently under investigation using a very different approach and the result will be reported in due course.

Adiabatic solutions given in this paper can give explicit analytical description for the frequency and the amplitude of the modified source wave except in the neighborhood of $\omega_b \approx \omega_o$. Based on the qualitative results, one may conclude that the mode conversion takes place in this neighborhood

References

- [1] C. L. Jiang, "Wave propagation and dipole radiation in a suddenly created plasma," *IEEE Trans. Antennas Propagat.*, vol. AP-23, no. 1, pp. 83-90, 1975
- [2] D. K. Kalluri, "On Reflection from a Suddenly Created Plasma Half-Space: Transient Solution," *IEEE Trans. Plasma Sci.*, vol. 16, no. 1, pp. 11-16, 1988
- [3] V. R. Goteti and D. K. Kalluri, "Wave Propagation in a Switched-on Time-varying Plasma Medium," *IEEE Trans. Plasma Sci.*, vol. 17, pp. 828-833, 1989.
- [4] D. K. Kalluri and V. R. Goteti, "Frequency Shifting of Electromagnetic Radiation by Sudden Creation of a Plasma Slab," *J. Appl. Phys.*, vol. 72, no. 10, pp. 4575-4580, 1992.
- [5] C. J. Joshi, C. E. Clayton, K. Marsh, D. B. Hopkins, A. Sessler, and D. Whittum, "Demonstration of the Frequency Upshifting of Microwave Radiation by Rapid Plasma Creation," *IEEE Trans. Plasma Sci.*, vol. 18, no. 5, pp. 814-818, 1990.
- [6] S. P. Kuo and A. Ren, "Experiment Study of Wave Propagation Through a Rapidly Created Plasma," *IEEE Trans. Plasma Sci.*, vol. 21, no. 1, pp. 53-56, 1993.
- [7] D. K. Kalluri, V. R. Goteti, "Damping Rates of Waves in a Switched Magnetoplasma Medium: Longitudinal Propagation," *IEEE Trans. Plasma Sci.*, vol. 18, no. 5, pp. 797-801, 1993.
- [8] V. R. Goteti and D. K. Kalluri, "Wave Propagation in a Switched Magnetoplasma Medium: Transverse Propagation," *Radio Science*, vol. 25, no. 1, pp. 61-72, 1990
- [9] S. R. V. Madala and D. K. Kalluri, "Frequency Shifting of a Wave Traveling in an Isotropic Plasma Medium due to Slow Switching of a Magnetic Field," *Plasma Sources Sci. Technol.*, vol. 1, pp. 242-248, 1992
- [10] S. R. V. Madala and D. K. Kalluri, "Longitudinal Propagation of Low-frequency Waves in a Switched Magnetoplasma Medium," *Radio Science*, vol. 28, no. 2, pp. 121-129, 1993.
- [11] C. H. Lai, T. C. Katsouleas, "Frequency Upshifting by an Ionization Front in a Magnetized Plasma," *IEEE Trans. Plasma Sci.*, vol. 21, no. 1, pp. 45-51, 1993.
- [12] A. Baños, Jr., W. B. Mori, and J. M. Dawson, "Computation of the Electric and Magnetic Fields Induced in a Plasma Created by Ionization Lasting a Finite Interval of Time," *IEEE Trans. Plasma Sci.*, vol. 21, no. 1, pp. 57-69, 1993
- [13] D. K. Kalluri, V. R. Goteti, and A. M. Sessler, "WKB Solution for Wave Propagation in a Time-Varying Magnetoplasma Medium: Longitudinal Propagation," *IEEE Trans. Plasma Sci.*, vol. 21, no. 1, pp. 70-76, 1993.

- [14] J. H. Lee, "Wave Propagation in a Time-Varying Switched Magnetoplasma Medium: Transverse Propagation", *M.S. Thesis, University of Massachusetts Lowell*, 1994.
- [15] D. K. Kalluri, "Frequency Shifting Using Magnetoplasma Medium: Flash Ionization," *IEEE Trans. Plasma Sci.*, vol. 21, no. 1, pp. 77-81, 1993
- [16] D. K. Kalluri, "Conversion of a whistler wave into a controllable helical wiggler magnetic field," *J. Appl. Phys.*, vol. 79, no. 9, pp. 6770-6774, 1996.
- [17] D. D. Kalluri, "Frequency upshifting with power intensification of a whistler wave by a collapsing plasma medium," *J. Appl. Phys.*, vol. 79, no. 8, pp.3895-3899, 1996.
- [18] M. A. Heald and C. B. Wharton, *Plasma Diagnostics with Microwaves*, New York: Wiley, 1965, p. 36.
- [19] Joo Hwa Lee and D. K. Kalluri, "Modification of an Electromagnetic Wave by a Time-varying Switched Magnetoplasma Medium: Transverse Propagation," *IEEE Trans. Plasma Sci.*, Feb. 1998 Issue.
- [20] N. Blachman, *Mathematica: A Practical Approach*, Prentice Hall, Englewood Cliffs, New Jersey, 1992

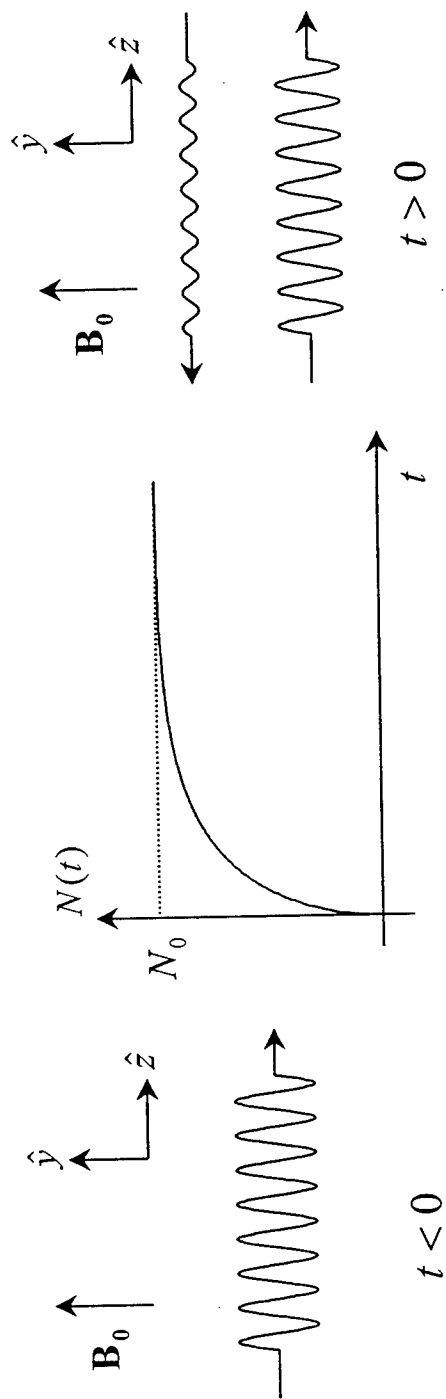


Fig. 1 Geometry of the problem. Modification of the source wave by a time-varying magnetoplasma medium: transverse propagation.

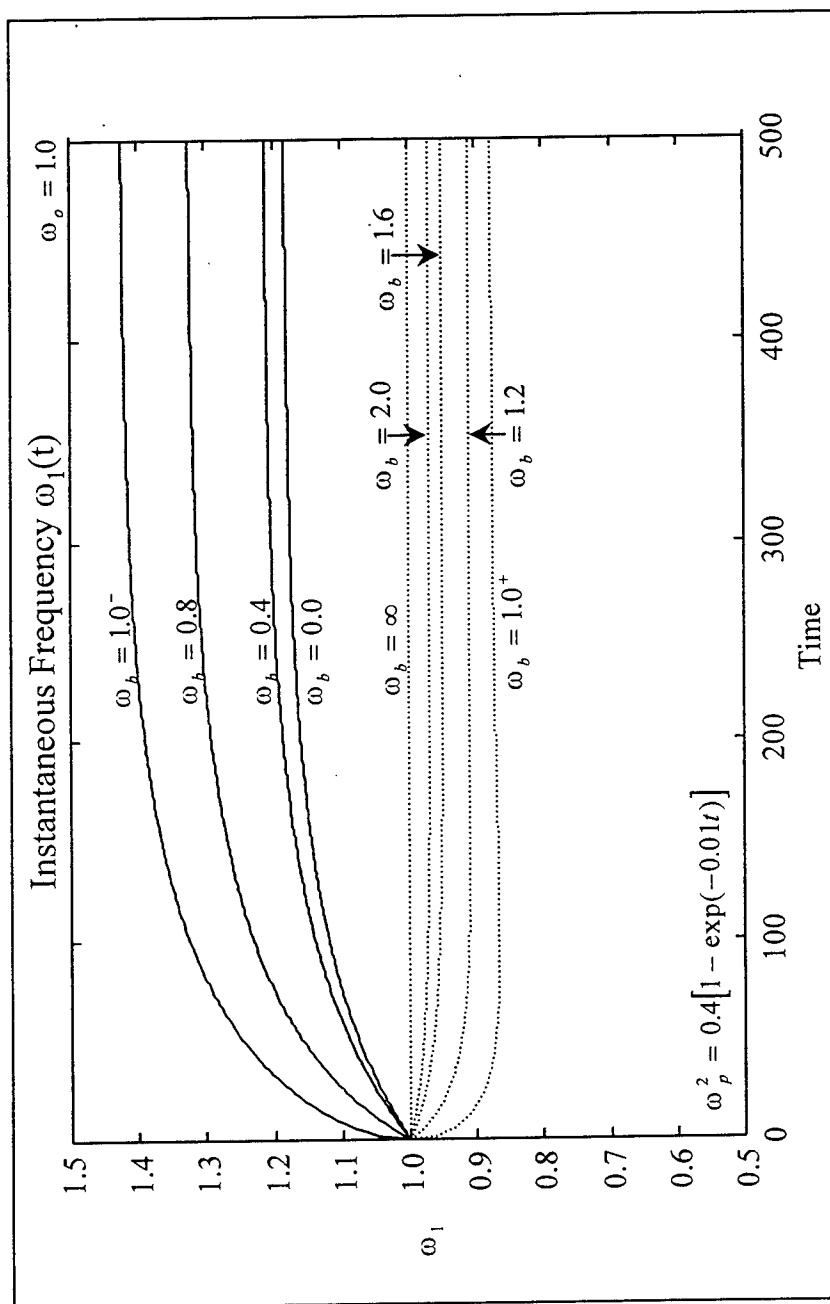


Fig. 2 Instantaneous frequency of the modified source wave(MSW).

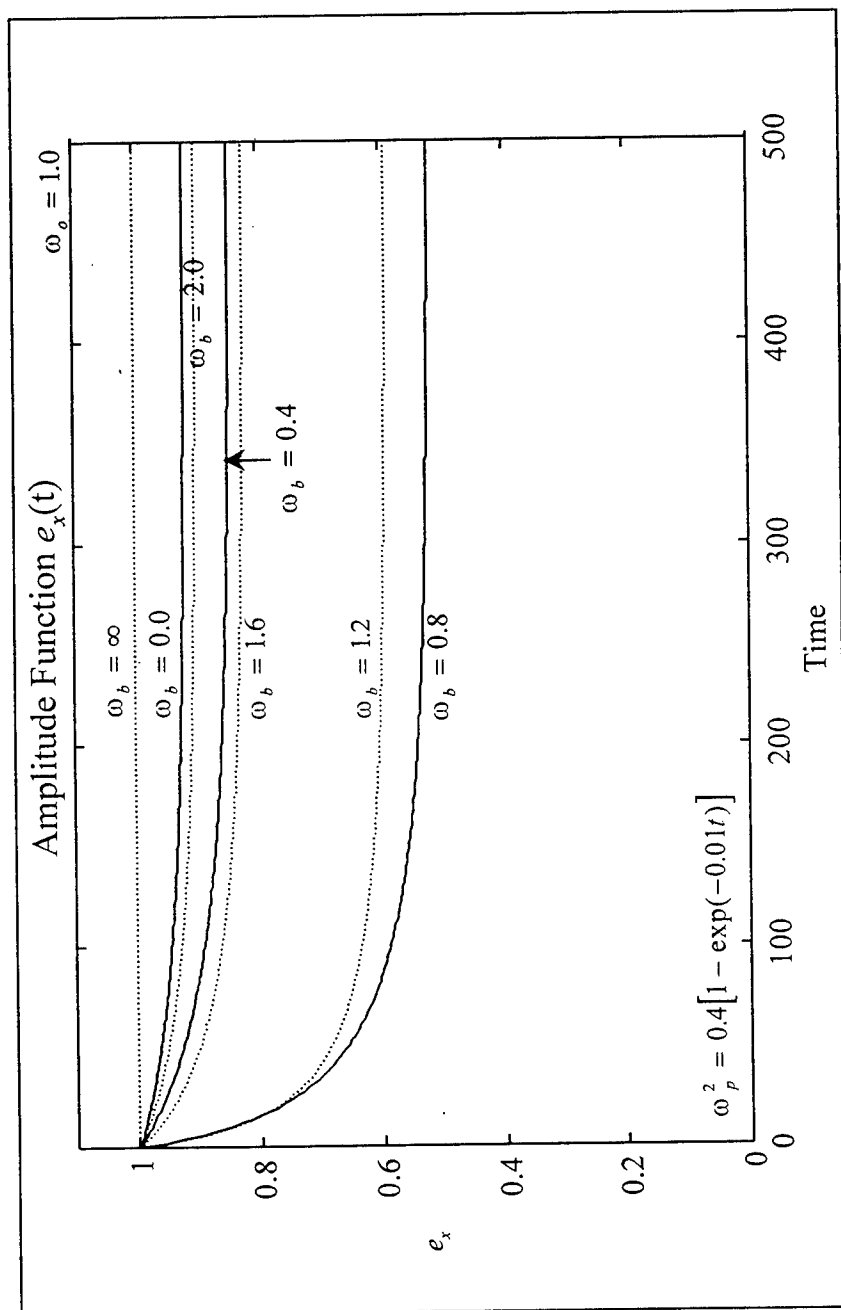


Fig. 3 Amplitude function of the x component of the electric field of MSW.

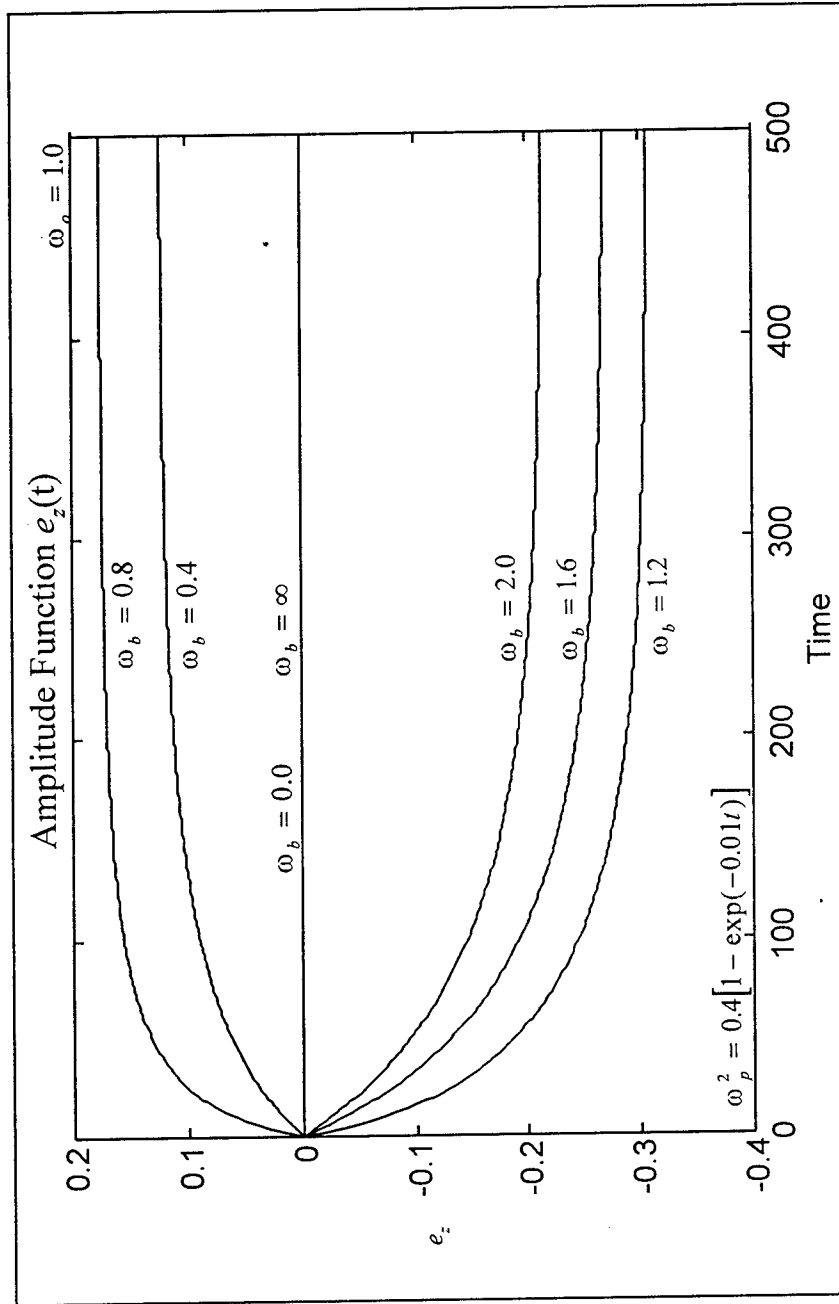


Fig. 4 Amplitude function of the z component of the electric field of MSW.

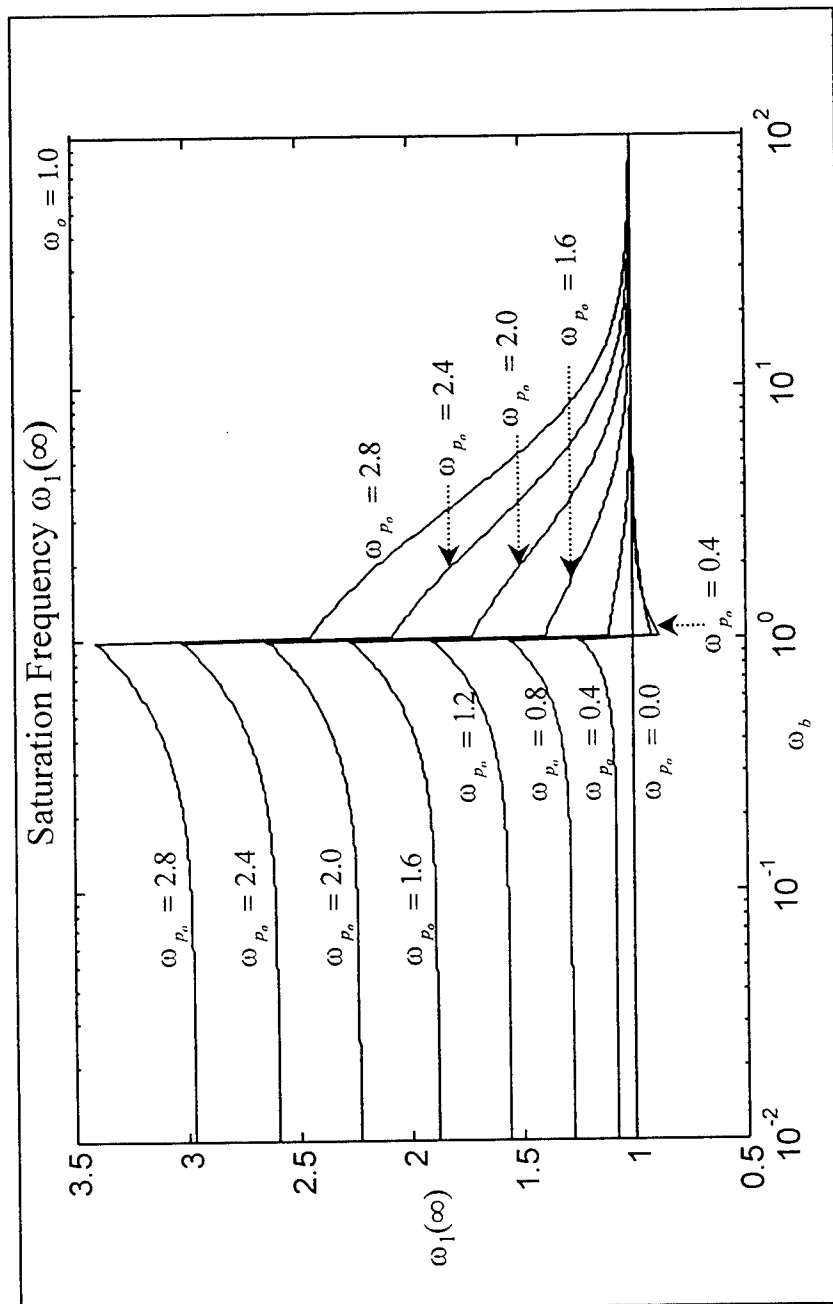


Fig. 5 Variation of the saturation frequency of the MSW with the electron cyclotron frequency(ω_b) and the saturation plasma frequency(ω_{p_o}).

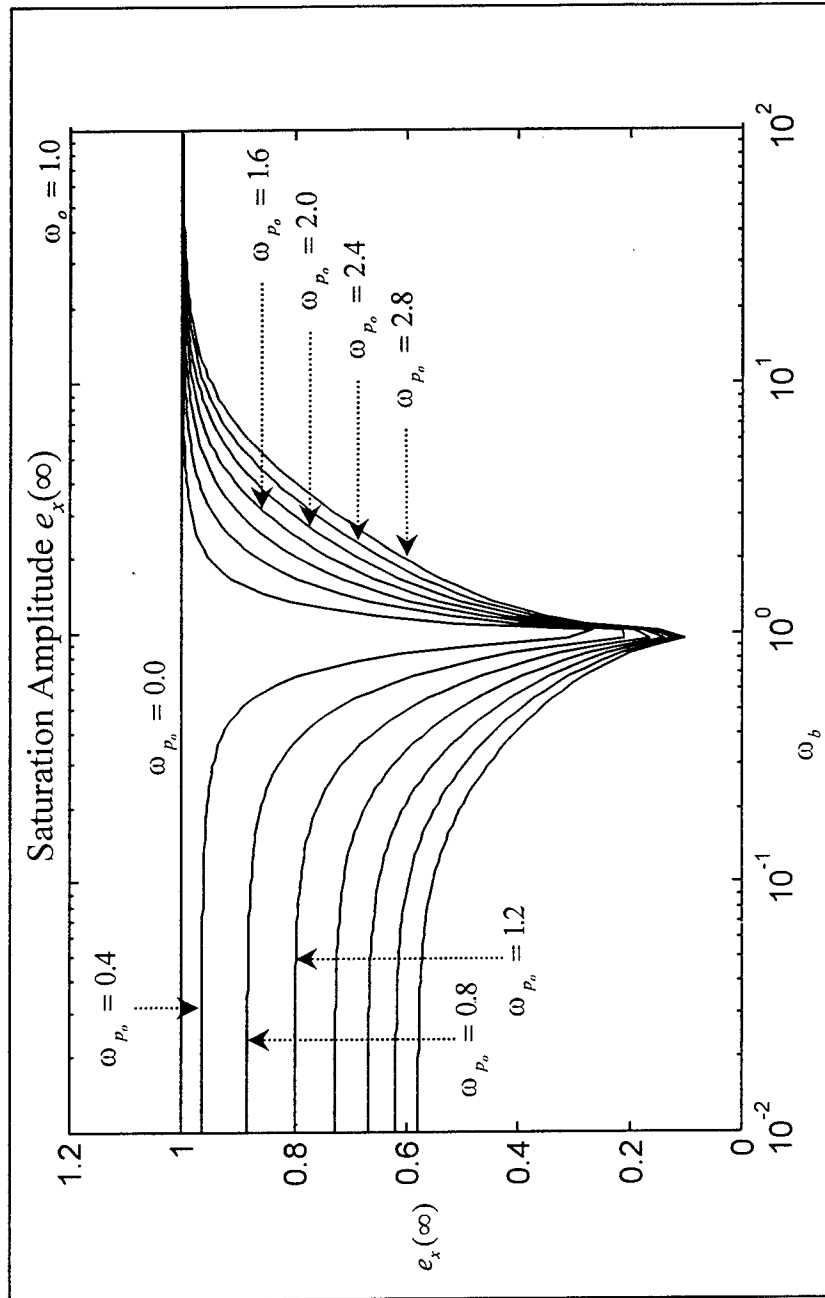


Fig. 6 Variation of the saturation amplitude of the x component of the electric field of the MSW with ω_b and ω_{p_0} .

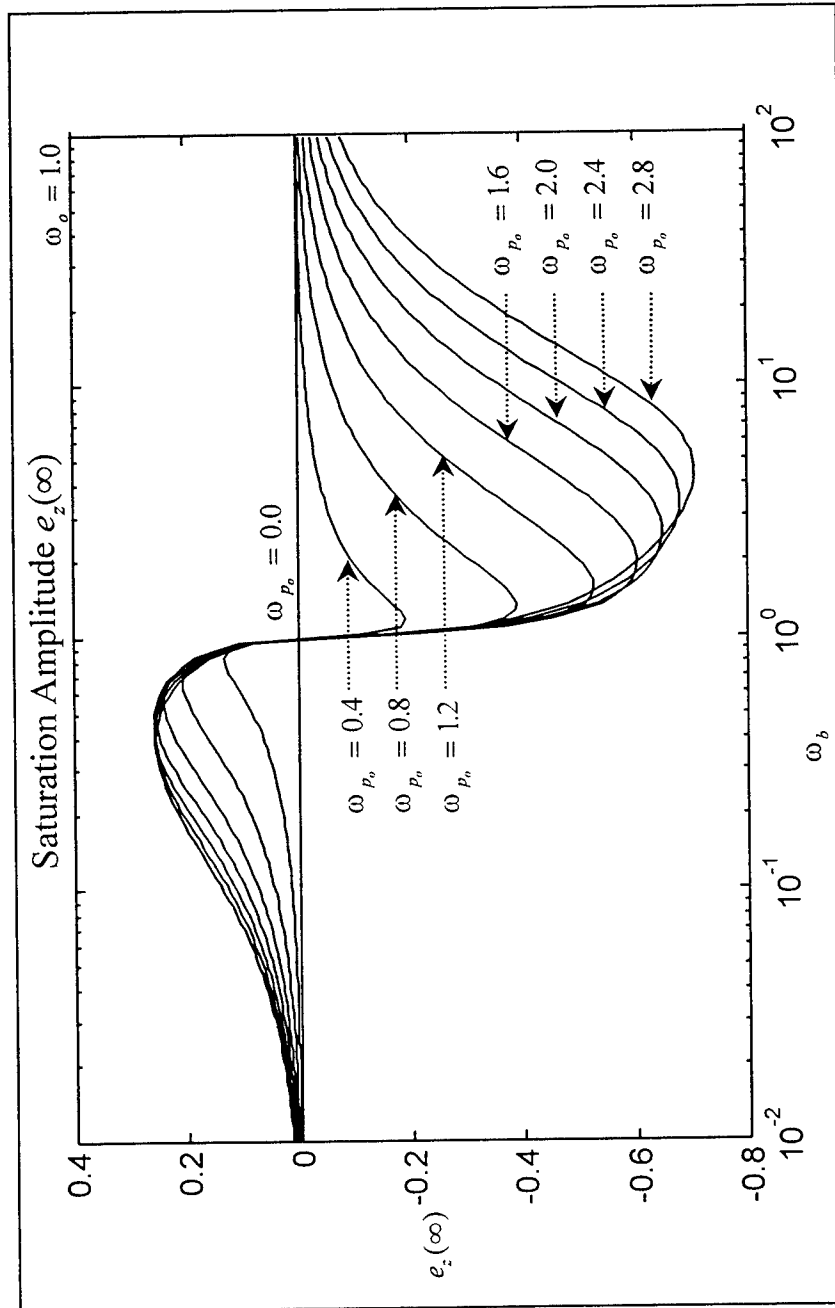


Fig. 7 Variation of the saturation amplitude of the z component of the electric field of the MSW with ω_b and ω_{p0} .

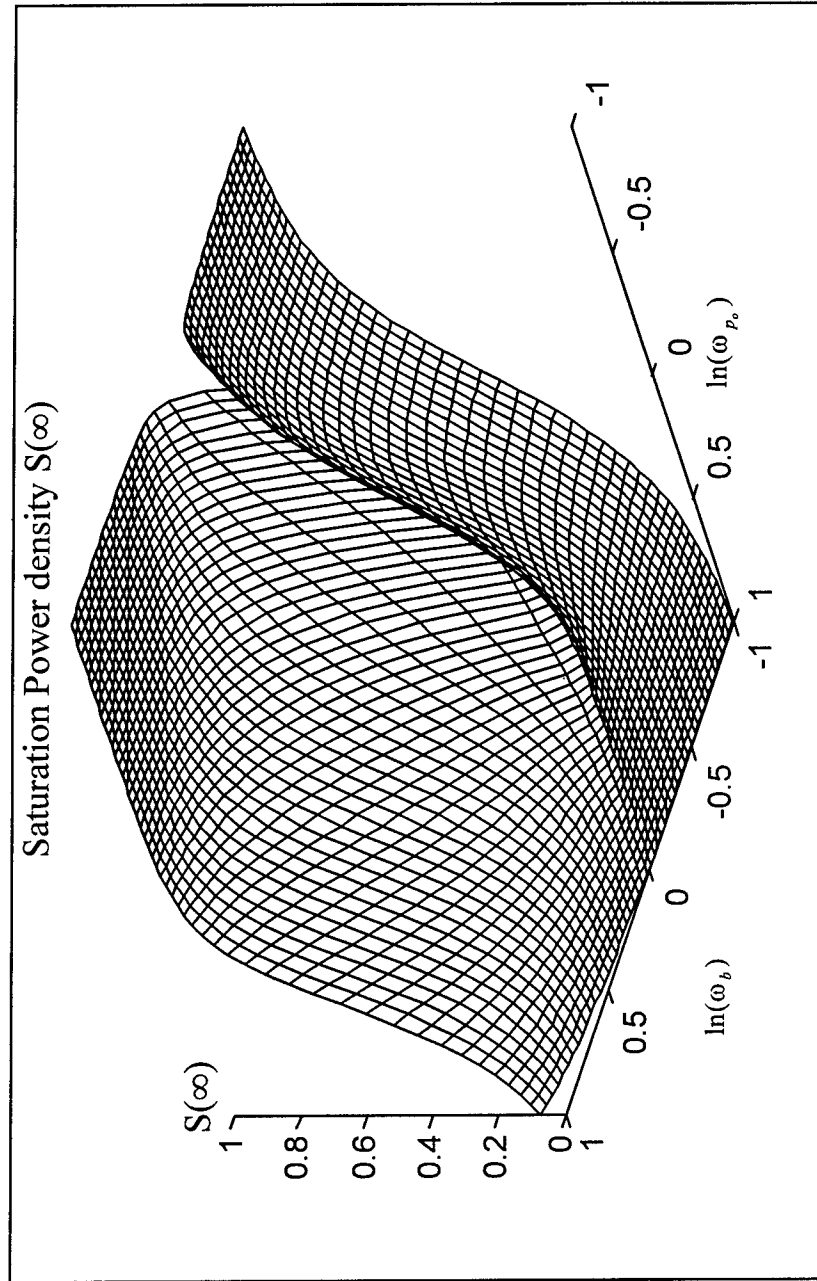


Fig. 8 Variation of the saturation power density of the MSW with ω_b and ω_p .

**MEASUREMENT OF THE CUTTING PERFORMANCE OF A HIGH BEAM
QUALITY CHEMICAL OXYGEN-IODINE LASER OF AEROSPACE AND
INDUSTRIAL MATERIALS**

Aravinda Kar
Associate Professor
Department of Mechanical and Aerospace Engineering

University of Central Florida
P.O. Box 162700
Orlando, FL 32816-2700

Final Report for:
Summer Research Program
Phillips Laboratory

Sponsored by:
Air Force Office of Scientific Research
Bolling Air Force Base, Washington, DC

And

Phillips Laboratory

July, 1997

MEASUREMENT OF THE CUTTING PERFORMANCE OF A HIGH BEAM QUALITY CHEMICAL OXYGEN-IODINE LASER ON AEROSPACE AND INDUSTRIAL MATERIALS

Aravinda Kar
Assistant Professor
Department of Mechanical, Materials and Aerospace Engineering
Center for Research and Education in Optics and Lasers
University of Central Florida

Abstract

Chemical Oxygen-Iodine Laser (COIL) technology has received considerable interest over the last several years due to its short, fiber-deliverable wavelength (1.315 microns), scalability to high powers (tens of kilowatts, cw), and potentially high beam quality. Unfortunately, materials processing demonstrations to date have been performed with relatively small COILs producing very poor quality beams ($M^2 > 100$). This paper documents the cutting performance of a high beam quality COIL. Cut depth and width on a variety of materials is documented as a function of various process parameters. Also, the optical quality of the laser beam is evaluated in this study.

MEASUREMENT OF THE CUTTING PERFORMANCE OF A HIGH BEAM QUALITY CHEMICAL OXYGEN-IODINE LASER ON AEROSPACE AND INDUSTRIAL MATERIALS

Aravinda Kar

1. Introduction

Lasers have been successfully used for commercial cutting applications. CO₂ and Nd:YAG lasers are usually used for such applications. Chemical Oxygen-Iodine Laser (COIL) is a scalable high power laser at wavelength 1.315 μm that can be used for various types of materials processing. Kar et al.¹ briefly discussed the basic principle of COIL and demonstrated the thick-section cutting capability of COIL. Atsuta, et al.² showed that the cutting capability of a 1 kW COIL is equivalent to a 1 kW Nd:YAG laser and about 2.5 times better than a 1 kW CO₂ laser. They presented a simple two-parameter model and empirically determined these two parameters by fitting the model to their experimental data in order to predict the scaled cutting capability of COIL².

Tikhomirov³, Schuocker⁴, and Powell⁵ summarized earlier studies on laser cutting of various types of materials. Chryssolouris and Choi⁶, Biermann et al.⁷, and Molian and Baldwin⁸ examined the effects of cutting gas jet on laser cutting. Ohlsson et al.⁹ compared the effectiveness of laser and abrasive water jet cutting processes. Laser cutting of highly reflective materials such as copper and aluminum was investigated by Thompson¹⁰. Hack et al.¹¹ used glass fibers to deliver Nd:YAG laser to the workpiece in the power range up to 2.3 kW to cut materials.

The interactions of various process parameters during laser cutting have also been studied by using mathematical models. Schuocker and Abel¹², and Schuocker¹³ analyzed the material removal process during laser cutting. Li and Mazumder¹⁴ presented a mathematical model for laser cutting of wood. Modest and Abakians¹⁵, Bang and Modest¹⁶, and Roy and Modest¹⁷ carried out heat transfer analysis for evaporative cutting. Belic and Stanic¹⁸, and Belic¹⁹ used empirical parameters to develop a simple model for laser cutting.

The purpose of this work is to investigate the cutting capability of COIL for various types of materials such as aluminum, copper, nickel and titanium. The experimental data are also compared with a scaling law to evaluate the accuracy of the theoretical model.

2. Mathematical Model

Various cutting parameters, such as the laser power, spot size, cutting velocity, and cut depth and width, can be shown to be related to one another through a scaling law¹. In many instances, the laser resonators produce multimode beams. A detailed thermal analysis for heating due to multimode laser beams can be found in Ref. [20]. However, the scaling law of Ref. [1] provides a simple relationship among various cutting parameters. That scaling law, which was obtained by considering lumped energy balance, is given by the following expression.

$$\frac{d}{P} = \frac{A_0}{vw_k + A_3 \sqrt{vw_k}} \quad (1)$$

where the coefficients A_0 and A_3 are defined as

$$A_0 = \frac{10^6 A}{a_0} \quad (2)$$

$$A_3 = 4.08 \times 10^{-3} \times \frac{1}{a_0} \frac{w_k + 2l}{\sqrt{lw_k}} \frac{k(T_m - T_0)}{2\sqrt{\alpha}} \quad (3)$$

and

$$a_0 = 1.67 \times 10^{-5} \times \rho [c_p(T_m - T_0) + L_m + \beta L_b]. \quad (4)$$

In these expressions, d , l and w_k are in units of mm, v is in m per min, P is in kW, and all other variables are in standard SI units. A_0 is related to the absorptivity of the substrate at the laser-material interaction zone, and the term containing A_3 is associated with the loss of energy by heat conduction from the melt pool at the kerf to the surrounding solid region of the workpiece. Most of the molten material is usually removed from the kerf by the assist gas during metal cutting. Only a fraction, β , of the melt is vaporized. Since β is generally unknown, it is arbitrarily chosen to be 0.1 in this study. Eq. (1) is written for a COIL beam of rectangular spot. It is applied to circular spots in this study by taking l and w_k equal to the diameter of the beam in Eq. (3).

3. Experimental Procedure

A RADICL device (Research Assessment, Device Improvement Chemical Laser) located at the U.S. Air Force's Phillips Laboratory in Albuquerque, New Mexico, was used to carry out cutting experiments. The laser was operated with a stable resonator to produce a circular COIL beam with very few transverse modes. The multimode focal spot diameter was calculated to be 0.24 mm. Each cutting sample was mounted on a stepper motor-controlled, horizontal translation stage, and scanned through the focal region at a constant speed. High pressure nitrogen gas was used as the cutting gas that was delivered to the laser focal spot region with a rectangular nozzle. A stainless steel tube of internal diameter 16 mm was flattened and shaped to form a rectangular nozzle with dimensions approximately 1.5 mm wide by 27 mm long. The nozzle was oriented to coincide its length with the laser focal spot in a horizontal plane, and was fixed at a 45° angle from the normal to the workpiece.

4. Results and Discussion

The above scaling law is used to analyze the effects of various process parameters during laser cutting. The values of thermophysical properties, that are reported in Table 1 from Ref. [21], are used in this study for numerical calculations by using Eq. (1). These theoretical results are compared with experimental data that are listed in Table 2. Some of these data are taken from Ref. [22] as pointed out in Table 2. The absorptivity of the workpiece was chosen to be the calculated values²¹ based on the Hagen-Ruben relation for the liquid phase at the melting temperature. The absorptivities for Al, Cu, Ni and Ti are taken²¹ to be 0.18, 0.14, 0.29 and 0.39 respectively.

Figure 1 shows comparisons between the scaling law [Eq. (1)] and experimental data for cutting aluminum. The theoretical curve passes through some of the data points, and exhibits similar trend as the experimental data. Another curve is plotted in this figure by choosing $A_0 = 1.1$ and $A_3 = 0.4$ to show the effects of these two parameters on the cut depth per unit power (d/P). It should be noted that extremely good kerf edge quality (very little dross) was obtained when an aluminum workpiece of thickness 9.83 mm was cut at the speed, $v = 16$ mm/s with a

COIL beam of focal spot diameter 0.24 mm and power, $P = 4.7$ kW with nitrogen cutting gas of gauge pressure about 75 psig. The kerf width for this case was found to be about 0.91 mm.

Figure 2 shows a comparison between the scaling law and experimental data, where the theoretical prediction is very close to the experimental result. However, more data are needed to correctly evaluate the model predictions. As in the case of aluminum, extremely good kerf edge quality (very little dross) was also obtained for copper for the cutting parameters listed in Table 2.

Table 1. Typical values of thermophysical properties.

Thermophysical properties	Values of thermophysical properties			
	Aluminum	Copper	Nickel	Titanium
Density, ρ [kg m^{-3}]	2700	9600	8900	4510
Melting point, T_m [K]	933	1356	1728	1940
Boiling point, T_b [K]	2723	2833	3180	3558
Specific heat, c_p [$\text{J kg}^{-1} \text{K}^{-1}$]	899	385	444	523
Thermal conductivity ^a , k [$\text{W m}^{-1} \text{K}^{-1}$]	92	170	90.7	28
Thermal diffusivity ^a , α [$\text{m}^2 \text{s}^{-1}$]	3.8×10^{-5}	4.3×10^{-5}	2.3×10^{-5}	0.82×10^{-5}
Latent heat of melting, L_m [J kg^{-1}]	3.88×10^5	2.05×10^5	2.92×10^5	3.65×10^5
Latent heat of boiling, L_b [J kg^{-1}]	1.08×10^7	4.80×10^6	6.38×10^6	8.89×10^6

^aValues at the melting temperature in the liquid phase for Al, Cu and Ti, and values at the melting temperature in the solid phase for Ni.

Table 2. Laser cutting data for various materials.

Material	Gas Pr. [psig]	Power, P [kW]	Cut depth d [mm]	Kerf width w _k [mm]	Cutting speed v [m/min]	vw _k [m mm/min]	d/p [mm/kW]
Al	75	4.7	9.83	0.91	0.96	0.8736	2.09
	--	--	--	--	--	0.2136*	2.5953
	--	--	--	--	--	0.2136*	2.8015
	--	--	--	--	--	0.0534*	4.0733
	--	--	--	--	--	0.534*	1.9225
	--	--	--	--	--	1.335*	0.8930
	--	--	--	--	--	2.475*	0.7630
Cu	10	4.6	1.09	1.02	2.4	2.448	0.2370
Ni	70	4.2	8.76	1.02	0.6	0.612	2.086
	80	4.46	6.5	1.14	0.9	1.026	1.457
	80	3.43	12.95	0.94	0.3	0.282	3.775
Ti	75	4.2	8.38	1.27	2.16	2.7432	1.9952
	75	4.2	13.41	1.14	1.08	1.2312	3.1929
	75	5.65	11.73	1.09	1.62	1.7658	2.0761

*Data from Ref. [22]

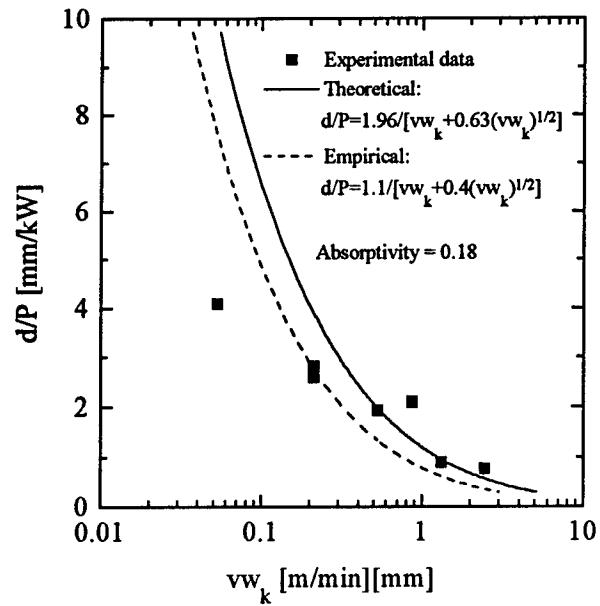


Figure 1. Comparison between theoretical results and experimental data for cutting aluminum using COIL.

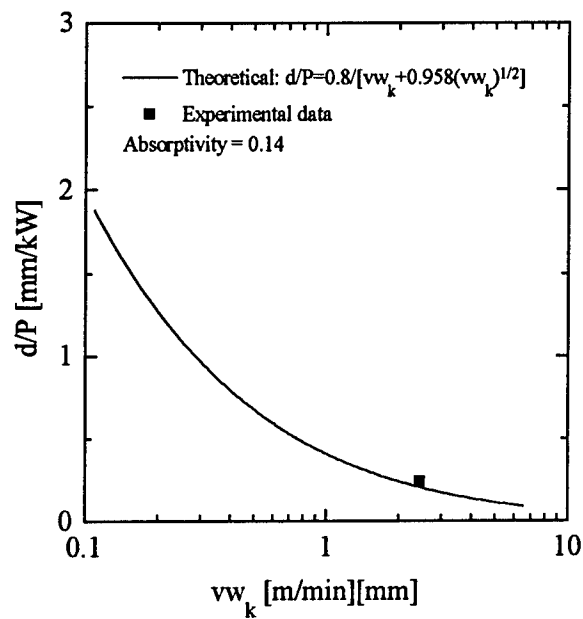


Figure 2. Comparison between theoretical results and experimental data for cutting copper using COIL.

Figures 3 and 4 represent results for titanium and nickel respectively. The theoretical curves

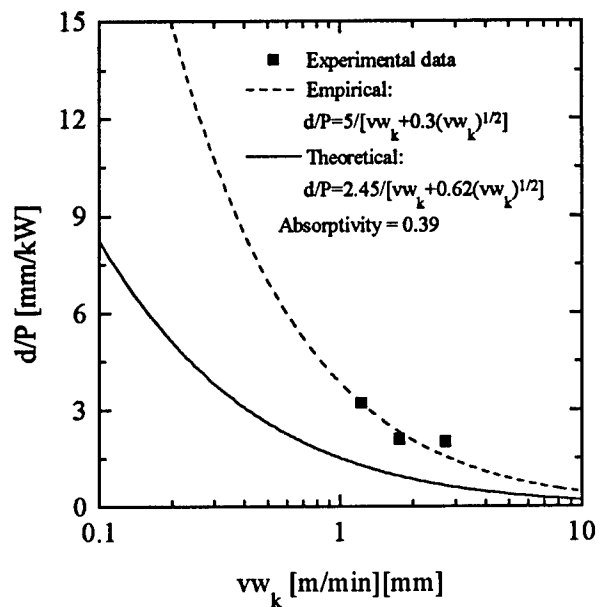


Figure 3. Comparison between theoretical results and experimental data for cutting titanium using COIL.

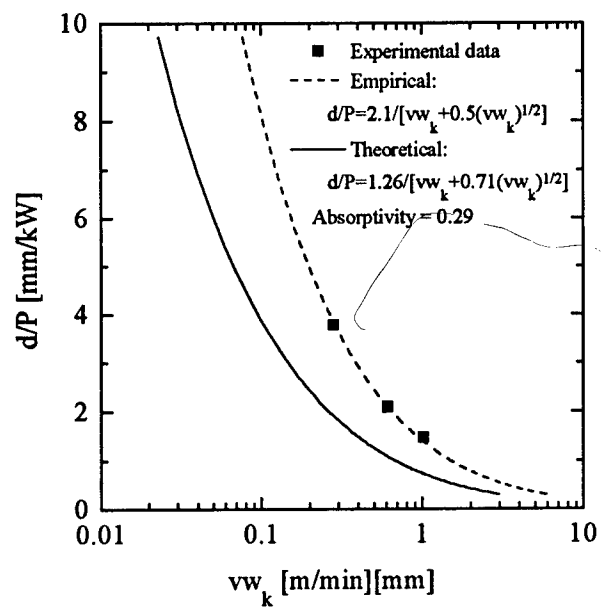


Figure 4. Comparison between theoretical results and experimental data for cutting nickel using COIL.

in these figures underestimate the cutting capability. Good agreement is achieved between the theory and experiment by choosing $A_0 = 2.45$ and $A_3 = 0.62$ for titanium and $A_0 = 2.1$ and $A_3 = 0.5$ for nickel. Since the theory predicts the cutting data fairly well for aluminum and copper, it suggests that the energy utilization mechanism during titanium and nickel cutting is different from the cases of aluminum and copper.

Besides cutting experiments, the divergence angles and mode number for the COIL beam are also evaluated in this study because they determine the optical quality of the laser. The aluminum, copper and titanium cutting data in Table 2 except those taken from Ref. [22] were obtained from a chemical oxygen-iodine laser (COIL) stable resonator with the z-pass configuration in which the reflectors at the output coupler and diagonal pass were flat mirrors, and the farthest reflector from the output coupler was a concave mirror. Circular laser beam was produced by using a circular output aperture in the resonator. The divergence angles are calculated at the output aperture based on the resonator and laser parameters given below. It should be noted that the calculated divergence angles provide the theoretical minimum values that are expected to be higher in practice due to the aberrations caused by the focusing lens. Calculations of divergence angles for both circular and rectangular laser beams are presented below for stable resonators.

4.1. Resonator parameters

Circular beam:

Radius of curvature of the output coupler, $R_1 = \infty$

Radius of curvature of the concave mirror, $R_2 = 2500$ cm

Distance between the concave mirror and output coupler, $L = 710$ cm

Diameter of the output aperture, $D_a = 2.54$ cm

Rectangular beam:

Radius of curvature of the output coupler, $R_1 = \infty$

Radius of curvature of the concave mirror, $R_2 = 2558$ cm

Distance between the concave mirror and output coupler, $L = 770$ cm

Width of the output aperture in the x direction, $D_x = 2.48$ cm

Width of the output aperture in the y direction, $D_y = 1.22$ cm

4.2. Radius of the TEM_{00} mode at the output aperture, w_0 for stable resonators²³

$$w_0^2 = \frac{\lambda L}{\pi} \left(\frac{g_1 g_2 (1 - g_1 g_2)}{(g_1 + g_2 - 2g_1 g_2)^2} \right)^{1/2}, \quad g_1 = 1 - L/R_1, \text{ and } g_2 = 1 - L/R_2$$

4.3. Beam parameters for the higher order Gaussian COIL beam of wavelength, $\lambda = 1.315$ μm

Circular beam of mode TEM_{pl} :

$$w_0 = 0.217228 \text{ cm}$$

$$\text{Mode number, } M = (2p+l+1)^{1/2} = D_x/(2w_0) = 5.846392$$

$$\text{Divergence of the } TEM_{00} \text{ mode, } \theta = 2\lambda/(\pi w_0) = 0.38538 \text{ mrad}$$

$$\text{Divergence of the } TEM_{pl} \text{ mode, } \theta_{pl} = M\theta = 2.253 \text{ mrad}$$

Rectangular beam of mode TEM_{mn} :

$$w_0 = 0.2216167 \text{ cm}$$

$$\text{Half-length of the waist in the x direction, } w_{0x} = 0.2216167 \text{ cm}$$

$$\text{Half-width of the waist in the y direction, } w_{0y} = 0.2216167 \text{ cm}$$

$$\text{Mode number in the x direction, } M_x = (2m+1)^{1/2} = D_x/(2w_{0x}) = 5.595$$

$$\text{Mode number in the y direction, } M_y = (2n+1)^{1/2} = D_y/(2w_{0y}) = 2.753$$

$$\text{Divergence of the } TEM_{00} \text{ mode in the x direction, } \theta_x = \lambda/(\pi w_{0x}) = 0.18887 \text{ mrad}$$

$$\text{Divergence of the } TEM_{00} \text{ mode in the y direction, } \theta_y = \lambda/(\pi w_{0y}) = 0.18887 \text{ mrad}$$

$$\text{Divergence of the } TEM_{mn} \text{ mode in the x direction, } \theta_{mnx} = M_x \theta_x = 1.0567 \text{ mrad}$$

$$\text{Divergence of the } TEM_{mn} \text{ mode in the y direction, } \theta_{mny} = M_y \theta_y = 0.52 \text{ mrad}$$

5. Conclusions

Experiments have been conducted to cut different types of materials, and the data are compared with the results obtained from a scaling law. The scaling law for cut depth per unit power, d/P , agrees well with the experimental data for aluminum and copper, and deviates appreciably from the titanium and nickel cutting data. This suggests that the mechanism of the

laser and thermal energy utilization during aluminum and copper cutting is different from the cases of titanium and nickel cutting. The COIL beams used in the cutting experiments had very few higher order modes.

Nomenclature

A	Absorptivity of the substrate at the laser-material interaction zone
α	Thermal diffusivity of the substrate
β	"Boiling coefficient", the fraction of the kerf width above the boiling temperature
c_p	Specific heat of the substrate at constant pressure
d	Kerf depth
k	Thermal conductivity
l	Length of the rectangular COIL beam spot
L_b	Latent heat of boiling
L_m	Latent heat of melting
P	Laser power of the incident beam at the surface of the workpiece
T_m	Melting temperature of the substrate
T_0	Initial temperature of the substrate
v	Velocity of the scanning laser beam
w_k	Kerf width

References

1. A. Kar, J. E. Scott and W. P. Latham, "Theoretical and Experimental Studies of Thick-Section Cutting with a Chemical Oxygen-Iodine Laser (COIL)," J. Laser Applications, Vol. 8, 1996, pp. 125-133.
2. T. Atsuta, K. Yasuda, T. Matsumoto, T. Sakurai and H. Okado, "COIL and the Material Processing," in Conference on Lasers and Electro-Optics (CLEO)'94, Vol. 8, 1994, OSA Technical Digest Series (Optical Society of America, Washington D. C.), P. 351, 1994.
3. A. V. Tikhomirov, "State of Laser Cutting Technology and Prospects for its Development," Bull. Academy of Sciences of the USSR, Vol. 47, 1983, pp. 23-28.

4. D. Schuocker, "Laser Cutting," in The Industrial Laser Annual Handbook, D. Belforte and M. Levitt, Editors, (PennWell Books, Tulsa, Oklahoma), 1986, pp. 87-107.
5. J. Powell, "Guidelines and Data for Laser Cutting," in The Industrial Laser Annual Handbook, D. Belforte and M. Levitt, Editors, (PennWell Books, Tulsa, Oklahoma), 1990, pp. 56-67.
6. G. Chryssolouris and W. C. Choi, "Gas Jet Effects on Laser Cutting," in SPIE Proc. CO₂ Lasers and Applications, Vol. 1042, J. D. Evans and E. V. Locke, Editors, (Society of Photo-Optical Instrumentation Engineers - The International Society for Optical Engineering, Bellingham, Washington), 1989, pp. 86-96.
7. B. Biermann, S. Biermann and H. W. Bergmann, "Cutting of Al Alloys using High-Pressure Coaxial Nozzle," J. Laser Applications, Vol. 3, 1991, pp. 13-20.
8. P. A. Molian and M. Baldwin, "Combustion-Assisted Laser Cutting of a Difficult-to-Machine Superalloy," J. Laser Applications, Vol. 4, 1992, pp. 9-14.
9. L. Ohlsson, A. Powell, A. Ivanson and C. Magnusson, "Comparison between Abrasive Water Jet Cutting and Laser Cutting," J. Laser Applications, Vol. 3, 1991, pp. 46-50.
10. A. Thompson, "CO₂ Laser Cutting of Highly Reflective Materials," in The Industrial Laser Annual Handbook, D. Belforte and M. Levitt, Editors, (PennWell Books, Tulsa, Oklahoma), 1989, pp. 149-153.
11. R. Hack, F. Dausinger and H. Hugel, "Cutting and Welding Applications of High Power Nd:YAG Lasers with High Beam Quality," in Laser Materials Processing, Proc. ICALEO'94, Vol. 2500, T. D. McCay, A. Matsunawa and H. Hugel, Editors, (Laser Institute of America and The Society of Photo-Optical Instrumentation Engineers - The International Society for Optical Engineering, Orlando, Florida), 1994, pp. 210-219.
12. D. Schuocker and W. Abel, "Material Removal Mechanism of laser cutting," in SPIE Proc. Industrial Applications of High Power Lasers, Vol. 455, (Society of Photo-Optical Instrumentation Engineers - The International Society for Optical Engineering, Bellingham, Washington), 1984, pp. 88-95.
13. D. Schuocker, "The Physical Mechanism and Theory of Laser Cutting," in The Industrial Laser Annual Handbook, D. Belforte and M. Levitt, Editors, (PennWell Books, Tulsa, Oklahoma), 1987, pp. 65-79.

14. L. Li and J. Mazumder, "A Study of the Mechanism of Laser Cutting of Wood," *Forest Products Journal*, Vol. 41, 1991, pp. 53-59.
15. M. F. Modest and H. Abakians, "Evaporative Cutting of a Semi-Infinite Body with a Moving CW Laser," *J. Heat Transfer*, Vol. 108, 1986, pp. 602-607.
16. S. Y. Bang and M. F. Modest "Multiple Reflection Effects on Evaporative Cutting with a Moving CW Laser," *J. Heat Transfer*, Vol. 113, 1991, pp. 663-669.
17. S. Roy and M. F. Modest "Evaporative Cutting with a Moving CW Laser - Part I: Effects of Three-Dimensional Conduction and Variable Properties," *Int. J. Heat Mass Transfer*, Vol. 36, 1993, pp. 3515-3528.
18. I. Belic and J. Stanic, "A Method to Determine the Parameters of Laser Iron and Steel Cutting," *Optics and Laser Technology*, Vol. 19, 1987, pp. 309-311.
19. I. Belic, "A Method to Determine the Parameters of Laser Cutting," *Optics and Laser Technology*, Vol. 21, 1989, pp. 277-278.
20. A. Kar, J. E. Scott and W. P. Latham, Effects of mode structure on three-dimensional laser heating due to single or multiple rectangular laser beams, *J. Appl. Phys.*, Vol. 80, 1996, pp. 667-674.
21. J. Xie, A. Kar, J. A. Rothenflue and W. P. Latham, "Temperature-Dependent Absorptivity and Cutting Capability of CO₂, Nd:YAG and Chemical Oxygen-Iodine Lasers," *J. Laser Applications*, Vol. 9, 1997, pp. 77-85.
22. D. L. Carroll and J. A. Rothenflue, "Experimental Study of Cutting Thick Aluminum and Steel with a Chemical Oxygen-Iodine Laser using N₂ or O₂ gas assist," In: *Proc. XI Inter. Symp. Gas Flow and Chemical lasers and High Power Laser (GCL/HPL '96)*, Edinburgh, Scotland, UK.
23. A. E. Siegman, *Lasers*, University Science Books, New York, 1986, pp. 663-685.

**QUANTUM CHEMICAL CHARACTERIZATION OF THE ELECTRONIC
STRUCTURE AND REACTIONS OF SILICON DANGLING BONDS IN Si/ SiO₂
REACTIONS OF H₂ AND H AT THE SILICON (111) INTERFACE**

Bernard Kirtman
Associate Professor
Department of Chemistry

University of California
Santa Barbara, California 93106

Final Report for:
Summer Research Program
Phillips Laboratory

Sponsored by:
Air Force Office of Scientific Research
Bolling Air Force Base, Washington, DC

And

Phillips Laboratory

September 1997

QUANTUM CHEMICAL CHARACTERIZATION OF THE ELECTRONIC
STRUCTURE AND REACTIONS OF SILICON DANGLING BONDS IN Si/SiO₂.
REACTIONS OF H₂ AND H AT THE SILICON (111) INTERFACE.

Bernard Kirtman
Professor
Department of Chemistry
University of California, Santa Barbara

Abstract

The finite cluster method is employed to calculate activation energies for the passivation/depasivation reactions of hydrogen with the dangling bond center at the (111) Si/SiO₂ interface. Initial results including only nearest neighbors do not reproduce the experimental values. It is shown that an accurate and reliable quantum chemical treatment is feasible for a large cluster model using a general "model within a model" approach. Possible further simplifications are discussed along with future applications and developments.

QUANTUM CHEMICAL CHARACTERIZATION OF THE ELECTRONIC
STRUCTURE AND REACTIONS OF SILICON DANGLING BONDS IN Si/SiO₂.
REACTIONS OF H₂ AND H AT THE SILICON (111) INTERFACE.

Bernard Kirtman

Introduction

The creation of a silicon surface will leave unpaired electrons in dangling bonds located at the silicon atoms where Si-Si bonds have been broken. In the production of metal/oxide/silicon (MOS) devices most of these sites are passivated by the thermal oxidation which is used to form the amorphous SiO₂ (a-SiO₂) layer. However, the defect sites that remain at the Si/SiO₂ interface (known as P_b centers) are electrically active and sufficient in number to seriously impede device performance. It has been found [1] that annealing at $\sim 400^\circ\text{C}$ in a hydrogen ambient leads to a dramatic decrease in their density, which tends to resolve this difficulty. On the other hand, the devices can be damaged by hot electrons or radiation which causes depassivation due to (re-)generation of P_b centers. In either case the damage is enhanced by the presence of hydrogen [2-5]. Thus, characterization of reactions involving the interfacial P_b defects with hydrogenic species is crucial to understanding the passivation/depassivation of MOS devices.

The properties of a particular P_b center will depend upon its nearest neighbors and, to a greater or lesser extent, on the non-local environment as well. From an experimental point of view the most potent tool for characterizing the local geometry has been ESR spectroscopy [6]. On the basis of ESR a single dangling bond center, known simply as P_b , has been identified at the (111) interface and two centers, known as P_{b0} and P_{b1} , at the (100) interface. The g-tensors observed for P_b and P_{b0} are almost identical. Both exhibit axial (or near axial) symmetry about the (111) direction with component values that are typical of silicon dangling bond centers having three silicon atoms as nearest neighbors. The ²⁹Si hyperfine satellite data for these two centers yields A-tensor parameters that are consistent with the above analysis and yield an estimated *p*-character substantially greater than *sp*³ for the dangling bond orbital. It is interesting that the P_{b1} g-tensor shows a deviation from axial symmetry in the (111) direction, although the component values are not very dissimilar from P_{b0} and P_{b1} . The one hyperfine measurement carried out for P_{b1} at a

single orientation shows that the separation of the satellite lines is comparable to that of P_{b0} .

The primary ESR signal can also be used to monitor the density of paramagnetic centers during the course of a reaction. In particular, this technique has been used to obtain rate constants for H_2 passivation of P_b centers and for dissociation of hydrogen atoms from the (diamagnetic) passivated HP_b defect. For the (111) interface Brower [7] found that the rate of passivation by H_2 is proportional to the density of P_b centers at the interface and to the H_2 concentration. From this one may infer the reaction:

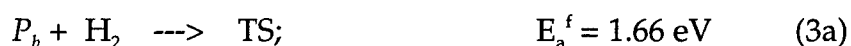


The observed rate constant, measured as a function of temperature in the range 230°-260° C, is accurately described by the Arrhenius equation with an activation energy $E_a^f = 1.66 \pm .06$ eV. Subsequent vacuum thermal annealing of the passivated HP_b centers in the temperature range 500°-600° C leads to recovery of paramagnetic P_b . Since the dissociation rate is proportional to the HP_b density, and there is a large deuterium isotope effect, it was concluded [8,9] that the pertinent reaction is:



Again, the rate constant data is well fit [8,9] by the Arrhenius expression giving an activation energy for dissociation of $E_d = 2.56 \pm 0.06$ eV.

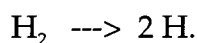
In addition to the passivation reaction of Eq.(1) it is useful to consider the reverse abstraction reaction. Thus, if TS refers to the common transition state, then -



and



Evidently, the combination Eq.(3a) - Eq.(3b) + Eq.(2) corresponds to the overall reaction -



This means that $E_a^f - E_a^r + E_d = 4.22 \text{ eV} - E_a^r$ should equal [10] the dissociation energy of H_2 in SiO_2 . It has been argued [8,9] that the latter cannot be very different from the dissociation energy of H_2 *in vacuo*, which is 4.52 eV. That being the case, E_a^r should

be close to 0.0 eV since any greater value will increase the discrepancy beyond 0.30 eV.

Passivation kinetics corresponding to Eq.(3a) have been investigated [11] for the P_{b0} and P_{b1} centers at the (100) interface over the temperature range 213°-234° C. Although the results were similar to those obtained at the (111) surface, it was found that the data could not be fit by a single-valued E_a^f . Thus, the activation energies were determined as a mean value plus a Gaussian spread. For the P_{b0} and P_{b1} centers $E_a^f = 1.51 \pm 0.30$ eV and 1.57 ± 0.30 eV respectively. As far as the activation energies are concerned P_{b1} is somewhat closer to P_b than is P_{b0} . Indeed, on the basis of several different passivation experiments, Stathis and co-workers [12-14] have argued that P_{b0} is certainly different from P_b and that the latter behaves more like P_{b1} . Very recently, Vanheusden, *et al.* [15] have made analogous observations in the course of examining Si/SiO₂/Si structures. In this regard, then, there is an inconsistency between ESR and hydrogen passivation studies that remains to be resolved.

Quantum chemical calculations may be able to play a significant role in characterizing the several P_b centers. In principle, such calculations can be used to test atomic scale models based on the interpretation of experimental data. Different models can be compared and new experiments suggested to verify predicted structures. In order to succeed, however, it must be demonstrated that the computational methods employed are of sufficient accuracy and reliability. Thus, we focused our attention initially on determining activation energies for hydrogen passivation/depasivation at the (111) P_b center. This is the center that is best characterized experimentally and stationary points on the reactive potential energy surface (equilibrium geometries and energies; TS geometries and energies) are the most straightforward properties to obtain.

Once a satisfactory approach has been developed, then the stage will be set for branching out in several directions. Thus, we will be able to investigate the technologically dominant P_{b0} and P_{b1} centers at the (100) interface. Also of interest are the radiation-induced (as well as intrinsic) E' silicon dangling bond centers in the a-SiO₂ layer that are thought [16] to play a key role in the transport of hydrogenic species to the Si/SiO₂ interface. This is not to mention the occurrence of oxygen paramagnetic centers which, so far, have been of lesser concern.

Other key properties apart from activation energies will also become accessible. The electronic g-tensors and hyperfine coupling tensors fall into this

category. Measurements have also been made {17,18} which yield the population of P_b electronic energy levels within the silicon bandgap as a function of the position of the Fermi level. Computation of this property can provide yet another important handle on the microscopic characterization of the P_b center.

The use of quantum chemical computations as an interpretive tool of its own is worthy of mention here. From such calculations one can distinguish between local contributions to physical properties and medium-long range effects. Furthermore, it is possible to analyze results in terms of classical electrostatics, exchange effects, electron correlation, ... and to investigate the role of through-bond vs. through-space interactions, orbital hybridization, etc.

In the next section we discuss briefly three main approaches that may be utilized to carry out quantum chemical modeling of large aperiodic systems. Of these the finite cluster treatment has been chosen for our initial studies. In order to combine practicality with accuracy and reliability a variety of what may be called "model within a model" techniques are employed. Similar techniques have been used in the past to improve the accuracy for a given finite cluster and, recently, a general approach to extending the size of the cluster has been presented by Morokuma and co-workers {19-23}. Both modalities are employed here with systematic testing in so far as possible. In addition, it is shown that the treatment of Morokuma, *et al.* may be extended to give the local geometry at stationary points directly rather than through an indirect energy optimization.

The "model within a model" method for large clusters requires a high level treatment of a small cluster followed by correction for the difference between the large cluster and the small one obtained at a lower level. The small cluster is defined in the third section where it is also demonstrated that calculations can be done at a sufficient accuracy for our purposes. Then we construct the large cluster, test various lower levels of treatment and consider further reductions of level. Finally, the major conclusions of this work are presented along with a discussion of proposed future developments.

Methods

There are three major approaches to the quantum chemical treatment of large aperiodic systems. The one that we shall utilize here is the most straightforward, namely the finite cluster method. It assumes that the property in question is

sufficiently local so that it can be well-represented by means of a relatively small finite cluster molecular model. In applying this method the dependence of the property on cluster size should be carefully monitored for convergence.

A variety of techniques are available for embedding a small cluster within a larger system. All of these, either implicitly or explicitly, make some approximation regarding the interaction terms. This leads to an "effective" Hamiltonian, or an "effective" projected Hamiltonian, which is used to represent the embedded cluster. Although we do not employ an embedding technique in this investigation it is a consideration for the future as noted in the final section.

The third general approach is the supercell method. It is the theoretical analogue of biomolecular crystallography. That is to say, one defines a unit cell containing a finite cluster model and reproduces that cell so as to form an infinite periodic array. This makes it possible for band structure computational techniques to be applied. The supercell method does not appear to be advantageous for the current investigation and will, therefore, not be considered further.

If it were possible to determine accurate and reliable electronic structures from semiempirical calculations, then it would be feasible to treat large finite clusters directly. In order to test that proposition we carried out MNDO calculations on the first nearest neighbors (NN=1) cluster model. As shown in Fig. 1(b) the nearest neighbor silicons are terminated by hydrogen atoms. In the TS of Eqs.(3a) and (3b) the silicon P_b center and the original H_2 molecule are linearly aligned as expected. The P_b -H distance, R_1 , and the H-H distance, R_2 , are reported in Table I where it is clear that very different values are obtained by a high level *ab initio* treatment (to be discussed later). Likewise large discrepancies (0.78,1.00 eV) can be seen for E_a^f and E_d . This confirms the lore that semiempirical methods are inadequate for transition states. The same is true for molecular force fields, i.e. molecular mechanics.

We conclude that *ab initio* methods are required to give even reasonable TS results for small model clusters. In fact, we will see that only a high level *ab initio* treatment will provide E_a^f , E_a^r and E_d to within the desired accuracy of 0.05 eV. This does not mean that lower level *ab initio* calculations, or even a semiempirical treatment, will be unsuitable for accomplishing the transition from small to large clusters. In fact, as mentioned in the Introduction, Morokuma and co-workers {19-23} have presented a general framework for achieving high accuracy using lower

level methods. The general (approximate) relation that they exploit may be written as -

$$\begin{aligned} (\text{large; high level}) = & (\text{small; high level}) + [(\text{large; lower level}) - \\ & (\text{small; lower level})] \end{aligned} \quad (4)$$

It is presumed that the correction term in square brackets may be evaluated with sufficient accuracy at a lower level of treatment. Of course, the definition of "high level" and "lower level" must be specified and, for that matter, the same is true of "small" and "large". In arriving at the definitions tests should be carried out to verify that a justifiable claim of accuracy can be made. Eq.(4) is a one-step procedure. Of course, it is also possible to make the transition from the small to large cluster through any number of intermediate steps as Morokuma, *et al.* have noted. Morokuma's prescription has been used to determine energies and, thereby, stationary point geometries. We will see that it can also be employed directly to obtain values for local internal coordinates at the stationary points.

In *ab initio* calculations, the level is specified by the electronic structure method and the basis set indicated by (method/basis). For a given cluster a desired (accurate/large) result may be estimated from -

$$\begin{aligned} (\text{accurate/large}) = & (\text{less accurate/smaller}) \\ & + [(\text{accurate/smaller}) - (\text{less accurate/smaller})] \\ & + [(\text{less accurate/large}) - (\text{less accurate/smaller})] \end{aligned} \quad (5)$$

This relation presumes that the method and basis set corrections are additive. The validity of Eq.(5), like that of Eq.(4), must be established for each individual case. In this study we will see that it can be used to obtain a high level small cluster result to be used for the first term on the *rhs* of Eq.(4).

Small Model Clusters

The first small cluster that we examined was the model without any nearest neighbors, i.e. NN=0 in Fig.1(a). It may be noted that the value of E_a^f for the (111) P_b center is not very different from that of the (100) P_{b0} and P_{b1} centers. Indeed all three values lie within the range 1.51-1.66 eV. Thus, an NN=0 cluster model is not entirely absurd.

A UMP2/6-31G** calculation is generally sufficient for determining a good geometry. So this is where we began. The key TS structural parameters, i.e. R_1 and R_2 , obtained at this level are reported in Table II(A). By comparison with UMP2/6-311G** we see that the basis set is adequate. On the other hand, upon going from UMP2 to CCSD(T) R_1 and R_2 change by 0.02 Å and 0.06 Å respectively. We conclude that CCSD(T) is required for an accurate TS geometry. If CCSD(T) is taken as the standard, then the UHF bond lengths show substantially larger errors than the MP2 values.

The commonly used B3LYP version of density functional theory will often give *equilibrium* geometries that are closely comparable to MP2. Recently, Truong {24} has pointed out that the same is not true for transition states. He has found, however, that Becke's {25} Half and Half (BHH) treatment of electron exchange along with the Lee, Yang and Parr {26} correlation potential (LYP) will give satisfactory results. We have confirmed Truong's observations for the NN=0 cluster model. The last column of Table II(A) shows that, compared to CCSD(T), the error in both R_1 and R_2 has about the same magnitude as for MP2, but is opposite in sign. What surprised us was the fact that the BHHLYP geometry optimization took much longer than MP2 to execute using GAUSSIAN94.

Although CCSD(T) is required for an accurate TS geometry, such a high quality geometry is not necessary in order to obtain accurate activation energies. This is demonstrated in Table II(B) where we show the results of CCSD(T) energy calculations carried out at the MP2 and CCSD(T) geometries. In all circumstances a 6-31G** basis set was employed. As we've already seen that this basis yields satisfactory geometries (its suitability for the calculation of activation energies will be discussed shortly). Evidently, the differences in E_a^f , E_a^r and E_d for the two geometries are on the order of 0.01 eV, which means that the MP2/6-31G** geometry should be sufficient for our purposes.

The next step was to determine the effect of increasing the level of treatment for the energies with the geometry calculations done always at the MP2/6-31G** level. In Table II(C) the first two rows yield a comparison of MP2 values for E_a^f , E_a^r and E_d obtained with either the 6-311G** or the 6-31G** basis set. The discrepancy between the two rows ranges from 0.043 eV for E_d to 0.111 eV for E_a^f . We conclude that the difference between a valence double zeta and a valence triple zeta basis is small but significant. Adding additional diffuse functions (for both hydrogen and

silicon), as in the last row of the table, leads to negligible changes ($< \sim 0.005$ eV). By comparing the first and third rows we obtain the effect of using the CCSD(T) method rather than MP2 with the same 6-31G** basis in either case. It turns out that the effect varies from 0.006 eV for E_a^f to 0.107 eV for E_a^r to 0.103 for E_a . In this case our conclusion is that the effect is, again, small but significant.

On the basis of the calculations reported in Table II we judge that the desired high level treatment for the small model cluster in Eq.(4) is CCSD(T)/6-311G**//MP2/6-31G**. Is it satisfactory to reach this level using Eq.(5) with MP2/6-31G**//MP2/6-31G** as the starting point? A test of that notion for the NN=0 cluster is provided in Table III. The first row of the table gives the "exact" result and the last row the predicted value. Rows 2 and 3 are the corrections due to the basis set and the method respectively. The total correction varies in magnitude from 0.117 to 0.160 eV while the error in the predicted value is less than 0.026 eV for each activation energy. It appears that the goal of 0.10 eV accuracy in the final result can be met by the approximate additive approach of Eq.(5).

It is straightforward to extend the approximate calculations of Table III to the NN=1 cluster. A summary of the values obtained for NN=0, NN=1 and experiment is provided in Table IV. Note that including first nearest neighbors leads to substantial changes in the (non-observable) TS geometry. It is also true that, in each case, the presence of the first neighbors leads to significantly improved agreement with experiment. However, the remaining discrepancy is still large. It is certainly larger than one might expect [27] from corrections to the barrier height due to zero-point vibrations, tunneling, etc. Thus, one must conclude that it is critical to take account of more distant neighbors and/or non-bonding interactions with atoms in the a-SiO₂ layer. Alternatively, one may have to consider the possibility that the experimental interpretation is not completely correct.

Large Cluster Model

The addition of second nearest neighbors to form the NN=2 cluster model includes more silicons but introduces no new qualitative features. With third nearest neighbors (see Fig.2) oxygen atoms appear for the first time and closed silicon rings as well. Since the effect of these features would need to be investigated in any event it was decided to skip the NN=2 case and proceed immediately to the simplest model which has oxygen and closed silicon rings. Thus, we constructed a Si₁₉O₆H₂₇

cluster containing: (1) all second nearest neighbors, plus (2) all third nearest neighbor oxygen atoms, plus (3) all third nearest neighbor silicon atoms that give rise to ring closure. The resulting cluster model is presented in Fig.2. (not shown are the terminating hydrogen atoms). A similar model has been investigated by Edwards {28,29} who included all third nearest neighbors and carried out an MNDO electronic structure calculation.

For the large $\text{Si}_{19}\text{O}_6\text{H}_{27}$ cluster we employ the general approach of Eq.(4). The low level treatment considered initially was UHF/6-31G**. As a test we carried out calculations in which the NN=0 model was taken to be the small cluster and the NN=1 model the large cluster. An argument can be made that this is a worst case scenario. The results reported in Table IV were obtained using a 6-31G** basis throughout; thus only the method is listed. It is readily seen from the table that the UHF//UHF energy corrections reproduce the CCSD(T)//MP2 values to within 0.015 eV for E_a^f , E_a^r and E_d . The numbers in parentheses are the best high level estimates found by applying Eq. (5) to determine CCSD(T)/6-311G**//MP2/6-31G** values as described earlier. In comparison with the latter our conclusion given above (i.e. agreement of UHF//UHF to within 0.015 eV) remains unchanged.

Since geometry optimization is the most time-consuming step we have undertaken some calculations to see if the UHF/3-21G geometry would be acceptable instead of UHF/6-31G**. Table V(A) shows that there is remarkably close agreement (0.005 eV) between UHF activation energies obtained with the two different geometries. Indeed, this close agreement prompted us to look at the possibility of utilizing Eq.(4) directly to predict the geometry of large clusters. We focused specifically on the TS parameters R_1 and R_2 since they are, by far, the most sensitive to changes in the description of the electronic structure. The values reported in Table V(B) show that the difference in these bond lengths due to transition from the NN=0 to the NN=1 cluster varies little, i.e. $< 0.006 \text{ \AA}$, from a UHF/3-21G to a UHF/6-31G** calculation. The variation from UHF/6-31G** to MP2/6-31G** is a bit larger, but still less than 0.036 \AA (out of 0.111 \AA for the difference between NN=0 and NN=1) in the worst case.

Accurate calculations for the large cluster are feasible at the UHF/6-31G**//UHF/3-21G level of approximation. However, such a treatment requires extensive computational resources. Further simplifications will, therefore, be explored before proceeding along this path. As far as geometry optimization is concerned, it should

be possible to accurately guess most of the optimized internal coordinates from calculations that have already been done plus other small model results. Geometrical parameters for the bonds and bond angles involving oxygen, for example, can be obtained from a cluster where the dangling bond of the NN=1 model is replaced by a hydroxyl group. In a similar vein, relatively small models containing 6-membered silicon rings can be constructed to yield the geometrical parameters for these structures. At the very least, we should be able to limit the optimization on the large cluster to just R_1 , R_2 and, perhaps, a couple of other internal coordinates. If these coordinates cannot be accurately guessed, then we will proceed to consider effective core potentials, smaller basis sets and semiempirical methods. The latter will be tested in conjunction with Eq.(4) before moving on, if necessary, to the *ab initio* UHF/3-21G level. The same options will be considered for the single point energy calculations at the optimized geometries.

Conclusions and Future Developments

From our work thus far we can draw two major conclusions: (1) sufficiently accurate quantum chemical calculations can be carried out on large clusters to definitively characterize the atomic level structure and reactions of silicon dangling bonds in Si/SiO₂; and (2) for hydrogen passivation/depasivation reactions of the P_b dangling bond at the (111) interface a first nearest neighbors model does not confirm the currently accepted microscopic description. Our next step will be to see whether the experimental activation energies are reproduced by a large cluster containing oxygens from the a-SiO₂ layer and 6-membered silicon rings. We wish to apply a similar approach to study the P_{b0} and P_{b1} dangling bonds at the (100) interface as well as E' defects in the SiO₂ layer. In addition to activation energies other dangling bond properties, particularly the density of intra-gap states as a function of the Fermi level and {29} ESR spectra (g-tensor, A-tensor), will be calculated to provide a complete characterization. Finally, in terms of methodology, the local space embedding approximation {30} will be considered as an alternative to the finite cluster approach and we also plan to develop a customized molecular mechanics especially suited for treating dynamics in MOS systems.

Table I. *Ab initio* vs. MNDO semiempirical calculation of the activation energies and transition state geometry for passivation/depassivation of the (111) P_b center by H_2 and H. The reactions are defined in Eqs.(2), (3a) and (3b); the NN=1 cluster model used in these calculations is shown in Fig.1(b).

method	<u>activation energies</u>			<u>TS geometry</u>	
	$E_a^f(\text{eV})$	$E_a^r(\text{eV})$	$E_d(\text{eV})$	$R_1(\text{\AA})$	$R_2(\text{\AA})$
MNDO	1.85	0.06	2.69	1.400	1.575
<i>ab initio</i> ^a	1.07	0.19	3.69	1.587	1.175

^a Estimated CCSD(T)/6-311G**//MP2/6-31G** values (see Table IV).

Table II. Transition state geometry and activation energies for the NN=0 cluster model.

(A) Variation of geometry with basis set and method of calculation. B1 is the 6-31G** basis; B2 is the 6-311G** basis.

	MP2/B1	MP2/B2	CCSD(T)/B1	UHF/B1	BHHLYP ^a /B1
R ₁ (Å)	1.6268	1.6221	1.6067	1.6897	1.5835
R ₂ (Å)	1.0636	1.0657	1.1243	1.0249	1.1759

^a This is the density functional method with Becke's Half and Half exchange approximation [25] and the Lee, Yang and Parr [26] correlation potential. See text for further discussion.

(B) Comparison of CCSD(T) activation energies obtained at the MP2 vs. CCSD(T) geometry. All calculations were done in the 6-31G** basis.

geometry	E _a ^f (eV)	E _a ^r (eV)	E _d (eV)
MP2	0.976	0.367	3.981
CCSD(T)	0.986	0.374	3.981

(C) Effect of method and basis set on activation energies calculated at the MP2/6-31G** geometry.

level	E _a ^f (eV)	E _a ^r (eV)	E _d (eV)
MP2/6-31G**	0.982	0.474	3.878
MP2/6-311G**	0.871	0.421	3.921
CCSD(T)/6-31G**	0.976	0.367	3.981
MP2/6-311++G**	0.870	0.416	3.917

Table III. Additivity of method and basis set corrections for activation energies of NN=0 cluster model: MP2/6-31G** \rightarrow CCSD(T)/6-311G**. B1 is the 6-31G** basis; B2 is the 6-311G** basis. The MP2/B1 geometry is used in all calculations.

level	$E_a^f(\text{eV})$	$E_a^r(\text{eV})$	$E_d(\text{eV})$
CCSD(T)/B2	0.839	0.294	4.044
MP2/B1	0.982	0.474	3.878
CCSD(T)/B1 - MP2/B1	-0.006	-0.107	0.103
MP2/B2 - MP2/B1	-0.111	-0.053	0.043
CCSD(T)/B2 (est.)	0.865	0.314	4.024

Table IV. Best *ab initio* activation energies and transition state geometries for small model clusters. Geometries were calculated at the MP2/6-31G** level; activation energies were corrected to the CCSD(T)/6-311G** level using the additivity approximation of Eq.(5).

model	<u>activation energies</u>			<u>TS geometry</u>	
cluster	$E_a^f(\text{eV})$	$E_a^r(\text{eV})$	$E_d(\text{eV})$	$R_1(\text{\AA})$	$R_2(\text{\AA})$
NN=0	0.87	0.31	4.02	1.627	1.064
NN=1	1.07	0.19	3.69	1.587	1.175
experiment	1.66 ^a	0.0 ^a	2.56 ^b	--	--

^a K.L. Brower, Appl. Phys. Lett 53, 508 (1988); Phys. Rev. B38, 9657 (1988).

^b K.L. Brower and S.M. Meyers, Appl. Phys. Lett 57, 162 (1990).

Table V. Tests of lower level treatment for extension from small to large model clusters.

(A) Change in the UHF activation energy from NN=0 to NN=1 vs. high level estimate. All results were obtained in a 6-31G** basis (except for those given in parentheses); ΔE is the correction term $E(\text{NN}=1) - E(\text{NN}=0)$.

	<u>UHF//UHF</u>			<u>CCSD(T)//MP2</u>		
	NN=0	NN=1	ΔE	NN=0	NN=1	ΔE
$E_a^f(\text{eV})$	1.017	1.230	0.215	0.976	1.202	0.226(0.208) ^a
$E_a^r(\text{eV})$	0.668	0.528	-0.140	0.367	0.240	-0.127(-0.125) ^a
$E_d(\text{eV})$	3.310	2.968	-0.342	3.981	3.626	-0.355(-0.334) ^a

^a Includes correction for evaluation of CCSD(T) activation energy in 6-311G** basis.

(B) Effect of reducing the basis set in geometry optimization. Comparison of $\Delta E = E(\text{NN}=1) - E(\text{NN}=0)$ for UHF/6-31G**//UHF/6-31G** vs. UHF/6-31G**//UHF/3-21G.

	<u>UHF/6-31G** geometry</u>			<u>UHF/3-21 geometry</u>		
	NN=0	NN=1	ΔE	NN=0	NN=1	ΔE
$E_a^f(\text{eV})$	1.017	1.230	0.215	1.012	1.220	0.208
$E_a^r(\text{eV})$	0.668	0.528	-0.140	0.663	0.523	-0.140
$E_d(\text{eV})$	3.310	2.968	-0.342	3.321	2.973	-0.348

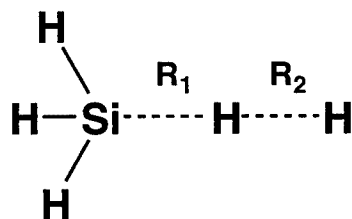
(C) Change in the transition state geometry from NN=0 to NN=1 at various levels of treatment.

	NN=0	$R_1(\text{\AA})$	ΔR	NN=0	$R_2(\text{\AA})$	ΔR
		NN=1			NN=1	
UHF/6-31G**	1.6897	1.6480	-0.0417	1.0249	1.1007	0.0758
UHF/3-21G	1.6686	1.6303	-0.0383	1.0593	1.1293	0.0700
MP2/6-31G**	1.6268	1.5862	-0.0406	1.0636	1.1749	0.1113

References

1. P. Balk, Extended Abs., Electronics Div.; Electrochem. Soc. **14**, 237 (1965).
2. D.J. DiMaria and J.W. Stasiak, J. Appl. Phys. **65**, 2342 (1989).
3. N.S. Saks and R.W. Rendell, IEEE Trans. Nucl. Sci. NS-39, 2220 (1992).
4. R.E Stahlbush, A.H. Edwards, D.L. Griscom and B.J. Mrstik, J. Appl. Phys. **73**, 658 (1993).
5. F.B. McLean, IEEE Trans. Nucl. Sci NS-27, 1651 (1980).
6. For a recent review see J.F. Conley, Jr. and P.M. Lenahan in The Physics and Chemistry of SiO₂ and the Si-SiO₂ Interface, H.Z. Massoud, E.H. Poindexter and C.R. Helms, eds., Vol. 96-1 (The Electrochemical Society, Pennington, New Jersey, 1996), p.214.
7. K.L. Brower, Phys. Rev. B **38**, 9657 (1988).
8. K.L. Brower, Appl. Phys. Lett. **53**, 508 (1988); Phys. Rev. B **42**, 3444 (1990).
9. K.L. Brower and S.M. Myers, Appl. Phys. Lett. **57**, 162 (1990).
10. S.M. Myers and P.M. Richards, J. Appl. Phys. **67**, 4064 (1990).
11. A. Stesmans, Solid State Commun. **97**, 255 (1996).
12. J.H. Stathis and L. Dori, Appl. Phys. Lett. **58**, 1641 (1991).
13. E. Cartier, J.H. Stathis and D.A. Buchanan, Appl. Phys. Lett. **63**, 1510 (1993).
14. J.H. Stathis and E. Cartier, Phys. Rev. Lett. **72**, 2745 (1994).
15. K. Vanheusden, private communication.
16. For a recent discussion including ab initio calculations see A.H. Edwards, J.A. Pickard and R.E. Stahlbush, J. Non-Cryst. Solids **179**, 148 (1994).
17. P.M. Lenahan and P.V. Dressendorfer, J. Appl. Phys. **55**, 3495 (1984).
18. N.M. Johnson, D.K. Biegelsen, M.D. Moyer, S.T. Chang, E.H. Poindexter, and P.J. Caplan, Appl. Phys. Lett. **43**, 563 (1983); E.H. Poindexter, G.J. Gerardi, M.E. Rueckel, P.J. Caplan, N.M. Johnson and D.K. Biegelsen, J. Appl. Phys. **56**, 2844 (1984).
19. F. Maseras and K. Morokuma, J. Comp. Chem. **16**, 1170 (1995).
20. T. Matsubara, F. Maseras, N. Koga and K. Morokuma, J. Phys. Chem. **100**, 2573 (1996).
21. S. Humbel, S. Sieber and K. Morokuma, J. Chem. Phys. **105**, 1959 (1996).
22. M. Svensson, S. Humbel and K. Morokuma, J. Chem. Phys. **105**, 3654 (1996).
23. M. Svensson, S. Humbel, R.D.J. Froese, T. Matsubara, S. Sieber and K. Morokuma, J. Phys. Chem. **100**, 19357 (1996).
24. T.N. Truong and W. Duncan, J. Chem. Phys. **101**, 7408 (1994); T.N. Truong, J. Phys. Chem. B **101**, 2750 (1997).
25. A.D. Becke, J. Chem. Phys. **98**, 1372 (1993).
26. C. Lee, W. Yang and R.G. Parr, Phys. Rev. B **37**, 785 (1988).
27. H.A. Kurtz, private communication.
28. A.H. Edwards, Phys. Rev. B **44**, 1832 (1991).
29. A.H. Edwards, Phys. Rev. B **36**, 9638 (1987).
30. For a recent paper with references to earlier work see B. Kirtman and H. Sekino, Chem. Phys. Lett. **263**, 313 (1996).

(a) NN = 0 model



(b) NN = 1 model

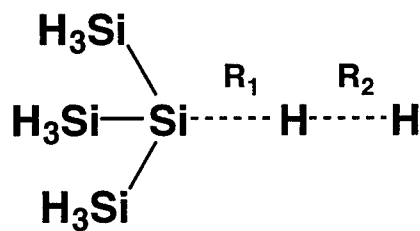


Figure 1. Small cluster models for the transition state in the reaction of the (111) P_b dangling bond center with H_2 . The NN=0 model in (a) contains no nearest neighbors of the P_b center; the NN=1 model in (b) contains only first nearest neighbors. Hydrogen atoms are used to terminate the cluster.

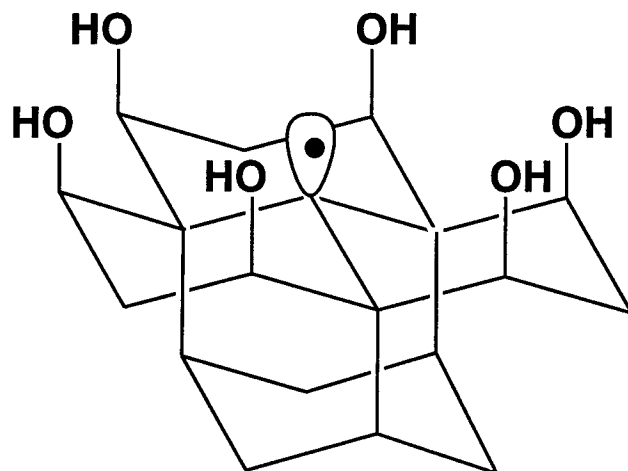


Figure 2. Large $\text{Si}_{19}\text{O}_6\text{H}_{27}$ cluster model for the (111) P_b dangling bond center. This model contains all second nearest neighbors of the dangling bond center (the dangling orbital is shown schematically) plus all third nearest neighbors that are either oxygen atoms or silicon atoms that close a six-membered ring. Hydrogen atoms used to terminate silicon atoms of cluster are not shown.

**EXCITATION OF OSCILLATING TWO STREAM INSTABILITY BY UPPER
HYBRID PUMP WAVES IN IONOSPHERIC HEATING EXPERIMENTS AT
TROMSO**

S. P. Kuo
Professor
Department of Electrical Engineering

Polytechnic University
Route 110
Farmingdale, New York 11735

Final Report for:
Summer Research Program
Phillips Laboratory

Sponsored by:
Air Force Office of Scientific Research
Bolling Air Force Base, Washington, DC

And

Phillips Laboratory

August 1997

Excitation of Oscillating Two Stream Instability by Upper Hybrid Pump Waves in Ionospheric Heating Experiments at Tromso

S. P. Kuo
Professor
Department of Electrical Engineering
Polytechnic University

Abstract

It is shown that upper hybrid waves generated by the HF heater wave in the Tromso' heating experiments can excite oscillating two stream instability near the upper hybrid resonance layer of the heater wave. The sidebands of the investigated parametric instability are obliquely propagating Langmuir waves. These Langmuir waves can be excited in milliseconds and have a broad angular distribution. Thus, those waves propagating obliquely at small angles with respect to the geomagnetic field can contribute to the zero off-set frequency component of the plasma line spectrum detected by a backscatter radar. The analyses also show that the wavelengths of the Langmuir waves have an upper bound and consequently, explain why the zero off-set frequency plasma line has been detected by the EISCAT 933 MHz (UHF) radar, but not by the EISCAT 244 MHz (VHF) radar as reported in Stubbe et. al. [1992].

Excitation of Oscillating Two Stream Instability by Upper Hybrid Pump Waves in Ionospheric Heating Experiments at Tromso

S. P. Kuo

I. Introduction

During the HF heating of the ionosphere, parametric instabilities can provide effective channels to convert electromagnetic waves into electrostatic plasma waves with high and low frequencies [Perkins et al., 1974; Fejer, 1979; Kuo, 1992]. In the midlatitude region such as Arecibo, Puerto Rico, the instabilities are excited by the o-mode heater wave near its reflection height [Carlson et al., 1972; Djuth et al., 1990], where the heater wave electric field is polarized nearly parallel to the geomagnetic field. Thus, the sidebands of the parametric decay instability (PDI) and oscillating two stream instability (OTSI) are Langmuir waves, which propagate within a small cone around the geomagnetic field [Fejer and Kuo, 1973]. By contrast, in the high-latitude region such as Tromso, Norway, the heater wave can effectively interact with the ionosphere at its upper hybrid resonance layer, where the o-mode heater wave is still characterized by the right-hand circular polarization, before the heater wave reaches its reflection height [Stubbe et al., 1982; Lee and Kuo, 1983; Leyser, 1991]. It has been shown that thermal parametric instabilities [Lee and Kuo, 1983; Huang and Kuo, 1994] can be effectively excited in this region, and the sidebands are upper hybrid waves propagating nearly perpendicular to the geomagnetic field. The upper hybrid waves can also be generated by linear mode conversion of the HF heater wave [Mjølhus, 1990]. The upper hybrid waves are found to play a key role in the

generation of “ stimulated electromagnetic emissions (SEEs) “, observed in Tromso’s heating experiments [Stubbe et al., 1984; Stenflo, 1990; Leyser, 1994; Zhou et al., 1994].

Due to the field-aligned nature of the upper hybrid waves, they can not be detected by EISCAT’s VHF and UHF backscatter radars. However, Langmuir waves referred to as “ HFPLs “, have been detected by EISCAT’s UHF and VHF radars during Tromso’s heating experiments [Hagfors et al., 1983; Stubbe et al., 1985; Isham et al., 1990; Stubbe et al., 1992]. Similar to the Arecibo’s situation, these Langmuir waves can be excited by the o-mode heater wave near its reflection height via the PDI or OTSI processes. However, these instabilities have to compete with those occurring in the upper hybrid resonance region located at a lower height and depleting the heater wave power. Experimental results show that the intensity ratio of the OTSI to decay lines, while virtually independent of heater power, depends markedly on radar frequency. The OTSI line is strong as monitored with the EISCAT UHF radar, but very weak or absent with the EISCAT VHF radar [Stubbe, et al., 1992].

The present work is aimed at understanding the afore-mentioned observations at Tromso using the EISCAT’s radar facilities. We show that the Langmuir waves at the heater frequency (viz., OTSI lines) observed in the Tromso’s heating experiments can, in fact, be excited parametrically by the upper hybrid waves. These upper hybrid waves are excited directly by the o-mode heater wave via either the thermal OTSI process [Lee and Kuo, 1983; Huang and Kuo, 1994] or the mode conversion process [Mjølhus, 1990]. In section II, the theory of the proposed instability process is presented. The formulation

includes the derivation of coupled mode equations and the dispersion relation. The dispersion relation is analyzed in section III, in which the threshold fields and growth rates of instabilities for two different decay modes are derived analytically and evaluated numerically. A comparison of the two instability processes is made to show the dominant one related to the observations at Tromsø. The concluding remarks are finally drawn in section IV.

II. Theory

Experiments and theories have shown that upper hybrid waves can be excited by the HF heater wave near the upper hybrid resonance layer via thermal parametric instabilities and/or mode conversion in the heating experiments conducted at Tromsø, Norway. After the excited upper hybrid waves grow and acquire sufficiently large intensities, they become pump waves to excite various parametric instabilities, broadening the spectral distribution of plasma waves.

In the following we analyze the decay of a field-aligned upper hybrid pump wave $(\omega_1, \vec{k}_1 = \hat{x}k_1)$ into two obliquely propagating Langmuir waves (ω_0, \vec{k}_0) and (ω_2, \vec{k}_2) , and an ion mode $(\omega_s, \vec{k} = \hat{z}k)$ which is either a purely growing mode or an ion acoustic mode. The geomagnetic field is chosen to be in the z-direction, ie. $\vec{B}_0 = \hat{z}B_0$. The process under consideration can be represented by the following matching relations:

$$\omega_1 = \omega_2 + \omega_s^* = \omega_0 - \omega_s, \quad \vec{k}_1 = \vec{k}_2 + \vec{k} = \vec{k}_0 - \vec{k}$$

where the wave vector matching conditions are illustrated in Figure 1.

A. Coupled Mode Equations for Obliquely Propagating Langmuir Waves:

The coupled mode equations for Langmuir sidebands $(\omega_0, \vec{k}_0; \omega_2, \vec{k}_2)$ in terms of the upper hybrid pump wave (ω_1, \vec{k}_1) and the ion decay mode (ω_s, \vec{k}) can be derived from the electron continuity equation and electron momentum equation together with Poisson's equation, as

$$\{(\partial_t + \nu_e)^2 [\partial_t (\partial_t + \nu_e) + \omega_{kt}^2] + \Omega_e^2 [\partial_t (\partial_t + \nu_e) + (k/k_i)^2 \omega_{kt}^2]\} \phi_{0,2} \\ = -\omega_p^2 (k_i/k_t)^2 (\partial_t + \nu_e)^2 [\phi_1 (n_{s0,2}/n_0)] \quad (1)$$

where ϕ_1 , ϕ_0 and ϕ_2 are electric potentials of the upper hybrid pump wave, up-shifted and down-shifted Langmuir sidebands; $n_{s0} = n_s = n_{s2}^*$ is the density perturbation associated with the ion decay mode and n_0 is the unperturbed electron density; $k_t^2 = k_1^2 + k^2$, $\omega_{kt}^2 = \omega_p^2 + 3k_t^2 v_{te}^2$, $v_{te} = (T_e/m_e)^{1/2}$ is the electron thermal speed and ω_p is the electron plasma frequency; $\Omega_e = eB_0/mc$ and ν_e are the electron cyclotron and collision frequency respectively.

Assuming that all the physical quantities of the waves involved have a time harmonic function form, ie., $s = \tilde{s}e^{-i\omega t}$, the coupled mode equations (1) are reduced to

$$\tilde{\phi}_{0,2} = (k_i/k_t)^2 \omega_p^2 \tilde{\phi}_1 (\tilde{n}_{s0,2}/n_0) / [(k/k_t)^2 (\Omega_e^2 \omega_{kt}^2 / \omega_1^2 - 3k_t^2 v_{te}^2) + \omega_1 (i\nu_e \pm 2\omega_{s0,2})] \quad (2)$$

where $\omega_{s0} = \omega_s = \omega_{s2}^*$; $\Omega_e^2 / \omega_1^2 \ll 1$ is assumed.

To complete the description of the considered instability process, a coupled mode equation relating n_s to $\phi_{0,2}$ is derived as follows.

B. Coupled Mode Equation for the Low Frequency Decay Mode:

The low frequency decay mode is either a purely growing mode (ie. $\omega_s = i\gamma$) or an ion acoustic wave (ie. $\omega_s = kC_s + i\gamma$, where $C_s = [(T_e + 3T_i)/m_i]^{1/2}$ is the ion acoustic speed

). In either case, the wave vector of the decay mode is assumed to be along the geomagnetic field (ie. $\vec{k} = \hat{z}k$). The damping mechanisms of these two decay waves are, however, quite different. The damping rate of the purely growing mode is proportional to ν_{in} , the ion-neutral collision frequency, while the ion acoustic wave is heavily damped by the ion Landau damping process. From ion continuity equation and momentum equation, the coupled mode equation is derived to be

$$(\omega_s^2 + i\nu_i\omega_s - k^2 C_s^2) (\tilde{n}_s/n_0) = (m/M) k^2 (\tilde{v}_0 \cdot \tilde{v}_1^* + \tilde{v}_1 \cdot \tilde{v}_2^*) \quad (3)$$

where ν_i is the ion-neutral collision frequency ν_{in} for the purely growing mode and is twice the ion Landau damping rate $2\Gamma_i = (\pi/2)^{1/2} \omega_s \{ (m/M)^{1/2} + (T_e/T_i)^{3/2} \exp[-(T_e/2T_i + 3/2)] \}$ for the ion acoustic wave; the coupling term on the right hand side of Eq.(3) is contributed by the ponderomotive force of high frequency electrostatic waves on the plasma electrons. \tilde{v}_1 , \tilde{v}_0 and \tilde{v}_2 are the linear velocity responses of electrons to the high frequency electrostatic wave fields $\tilde{\phi}_1, \tilde{\phi}_0$ and $\tilde{\phi}_2$ respectively. Using the electron continuity equation and momentum equation, these velocity responses can be determined in terms of the corresponding wave field. The results are then substituted into Eq.(3), leading to

$$\begin{aligned} & (\omega_s^2 + i\nu_i\omega_s - k^2 C_s^2) (\tilde{n}_s/n_0) = \\ & (m/M) \{ (ekk_1\omega_1/m\omega_p)^2 / [\omega_p^2 - 3k^2\nu_{ie}^2(1 - \Omega_e^2/\omega_1^2)] \} \{ (1 + \Omega_e^2/\omega_1^2) (\tilde{\phi}_0\tilde{\phi}_1^* + \tilde{\phi}_1\tilde{\phi}_2^*) - \\ & [(1 + 2\Omega_e^2/\omega_1^2)(\omega_s/\omega_1) + i(1 + \Omega_e^2/\omega_1^2)(3k^2\nu_{ie}^2/\omega_p^2)(\nu_e/\omega_1)] (\tilde{\phi}_0\tilde{\phi}_1^* - \tilde{\phi}_1\tilde{\phi}_2^*) \} \quad (4) \end{aligned}$$

With the aid of Eq.(2), the coupling terms on the right hand side (RHS) of Eq.(4) can be expressed explicitly as

$$\begin{aligned} \tilde{\phi}_0 \tilde{\phi}_1^* + \tilde{\phi}_1 \tilde{\phi}_2^* = & (k_1 \omega_p / k_t)^2 \{ 2(k/k_t)^2 (\Omega_e^2 \omega_{kt}^2 / \omega_1^2 - 3k_t^2 v_{te}^2) / [(k/k_t)^4 (\Omega_e^2 \omega_{kt}^2 / \omega_1^2 - 3k_t^2 v_{te}^2)^2 \\ & + \omega_1^2 (v_e - 2i\omega_s)^2] \} |\tilde{\phi}_1|^2 (\tilde{n}_s / n_0) \end{aligned} \quad (5)$$

$$\tilde{\phi}_0 \tilde{\phi}_1^* - \tilde{\phi}_1 \tilde{\phi}_2^* = -i[\omega_1 (v_e - 2i\omega_s) / (k/k_t)^2 (\Omega_e^2 \omega_{kt}^2 / \omega_1^2 - 3k_t^2 v_{te}^2)] (\tilde{\phi}_0 \tilde{\phi}_1^* + \tilde{\phi}_1 \tilde{\phi}_2^*) \quad (6)$$

Substituting Eqs.(5) and (6) into Eq.(4), leads to the dispersion relation for the considered instability processes. It is noted that the contribution of Eq.(6) to the coupling terms on the RHS of Eq.(4) is, in general, very small because $|\omega_s|, v_e \ll \omega_1$. However, it may become significant as the denominator $\Omega_e^2 \omega_{kt}^2 / \omega_1^2 - 3k_t^2 v_{te}^2 \approx 0$, for the resonance case, in which both sidebands and the decay mode are the eigenmodes of the plasma, namely, $\omega_s \approx kC_s$ and $\omega_0^2 \approx \omega_2^2 \approx \omega_{kt}^2 + \Omega_e^2 k_1^2 / k_t^2 \approx \omega_{k1}^2 + \Omega_e^2 = \omega_1^2$.

III. Dispersion Relation and Analysis

We now derive and analyze the dispersion relation for the excitation of obliquely propagating Langmuir waves together with purely growing decay modes via the OTSI (as case A) and ion acoustic waves via the resonance instability (as case B) by the HF heater wave-generated upper hybrid pump waves.

A. Purely growing decay mode (ie., $\omega_s = i\gamma$) :

In this case, $|\Omega_e^2 \omega_{kt}^2 / \omega_1^2 - 3k_t^2 v_{te}^2| \gg (k_t/k)^2 \omega_1 (v_e + 2\gamma)$ and the ratio of Eq.(6) to Eq.(5) is very small. Thus, the second term on the RHS of Eq.(4) can be neglected and the dispersion relation is obtained, by substituting Eq.(5) into Eq.(4), to be

$$\begin{aligned}
 (\gamma^2 + v_{in}\gamma + k^2 C_s^2) = & \\
 & 2(m/M)(k/k_t)^4 (1 + \Omega_e^2 / \omega_1^2) (3k_t^2 v_{te}^2 - \Omega_e^2 \omega_{kt}^2 / \omega_1^2) (ek_1^2 \omega_1 \tilde{\phi}_1 / m)^2 / \\
 & [\omega_p^2 - 3k^2 v_{te}^2 (1 - \Omega_e^2 / \omega_1^2)] \{ (k/k_t)^4 (3k_t^2 v_{te}^2 - \Omega_e^2 \omega_{kt}^2 / \omega_1^2)^2 + \omega_1^2 (v_e + 2\gamma)^2 \} \quad (7)
 \end{aligned}$$

It is shown by the coupling term on the RHS of Eq.(7) that the instability process can occur only when $3k_t^2 v_{te}^2 > \Omega_e^2 \omega_{kt}^2 / \omega_1^2$. Near the instability threshold, ie., $\gamma \approx 0$, the coupling term is maximized under the condition $3k_t^2 v_{te}^2 - \Omega_e^2 \omega_{kt}^2 / \omega_1^2 = v_e \omega_1 (k_t/k)^2$. Thus, the minimum threshold field of the instability is found to be

$$|ek_1 \phi_1 / m \omega_1|_{th} = (v_e / \omega_1)^{1/2} (M/m)^{1/2} (k/k_t) [\omega_p^2 - 3k^2 v_{te}^2 (1 - \Omega_e^2 / \omega_1^2)]^{1/2} C_s / (\omega_1^2 + \Omega_e^2)^{1/2} \quad (8)$$

In terms of this minimum threshold field $\tilde{\phi}_{1th}$ given by Eq.(8), Eq.(7) can be expressed to be

$$(\bar{\gamma}^2 + \alpha^2) (2\bar{\gamma}^2 + 2\bar{\gamma} + 1) = \alpha^2 |\tilde{\phi}_1/\tilde{\phi}_{1th}|^2 \quad (9)$$

where $\bar{\gamma} = \gamma/v_e$ and $\alpha^2 = k^2 C_s^2 / v_e^2$. Eq. (9) is then solved approximately (for $\alpha > 1$) to obtain

$$\begin{aligned} \bar{\gamma} \cong \{ & (1/2) \{ [2|\tilde{\phi}_1/\tilde{\phi}_{1th}|^2 - 1]^{1/2} - 1 \} & \text{for } |\tilde{\phi}_1/\tilde{\phi}_{1th}| < \sqrt{2} \alpha \\ & [(\alpha/\sqrt{2}) |\tilde{\phi}_1/\tilde{\phi}_{1th}|]^{1/2} & \text{for } |\tilde{\phi}_1/\tilde{\phi}_{1th}| > \sqrt{2} \alpha \end{aligned} \quad (10)$$

It is noted that the condition $3k_t^2 v_{te}^2 > \Omega_e^2 \omega_{kt}^2 / \omega_1^2$ for the existence of the instability process is, in essence, the same as that of OTSI excited by a dipole pump, namely, the pump frequency is lower than the eigenfrequency of the sidebands.

B. Ion Acoustic Decay Mode (ie., $\Omega_e^2 \omega_{kt}^2 / \omega_1^2 = 3k_t^2 v_{te}^2$) :

In this case, the contribution of Eq.(5) to the first term on the RHS of Eq.(4) is zero. The dispersion relation is obtained by substituting Eq.(6) into Eq.(4) to be

$$\begin{aligned} (v_e - i2\omega_s) (\omega_s^2 + i\nu_i \omega_s - k^2 C_s^2) = \\ 2(m/M) \{ (ek k_1^2 \omega_1 / m k_i)^2 |\phi_1|^2 / \omega_1 [\omega_p^2 - 3k^2 v_{te}^2 (1 - \Omega_e^2 / \omega_1^2)] \} \\ \times [i(1 + 2\Omega_e^2 / \omega_1^2)(\omega_s / \omega_1) - (1 + \Omega_e^2 / \omega_1^2)(3k^2 v_{te}^2 / \omega_p^2)(v_e / \omega_1)] \end{aligned} \quad (11)$$

where $\nu_i = 2\Gamma_i$, twice the ion Landau damping rate. Let $\omega_s \cong kC_s + i\gamma$, Eq.(11) is reduced to

$$(2\gamma + \nu_e)(2\gamma + \nu_i) = A \quad (12)$$

where $A = 2(m/M) \{ (ek k_i^2 / mk_i)^2 (1 + 2\Omega_e^2 / \omega_1^2) |\tilde{\phi}_i|^2 / [\omega_p^2 - 3k^2 \nu_{te}^2 (1 - \Omega_e^2 / \omega_1^2)] \}$.

Thus, the threshold field of the instability is obtained, by setting $\gamma = 0$ in Eq.(12), to be

$$|ek_i \tilde{\phi}_{1th} / m\omega_1| = (M/2m)^{1/2} (\nu_e \nu_i)^{1/2} (k_i / k k_1) [\omega_p^2 - 3k^2 \nu_{te}^2 (1 - \Omega_e^2 / \omega_1^2)]^{1/2} / (\omega_1^2 + 2\Omega_e^2)^{1/2} \quad (13)$$

In terms of $\tilde{\phi}_{1th}$, the growth rate $\bar{\gamma}$ is obtained as

$$\bar{\gamma} = [(1 + \bar{\nu}_i^2 + 2\bar{\nu}_i |\tilde{\phi}_i / \tilde{\phi}_{1th}|^2) - 1 - \bar{\nu}_i] / 4 \quad (14)$$

where $\bar{\nu}_i = \nu_i / \nu_e$.

A much higher threshold field is required for the resonance mode case than for the nonresonance mode case as seen by dividing Eq.(13) by Eq.(8):

$$\begin{aligned} |\tilde{\phi}_{1th}|_{res}^2 / |\tilde{\phi}_{1th}|_{nonres}^2 &\cong \nu_i \omega_1 (\omega_1^2 + \Omega_e^2) / 2k^2 C_s^2 (\omega_1^2 + 2\Omega_e^2) \\ &= (\omega_1 / k C_s) \sqrt{\pi} / 8 \{ (m/M)^{1/2} + (T_e / T_i)^{3/2} \exp[-(3/2 + T_e / 2T_i)] \} \gg 1 \\ &\cong \sqrt{\pi} e^{-2.5} (\omega_1 / k C_s) \gg 1 \quad \text{for } T_e \cong 2T_i \end{aligned} \quad (15)$$

Therefore, the instability favorably excited by the upper hybrid pump generates a nonpropagating purely growing mode as the decay mode. Considering the heating experiments at Tromso, where the geomagnetic dip angle is about 78° , we adopt the following parameters for evaluating the threshold field and the growth rate of the instability: $\omega_1/2\pi=4\text{MHz}$, $\Omega_e/\omega_1=1/3$, $v_e=500 \text{ s}^{-1}$, $T_e \approx 2T_i=2000\text{K}$, $v_{te}=1.8 \times 10^5 \text{ m/s}$, $m/M=3.4 \times 10^{-5}$, and $C_s=1.66 \times 10^3 \text{ m/s}$.

The threshold field $\hat{E}_{1th}=|k_1\tilde{\phi}_{1th}|$ calculated from Eq.(8) is found to be

$$\hat{E}_{1th} = 0.15 [1 + (k/k_1)^2]^{1/2} \quad (\text{V/m}) \quad (16)$$

Thus, to convert the field-aligned upper hybrid wave (propagating perpendicular to the geomagnetic field) into up- or down-going Langmuir waves (propagating at 12° to the geomagnetic field), it requires $k/k_1=\cot 12^\circ=4.7$ and the threshold field obtained from Eq.(16) is about 0.7 V/m . Assuming that $\hat{E}_1 = |k_1\tilde{\phi}_1| = 1 \text{ V/m}$, the growth rate of the Langmuir waves propagating vertically (ie., having $k/k_1 = 4.7$) is obtained from Eq.(10) to be about 190 s^{-1} , ie., $\bar{\gamma} = 0.38$. Those Langmuir waves with $k/k_1 < 4.7$ have lower threshold fields and thus, higher growth rates. For example, Langmuir waves propagating at 45° with respect to the geomagnetic field have $k/k_1=1$ and thus, $\tilde{E}_{1th}=0.212 \text{ V/m}$ and $\gamma=1.4 \times 10^3 \text{ s}^{-1}$ (or $\bar{\gamma}=2.8$). However, those Langmuir waves propagate obliquely to the vertical direction and thus, are unable to be detected by the backscatter radars.

Because case A is the dominant process, thus, the frequencies of the excited Langmuir waves are the same as those of the upper hybrid pump waves, which are

identical to the heater wave frequency. As afore-mentioned, the case A process can only occur when $3k_t^2 v_{te}^2 > \Omega_e^2 \omega_{kt}^2 / \omega_1^2 \cong \Omega_e^2$. Substituting the parametric values into this inequality, it leads to $\lambda_t < 0.23$ m. Since the wavelengths of the plasma lines detected by EISCAT 933 MHz UHF and 224 MHz VHF radars are 0.161 m and 0.67 m respectively, it explains why the EISCAT UHF radar has detected the ‘ OTSI line’ (ie. zero off-set frequency line), while the EISCAT VHF radar has not [see Stubbe et al., 1992].

IV. Conclusion

A parametric instability process which renders the decay of an upper hybrid pump wave into two obliquely propagating Langmuir sidebands and a purely growing mode is studied. The results show that the Langmuir waves can be excited in milliseconds and have a broad angular distribution. However, the wavelengths of the Langmuir waves are limited to $\lambda_e < 0.23$ m. Thus, the proposed process can be based on to understand why the EISCAT 933 MHz backscatter radar (half wavelength=0.161 m < 0.23 m) but not the 244 MHz radar (half wavelength=0.67 m > 0.23 m) can detect the Langmuir waves which have a zero off-set frequency [Stubbe et al., 1992].

The other outstanding feature observed at Tromso is that the intensity ratio of the OTSI plasma lines to the PDI lines is virtually independent of the input heater power. The OTSI lines are radar-detected Langmuir waves with zero off-set frequency from the heater wave frequency, while the PDI lines are those with frequencies off-set from the heater wave frequency by the ion acoustic wave frequency. This feature can be understood by means of the following facts : (1) the upper hybrid pump waves producing the OTSI lines can be generated by the HF heater wave via the mode conversion process [Mjølhus, 1990], which requires no threshold, and (2) the threshold of the PDI process can be easily exceeded in Tromso experiments. In other words, both the OTSI plasma lines and the PDI lines can be produced by rather low heater power. Consequently, the intensity ratio of the OTSI to PDI lines is not sensitive to the variation of the heater power. In the present work, the wave vectors of the excited purely growing (ie., zero-frequency) modes are

modes propagating at a small but finite angle with respect to the geomagnetic field can also be excited by the upper hybrid waves. These obliquely propagating, namely, zero-frequency modes can contribute to the zero-frequency component (known as the central line) of the ion line spectrum detected by the EISCAT UHF (933 MHz) radar [Stubbe et al., 1992].

Acknowledgments

The author gratefully acknowledges useful discussions with M. C. Lee, Keith Groves, Ed Weber, Paul Kossey, and John Heckscher. This work was completed at the Air Force Phillips Laboratory, Hanscom AFB, Massachusetts, whose hospitality is appreciated.

References

- Carlson, H. C., W. E. Gordon, and R. L. Showen, High-frequency induced enhancements of the incoherent scatter spectrum at Arecibo, *J. Geophys. Res.*, 77, 1242, 1972.
- Diuth, F. T., M. P. Sulzer, and J. H. Elder, High-resolution observations of the HF-induced plasma waves in the ionosphere, *Geophys. Res. Lett.*, 17, 1893, 1990.
- Fejer, J. A., Ionospheric modification and parametric instabilities, *Rev. Geophys.*, 17, 135, 1979.
- Fejer, J. A. and Y. Y. Kuo, Structure in the nonlinear saturation spectrum of parametric instabilities, *Phys. Fluids*, 16, 1490, 1973.
- Hagfors, T., W. Kofman, H. Kopka, P. Stubbe, and T. Aijanen, Observations of enhanced plasma lines by EISCAT during heating experiments, *Radio Sci.*, 18, 861, 1983.
- Huang, J. and S. P. Kuo, Cyclotron harmonic effect on the thermal oscillating two-stream instability in the high latitude ionosphere, *J. Geophys. Res.*, 99, 2173, 1994.
- Isham, B., W. Kofman, T. Hagfors, J. Nordling, B. Thide, C. LaHoz, and P. Stubbe, New phenomena observed by EISCAT during an RF ionospheric modification experiment, *Radio Sci.*, 25, 251, 1990.
- Kuo, S. P., Criteria for excitation of parametric instability in the ionosphere by an obliquely incident high-frequency heater, *Phys. Fluids B*, 4, 1012, 1992.
- Lee, M. C. and S. P. Kuo, Excitation of upper hybrid waves by a thermal parametric instability, *J. Plasma Phys.*, 30, 463, 1983.
- Leyser, T. B., Parametric interaction between upper hybrid and lower hybrid waves in heating experiments, *Geophys. Res. Lett.*, 18, 408, 1991.

- Leyser, T. B., Electromagnetic radiation by parametric decay of upper hybrid waves in ionospheric modification experiments, *Phys. Plasmas*, 1, 2003, 1994.
- Mjølhus, E., On linear conversion in a magnetized plasma, *Radio Sci.*, 25, 3121, 1990.
- Perkins, F. W., C. Oberman, and E. J. Valeo, Parametric instabilities and ionospheric modification, *J. Geophys. Res.*, 79, 1478, 1974.
- Stenflo, L., Stimulated scattering of large amplitude wave in the ionosphere, *Phys. Scr.*, T30, 166, 1990.
- Stubbe, P., H. Kopka, T. B. Jones, and T. Robinson, Wideband attenuation of radio waves caused by powerful HF waves: saturation and dependence on ionospheric variability, *J. Geophys. Res.*, 87, 1151, 1982.
- Stubbe, P., H. Kopka, B. Thide, and H. Derblom, Stimulated electromagnetic emission: a new technique to study the parametric decay instability in the ionosphere, *J. Geophys. Res.*, 89, 7523, 1984.
- Stubbe, P., et al., Ionospheric modification experiments with the Tromsø heating facility, *J. Atmos. Terr. Phys.*, 47, 1151, 1985.
- Stubbe, P., H. Kohl, and M. T. Rietveld, Langmuir turbulence and ionospheric modification, *J. Geophys. Res.*, 97, 6285, 1992.
- Zhou, H. L., J. Huang, and S. P. Kuo, Cascading of the upper hybrid/electron Bernstein wave in the ionospheric heating experiments, *Phys. Plasmas*, 1, 3044, 1994.

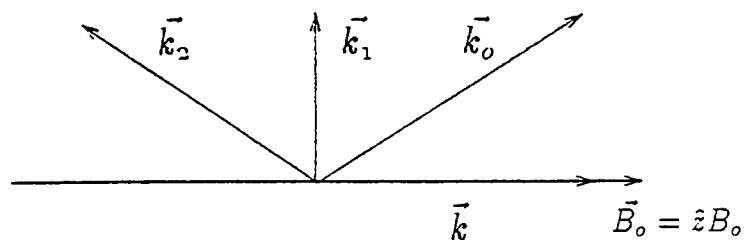


Fig.1 Wave vector matching diagram. Here, k_1 , k_0 (k_2), k , and B_0 denote the wave vectors of the upper hybrid pump wave, the up-shifted (down-shifted) Langmuir sideband wave, and the ion decay mode, respectively, and the geomagnetic field.

H2 REACTIONS AT DANGLING BONDS IN SiO2

Henry A. Kurtz
Professor
Department of Chemistry

University of Memphis
Memphis, TN 36152-6060

Final Report for:
Summer Research Program
Phillips Laboratory

Sponsored by:
Air Force Office of Scientific Research
Bolling Air Force Base, Washington, DC

And

Phillips Laboratory

September 1997

H₂ REACTIONS AT DANGLING BONDS IN SiO₂

Henry A. Kurtz
Professor
Department of Chemistry
University of Memphis

Abstract

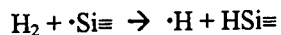
The hydrogen passivation reaction at the dangling bond on an E' center in SiO₂ is studied using the model reaction $\text{H}_2 + \cdot\text{Si}(\text{OH})_3 \rightarrow \cdot\text{H} + \text{HSi}(\text{OH})_3$. A study of the energetics of this reaction at the Hartree-Fock and MP2 level is presented with a variety of basis sets. Direct dynamics calculations are also performed to evaluate rate constants and activation energies for the process, with and without the inclusion of quantum tunneling effects. The results are compared to an experimental value for the activation energy of H₂ annealing of E' centers.

H₂ REACTIONS AT DANGLING BONDS IN SiO₂

Henry A. Kurtz

I. INTRODUCTION

The passivation of reactive defects due to unfilled valences of Si atoms (called dangling bonds) in amorphous silicon dioxide by H₂ is thought to proceed via the reaction



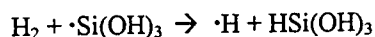
where the symbol \equiv represents the three satisfied valences (bonds).¹ This is a very general reaction that may take place both at the Si/SiO₂ interface and in bulk SiO₂. At the interface the three bonds are to other silicon atoms and the defect is known as a P_b center. In the bulk SiO₂ the three bonds are to oxygen atoms and is part of an E' center. It is these latter defects that will be the focus of this work.

Hydrogen annealing of E' centers has been studied by Li *et al.*² They used ESR measurements of E' center concentrations to estimate rate constants and an activation energy for the annealing process. The activation energy they obtained is 0.3 eV and was attributed to a process like the one shown above. However, the experiment is not really able to identify the actual molecular processes for which the activation energy was measured. An alternate explanation for this results could be the measured activation energy is due to H₂ complexation or some other physical process. The activation associated with diffusion of H₂ in amorphous SiO₂ is 0.38 eV, about the same size.³ Edwards^{4,1} performed Hartree-Fock calculations on model systems to estimate an activation energy for this process of around 0.7 eV – much larger than the experimental value. Edwards further suggested that the discrepancy may arise because quantum tunneling effects were not included. He estimated that the tunneling corrections may lower the theoretical activation energy to about 0.1 eV – now much lower than Li *et al.*'s experiment.

The goal of this Summer Faculty Research project is to re-examine the theoretical methods and models for H₂ reactions with Si dangling bonds in SiO₂ and to calculate rate constants for this process via direct dynamics, with and without tunneling.

II. ENERGETICS

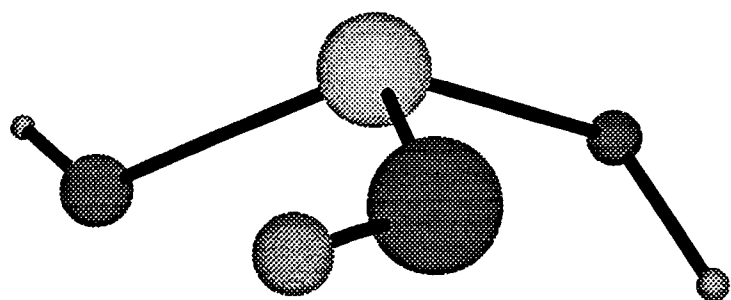
The first model studied in this work for the reactions is the small cluster reaction:



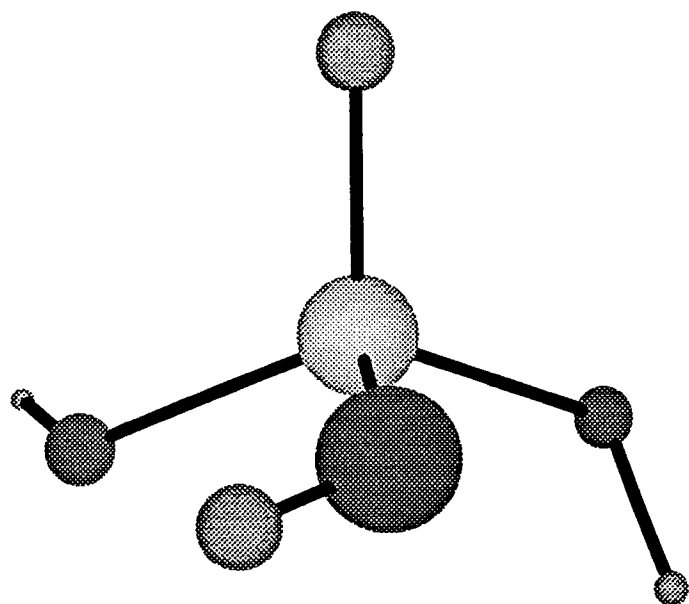
which is one of the cluster models used by Edwards.⁴ The energetics of the model reaction is studied by calculating the molecular structure and energies of the reactants and products. The reactants and products are characterized by having all positive harmonic vibrational frequencies (i.e., all positive second derivatives of the energy with respect to atomic motion). The energetic barrier to the reaction is found by calculating the molecular structure and energy corresponding to the highest point on the minimum energy pathway connecting the reactants and products. This point is called the transition state or transition structure (TS). The transition structure corresponds to a saddle point on the potential energy surface and is characterized by having one, and only one, imaginary vibrational frequency (i.e., having one negative eigenvalue of the matrix of energy second derivatives).

This model is small enough that a good test of the methods for obtaining energies and structures can be performed. Initially, for each of the reactants, products, and transition structure, the molecular structures were optimized using the unrestricted Hartree-Fock method (UHF) for the radical, open-shell species and restricted Hartree-Fock (RHF) for the closed shell species. The 6-31G** one-electron basis set was used.⁵ This is a standard split-valence basis set augmented by polarization functions on all atoms (d-functions on the Si and O atoms and p-functions on the H atoms). For this study, the 6-31G** basis set used for Si was the one developed by Gordon and co-workers.⁶ The resulting structures for $\cdot\text{Si}(\text{OH})_3$, $\text{HSi}(\text{OH})_3$, and $\text{H-H-Si}(\text{OH})_3$ are shown in Figure 1. This model differs from the previous same sized model of Edwards³ in that no artificial symmetry was imposed. Each of the species other than H and H_2 are of C1 point group symmetry (i.e., no symmetry constraints). At this level of theory, the energy of the reaction ($E_{\text{products}} - E_{\text{reactants}}$) is -0.017 eV (-0.402 kcal/mole) - slightly exothermic. The activation energy for the reaction calculated as the energy difference $E_{\text{TS}} - E_{\text{reactants}}$ is 0.795 eV (18.341 kcal/mole). This value is considerably larger than the value of 0.3 eV obtained for the experiment of Li, *et al.*²

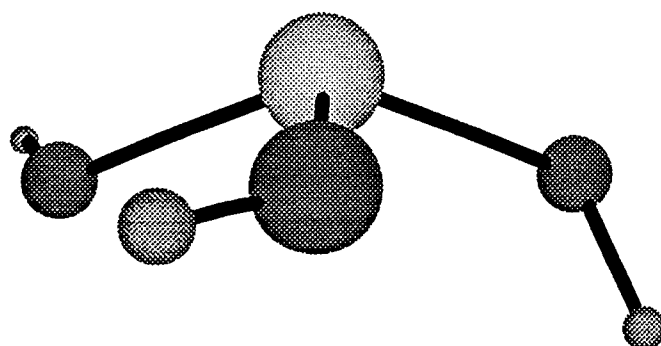
The first goal of this research project was to explore reasonable improvements in the methods used. Table 1 shows the energy of reaction obtained using improved one-electron basis sets and/or adding electron correlation effects via second-order Moller Plesset perturbation theory (MP2). In this table and the rest of this report, the notation Method1(basis1)//Method2(basis2) refers to calculations done using method 1 (either Hartree-Fock or MP2) with basis set 1 at an optimized geometry obtained from method 2 with basis set 2. For example, MP2(6-31G**++)//UHF(6-31G**) uses energies obtained from an MP2 calculation using the 6-31G**++ basis set with the molecular geometries from an UHF calculation using a 6-31G** basis set. The structure and energy results presented in this report were obtained using the GAMESS⁷ and GAUSSIAN94⁸ programs.



Si(OH)₃



HSi(OH)₃



H-H-Si(OH)₃

Figure 1

Table 1: Reaction Energies for $\text{H}_2 + \cdot\text{Si}(\text{OH})_3 \rightarrow \cdot\text{H} + \text{HSi}(\text{OH})_3$

UHF(6-31G**)/UHF(6-31G**)	-0.0006405 a.u.	-0.017 eV	-0.402 kcal/mole
UHF(6-311G**)/UHF(6-31G**)	-0.0024469 a.u.	-0.067 eV	-1.535 kcal/mole
UHF(6-31G****)/UHF(6-31G**)	0.0022961 a.u.	0.062 eV	1.441 kcal/mole
UHF(6-31G**)/MP2(6-31G**)	-0.0008755 a.u.	-0.024 eV	-0.549 kcal/mole
UHF(6-31G****)/MP2(6-31G**)	0.0020546 a.u.	0.056 eV	1.289 kcal/mole
MP2(6-31G**)/UHF(6-31G**)	0.0068737 a.u.	0.187 eV	4.313 kcal/mole
MP2(6-311G**)/UHF(6-31G**)	0.0036013 a.u.	0.098 eV	2.260 kcal/mole
MP2(6-31G****)/UHF(6-31G**)	0.0097772 a.u.	0.266 eV	6.135 kcal/mole
MP2(6-31G**)/MP2(6-31G**)	0.0070781 a.u.	0.193 eV	4.442 kcal/mole
MP2(6-31G****)/MP2(6-31G**)	0.0101345 a.u.	0.276 eV	6.360 kcal/mole

Basis set improvements, as illustrated by the first three rows of Table 1, have contradictory effects but the magnitudes are very small. In the 6-311G** basis set, the size of the one-electron basis used to describe the valence shell is increased and, in the 6-31G**** basis set, extra diffuse functions were added to each atom. Calculations on the combined basis set (6-311G****) are underway currently. The inclusion of electron correlation at the MP2 level has a larger effect on the results – changing the essentially energy neutral reaction into definitely being endothermic. However, the resulting reaction energy is still quite small. Table 1 also illustrates that the overall energetics of this reaction are not particularly sensitive to geometry – results based on UHF structures agree quite well with results based on MP2 structures. Allendorf *et al.*⁹ obtained an MP4/6-31G* estimate of $\Delta H^\circ(298\text{K})$ of 3.30 kcal/mole, close to the MP2 estimate here. Further improvements in the theory maybe be needed to refine the reaction energy but no significant change is expected.

The main quantities of interest in this study are the activation energies for the reaction of $\text{H}_2 + \cdot\text{Si}(\text{OH})_3$ and these results are shown in Table 2. The important thing to note is that there is very little variation in the computed activation energy with improvements in the basis sets or with the inclusion of electron correlation. It seems very unlikely that making further improvements of this type will change the activation barrier out of the 0.7-0.8 eV range – still quite far from the experimental value of 0.3 eV.

Table 2. Activation Energy for $\text{H}_2 + \cdot\text{Si}(\text{OH})_3$

UHF(6-31G**)/UHF(6-31G**)	0.0292279 a.u.	0.795 eV	18.341 kcal/mole
UHF(6-311G**)/UHF(6-31G**)	0.0277876 a.u.	0.756 eV	17.437 kcal/mole
UHF(6-31G****)/UHF(6-31G**)	0.0320129 a.u.	0.871 eV	20.089 kcal/mole
UHF(6-31G**)/MP2(6-31G**)	0.0288851 a.u.	0.786 eV	18.126 kcal/mole
UHF(6-31G****)/MP2(6-31G**)	0.0316718 a.u.	0.862 eV	19.874 kcal/mole
MP2(6-31G**)/UHF(6-31G**)	0.0272257 a.u.	0.741 eV	17.084 kcal/mole
MP2(6-311G**)/UHF(6-31G**)	0.0230080 a.u.	0.626 eV	14.438 kcal/mole
MP2(6-31G****)/UHF(6-31G**)	0.0294786 a.u.	0.802 eV	18.498 kcal/mole
MP2(6-31G**)/MP2(6-31G**)	0.0274339 a.u.	0.747 eV	17.215 kcal/mole
MP2(6-31G****)/MP2(6-31G**)	0.0292858 a.u.	0.797 eV	18.377 kcal/mole

It is also possible to compute the activation energy of the reverse, de-passivation reaction where a hydrogen atom picks off the bound H to form H₂ and the dangling bond defect. The activation energies obtained for this process are shown in Table 3. Unlike the H₂ reaction, the activation energy for this reverse process changes significantly with the inclusion of electron correlation. To my knowledge, there has been no experimental determination of this quantity.

Table 3: Activation Energy for $\cdot\text{H} + \text{HSi}(\text{OH})_3$

UHF(6-31G**)/UHF(6-31G**)	0.0298684 a.u.	0.813 eV	18.742 kcal/mole
UHF(6-311G**)/UHF(6-31G**)	0.0302345 a.u.	0.823 eV	18.972 kcal/mole
UHF(6-31G**++)/UHF(6-31G**)	0.0297168 a.u.	0.809 eV	18.648 kcal/mole
UHF(6-31G**)/MP2(6-31G**)	0.0297606 a.u.	0.810 eV	18.675 kcal/mole
UHF(6-31G**++)/MP2(6-31G**)	0.0296172 a.u.	0.806 eV	18.585 kcal/mole
MP2(6-31G**)/UHF(6-31G**)	0.0203519 a.u.	0.554 eV	12.771 kcal/mole
MP2(6-311G**)/UHF(6-31G**)	0.0194067 a.u.	0.528 eV	12.178 kcal/mole
MP2(6-31G**++)/UHF(6-31G**)	0.0197014 a.u.	0.536 eV	12.363 kcal/mole
MP2(6-31G**)/MP2(6-31G**)	0.0203558 a.u.	0.554 eV	12.773 kcal/mole
MP2(6-31G**++)/MP2(6-31G**)	0.0191513 a.u.	0.521 eV	12.018 kcal/mole

In order to explore the importance of using bigger clusters that include next-nearest neighbor effects, the model was expanded by adding another set of Si atoms, leading to the following reaction



At the UHF(6-31G**)/UHF(6-31G**) level of theory, using this larger cluster model had very little effect. The reaction energy changed from -0.017 eV to 0.004 eV (still an essentially energy neutral reaction), the H₂ reaction activation energy changed from 0.795 to 0.817 eV, and the H reaction activation energy did not change from the 0.813 eV value. Further work with this model is currently underway to evaluate larger basis sets and structure optimization with the MP2 theory.

III. Generalized TST Theory

In order to calculate “correct” activation energies (i.e., the way it is done from experimental data) rate constants at different temperatures must be calculated for the process of interest. The method chosen in this work for obtaining rate constants is the generalized transition state theory (GTST) of Truhlar and co-workers¹⁰ using direct dynamics based on our previously computed *ab initio* data. A very brief outline of the method will be given in this section, with the main emphasis on definition of the terms to be used. Detailed discussions and derivations

of GTST can be found elsewhere.¹⁰ All dynamics (rate constant) calculations presented here were done with the POLYRATE program.¹¹

Conventional transition state theory (TST) calculates the thermal rate constants by assuming that all transition state species came directly from reactants and will be converted into products. The rate is then the flux across a surface in phase space in the product direction. This rate is given by

$$k(T) = \frac{\sigma}{\beta h} \frac{Q(T)}{\Phi(T)} e^{-\beta V}$$

where β is $(k_B T)^{-1}$, h is Planck's constant, $Q(T)$ is the conventional transition state classical partition function with its zero of energy at the saddle point, $\Phi(T)$ is the reactants classical partition function with its zero of energy at the overall zero of energy, and V is the energy of the saddle point relative to the overall zero of energy.

The generalized transition state theory rate constant is obtained by varying the position of the dividing surface along the minimum energy path to minimize the value of the computed rate constant.

$$k^{GT}(T) = \min k^{GT}(T, s) = k^{GT}(T, s^{CVT}(T))$$

where

$$k^{GT}(T, s) = \frac{\sigma}{\beta h} \frac{Q(T, s)}{\Phi(T)} e^{-\beta V_{MEP}(s)}$$

Results from this generalized treatment will be referred to as canonical variational theory (CVT). CVT corresponds to a maximum free energy of activation and includes both "entropic" and energetic effects and has been demonstrated to be more accurate than TST.

To obtain TST and CVT rate constants all that is needed are the partition functions Q and Φ . In this work, the separable, harmonic approximation is used which neglects that couplings between the electronic, vibrational, and rotational energies. The partition function can then be written as

$$Q(T, s) = Q_{el}(T, s) Q_{vib}(T, s) Q_{rot}(T, s).$$

The formulas for each of these partition functions are discussed in detail in reference 10. Using only one electronic surface, Q_{el} depends on the degeneracy of the electronic state, Q_{vib} depends on the harmonic vibrational frequencies, and Q_{rot} depends on the moments of inertia. All these quantities are easily calculated from the structural and energetic data discussed previously.

The above two methods give a hybrid treatment of the rate constant in that motion in the degrees of freedom orthogonal to the reaction path are treated quantum mechanically and motion along the reaction path is treated classically - neglecting quantum tunneling effects. This means that k^{CVT} often underestimates the rate, particularly at low temperatures. One way to include quantum reaction path effects is via a multiplicative transmission coefficient as

$$k^{CVT/Y}(T) = \kappa^{CVT/Y}(T) k^{CVT}(T)$$

For the reactions studied in this work, the method chosen for obtaining the κ factors is the small reaction-path curvature method.^{10,12} In this method the κ factor is calculated via

$$\kappa(T) = \frac{\int_0^\infty P(E) e^{-E/k_B T} dE}{\int_{E^*(T)}^\infty e^{-E/k_B T} dE}$$

where $E^*(T)$ is the quasiclassical ground-state threshold energy. The approximation for $P(E)$ used in this work is the centrifugal-dominant small-curvature adiabatic ground-state approximation (SCT), which gives

$$P(E) = \frac{1}{\{1 + e^{-2\theta(E)}\}}$$

where $\theta(E)$ is the imaginary action integral evaluated along the tunneling path,

$$\theta(E) = \frac{2\pi}{h} \int_{s_l}^{s_r} \sqrt{2\mu_{\text{eff}}(s) |E - V_a(s)|} ds$$

where s_l and s_r are the reaction coordinate turning points.

A detailed description of this procedure is given by references 10 and 12. The essential feature is that centrifugal effect is included by replacing the reduced mass by an effective reduced mass, $\mu_{\text{eff}}(s)$ in the action integral. A special case of the SCT approximation is called the zero-curvature tunneling approximation (ZCT) and is obtained by setting $\mu_{\text{eff}}(s)$ equal to μ . The effect of this is to include tunneling only along the minimum energy path.

IV. Dynamics Results

In order to perform the direct dynamics calculations including tunneling as discussed above, many points along the internist reaction coordinate (IRC) [also known as the minimum energy path (MEP)] are needed.¹³ Examples of direct dynamics calculations are given for the reaction $\text{OH} + \text{HCl} \rightarrow \text{Cl} + \text{H}_2$ ¹⁴ and the similar reaction $\text{CH}_4 + \text{H} \rightarrow \text{CH}_3 + \text{H}_2$ ¹². The large computational effort for direct dynamics comes from the fact that at each point along the IRC, the geometry, potential energy, energy gradient vector and the hessian (energy second-derivative) matrix is needed. In the present study 83 points were used along the IRC - the reactants, the products, the TS, and 40 points on each side of the TS. The calculated potential energy along the IRC is shown in Figure 2. The reaction coordinate is a mass-weighted cartesian coordinate and is arbitrarily set to + toward the reactants and - toward the products.

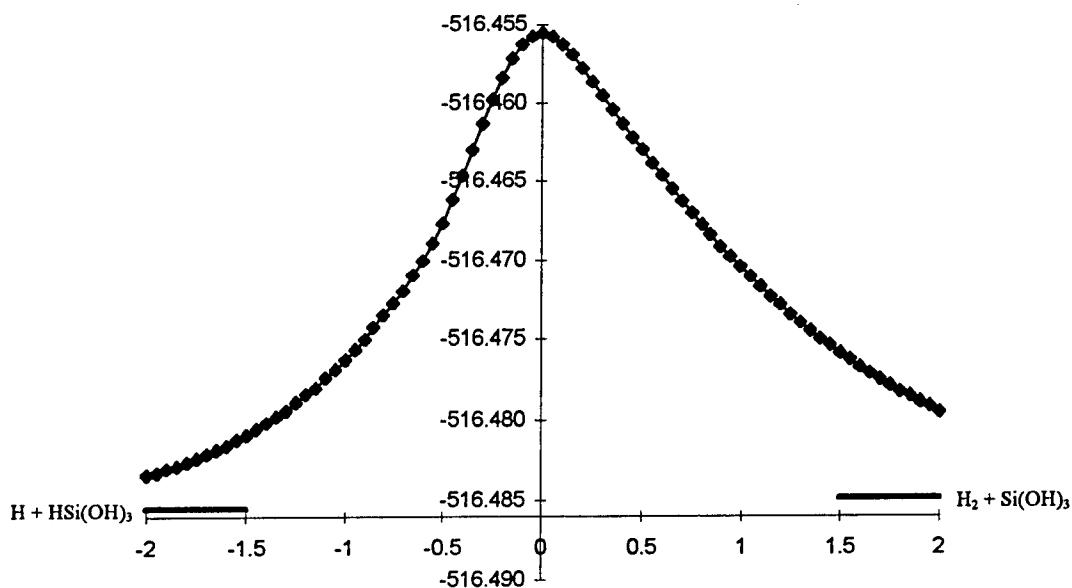


Figure 2: UHF(6-31G**) IRC Potential Energy Curve

In addition to its use in direct dynamics, the IRC is the only way to verify that the TS calculated is the correct one for the reaction of interest, i.e. it connects the reactants and products. Figure 3 shows how the H-H and H-Si distances vary along the IRC indicating the loss of H₂ toward the right (indicating the correct reactants) and loss of H toward the left (indicating the correct products).

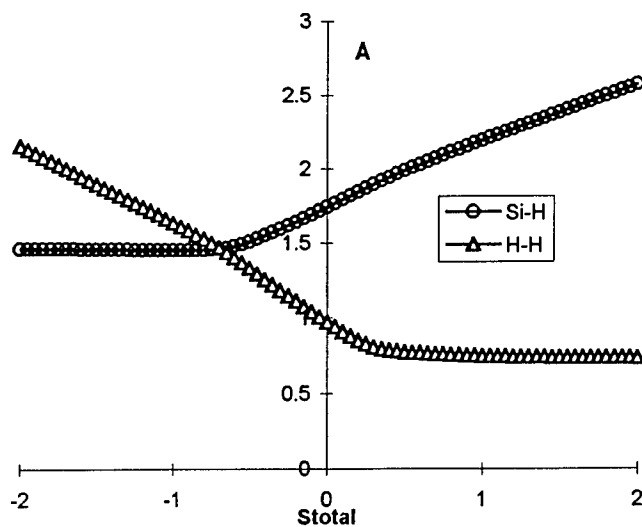


Figure 3: Important Internal Coordinate Changes Along the IRC

Table 4 shows the rate constants for the reaction $\text{H}_2 + \cdot\text{Si}(\text{OH})_3 \rightarrow \cdot\text{H} + \text{HSi}(\text{OH})_3$. As they should be, the k^{CVT} values are always slightly lower than the k^{TST} values, but for this system the difference is very slight. The $k^{\text{CVT/ZCT}}$ and $k^{\text{CVT/SCT}}$ values show that tunneling is indeed important at low temperatures, making about a two order of magnitude increase in the rate at room temperature.

Table 4: Rate Constants for $\text{H}_2 + \cdot\text{Si}(\text{OH})_3$ ($\text{cm}^3/\text{molecule}\cdot\text{sec}$)

T(K)	TST	CVT	CVT/ZCT	CVT/SCT
100	4.98×10^{-50}	4.65×10^{-50}	2.89×10^{-34}	8.13×10^{-31}
200	1.96×10^{-31}	1.92×10^{-31}	2.48×10^{-28}	7.76×10^{-27}
298	2.63×10^{-25}	2.60×10^{-25}	3.68×10^{-24}	2.16×10^{-23}
400	4.31×10^{-22}	4.28×10^{-22}	1.66×10^{-21}	4.53×10^{-21}
667	3.16×10^{-18}	3.15×10^{-18}	4.98×10^{-18}	7.15×10^{-18}
1000	3.75×10^{-16}	3.74×10^{-16}	4.54×10^{-16}	5.33×10^{-16}
1500	1.33×10^{-14}	1.32×10^{-14}	1.43×10^{-14}	1.54×10^{-14}

In order to extract values for the activation energy of this process the rate constant data is fit to the Arrhenius equation

$$k(T) = Ae^{-E_a/RT}$$

where E_a is the activation energy, A is referred to as the pre-exponential factor, and R is the Ideal Gas constant. This is the same fitting procedure Li, et al.² used to obtain their experimental rate constants. If the natural logarithm is taken of both sides of the Arrhenius equation, the following expression is obtained after some rearrangement

$$-\ln(k) = -\ln(A) + \frac{E_a}{R} \left(\frac{1}{T} \right)$$

This equation shows that the slope of a plot of $-\ln(k)$ vs. $1/T$ gives the activation energy. Plots of this type are shown in Figure 4 for the data from Table 4.

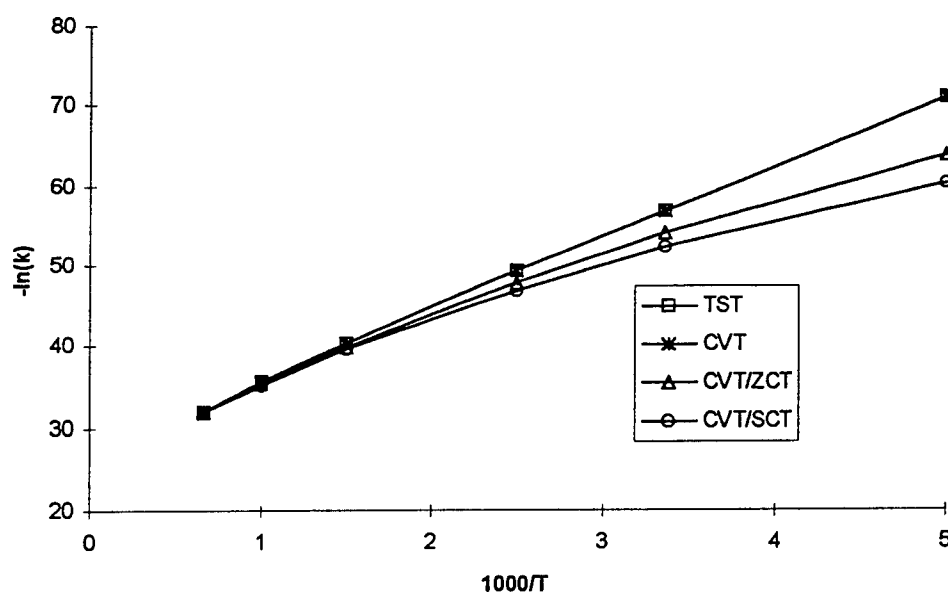


Figure 4: Plot of $-\ln(k)$ vs. $1000/T$

The value of the activation energy obtained from plots like these in Figure 4 clearly depend on the temperature range used to fit to the $-\ln(k)$ vs. $1/T$ equation. It is most obvious in the CVT/ZCT and CVT/SCT plots that the slope of the line increases with increasing T (decreasing $1/T$) and, therefore, the activation energy increases as a function of temperature. The experiments of Li et al.² used data over the temperature range of 23 °C to 299 °C (296 K - 473 K), so for comparison the range 298 K - 400 K will be used to extract activation energy estimates. A summary of activation energy results for the reaction of $H_2 + \cdot Si(OH)_3$ are shown in Table 5.

Table 5: Activation Energies for H_2 reaction

Method	E_a (eV)	E_a (kcal/mole)
$E_{TS} - E_{\text{reactants}}$	0.80	18.34
$E_{TS} - E_{\text{reactants}} + \text{ZPE}$	0.75	17.25
TST	0.75	17.19
CVT	0.75	17.20
CVT/ZCT	0.62	14.21
CVT/SCT	0.54	12.41
Experiment	0.3	6.9

The best direct dynamics estimate of 0.54 eV is indeed smaller than the .75 eV value obtained only from the energetics of the stationary points on the potential energy surface but is still larger than the 0.3 eV experimental quantity.

The rate and activation energy data is also obtained for the reverse reaction of $\cdot\text{H} + \text{HSi}(\text{OH})_3$ and this data is shown in Tables 6 and 7. These results indicate that, at the UHF(6-31G**) level, the reverse reaction is of comparable rate to the $\text{H}_2 + \cdot\text{Si}(\text{OH})_3$ reaction and that the activation energy for this process is also similar.

Table 6: Rate Constants for $\cdot\text{H} + \text{HSi}(\text{OH})_3$ ($\text{cm}^3/\text{molecule}\cdot\text{sec}$)

T(K)	TST	CVT	CVT/ZCT	CVT/SCT
100	5.55×10^{-50}	5.18×10^{-50}	3.23×10^{-34}	9.08×10^{-31}
200	2.04×10^{-30}	2.00×10^{-30}	2.59×10^{-27}	8.12×10^{-26}
298	6.80×10^{-24}	6.73×10^{-24}	9.51×10^{-23}	5.59×10^{-22}
400	1.89×10^{-20}	1.88×10^{-20}	7.32×10^{-20}	1.99×10^{-19}
667	2.62×10^{-16}	2.61×10^{-16}	4.13×10^{-16}	5.93×10^{-16}
1000	3.97×10^{-14}	3.96×10^{-14}	4.81×10^{-14}	5.65×10^{-14}
1500	1.44×10^{-12}	1.44×10^{-12}	1.56×10^{-12}	1.58×10^{-12}

Table 7: Activation Energies H Reaction

Method	E_a (eV)	E_a (kcal/mole)
$E_{\text{TS}} - E_{\text{reactants}}$	0.81	18.74
$E_{\text{TS}} - E_{\text{reactants}} + \text{ZPE}$	0.77	17.85
TST	0.80	18.42
CVT	0.80	18.43
CVT/ZCT	0.67	15.43
CVT/SCT	0.59	13.64

Since structural and energetic information has been calculated for the reactants, products, and transition structure at the MP2(6-31G**) level, correlation effects on the rate constant and activation energy at the TST level have been computed and are shown in Table 8. The MP2 rates are much faster than the corresponding UHF rates but the activation energy for the $\text{H}_2 + \cdot\text{Si}(\text{OH})_3$ process only slightly lowered. The activation energy for the reverse $\cdot\text{H} + \text{HSi}(\text{OH})_3$ process, however shows a significant lowering at the TST level. Clearly, the tunneling calculations are needed. However, based on the fact that the imaginary frequency of the MP2 transition structure is of smaller

magnitude than the imaginary frequency of the UHF transition structure, the reaction barrier is wider (smaller curvature) at the top and the tunneling effects should be smaller, at least at higher temperatures.

Table 8: TST data from MP2(6-31G**) Calculations

	$\text{H}_2 + \cdot\text{Si}(\text{OH})_3$	$\cdot\text{H} + \text{HSi}(\text{OH})_3$
Temperature (K)	Rate Constant ($\text{cm}^3/\text{molecule}\cdot\text{sec}$)	Rate Constant ($\text{cm}^3/\text{molecule}\cdot\text{sec}$)
100	1.03×10^{-46}	2.29×10^{-36}
298	1.18×10^{-23}	8.25×10^{-19}
400	1.18×10^{-20}	1.82×10^{-16}
667	4.84×10^{-17}	1.29×10^{-13}
1000	4.31×10^{-15}	4.43×10^{-12}
1500	1.26×10^{-13}	5.95×10^{-11}
Activation Energy (eV)	0.70	0.54

Table 9 shows some preliminary results at the TST level for the model reaction with a larger cluster. The results are nearly the same as the smaller cluster which indicates that simply increasing the size of the cluster by adding next-nearest neighbors has little effect on the chemistry.

Table 9: TST data from UHF(6-31G**) Calculations

	$\text{H}_2 + \cdot\text{Si}(\text{OSiH}_3)_3$	$\cdot\text{H} + \text{HSi}(\text{OSiH}_3)_3$
Temperature (K)	Rate Constant ($\text{cm}^3/\text{molecule}\cdot\text{sec}$)	Rate Constant ($\text{cm}^3/\text{molecule}\cdot\text{sec}$)
100	5.22×10^{-51}	2.75×10^{-50}
200	6.86×10^{-32}	1.16×10^{-30}
298	1.38×10^{-25}	4.02×10^{-24}
400	2.80×10^{-22}	1.14×10^{-20}
667	2.63×10^{-18}	1.62×10^{-16}
1000	3.54×10^{-16}	2.49×10^{-14}
1500	1.36×10^{-14}	9.12×10^{-13}
Activation Energy (eV)	0.77	0.80

V. Conclusions

This study presented a method for obtaining activation energies that can be used to examine model reactions which are used to interpret experimental data. With respect to the model reaction



the inclusion of tunneling effects at the UHF(6-31G**) level of calculation lowered the activation energy toward the experimental value but a sizable discrepancy still exists.

Current work is underway to continue this study and future work is planned. For the model reaction above, the direct dynamics including tunneling based on an IRC from a method with electron correlation (at least at the MP2 level) needs to be done. In addition, further benchmark calculations at a higher level of theory need to be done to firmly establish the relative energies of the reactants, products, and transition structure. The next steps in modeling the reaction of H_2 at E' centers is to develop better model system that include important interaction in bulk SiO_2 that are missing in the current cluster picture - such as nearby non-bonded oxygen atoms and the positive charged part of the E' center. The thermodynamics and kinetics of reactions at other sites (such as the positively charged centers) are also planned.

VI. Acknowledgments

RDL and AFOSR are gratefully acknowledged for supporting this work. I would also like to thank all the people at Phillips lab for making this a very productive period. The Maui HPCC is also acknowledged for computer support - without which most of these calculations could not have been performed.

V. References

1. A. H. Edwards, J. A. Pickard, and R. E. Stahlbush, *J. Non-Cryst. Solids* **179**, 148 (1994).
2. Z. Li, S. J. Fonash, E. H. Poindexter, M. Harmatz, F. Rong and W. R. Buchwald, *J. Non-Cryst. Solids* **126**, 173 (1990).
3. J. E. Shelby, *J. Appl. Phys.* **48**, 3387 (1977).
4. A. H. Edwards, *J. Non-Cryst. Solids* **187**, 232 (1995).
5. R. Ditchfield, W. J. Hehre, J. A. Pople, *J. Chem. Phys.* **54**, 724 (1971); W. J. Hehre, R. Ditchfield, J. A. Pople, *J. Chem. Phys.* **56**, 2257 (1972).
6. M. S. Gordon *Chem. Phys. Lett.* **76**, 163 (1980).
7. M. W. Schmidt, K. K. Baldridge, J. A. Boatz, S. T. Elbert, M. S. Gordon, J. H. Jensen, S. Koseki, N. Matsunaga, K. A. Nguyen, S. J. Su, T. L. Windus, M. Dupuis, J. A. Montgomery, *J. Comput. Chem.* **14**, 1347 (1993)
8. Gaussian 94, Revision E.2, M. J. Frisch, G. W. Trucks, H. B. Schlegel, P. M. W. Gill, B. G. Johnson, M. A. Robb, J. R. Cheeseman, T. Keith, G. A. Petersson, J. A. Montgomery, K. Raghavachari, M. A. Al-Laham, V. G. Zakrzewski, J. V. Ortiz, J. B. Foresman, J. Cioslowski, B. B. Stefanov, A. Nanayakkara, M. Challacombe, C. Y. Peng, P. Y. Ayala, W. Chen, M. W. Wong, J. L. Andres, E. S. Replogle, R. Gomperts, R. L. Martin, D.

- J. Fox, J. S. Binkley, D. J. Defrees, J. Baker, J. P. Stewart, M. Head-Gordon, C. Gonzalez, and J. A. Pople, Gaussian, Inc., Pittsburgh PA, 1995.
9. M. D. Allendorf, C. F. Melius, P. Ho, and M. R. Zachariah, *J. Phys. Chem.* **99**, 15285 (1995).
 10. D. G. Truhlar, A. D. Isaacson, and B. C. Garrett, "Generalized Transition State Theory", in *The Theory of Chemical Reaction Dynamics*, edited by M. Baer (CRC Press, Boca Raton, FL, 1985), Vol. 4, pp. 65-137.
 11. R. Steckler, Y.-Y. Chuang, P. L. Fast, E. L. Coitiño, J. C. Corchado, W.-P. Hu, Y.-P. Liu, G. C. Lynch, K. A. Nguyen, C. F. Jackels, M. Z. Gu, I. Rossi, S. Clayton, V. S. Melissas, B. C. Garrett, A. D. Isaacson, and D. G. Truhlar, POLYRATE-version 7.3.1, University of Minnesota, Minneapolis, 1997.
 12. T. H. Truong, *J. Chem. Phys.* **100**, 8014 (1994)
 13. K. K. Baldridge, M. S. Gordon, R. Stechkler, and D. G. Truhlar, *J. Phys. Chem* **93**, 5107 (1989).
 14. R. Steckler, G. M. Thruman, J. D. Watts, and R. J. Bartlett, *J. Chem. Phys.* **106**, 3926 (1997).